THE INTERPLAY OF GAS, DUST, AND MAGNETOROTATIONAL INSTABILITY IN MAGNETIZED PROTOPLANETARY DISKS

TIMMY N. DELAGE

August 2023

To my fantastic mum,
my wonderful cats,
my beloved ones...,

Dissertation

submitted to the

Combined Faculty of Mathematics, Engineering and Natural Sciences

of Heidelberg University, Germany

for the degree of

Doctor of Natural Sciences

Put forward by

M.Sc. Timmy N. Delage
born in: Colombes, France

Oral examination: November 8th, 2023

THE INTERPLAY OF GAS, DUST, AND MAGNETOROTATIONAL INSTABILITY IN MAGNETIZED PROTOPLANETARY DISKS

REFEREES:

PROF. DR. PAOLA PINILLA

PROF. DR. HENRIK BEUTHER

ABSTRACT

The rich diversity of exoplanets discovered in various physical environments clearly shows that planet formation is an efficient process with multiple outcomes. To understand the emergence of newborn planets, one can rewind the clock of planetary systems by investigating the formation and evolution of their natal environment, the so-called protoplanetary disks. In the core accretion scenario, rocky planets such as the Earth are thought to be formed from cosmic dust particles that grow into pebbles and planetesimals, the building blocks of planets, later assembling together. An intricate puzzle in this theory is how exactly these building blocks are formed and kept long enough in the natal protoplanetary disk.

Protoplanetary disks are weakly magnetized accretion disks that are subject to the magnetorotational instability (MRI). It is to date one of the main candidates for explaining their turbulence and angular momentum transport. The nonideal magnetohydrodynamic effects prevent the MRI from operating everywhere in the protoplanetary disk, leading to MRI active regions with high turbulence and non-MRI regions with low turbulence. It has been hypothesized that these variations in the disk turbulence can lead to pressure maxima where dust particles can be trapped. In these so-called dust traps, dust particles can grow efficiently into pebbles and potentially planetesimals. Yet, it is still an open question how this MRI-powered mechanism shapes the secular evolution of protoplanetary disks, and how it is involved in the *first steps* of planet formation. It is because the interplay of gas evolution, dust evolution (dynamics and grain growth processes combined) and MRI-driven turbulence over millions of years has never been investigated.

The central goal of this thesis is to bridge the gap in the core accretion scenario of planet formation by building the very first unified disk evolution framework that captures self-consistently this interplay. The unique approach adopted in this thesis leads to an exciting new pathway for the generation of spontaneous dust traps everywhere in the protoplanetary disk, which can be potential birth-sites for planets by forming and keeping their necessary building blocks.

ZUSAMMENFASSUNG

Die große Vielfalt an Exoplaneten, die in verschiedenen physikalischen Umgebungen entdeckt wurden, zeigt deutlich, dass die Planetenentstehung ein effizienter Prozess mit mehreren Endergebnissen ist. Um die Entstehung neugeborener Planeten zu verstehen, kann man die Uhr der Planetensysteme zurückdrehen, indem man die Entstehung und Entwicklung ihrer ursprünglichen Umgebung, der sogenannten protoplanetaren Scheiben, untersucht. Im Szenario der Kernakkretion geht man davon aus, dass Gesteinsplaneten wie die Erde aus kosmischen Staubpartikeln entstehen, die zu Kieselsteinen und Planetesimalen, den Bausteinen der Planeten, heranwachsen und sich später zusammenfügen. Ein kompliziertes Rätsel in dieser Theorie ist, wie genau diese Bausteine gebildet und lange genug in der ursprünglichen protoplanetaren Scheibe gehalten werden.

Protoplanetare Scheiben sind schwach magnetisierte Akkretionsscheiben, die der magnetorotationalen Instabilität (MRI) ausgesetzt sind. Die MRI ist bis heute einer der Hauptkandidaten für die Gas-Turbulenz und des Drehimpulstransports. Die nicht idealen magnetohydrodynamischen Effekte verhindern, dass die MRI überall in der protoplanetaren Scheibe wirkt, was zu MRI-aktiven Regionen mit hoher Turbulenz und Nicht-MRI-Regionen mit niedriger Turbulenz führt. Es wurde die Hypothese aufgestellt, dass diese Variationen in der Turbulenz der Scheibe zu Druckmaxima führen können, in denen Staubpartikel gefangen werden können. In diesen so genannten Staubfallen können die Staubpartikel effizient zu Kieselsteinen und möglicherweise zu Planetesimalen heranwachsen. Es ist jedoch immer noch eine offene Frage, wie dieser MRI-getriebene Mechanismus die säkulare Entwicklung protoplanetarer Scheiben gestaltet und wie er an den ersten Schritten der Planetenbildung beteiligt ist. Dies liegt daran, dass das Zusammenspiel von Gasentwicklung, Staubentwicklung (Dynamik und Kornwachstumsprozesse kombiniert) und MRI-getriebenen Turbulenzen über Millionen von Jahren noch nie untersucht wurde.

Das Hauptziel dieser Arbeit ist es, die Lücke im Kernakkretionsszenario der Planetenentstehung zu schließen, indem das erste einheitliche Rahmenwerk für die Scheibenentwicklung entwickelt wird, das dieses Zusammenspiel selbstkonsistent erfasst. Der einzigartige Ansatz, der in dieser Arbeit verfolgt wird, führt zu einem aufregenden neuen Weg für die Entstehung von spontanen Staubfallen überall in der protoplanetaren Scheibe, die potenzielle Geburtsstätten für Planeten.

PUBLICATIONS

This thesis features work and figures that have appeared previously in papers which were either published or in preparation throughout the course of my doctoral studies:

1. **Delage T. N.** et al.; "Spontaneous formation of long-lived dust traps during the secular evolution of magnetized protoplanetary disks"; to be submitted (2023).

2. **Delage T. N.**, Gárate M., Okuzumi S., Yang C.C., Pinilla P., Flock M., Stamler S. M., & Birnstiel T.; "The impact of dust evolution on the dead zone outer edge in magnetized protoplanetary disks"; A&A (2023), vol. 674, A190.

3. **Delage T. N.**, Okuzumi S., Flock M., Pinilla P., & Dzyurkevich N.; "Steady-state accretion in magnetized protoplanetary disks", A&A (2022), vol. 658, A97.

4. Pyerin M. A., **Delage T. N.**, Kurtovic N. T., Gárate M., Henning T., & Pinilla P.; "Constraining the properties of the potential embedded planets in the disk around HD 100546", A&A (2021), vol. 656, A150.

5. Gárate M., **Delage T. N.**, Stadler J., Pinilla P., Birnstiel T., Stammler S. M., Picogna G., Ercolano B., Franz R., & Lenz C.; "Large gaps and high accretion rates in photoevaporative transition disks with a dead zone", A&A (2021), vol. 655, A18.

ACKNOWLEDGMENTS

I strongly believe that anyone is defined through their life experiences. These experiences teach one lessons, make one grow, and are the essence of ones inner self. I am deeply indebted toward all those who have had an impact on my life, minor or major, good or bad. These experiences have led me to the person I am today. No work in life is ever done *ex-nihilo*, and the product of this dissertation is no exception. From my first steps in science to the finalization of this thesis, I would like to thank many people who have played a crucial role by offering help, guidance, and support along the way.

CONTENTS

LIST OF FIGURES

LIST OF TABLES

ACRONYMS

au   Astronomical Units

MRI   magnetorotational instability

MHD   magnetohydrodynamic

XR   X-rays

SPs   stellar energetic particles

FUV   far-ultraviolet

CR   cosmic rays

RA   radionuclides

HSI   Hall Shear instability

ISM   interstellar medium

SI   Streaming Instability

GI   Gravitational Instability

$=$	Equal to
$\propto$	Proportional to
$\sim$	On the order of
$\approx$	Approximately equal to
$\leqslant$	Less or equal to
$\lesssim$	Less or approximately equal to
$<$	Strictly less than
$\geqslant$	More or equal to
$\gtrsim$	More or approximately equal to
$>$	Strictly more than
m	Meter
g	Kilogram
s	Second
J	Joule
K	Kelvin
Hz	Hertz
H	Henry
c	Speed of light in vacuum, $c \approx 3 \times 10^8$ m s^{-1}
G	Gravitational constant, $G \approx 6.67 \times 10^{-11}$ m^3 kg^{-1} s^{-2}
k_B	Boltzmann constant, $k_B \approx 1.38 \times 10^{-23}$ J K^{-1}

INTRODUCTION

By way of an orthodox introduction, I set the stage of this thesis by discussing what observations have taught us about planet formation and protoplanetary disks. After raising some of the outstanding challenges in the field of planet formation, the thesis goal and outline are presented.

1.1 THE QUEST FOR UNDERSTANDING OUR COSMIC ORIGINS

Whether you, the eager reader, come from a different country, have a different culture, or live a very different lifestyle than me, we both have an undeniable and unbreakable link: we are both from the same planet called the Earth. From the high magnificent mountaintops, to the lush rainforests and the dark environment of the oceans, *homo sapiens* and many other species share this wonderful habitable terrestrial planet. The Earth itself is a member of the Solar System planets that dances around the Sun, which is itself a star among others of the Milky Way that dances around the central supermassive black hole Sagittarius A*, which is itself part of the mysterious, intriguing and mesmerizing Universe.

Throughout the humankind evolution, the night sky has stimulated our imagination, making Astronomy one of the oldest Science. Our unstoppable curiosity made us wonder about the essence of our existence: *How are we what we are? What is life? What makes the Earth suitable to sustain life? How did the Earth form? Is the Earth unique? What is the origin of our Solar System? Is our Solar System unique?* Contemplating and interrogating the vast Universe, a huge effort has been made by humankind's brightest minds in the hope of answering these questions. For centuries astronomers could only build a picture about the origin of our Solar System by looking at the other celestial bodies composing it. At the time, it would have not been inconceivable to think that the Solar System and its architecture was unique. Until not so long ago, astronomers thus thought to have partially answered most of the questions about the formation of the Earth and the Solar System.

It was during the mid 90s that this restricted "Solar System-centric" view broke down, with the detection of planets orbiting stars other than our Sun, referred to as "exoplanets" or "extra-solar planets". Historically, the first detection of an exoplanet was around the millisecond pulsar PSR B1257+12 [1, 2]. It was in 1995 that the first exoplanet around a Sun-like star called 51 Peg was discovered [3], for which the authors were awarded a shared Nobel Price in Physics in 2019. At the time of writing this thesis (August 2023), 5496 exoplanets have now been discovered and confirmed (based on the NASA Exoplanet Archive). They allow astronomers to understand the formation and evolution of planets on a population level, instead of solely relying on the Solar System planets. Nowadays, exoplanets are found

around stars of different ages, masses, metallicities, and in different regions of our Galaxy. The emerging general picture is that our Solar System is not unique in its architecture. However, it is the difference between the confirmed exoplanet properties and the planet properties of our own Solar System that is the most striking and puzzling (see Fig. 1). Indeed, the reported discovery of the planet orbiting 51 Peg was the first example of a type of planets called hot Jupiters, which is a type absent in our Solar System. These are planets with approximately the same mass and radius as Jupiter, but revolving their host star in orbits closer than the distance between Mercury and the Sun. Furthermore, cold Jupiters (exoplanets like our Jupiter) seem to be fairly rare[1] even around Sun-like stars [e.g., 4]. Also, super-Earths and mini-Neptunes (radius of order 1–4$R_\oplus$ and mass $\lesssim 20M_\oplus$, with $R_\oplus$ and $M_\oplus$ being the radius and mass of the Earth respectively) seem to be the most common type of planets in the Galaxy [e.g., 5], although these type of planets are also not present in the Solar System. These findings alienate our own Solar System from the rest of the Galaxy, making it look like a "weird one" [for a review, see 6].

Consequently, we are now rethinking the origin of our Solar System as well as the formation of planets in general. Although studying exoplanets and the Solar System bring invaluable constraints on planet formation and evolution, fundamental questions are still standing: *What are the mechanisms at play for planet formation to occur?, What is the timescale of planet formation? Which processes define the planet properties and chemical composition?* In order to tackle these and many other questions, the missing piece of the puzzle is to simultaneously point our antennas elsewhere, and "rewind the clock" of planetary systems. This is possible by studying the natal environment of planets, the so-called protoplanetary disks, which offer a unique perspective on planet formation processes.

1.2 TAKING A FIRST LOOK AT PLANET FORMATION IN PROTOPLANETARY DISKS

The rich diversity of exoplanets discovered in various physical environments with the Kepler mission and subsequent ones clearly shows that planet formation is an efficient process with multiple outcomes [e.g., 8]. To understand the emergence of newborn planets, it is crucial to study the formation and evolution of their natal environment. Going back in time to the XVIIIth century, it has been proposed that our Sun is the result of the collapse of a primordial solar nebula (molecular cloud within which the Sun formed). As a result of this star formation process, it has also been hypothesized that a gaseous and dusty disk remained orbiting the young Sun for around 4 Myrs, within which the planets of our Solar System formed. This is called the *Nebular Hypothesis*, which has been partially proposed by Swedenborg in 1737, further developed by Kant in 1755, and then modified by Laplace in 1797. Even though the *Nebular Hypothesis* was initially developed for the Sun and the

---

1 this could also be an observational bias due to their low surface temperature and large orbits
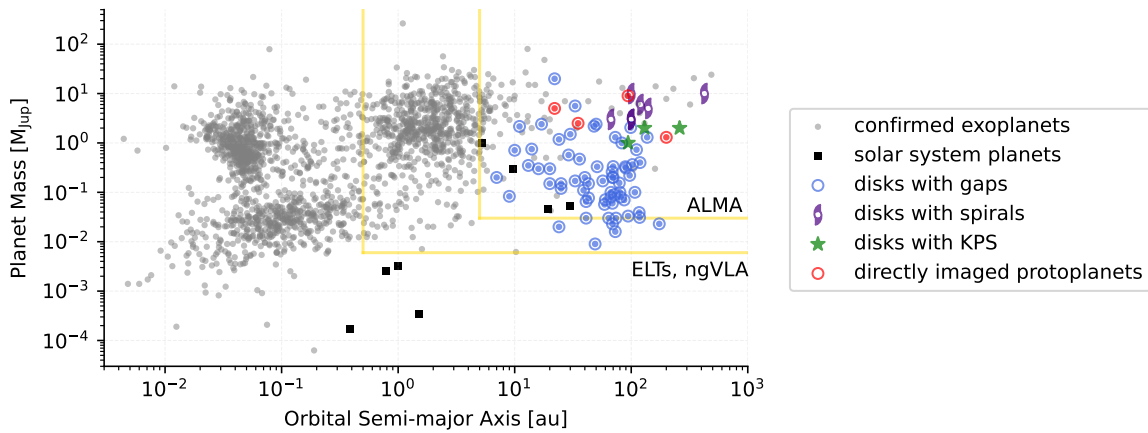
Figure 1: The distribution of the mass and orbital semi-major axis of confirmed exoplanets (gray circles), Solar System planets (black squares), and putative forming protoplanets proposed to reproduce the protoplanetary disk substructures (blue for annular substructures, purple for spirals, and green for kinematic planetary signatures). Directly observed protoplanets (PDS 70b/c, AB Aur b and As 209b) are shown in red. The yellow lines show illustrative regions where current and future observing facilities might find protoplanets directly or indirecly in their protoplanetary disks. Figure taken from Bae et al. [7].

planets of the Solar System, there is a general consensus that young stars[2] form from the collapse of molecular clouds and that planets are formed from the gaseous and dusty disks orbiting them [e.g., 9–12]. Since these circumstellar disks represent the natal environment of planets, they are historically called protoplanetary disks.

The field of planet formation aims to understand and explain the processes behind how the reservoir of gas and dust provided by protoplanetary disks "arrange itself" to lead to planetary systems. It is therefore intricately related to the formation process of these disk (intricately related to the star formation process itself) and their subsequent evolution. The eager reader should note that, despite the *Nebular Hypothesis* being around for quite some time, the study of protoplanetary disks is a very young field both observationally and theoretically speaking. It has exponentially grown during the last decades. For example, it is only late in the XXth century that the *Nebular Hypothesis* could be confirmed by optical and millimeter images of high angular resolution. These observations demonstrated, for the first time, the existence of these protoplanetary disks with the discovery of the disk around the young star β Pictoris [13].

1.2.1 *Protoplanetary disk formation*

As I mentioned above, protoplanetary disks are a natural outcome of the star formation process. In order for this process to be initiated, an interstellar region which is made of gas and dust, occupies a small fraction of the volume of the interstellar medium (ISM), and from which one or multiple stars are going to form must satisfy a basic requirement: the gravitational collapse can proceed unimpeded by the ther-

---

2 also called protostars

mal pressure that stabilizes a region against collapse. In other words, the free-fall timescale (t_{ff}) must be much less than the sound crossing timescale (t_{sc}). Using the virial theorem, one can show that $t_{ff}/t_{sc} \sim \rho^{-1/6}T^{1/2}$, where ρ is the gas density of the interstellar region and T its temperature. To obtain $t_{ff} \ll t_{sc}$, one thus needs a dense and cold interstellar region. These stellar nurseries display typical densities and temperatures where the gas is molecular, and are therefore commonly referred to as "giant molecular clouds" (Fig. 2a). These giant molecular clouds have two properties that will be crucial for the formation and evolution of the stars and protoplanetary disks: they are slowly rotating and strongly magnetized [e.g., 14, 15]. Given their size (of order parsecs), the former tells us that the molecular gas possesses significant amounts of angular momentum. The latter tells us that stars and protoplanetary disks are (weakly) magnetized. Specifically, the fact that protoplanetary disks are magnetized is fundamental for the accretion process, as I shall discuss many times in this thesis.

The formation of an individual low-mass[3] (focus of this thesis) young star begins when an individual region within the giant molecular cloud, which is called a star-forming molecular cloud, becomes gravitationally unstable and collapses. When this collapse begins the gas is optically thin and proceeds isothermally. Since isothermal collapse is a runaway process, the collapse proceeds in free-fall until the star-forming molecular cloud becomes dense enough to be optically thick to its own radiation and the gas to be adiabatic. The thermal pressure becomes important and slows down the collapse, reaching quasi-hydrostatic equilibrium. The first core is then formed [e.g., 16]. Since the first collapse has happened through many orders of magnitude in space, and that the initial angular momentum of the star-forming molecular cloud must be conserved, a fraction of the gaseous and dusty first core experiences a large increase of its angular velocity, which causes a flattering and the beginning of a disk-like structure. This phase is called the Class 0 phase (Fig. 2b).

A second collapse occurs within the first core when the temperature becomes high enough for molecular hydrogen to be dissociated due to the accretion process, which is an endothermic reaction that cools down very efficiently the gas. This second collapse lasts until the thermal pressure once again becomes important (i.e., the gas becomes adiabatic again) and hydrostatic equilibrium is established. The second core called the protostar is then formed at the center of the star-forming molecular cloud with material from the first core falling onto it [e.g., 17]. However, some material from the gaseous and dusty first core misses the protostar due to the very high angular velocities at play. Some gas and dust thus terminate their orbit near the central object, taking the shape of a thin magnetized quasi-Keplerian disk around it. A star-disk system is then born within the first core. This phase is called the Class I phase (Fig. 2c).

Once the material from the first core is dispersed through accretion by the central object and ejection by outflows, the now pre-main-sequence star (nuclear fusion has begun) has reached almost its final mass, and is left with the magnetized gaseous

---

[3] stellar mass of order $M_\star \lesssim 2\,M_\odot$, where $M_\odot$ is the mass of the Sun
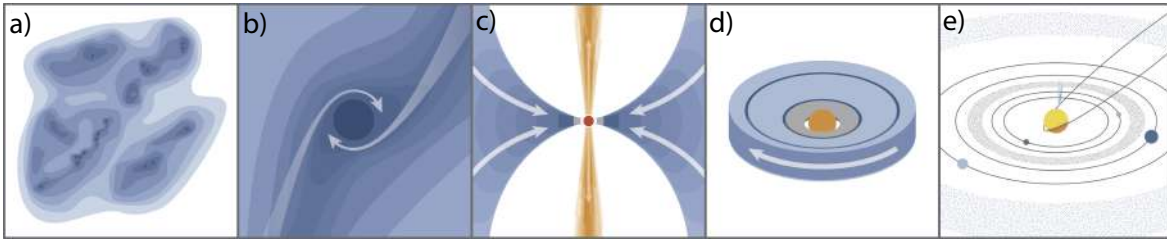
Figure 2: Simplified cartoon of the different stages of low-mass star formation, and its relation to protoplanetary disks and planet formation. Figure taken from Öberg and Bergin [22].

and dusty protoplanetary disk orbiting around it. The accretion process onto the central star still continues through the accretion protoplanetary disk. This phase is called the Class II phase (Fig. 2d). It is the main focus of this thesis because protoplanetary disks spend most of their lifetime in that phase (a few million years, compared to the approximate 0.5 Myrs for the Class 0 and I phases combined [e.g., 18, 19]), leaving plenty of time for planets to form there. One should note, though, that there are increasing observational evidence that planet formation might start during the Class I phase [e.g., 20, 21].

Finally, most of the gas component of the magnetized protoplanetary disk is dispersed within ~ 1–10 Myrs through accretion and dispersal mechanisms driven by disk winds, which I will not dive into in this thesis and will not be considered in the models. Since the gas is dispersed, but not necessarily the dust, the dusty circumstellar disk is now called a debris disk. It is characterized by the fact that giant gas planets formation is stopped, but rocky and icy planets can still continue to grow for another ~ 100 Myrs. This phase is called the Class III phase (Fig. 2e). After this phase, a mature planetary system exists and the protostar becomes a fully fledged main-sequence star.

One should note that the star formation process (the first and second cores formation and the circumstellar disk formation) I have pictured above is highly simplified, so that the eager reader can grasp the main idea on how protoplanetary disks form. In reality, star formation processes are much more rich and complicated topics. I invite the eager reader to look at specific reviews for further details [e.g., 14, 19].

1.2.2 *Two competing planet formation theories*

Now that I briefly reviewed how protoplanetary disks are a natural outcome of the star formation process, let us discuss the two main competing planet formation theories within these disks: the *gravitational instability scenario* [23–25], and the *core accretion scenario* [26–28].

1.2.2.1 *Gravitational instability scenario*

When the protoplanetary disk is massive and cold enough, it can be subject to the *gas* Gravitational Instability (GI). It occurs when the self-gravity of the gas compo-

nent of the protoplanetary disk overwhelms pressure support and rotation, which is determined by the Toomre's stability criterion. The disk becomes gravitationally unstable when $Q \lesssim 2$, with Q the Toomre parameter [29]. Due to the structure of protoplanetary disks (see Sect. 2.2), the gas is more likely to be self-gravitating (i.e, GI active) in the outer regions of the disk far from the central star.

In the gravitational instability scenario, the disk spontaneously fragments into many dense clumps made of gas and dust in the regions that are self-gravitating. These clumps can further contract to form gas giant protoplanets in very short timescales (several hundred of years) compared to the dissipation timescale of the gas. These protoplanets can thus accrete the surrounding disk material, which results in planets with masses larger than a few Jupiter mass [e.g., 30]. While accreting their surrounding, some of the protoplanets can significantly migrate to the inner regions of the disk, where their gaseous envelope is stripped away through tidal disruption, leaving behind the solid core which then becomes a terrestrial planet. This is called the tidal downsizing hypothesis [31].

As a rule of thumb, this scenario requires the protoplanetary disk to be more massive than ~ 10% the mass of its central mass star, and efficient cooling. It means that gravitational instability can be expected to operate at early stages of the disk formation (Class 0/I phases) where the disk is massive, but not so much in the Class II phase. Furthermore, efficient cooling in protoplanetary disks is not a given due to turbulence and external radiation. This brings tension on how efficient this scenario is to create the dense clumps in the first place. Finally, inward migration of giant gas protoplanets is not straighforward [for reviews, see 32, 33], which brings tension on how the terrestrial planets could be formed through the tidal downsizing hypothesis.

In this thesis, I will study protoplanetary disks that are not massive enough to be considered self-gravitating. The gravitational instability scenario is thus not the main focus.

1.2.2.2 *Core accretion scenario*

According to the core accretion scenario, planetary embryos are formed by the growth of interstellar dust particles originally contained in the protoplanetary disk due to its formation. These planetary embryos can obtain a gaseous envelop by accreting the surrounding disk material before the disperal of the gas [e.g., 34]. Depending on their mass, where they are formed in the disk, and how much they migrate through it, terrestrial planets and gas giant planets can be formed. This scenario is the favored one to explain the formation of rocky planets such as the Earth.

Figure 3 illustrates the main steps to form planets in the protoplanetary disk through the core accretion scenario. This can be divided into three main stages [e.g., 35]. First, the sub-micron ISM dust particles must grow to millimeter- and centimeter-sized particles (pebbles). Second, these larger dust particles assemble into planetesimals, which are kilometer-sized bodies. Last, the more massive planetesimals continue to grow through gravitational interactions, capture of lighter
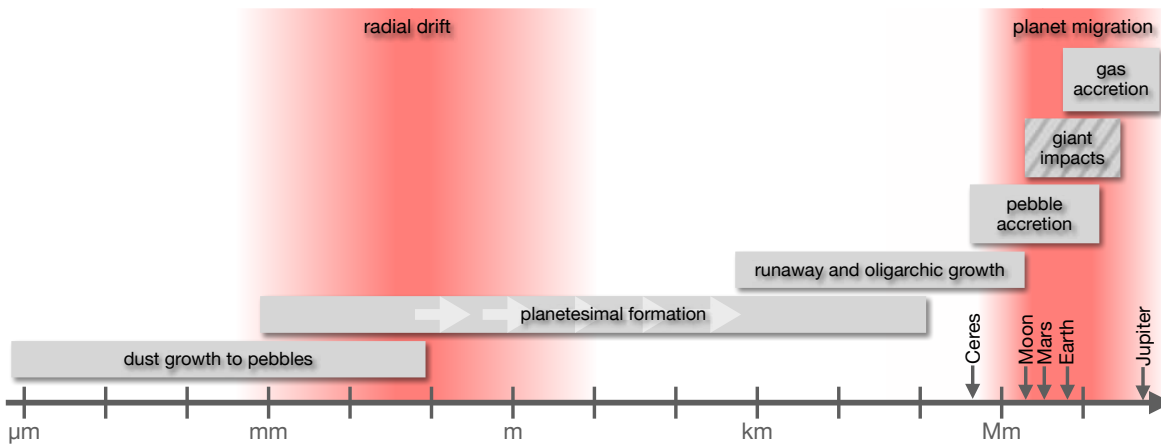
Figure 3: Overview of processes involved in planet formation for the core accretion scenario. The gray boxes represent growth processes and the red shaded regions represents where the radial mass redistribution is effective. The white arrows in the planetesimal formation box represent the lack of the intermediate sizes during the collapse of aerodynamic pebble clouds. The giant impacts may happen both before and after the gas component of the protoplanetary disk disperses, while the other processes happen in the presence of gas. Figure taken from Drążkowska et al. [35].

planetesimals and accretion of pebbles in order to form planetary embryos [e.g., 36]. This happens until the now protoplanets start interacting with the protoplanetary disk and open gaps, which prevent from further accreting the solids. These gaps occur because the protoplanets can gravitationally bind the surrounding gas, located within the sphere determined by the minimum between the Hill radius and the Bondi radius.

The core accretion scenario also faces several problems: (1) The formation of planetesimals in protoplanetary disks is still an open question in the field, although they are fundamental building blocks of planets. (2) The whole process from interstellar dust particles to planets covers more than forty orders of magnitude in mass, which makes the timescale over which planets form as long as the Class II phase. It means that the disk can be depleted from its gas component before any planets can form. (3) When planetary embryos form, their interactions with the gas component of the disk leads to exchange of angular momentum and planet migration [for reviews, see 32, 33]. This can lead to their rapid inward migration through the disk, and even their loss.

In this thesis, I will focus on the first two stages of the core accretion scenario (see Sect. 2.3.3 for further theoretical background), where the least understood stage that is the formation of planetesimals is at the core of the investigations.

1.3   PROTOPLANETARY DISK OBSERVATIONS

Clearly, one can argue that how, when and where planets form in their natal protoplanetary disks is a question far from being answered. If there is one result that the current models of planet formation agree on, is that the initial conditions (the

protoplanetary disk structure) is crucial to the final outcome (exoplanets properties and planetary systems architecture). In order to better constrain planet formation, one thus needs to understand the structure of protoplanetary disks (i.e., the distribution of gas and dust within the disk) and their global evolution. This relies on our ability to model these objects through theoretical and numerical work such as this thesis. Although theory has preceded the observations of exoplanets and proplanetary disks, the main driver of the field nowadays is these observations. They indeed bring key information that put constraints, challenge, and sometimes validate theoretical models, hence allowing the whole community to work toward a self-consistent theory encompassing all the stages of planet formation and understanding the very complex interdependencies between the processes at play.

1.3.1   *Disk structure*

Today's observations probe different regions of the protoplanetary disk. In order to interpret these observations and constrain theoretical models, it is essential to clearly understand the quantities and limitations of each observation. A typical disk can be divided into two main parts: an inner dust-free disk from a few stellar radius to the dust sublimation point (~ 0.1 au) made of hot gas, and an outer disk made of dust and gas that ranges from ~ 0.1 Astronomical Units (au) to a few hundreds of au. The outer disk can itself be roughly divided into a surface and midplane gas layer and a surface and dust layer, as illustrated in Fig. 4. While the hot inner dust-free regions probe the accretion signature of the star-protoplanetary disk system, hence providing constraints on the accretion rates for a system in the Class II phase (see Sect. 1.3.2.2), the gaseous and dusty regions probe the disk structure and provide constraints on how the material is distributed.

At the moment, there are three possible ways to study the outer disk observationally [for a review, see 37]:

- The near- and mid-infrared continuum (also known as the infrared excess, long been detected observationally [e.g., 38, 39]) is due to stellar photons scattered by small dust particles (typically sub-micron sized ones). Scattered light probes the uppermost surface of the dust layer, since the dust component of the disk is very optically thick at these wavelengths [for a review about scattered light, see 40]. As a result, the intensity of scattered light is not related to the column density of dust, but to the amount of stellar light received by the disk atmosphere and its temperature. It characterizes the disk geometry, and the disk-like geometry of protoplanetary disks have been confirmed with such observations [e.g., 41]. Furthermore, it can provide some rough insights on the gas component of the disk because small dust particles are coupled to the gas through a drag force (see Sect. 2.3).

- The (sub)-millimeter continuum is due to the thermal emission of larger dust particles (typically millimeter-sized ones). The radio wavelengths probe the dust layer of the disk near the midplane. If the dust is optically thin at these

wavelengths (as usually assumed [e.g., 42, 43]), the emissivity is related to the column density of dust, its temperature, and its opacity. With some assumptions on the last two, one can constrain disk dust masses. With further assumptions on the typical dust-to-gas mass ratio in protoplanetary disks, one can obtain very rough estimates on disk gas masses (10^{-3}–$10^{-1}\,M_\star$) for the Class II phase [e.g., 44].

- Spectral lines, both in the infrared and at radio wavelengths, emitted from gas tracers such as gas or molecular transitions. Since protoplanetary disks form out of the ISM, molecular hydrogen (H_2) is the main gaseous species. However, its emission is very faint in cold environment such as disks due the details of its molecular physics. It means that one must rely on indirect gas mass tracers. The closest molecule to H_2 is its less abundant isotopologue hydrogen deuteride (HD). Unlike H_2, HD has a permanent small dipole which makes its detection possible. Indeed, the energy needed to excite the HD fundamental rotational level (J = 1–0) is 128 K, which are temperature reached in protoplanetary disks. However, there is no current or planned facility that covers the HD J = 1–0 transition to carry out a large unbiased sample of disks [e.g., 44, 45]. Carbon monoxide (CO) and its less abundant isotopologues are thus often used as tracers of gas properties, structure and kinematics, since it is the second most abundant molecules after H_2. CO spectral lines are optically thick and probe the surface of the gas layer, while its isotopologues are more optically thin and can probe regions closer to the midplane. All in all, estimates of the gas distribution from these observations is very challenging since it requires knowledge of the C/H ratio [e.g., 46]. This is very problematic because the disk gas properties are ultimately related to its evolution, and dictate the architecture of the forming planetary system [e.g., 47].

Given that each tracer probes different regions and properties of the protoplanetary disk, a combination of multiple tracers at multiwavelength is highly desirable, when feasible, in order to provide the most information. For example, this has been done for the Class II protoplanetary disk around the star TW Hya (see Fig. 5). Such multiwavelength gas and dust observations clearly show that the gas and dust components of the disk behave differently, and that dust of different sizes behave differently.

1.3.2   *Disk evolution*

Since protoplanetary disks form out of the ISM, they are expected to start out with around 99% of their mass in gas and only 1% of their mass in solid dust particles. During the disk lifetime (mostly the Class II phase), both its gas and dust components are expected to drastically evolve.
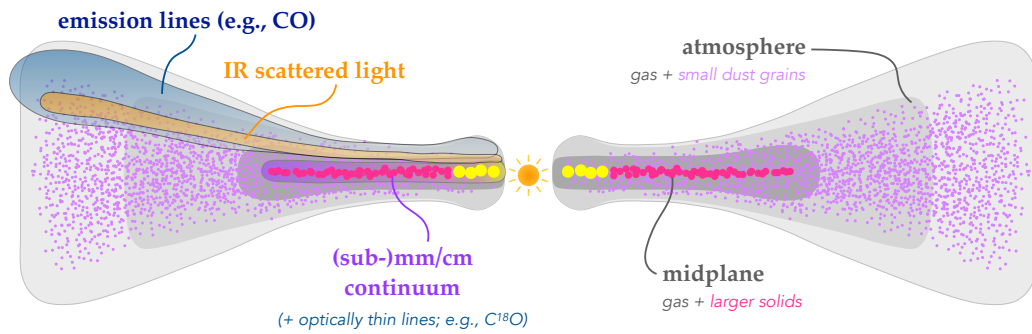
Figure 4: Schematic of a typical Class II protoplanetary disk structure viewed in cross-section. The gas is denoted in grayscale. The dust particles are marked with exaggerated sizes and colors. *Left Panel:* Approximate locations of emission tracers for the gas and dust. *Right Panel:* Disk content terminology. Figure taken from Andrews [37].
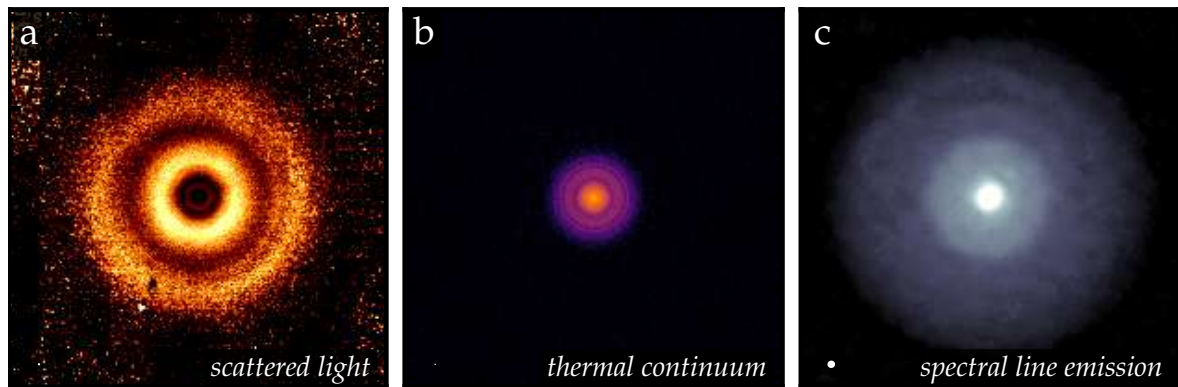
Figure 5: Morphology of the Class II protolanetary disk around TW Hya compared in three different tracers. *Panel a):* $\lambda = 1.6\,\mu$m scattered light emission from small dust particles (atmosphere of the protoplanetary disk). *Panel b):* $\lambda = 0.9$ mm continuum emission from pebble-sized dust particles (midplane of the disk). *Panel c):.* the CO J = 3–2 spectral line emission tracing the molecular gas (molecular layer of the disk). Each panel spans 500 au on a side, and resolutions are shown with ellipses in the lower left corner of each panel (too small to be visible for *Panels a, b*). It is helpful to put this figure in the perspective of Fig. 4. Figure taken from Andrews [37].
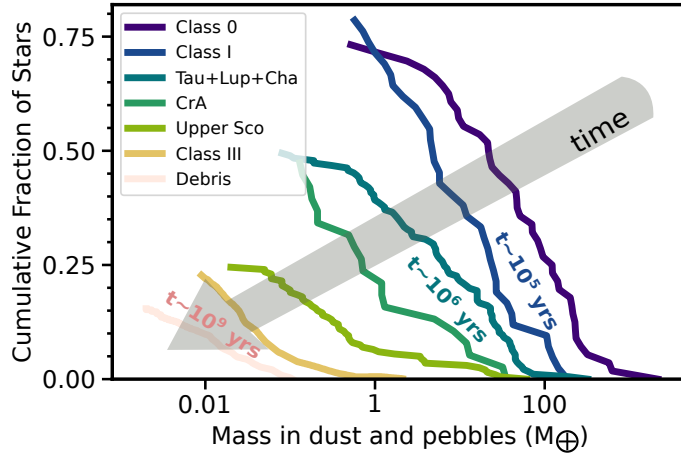
Figure 6: Cumulative distribution of dust mass around young stars in various star-forming regions that differ from their age. Both the dust mass and the fraction of stars with detectable dust decrease over time. Figure taken from Drążkowska et al. [35].

1.3.2.1 *Dust evolution*

The fact that there is detection for both scattered light and millimeter emission for a single target (e.g., TW Hya as shown by Figs. 5a and 5b) means that small and larger dust particles can coexist. Although it is not surprising that protoplanetary disks have ISM-like dust particles (since they originate from the ISM), the presence of millimeter-sized particles implies that the dust has grown quite a lot from the disk formation to until the time the observations were taken. In other words, the typical grain size in the protoplanetary disk drastically evolve in time. Since scattered light and millimeter observations probe distinct regions of the disk, it means that grain growth processes come hand in hand with size-dependent dynamical processes that transport and redistribute the dust within the disk.

Dust evolution in protoplanetary disks is even more noticeable when comparing the dust mass budget in various star-forming regions that differ from their age. Figure 6 shows the cumulative distribution of dust mass around young stars located in various star-forming regions. Going from dark- to light-colored lines, the star-forming regions are expected to be older on average (although a huge scatter exists). One can clearly see that both the dust mass budget and the fraction of stars with detectable dust observations decrease over time. This is another observational evidence that the dust component of protoplanetary disks is subject to significant change throughout the existence of the disk. In Sect. 2.3, I will explain how the dust evolves from a theoretical perspective.

1.3.2.2 *Gas accretion*

When observing a star-protoplanetary disk system, there is a UV excess that is a signature of accretion columns at the stellar surface [e.g., 48, 49]. These accretion columns are generated when the gas component of the disk gets lifted up and accreted by the stellar magnetic field (magnetospheric accretion). The gas ends up
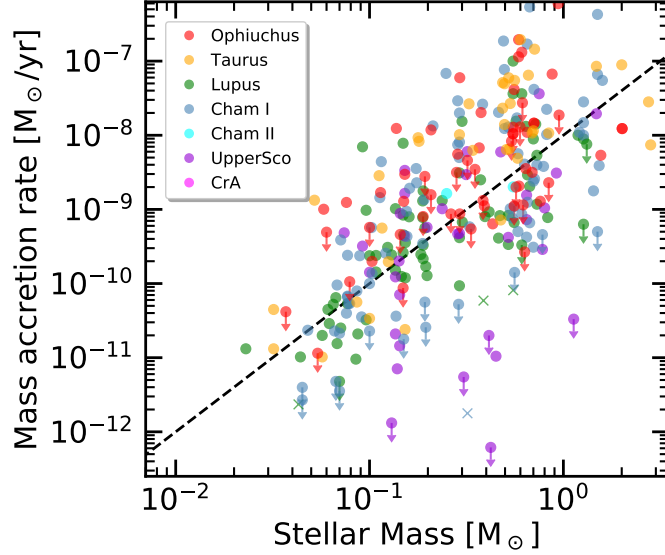
Figure 7: $\dot{M}_{acc}$ vs $M_\star$ for various star-forming regions. Figure taken from Manara et al. [51].

in a nearly free-fall speed and hits the stellar surface, which forms an accretion shock. The luminosity of the accretion shock observed in UV bands can be directly related to the accretion rate in the accretion columns located in the inner dust-free region of the protoplanetary disk [e.g., 50]. Measured accretion rates are in the range $\sim 10^{-12}$–$10^{-6}\,M_\odot.\mathrm{yr}^{-1}$ depending on the target, with a mean value around $\sim 10^{-9}$–$10^{-8}\,M_\odot.\mathrm{yr}^{-1}$ [e.g., 18, 51]. It is very important to note that a measured accretion rate is not necessarily the accretion rate in the entire protoplanetary disk, since protoplaetary disks are not steady-state objects and outflows due to disk winds generate loss of gas mass [see e.g., 52, 53].

The UV excess is an undeniable disk feature showing that protoplanetary disks are accretion disks, as expected from theoretical considerations. The fact that they are accretion disks means that their gas component is expected to significantly evolve over time. Gas evolution is noticeable when comparing the gas accretion rates in various star-forming regions that differ from their age. Figure 7 shows the $\dot{M}_{acc}$ vs $M_\star$ for various star-forming regions, with Ophiuchus being the youngest one and Upper Scorpius (UpperSco) the oldest one (on average). The *general* trend is that younger disks (Ophiuchus ones) seem to have larger gas accretion rates than the older disks (UpperSco ones). This can be interpreted as a signature of gas evolution (less gas to accrete over time, as some of the gas content slowly moves inward toward the central star), since the measured gas accretion rates are found to be correlated with the observed total disk dust mass [e.g., 54]. In Sect. 2.2, I will explain how the gas evolves due to the accretion process from a theoretical perspective.

1.3.3 *Dust substructures*

In recent years, progress in observational techniques such as adaptive optics and interferometry has allowed astronomers to spatially and spectrally resolve nearby protoplanetary disks as it has never been possible before. Our view into star-forming regions has cleared up drastically, mainly owing to the Spectro-Polarimetric High-contrast Exoplanet REsearch (SPHERE) instrument installed in the Very Large Telescope (VLT) and the Atacama Large Millimetre/submillimetre Array (ALMA) interferometer, both located in Chile. The first class of observations with SPHERE/-VLT relies on polarimetric differential imaging (PDI) of scattered light emission in the near-infrared (sub-micron to micron-sized dust particles). It allows astronomers to solely get the light scattered by dust particles, by removing the light of the central object [for futher details about PDI, see 40]. The second class of observations with ALMA is based on interferometry at (sub)-millimeter wavelengths (dust particles of size in the range $\sim 100\mu m$–1 cm).

The advent of such state-of-the-art facilities has made the field of planet formation enters a new area. First, they have allowed astronomers to directly detect two accreting protoplanets in their natal disk PDS 70 [40, 55–58]. Second, they have provided deep details about the structure of propoplanetary disks as single targets, as well as on a population level with large disk surveys.

Astonishing morphological features for the gas *and* dust components of the protoplanetary disk (commonly called disk substructures) have been discovered [e.g., 59–67]. Furthermore, the DSHARP [Disk Substructures at High Angular Resolution Project, 68] and the ODISEA [Ophiuchus DIsc Survey Employing ALMA, 69] surveys have revealed that dust morphological features (commonly called dust substructures) are actually quite common in bright and extended Class II protoplanetary disks. These dust substructures are categorized in ring/cavity, rings/-gaps, arcs, and spirals [for a review, see 37]. A gallery with examples of such dust morphologies is shown in Fig. 8. The general interpretation of dust substructures existence is that dust particles are trapped at some locations in the protoplanetary disk, a phenomenon called "dust trapping". Dust trapping can occur near local pressure maxima within the disk, where dust particles radially drift toward to become trapped and grow efficiently into millimeter-sized object, potentially forming planetesimals and planetary embryos. In Sect. 2.3.3, I will provide more theoretical details about dust trapping.

1.3.4 *Magnetic fields*

Magnetic fields are crucial in many aspects for planet formation and evolution. For example, the Sun's magnetic field is the origin of the Heliosphere, which shields the Solar System from significant galactic cosmic radiation. Similarly, the Earth's magnetic field is the origin of its magnetosphere, shielding the Earth from extremely energetic solar particles carried away by the solar wind, and allowing it to be habitable as we know it. Magnetic fields inherited from the slowly rotating and strongly

Ring/Cavity
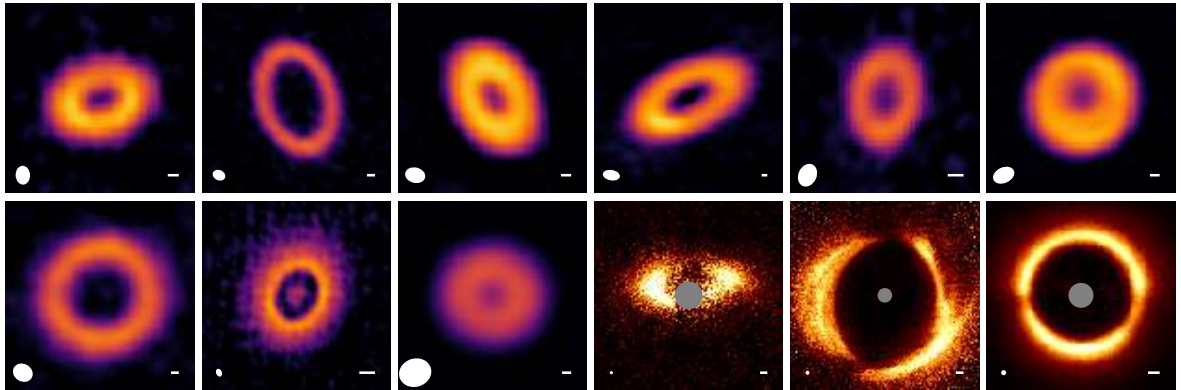
Rings/Gaps
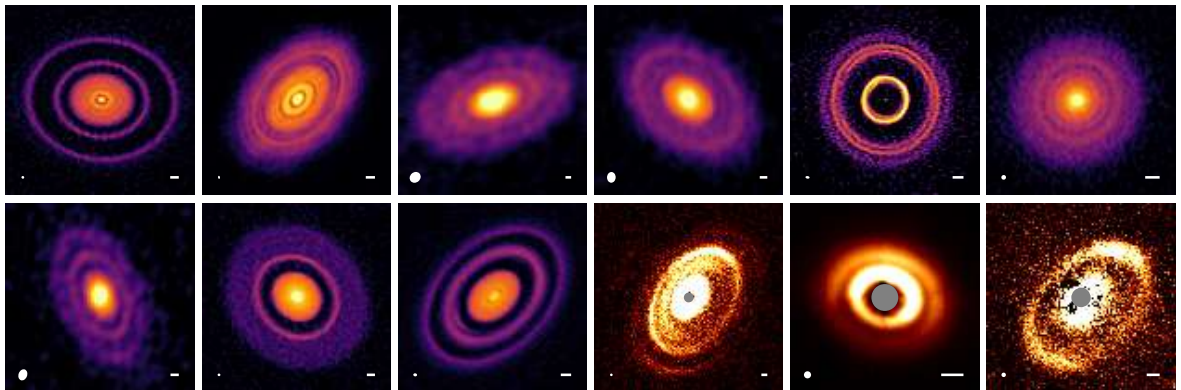
Arcs
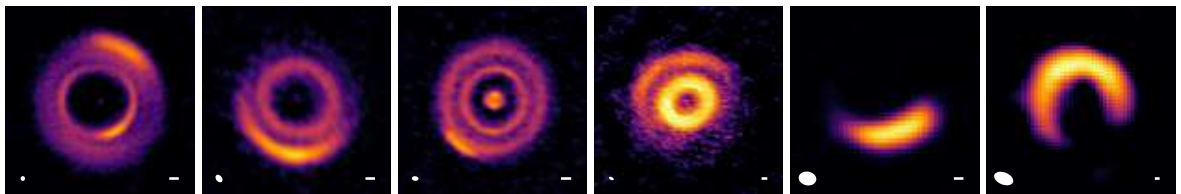
Spirals
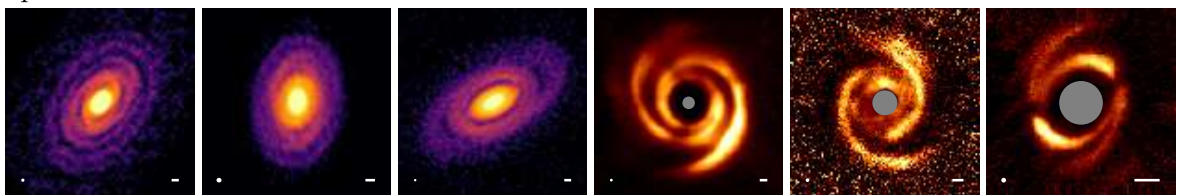
Figure 8: A gallery of dust substructure morphologies. The color maps for continuum and infrared scattered light match those in Fig. 5. Resolutions are marked with white ellipses in the lower corner of each panel, and 10 au scalebars are shown in the lower right corners. Figure taken from Andrews [37].

magnetized star-forming molecular cloud are also crucial for protoplanetary disks, the natal environment of planets. They play a major role in the disk formation [e.g., 19], as well as its evolution (see Sect. 1.4).

Despite its fundamental role, direct measurements of the magnetic field strength in protoplanetary disks by the Zeeman effect remain extremely challenging even with ALMA (because disks are weakly magnetized). Observations using the Zeeman effect has been so far somewhat conclusive in only one disk, which led to upper limits ($< 30\,\mathrm{mG}$) at tens of au from the central star [70]. Paleomagnetic measurements in the Solar System meteorites also allow for magnetic field strengths to be deduced, assuming that the field gets frozen in (see Sect. 2.1.3 for a definition) in the solid bodies during their formation in the parent protoplanetary disk. Field strength of order $500 \pm 200\,\mathrm{mG}$ at 1–3 au from the Sun and $\gtrsim 60\,\mathrm{mG}$ at 3–7 au until $\sim 2\,\mathrm{Myrs}$ from the formation of the first solids have been inferred from remnant magnetization in meteorites [e.g., 71, 72]. Moreover, upper limits ($< 30\,\mathrm{mG}$) in regions around 15–45 au have been deduced from the magnetization of Comet 67P/Churyumov-Gerasimenko [e.g., 73].

From the theoretical perspective, typical values for the magnetic field strength are expected to be of order $1\,\mathrm{G}$ at $\sim 1\,\mathrm{au}$ and a few mG at a few tens of au [e.g., 74]. Although this fall into the range of the observations, there are many unknown about the field topology and how it is distributed within the protoplanetary disk. This is an outstanding challenge because the accretion process is expected to be powered by the magnetic field in protoplanetary disks, as I will discuss in Sect. 1.4. An incomplete understanding of the magnetic field properties leads to our inability to fully grasp the accretion process in disks, which is fundamental in regulating their dynamics and evolution.

1.4   ON THE IMPORTANCE OF DISK ACCRETION AND TURBULENCE

Protoplanetary disks are accretion disks delivering material onto their central stars while forming planets. Their formation, evolution and dispersal are closely linked to their angular momentum content, and since the angular momentum is a conserved quantity, how it is transported. This question has been subject to a lot of work over the past fifty years, and essentially led to two transport mechanisms: turbulence and magnetized disk winds.

Historically, turbulence came first. Protoplanetary disks are differentially rotating disks where an azimuthal band of gas located close to the central star orbits faster than an azimuthal band of gas orbiting further away. As a result, there is a shear between two adjacent azimuthal band of gas because the gas is a fluid with a non-zero molecular viscosity. This should then lead to gas turbulence, with the angular momentum being radially transported outward from the faster azimuthal band of gas to the slower one, and the gas being simultaneously accreted radially inward. However, when plugging actual numbers, the measured gas accretion rates of Class II protoplanetary disks are way too large to be explained by the gas molecular viscosity [e.g., 75]. *What could then be source of disk turbulence that would provide*

enough effective viscosity from interacting turbulent gas eddies to explain the accretion rates of Class II disks? A first option is the gravitational instability (GI), which can transport very efficiently angular momentum outward (hence inward gas accretion) via non-axisymmetric spiral density waves when the cooling rate is less than the orbital frequency [76–79]. This is called gravitoturbulence. Nonetheless, as I discussed in Sect. 1.2.2.1, GI can definitely operate in Class 0/I protoplanetary disks, but less likely in less massive Class II disks. A second option is represented by pure hydrodynamic-driven mechanisms, such as the vertical shear instability [VSI; e.g., 80–84] or baroclinic instabilities (convective overstability and zombie vortex instability) [e.g., 85, 86]. Nevertheless, theoretical studies show that the resulting gas turbulence level is typically too weak to explain the observed accretion rates of protoplanetary disks, hence the accretion process [see the review of 87]. The last option is the magnetorotational instability (MRI) [88], which occurs because protoplanetary disks are differentially rotating disks that are weakly magnetized. The MRI directly causes magnetohydrodynamic (MHD) gas turbulence, which was undeniably thought to provide enough effective viscosity to explain the measured disk accretion rates until recently. The physics of the MRI, its link to MHD turbulence and gas accretion will be explained in great details in Chapter 2 (Sects. 2.1 and 2.2), as the MRI is at the core of this thesis.

Magnetized disk winds or also called MHD disk winds, initially proposed by Blandford and Payne [89], have regained popularity over the last ten years as a way to extract angular momentum vertically and generate radial gas accretion in protoplanetary disks [for reviews, see 87, 90]. They rely on the presence of large-scale open magnetic field lines connected to the disk surface with an inclination angle larger than $30°$ relative to the disk normal [e.g., 91–93]. Provided an outflow of gas from the disk be loaded to the open field lines, the gas at the disk surface can be centrifugally accelerated vertically along the field lines (extraction of angular momentum from the disk), and the gas within the bulk of the disk is subject to a magnetic braking torque (radial gas accretion). This new popularity of MHD disk winds can be explained by noting two points. The first point comes from theory, which has shown that the MRI cannot operate efficiently everywhere in disks because they are weakly ionized (nonideal MHD effects can suppress the MRI, as discussed in Sects. 2.1 and 3.5.1). The second point comes from gas tracer observations that can serve as a direct measurement of gas turbulence, by studying the impact of the turbulent motions onto the broadening of molecular lines. It is worth noting that obtaining the gas turbulent velocities magnitude is incredibly challenging at radio wavelengths, since the emission from rotational transitions of molecules have a significant contribution from thermal broadening [e.g., 94]. Furthermore, a deep understanding of the disk thermal structure is needed to extract the effect of non-thermal broadening, which is not necessarily the case in most of protoplanetary disks. Finally, such measurements require to know exactly what disk region is probed, which again comes with some caveats. Therefore, most studies of line broadening in sub-millimeter observations can only provide upper limits on the gas turbulence level. Having these uncertainties in mind, it seems

that protoplanetary disks are not turbulent but rather laminar, hence supporting the idea that the MRI is not efficient in most of the disk and that MHD disk winds are responsible for the accretion process. Nonetheless, it is important to emphasize that the physics of the MRI is far from being fully understood as the gas ionization level in protoplanetary disks are still very uncertain (see Sect. 3.4), which is key to know how strong the nonideal MHD effects are. How much the MRI plays a role in the accretion process in protoplanetary disks is thus still an open question.

Should the MRI not play a substantial role in the accretion process, it is nonetheless fundamental to better quantify the MHD turbulence driven by the MRI because MHD disk winds do not seem to generate turbulence according to current numerical simulations. Disk turbulence is indeed the key ingredient in a plethora of planet formation processes, ranging from the collision velocities of small particles to the formation of planetesimals (see Sect. 2.3) and the migration rate of low-mass planets [for reviews, see 32, 33]. Since the MRI and MHD disk winds can coexist [e.g., 95], it is very reasonable to believe that they can work together, where the former provides disk turbulence and the latter is at the core of the accretion process. Consequently, *both* processes clearly need to be studied separately and/or together in order to fully understand the evolution of protoplanetary disks and the formation of planets.

1.5 OUTSTANDING CHALLENGES

It is safe to say that our understanding of planet formation is still, broadly speaking, in its infancy. Although great leaps in knowledge have been made as to the diversity and architecture of planetary systems, the connection between formation and the population of planets that we observe (including our own) still remains a mystery. Planet formation is an intricate puzzle for many reasons. Here I will only emphasize on the ones that are directly related to the work conducted in this thesis, and justify it.

It is actually not that simple to "rewind the clock" of planetary systems, and understand what happened to them millions of years ago. Part of this challenge comes from the fact that planet formation processes are highly stochastic, with a ridiculously high number of parameters to account for. Even if the natal environment of planets, the protoplanetary disks, were to be perfectly understood, we would still need to solve a N-body problem between all the minor bodies in the forming planetary system and the protoplanets. This is numerically impossible to fully track. Events like giant impacts or meteorite impacts, which can definitely completely alter a forming planet properties, cannot thus be fully predicted over the whole evolution of planets. This implies that constraining the current exoplanet properties to provide information on their formation is a very challenging task to do.

The formation and evolution of protoplanetary disks are far from being understood. They form with nearly homogeneous distribution of gas and dust inherited from a star-forming molecular cloud, and subsequently evolve to host forming

planets. Terrestrial planets such as the Earth are thought to mainly form via the core accretion scenario (Sect. 1.2.2.2). One of the key ingredients of this planet formation theory are planetesimals. These are unfortunately poorly constrained observationally because they are not traceable by thermal emission. Also, their formation in their natal protoplanetary disk is still subject to a great deal of theoretical work due to the so-called meter-size barrier, which predicts that it is very challenging for interstellar dust particles to grow up to these objects (see Sect. 2.3.3 for further details). The advent of state-of-the art facilities have brought a glimpse of hope about this problem, by revealing that Class II protoplanetary disks have substructures (Sect. 1.3.3). Particularly, the discovery of dust substructures is fundamental because it shows that dust trapping can occur in protoplanetary disks. The existence of dust morphologies such as ring/cavity and rings/gaps circumvent the meter-size barrier, and provide new insights about the formation of planets in their natal environment (see Sect. 2.3.3 for further details). Nowadays one of the central questions in the field of planet formation is: *Are dust substructures where planets form or are planets the origin of dust substructures?*

In general, these dust morphologies can almost always be interpreted as a signature of embedded forming planets that perturb their natal protoplanetary disk structure through gravitational interaction, and generate pressure maxima beyond their location [e.g., 96–103]. This flexibility is due in part to ill-constrained disk properties such as the thermochemical structure, the turbulence level, and the accretion process. There have been a lot of effort from the community to explain observed ring/cavity and rings/gaps dust morphologies by invoking forming planets as the main origin. Figure 1 shows the population of such hypothesized forming planets that are proposed to reproduce the observed disk substructures using hydrodynamical planet-disk interaction simulations. This figure suggests that the observed ring/cavity and rings/gaps dust morphologies could have been generated by a population of planet with masses of order 0.1–10 Jupiter mass and orbital radii of order 10–500 au (blue dots in Fig. 1). However, many caveats need to be raised here. First, it is striking to see that these putative planets distinctively occupy a different region of parameter space with respect to the known exoplanet population and our own Solar System. Second, it is known that a *single* embedded forming planet can form *multiple* rings and gaps [for a review, see 33], implying that some of the putative forming planets in Fig. 1 can be false positive. Third, direct detection of embedded forming planets is still elusive with only four confirmed ones (red dots in Fig. 1), although the kinematic signatures of potential embedded forming planets in different systems are encouraging [e.g., 104, 105]. Finally, the analysis of current observational facilities suggests that several of the putative planets should have already been detected [e.g., 106]. All in all, planets may not be the universal origin for ring/cavity and rings/gaps morphologies, especially in the case of younger systems.

Some of these dust morphologies may thus be what triggers the formation of planets, rather than the manifestation of already formed planets interacting with their natal protoplanetary disk. A natural question is then, *What non-planetary phys-*

ical processes can induce dust substructures? There actually exists a plethora of such processes [for a review, see 7]. One of them is driven by the MRI, which is source of turbulence in all protoplanetary disks and perhaps intervene in their accretion process (Sect. 1.4). This MRI-powered mechanism briefly works as follows: The nonideal MHD effects prevent the MRI from operating everywhere in the protoplanetary disk, which creates a complex dichotomy between MRI active regions with high turbulence level and non-MRI regions with low turbulence level (see Sect. 2.1). These radial variations in the disk turbulence can lead to gas accumulation at the transitions between MRI active and non-MRI regions, hence triggering the formation of pressure maxima and potentially form dust traps [107–110]. This MRI-powered mechanism has received a lot of attention in the recent years as a potential non-planetary origin for the observed dust substructures, and a potential way to initiate planet formation. Nonetheless, the theoretical and numerical studies investigating such a mechanism have been missing crucial ingredients, which hinders the proper understanding on the MRI physics for Class II protoplanetary disks: (1) the full feedback of dust evolution (grain growth processes and dynamics combined) on the MRI has not been considered, and (2) the numerical simulations have been integrated on timescales much shorter than disk secular evolution timescales (millions of years), hence preventing from a meaningful comparison with the observed ring/cavity and rings/gaps dust morphologies. This thesis stands here, aiming to revisit this MRI-powered mechanism by improving what is currently lacking.

1.6 THESIS GOAL AND OUTLINE

The ultimate goal of this thesis is to build the very first unified disk evolution framework that captures self-consistently the MRI-powered mechanism discussed above. This will provide a better understanding on whether or not it is involved in the *first steps* of planet formation by setting the initial conditions for the emergence of planets in their natal protoplanetary disks. Specifically, the goal of this thesis is to investigate how the interplay of gas evolution, dust evolution and MRI-driven turbulence shapes the protoplanetary disk secular evolution in order to potentially trigger planetesimal formation. In other words, the two central questions I will attempt to address throughout this thesis are: *Can the interplay of gas evolution, dust evolution and MRI-driven turbulence explain the dust substructures observed in protoplanetary disks with telescopes such as ALMA or VLT/SPHERE?, Can these induced dust substructures host the building blocks of planets and be potential birth-sites for them?* The work conducted in this thesis is organized as follows:

- In *Chapter 2* I provide the eager reader the essential theoretical background.

- In *Chapter 3* the necessary preparations for our quest are made, by presenting a global MRI-driven disk accretion model that derives self-consistently the MRI-induced disk turbulence for the outer region of Class II protoplanetary disks. This model circumvents the outstanding issue of computationally very

expensive 3D nonideal MHD global simulations, allowing for a possible coupling with gas and dust evolution models on long evolution timescales. This is key for investigating the secular evolution of protoplanetary disks where the accretion process is dominated by the MRI.

- In *Chapter 4* the first detour of our adventure is featured, which is to get an idea about how the MRI activity is shaped by the various protoplanetary disk components (stellar, gas and dust). This is very important if one wants to really understand what physical processes need to be accounted for in order to complement the global MRI-driven disk accretion model. Particularly, I want to understand better the MRI activity in disks by investigating the simple but invaluable case of steady-state MRI-driven accretion.

- In *Chapter 5* the second detour of our adventure is presented, where I investigate the MRI–dust coevolution on secular timescales in protoplanetary disks. This is a crucial step for our quest, which has not received enough attention in the literature and is poorly understood.

- In *Chapter 6* the pinnacle of our adventure is reached, where I finally dive into the complex interdependencies between gas, dust and MRI activity for the secular evolution of protoplanetary disks.

- In *Chapter 7* the main findings of this thesis are summarized, and an outlook on the field of planet formation with areas that warrant future thought is given.

FOUNDATIONS

To understand the formation of planets, one first needs to understand the main properties of their natal protoplanetary disks. This Chapter provides important foundational tools and concepts that encompass such properties. While it aims to be as broad as possible, it mainly introduces the topics which are directly related to the work presented in the next Chapters. For the rest of this thesis, I consider a star-protoplanetary disk system that has entered the Class II phase. It means that the pre-main-sequence central star of mass $M_\star$ is formed, and the envelop has dispersed to reveal a gravitationally stable disk made of gas and dust. I further consider disks which are not massive enough to be self-gravitating, implying that the gravitational potential is only the one exerted by the central star.

2.1 THE MAGNETOROTATIONAL INSTABILITY

As I discussed in Sect. 1.2, protoplanetary disks form from the collapse of slowly rotating and strongly magnetized molecular clouds. They thus inevitably inherit non-zero magnetic flux at the time of formation with a net large-scale magnetic field. Since the gas component of the protoplanetary disk is ionized, the gas can couple to the magnetic field lines. Furthermore, protoplanetary disks are differentially rotating disks (they rotate faster closer to the star) leading to a shear between a gas parcel orbiting at radius r and another gas parcel at radius $r + \delta_r$ ($\delta_r > 0$ is an infinitesimally small distance between the two gas parcels).

If the protoplanetary disk is weakly magnetized, namely the magnetic field is sufficiently weak, the disk is subject to a local instability called the magnetorational instability (MRI). This instability –which is at the core of this thesis– can be a source of mass accretion and angular momentum transport, hence a source of disk viscosity (gas turbulence) and potential origin for the Shakura-Sunyaev α-disk model (See Sect. 2.2). Below I describe the basic idea behind this instability by first assuming the case of ideal MHD, where the gas is perfectly coupled to the magnetic field lines (Sect. 2.1.3). Since protoplanetary disks are actually weakly ionized objects (See Sects. 3.3 and 3.4 for further details), the quasi-ideal version of the MRI can only develop in regions very close to the central star. In most regions of the protoplanetary disk, though, nonideal MHD effects can stabilize the disk against the MRI and completely modify the onset of its behavior (See Sect. 3.5.1 for further details). I thus introduce these nonideal MHD effects in a second part (Sect. 2.1.4). Before all of that I introduce some elementary concepts about non-relativistic MHD theory (Sect. 2.1.1) and the single-fluid approach used to simplify the set of non-relativistic MHD equations (Sect. 2.1.2).

2.1.1   *Elementary concepts about non-relativistic MHD theory*

Magnetohydrodynamics (MHD) is the dynamics of an electrically conducting fluid[1] (a fully ionized gas or partially ionized gas or a liquid metal) containing a magnetic field. In a nutshell, it can be seen as a fusion between the equations of hydrodynamics and electromagnetism.

For the continuum fluid approach to be valid (i.e., applying the equations of hydrodynamics), the essential idea is that the fluid under consideration needs to be collisional, namely fluid particles need to be subject to many collisions during one dynamical timescale (characteristic timescale of the flow). At the microphysical level, this ensures that the velocity distribution of the fluid particles can be approximated by Maxwellian distributions. One can thus treat the bulk motion and properties of the fluid rather than each of the particles that it is made of. When it is not the case, the continuum fluid approach breaks down and kinetic theory (statistical mechanics) needs to be employed, namely all the fluid particles need to be treated simultaneously. In practice, one can determine the Knudsen number to know whether to apply the continuum fluid approach or the kinetic theory. It is defined as

$$\mathrm{Kn} = \frac{\lambda_{\mathrm{mfp}}}{L}, \tag{1}$$

where λ_{mfp} is the mean free path of the fluid particles and L is the characteristic length of the fluid element. If $\mathrm{Kn} \ll 1$, the continuum fluid approach is valid and the fluid particles must share their momentum through collisions before leaving the fluid element. Otherwise, kinetic theory should be used. In this thesis the fluid approach is valid, and it is used to model the gas and dust components of the protoplanetary disk[2]. Since such objects are non-relativistic, I will specifically use the non-relativistic continuum fluid approach whose equations are invariant under the Galilean transformation.

In electromagnetism theory the electric field $\vec{E}$ and magnetic field $\vec{B}$ are governed by the Maxwell–Heaviside equations. Written in CGS units, as the rest of this thesis, they read

$$\vec{\nabla} \cdot \vec{E} = 4\pi q, \quad \vec{\nabla} \cdot \vec{B} = 0, \quad \vec{\nabla} \times \vec{E} = -\frac{1}{c}\frac{\partial \vec{B}}{\partial t}, \quad \vec{\nabla} \times \vec{B} = \frac{1}{c}\left(4\pi\vec{J} + \frac{\partial \vec{E}}{\partial t}\right), \tag{2}$$

where $c \approx 3 \times 10^{10}$ cm.s^{-1} is the speed of light in vacuum. For a charged particle in the fluid called j with charge q_j, number density n_j and mean velocity $\vec{v}_j$, I define the net charge density of the fluid

$$q = \sum_{\mathrm{charged\ species\,} j} \left(n_j q_j\right), \tag{3}$$

---

1 also called a plasma
2 one should note that the uppermost layers of protoplanetary disks can be close to the colissionless regime

and the current density[3]

$$\vec{J} = \sum_{\text{charged species j}} \left(n_j q_j \vec{v}_j \right).$$ (4)

It is well know that the Maxwell–Heaviside equations are invariant under the Lorentz transformation of special relativity. A difficulty thus arises since the non-relativistic equations of hydrodynamics are invariant under the Galilean transformation as I mentioned above. For a consistent non-relativistic MHD theory, valid for situations in which the fluid motions are slow compared to the speed of light, one needs to make the Maxwell–Heaviside equations Galilean invariant by neglecting all terms of order $\mathcal{O}\left(U^2/c^2\right)$, where $U \ll c$ is the characteristic velocity of the fluid (the largest of the fluid particles velocities). In a highly conducting fluid, one can expect the field to vary on same characteristic length L and time T of the fluid because any variation on smaller scales would be quickly smeared out by the rearrangement of charges, while changes on the typical scales of the fluid are maintained by the fluid motions. One has $U \sim L/T$, $|\vec{\nabla}| \sim 1/L$ and $\partial/\partial t \sim 1/T$. From the third equation of Eq. (2), one can find that $|\vec{E}| \sim (U/c)|\vec{B}|$ in orders of magnitude, namely $|\vec{E}| \ll |\vec{B}|$. It means that the electric fields generated by charges are much smaller than magnetic fields generated by currents. Inverting the fourth equation of Eq. (2) for $\vec{J}$ and taking the curl, one has

$$\frac{4\pi}{c}\vec{\nabla} \times \vec{J} = \vec{\nabla} \times \left(\vec{\nabla} \times \vec{B} \right) + \frac{1}{c^2}\frac{\partial^2 \vec{B}}{\partial t^2}$$ (5)

where the third equation of Eq. (2) has been used. The first term of Eq. (5) has orders of magnitude $\sim |\vec{B}|/L^2$, whereas the second term has orders of magnitude $\sim \left(|\vec{B}|U^2 \right)/\left(L^2 c^2 \right)$. Since the second term is of order $\mathcal{O}\left(U^2/c^2\right)$, it can be neglected and one can find that $|\vec{J}| \sim \left(|\vec{B}|c \right)/L$. It leads to $|\partial \vec{E}/\partial t| \sim |\vec{E}|/T \sim \left(U^2/c^2\right)|\vec{J}|$, using $|\vec{E}| \sim (U/c)|\vec{B}|$. As a result, the displacement current $\partial \vec{E}/\partial t$ is negligible in the fourth equation of Eq. (2). Finally, $|\vec{\nabla} \cdot \vec{E}| \sim |\vec{E}|/L \sim (U|B|)/(cL) \sim \left(U|\vec{J}| \right)/c^2 \sim \left(U^2/c^2\right) q$, where I used $|\vec{E}| \sim (U/c)|\vec{B}|$, $|\vec{J}| \sim \left(|\vec{B}|c \right)/L$ and $|\vec{J}| \sim qU$ (definition of the current density). $|\vec{\nabla} \cdot \vec{E}|$ is thus of order $\mathcal{O}\left(U^2/c^2\right)$ and can be ignored. Here the quasi charge neutrality of a non-relativistic MHD fluid has been retrieved

$$q = \sum_{\text{charged species j}} \left(n_j q_j \right) \approx 0.$$ (6)

This implies that the net charge density of the fluid is very small, but large currents can be present because charged fluid particles of opposite signs can flow in different directions. In the rest of this thesis, the charge neutrality condition will be written as $q = \sum_j n_j q_j = 0$ for simplicity.

---

[3] note that mobile charged particles is what matters for the current density

In summary, the Maxwell–Heaviside equations in the non-relativistic limit are given by

$$\vec{\nabla} \cdot \vec{E} \approx 0, \quad \vec{\nabla} \cdot \vec{B} = 0, \quad \vec{\nabla} \times \vec{E} = -\frac{1}{c}\frac{\partial \vec{B}}{\partial t}, \quad \vec{\nabla} \times \vec{B} \approx \frac{4\pi}{c}\vec{J}, \tag{7}$$

and they are Galilean invariant if the fields transform according to

$$\vec{E'} = \vec{E} + \vec{v} \times \vec{B}, \quad \vec{B'} = \vec{B}, \quad \vec{J'} = \vec{J}, \tag{8}$$

where prime quantities are in the rest (or co-moving) frame of the fluid. Non-prime quantities are in a frame where the fluid velocity is $\vec{v}$.

Finally, one need to couple these Maxwell–Heaviside equations to the equations of hydrodynamics. This is done by noting that the dynamical backreaction of the fields $(\vec{E}, \vec{B})$ on a charged fluid particle called j, with charge q_j, number density n_j and mean velocity $\vec{v}_j$, is the Lorentz force density defined as

$$\vec{f}_{L,j} = q_j n_j \left(\vec{E} + \frac{\vec{v}_j \times \vec{B}}{c} \right). \tag{9}$$

One should note that the Lorentz fore density only applies on the charged particles of the fluid, not on the neutrals in the case of a partially ionized fluid.

2.1.2 *Single-fluid approach*

Let us consider the gas component of the protoplanetary disk and ignore its dust component for now. Let us assume the gas to be partially ionized made of three fluids: the free electrons, ions, and neutral gas particles. Let the neutrals in the gas-phase have mass m_n, number density n_n, mass density $\rho_n = m_n n_n$, thermal pressure P_n, and mean velocity $\vec{v}_n$. Let charged particle j in the gas-phase (free electrons $j = e$, ions $j = i$) have mass m_j, charge $q_j = eZ_j$ (where Z_j can be either positive or negative), number density n_j, mass density $\rho_j = m_j n_j$, pressure P_j, and mean velocity $\vec{v}_j$. Here $Z_e = -1$ and $Z_i = +Z$ with $Z > 0$. Since charge neutrality condition applies in non-relativistic MHD theory (see Sect. 2.1.1), the net charge density of the gas, q, is zero and one has $q = \sum_{\text{charged species } j} (n_j q_j) = e(Zn_i - n_e) = 0$, namely

$$n_i = \frac{n_e}{Z}. \tag{10}$$

Let us define some macroscopic parameters for the gas, such as the total mass density

$$\rho_{\text{gas}} = \sum_{\text{all species } k} (\rho_k) = m_n n_n + m_e n_e + m_i n_i, \tag{11}$$

the current density

$$\vec{J} = \sum_{\text{charged species } j} (n_j q_j \vec{v}_j) = e(Zn_i \vec{v}_i - n_e \vec{v}_e) = en_e(\vec{v}_i - \vec{v}_e), \tag{12}$$

the mean mass velocity of the gas (bulk velocity)

$$\vec{v}_{\text{gas}} = \frac{1}{\rho_{\text{gas}}} \sum_{\text{all species } k} (\rho_k \vec{v}_k) = \frac{m_n n_n \vec{v}_n + m_e n_e \vec{v}_e + m_i n_i \vec{v}_i}{\rho_{\text{gas}}}, \tag{13}$$

and the total pressure of the gas

$$P_{\text{gas}} = \sum_{\text{all species } k} (P_k) = P_n + P_e + P_i. \tag{14}$$

Let us begin with the conservation of mass equation for all species in the gas-phase. For species k (neutrals $k = n$, free electrons $k = e$, ions $k = i$), it reads

$$\frac{\partial \rho_k}{\partial t} + \vec{\nabla} \cdot (\rho_k \vec{v}_k) = 0, \tag{15}$$

where $\vec{\nabla}$ is the Nabla operator.

Let us now write down the conservation of momentum equation for the neutrals, free electrons, and ions, remembering that the Lorentz force density only applies on charged particles. Let $\vec{B}$ be the magnetic field threading the protoplanetary disk, and $\vec{E}$ be the electric field. Since protoplanetary disks are weakly-ionized (which implies what the charge state of the ions Z is of order $\mathcal{O}(1)$), the gas is almost entirely neutral with only a small admixture of free electrons and ions. As a result, one can neglect the collisions between free electrons/ions and only consider the collisions between neutrals/free electrons as well as neutrals/ions, when writing down the conservation of momentum equations. For the neutrals, free electrons and ions, respectively, they read

$$\rho_n \underbrace{\left[\frac{\partial \vec{v}_n}{\partial t} + \left(\vec{v}_n \cdot \vec{\nabla} \right) \vec{v}_n \right]}_{\text{material derivative}} = -\vec{\nabla} P_n - \rho_n \vec{\nabla} \Phi - \vec{p}_{n \leftrightarrow e} - \vec{p}_{n \leftrightarrow i}, \tag{16}$$

$$\rho_e \left[\frac{\partial \vec{v}_e}{\partial t} + \left(\vec{v}_e \cdot \vec{\nabla} \right) \vec{v}_e \right] = -\vec{\nabla} P_e - \rho_e \vec{\nabla} \Phi - e n_e \left(\vec{E} + \frac{\vec{v}_e \times \vec{B}}{c} \right) - \vec{p}_{e \leftrightarrow n}, \tag{17}$$

and

$$\rho_i \left[\frac{\partial \vec{v}_i}{\partial t} + \left(\vec{v}_i \cdot \vec{\nabla} \right) \vec{v}_i \right] = -\vec{\nabla} P_i - \rho_i \vec{\nabla} \Phi + e Z n_i \left(\vec{E} + \frac{\vec{v}_i \times \vec{B}}{c} \right) - \vec{p}_{i \leftrightarrow n}. \tag{18}$$

where Φ is the gravitational potential, $\vec{p}_{n \leftrightarrow e}$ (resp. $\vec{p}_{n \leftrightarrow i}$) is the rate of momentum exchange due to collisions between neutrals and free electrons (resp. ions) in the gas-phase. One should note that $\vec{p}_{n \leftrightarrow e} = -\vec{p}_{e \leftrightarrow n}$ and $\vec{p}_{n \leftrightarrow i} = -\vec{p}_{i \leftrightarrow n}$, in accordance with Newton's third law.

To overcome the difficulty of dealing with multi-fluids in the gas and avoid this large number of equations, one can adopt a single-fluid approach by noting that the timescale for macroscopic evolution of the gas as a whole is generally much

longer than the timescale for collisional or magnetic forces to alter the momentum of a charged particle. Roughly speaking this approach can be used when the charged fluids (free electrons and ions) inertia are negligible compared to that of the neutral fluid, the coupling between charged and neutral particles is strong, and the recombination timescale is short compared to the dynamical timescale. This approach, also called the strong coupling limit [111], is argued to be justified in protoplanetary disks [e.g., 112, 113]. In this thesis, I will thus make use of this approach. Since $m_n \gg m_i, m_e$ and the gas is weakly ionized, one can notice that $\rho_{gas} \approx \rho_n$, $n_{gas} \approx n_n$ and $\vec{v}_{gas} \approx \vec{v}_n$. It implies that the momentum contributions for the gas as a whole is much less from the free electrons and ions than it is from the neutrals. Consequently, the bulk motion of the gas can be approximated by the motion of the neutrals.

The goal now is to obtain the conservation of mass and momentum equations for the gas as a whole in this single-fluid approach. The former can be easily obtained by simply adding up the conservation of mass equation for the neutrals, free electrons, and ions. The conservation of mass equation for the gas as a whole then reads

$$\frac{\partial \rho_{gas}}{\partial t} + \vec{\nabla} \cdot \left(\rho_{gas} \vec{v}_{gas} \right) = 0. \tag{19}$$

The conservation of momentum equation for the gas as whole is obtained by adding up the conservation of momentum equation for the neutrals, free electrons and ions while using the single-fluid approximation. Let us first add together Eqs (16), (17) and (18). The right-hand side (RHS) of the resulting equation is given by (using the compatibility of the cross-product with scalar multiplication)

$$-\vec{\nabla} \left(P_n + P_i + P_e \right) - \left(\rho_n + \rho_i + \rho_e \right) \vec{\nabla} \Phi + e \left(Z n_i - n_e \right) \vec{E} + \frac{e \left(Z n_i \vec{v}_i - n_e \vec{v}_e \right) \times \vec{B}}{c}. \tag{20}$$

With the charge neutrality condition and the notations introduced above, the RHS can be written as

$$-\vec{\nabla} P_{gas} - \rho_{gas} \vec{\nabla} \Phi + \frac{\vec{J} \times \vec{B}}{c}. \tag{21}$$

The left-hand side (LHS) of the resulting equations is

$$\rho_n \left[\frac{\partial \vec{v}_n}{\partial t} + \left(\vec{v}_n \cdot \vec{\nabla} \right) \vec{v}_n \right] + \rho_i \left[\frac{\partial \vec{v}_i}{\partial t} + \left(\vec{v}_i \cdot \vec{\nabla} \right) \vec{v}_i \right] + \rho_e \left[\frac{\partial \vec{v}_e}{\partial t} + \left(\vec{v}_e \cdot \vec{\nabla} \right) \vec{v}_e \right]. \tag{22}$$

Using the single-fluid approximation, the LHS can be written as

$$\rho_{gas} \left[\frac{\partial \vec{v}_{gas}}{\partial t} + \left(\vec{v}_{gas} \cdot \vec{\nabla} \right) \vec{v}_{gas} \right]. \tag{23}$$

The conservation of momentum equation for the bulk of the gas is thus

$$\rho_{gas} \left[\frac{\partial \vec{v}_{gas}}{\partial t} + \left(\vec{v}_{gas} \cdot \vec{\nabla} \right) \vec{v}_{gas} \right] = -\vec{\nabla} P_{gas} - \rho_{gas} \vec{\nabla} \Phi + \underbrace{\frac{1}{4\pi} \left(\vec{\nabla} \times \vec{B} \right) \times \vec{B}}_{\text{magnetic force density}} \tag{24}$$

where I used $\vec{J} = (c/4\pi)\, \vec{\nabla} \times \vec{B}$ (fourth equation of Eq. 7). By expanding $\left(\vec{\nabla} \times \vec{B}\right) \times \vec{B}$, the magnetic force density above can be seen as the sum of the magnetic pressure gradient of the fields lines and their magnetic tension. The conservation of momentum equation for the bulk of the gas, in its convective form, can finally be written as

$$\rho_{\text{gas}} \left[\frac{\partial \vec{v}_{\text{gas}}}{\partial t} + \left(\vec{v}_{\text{gas}} \cdot \vec{\nabla}\right) \vec{v}_{\text{gas}} \right] = -\vec{\nabla}\left(P_{\text{gas}} + P_B\right) - \rho_{\text{gas}}\vec{\nabla}\Phi + \underbrace{\frac{1}{4\pi}\left(\vec{B} \cdot \vec{\nabla}\right)\vec{B}}_{\text{magnetic tension}}, \quad (25)$$

where I introduced $P_B = B^2/8\pi$ the magnetic pressure, and $B = |\vec{B}|$ the r.m.s. of the magnetic field. The magnetic field thus acts in two ways on the gas flow: It resists gas motions that compress and bend the magnetic field lines. This is fundamental, and the effect of magnetic tension needs to be kept in mind to understand the nature of the MRI. One should note that the molecular viscosity of the gas has been neglected in the derivation above. It is because its contribution to the momentum is negligible compared to the other terms (See Sect. 1.4).

In summary, the conservation of mass and momentum equations for the gas in the single-fluid approach, where the motion of the gas as whole can be approximated by the motions of the neutrals, are given by Eqs. (19) and (25), respectively. In order to proceed, one needs an evolutionary equation for the magnetic field $\vec{B}$ also called the induction equation. This the topic of the next two Sections, where I finally reveal what is the MRI.

2.1.3 *MRI in ideal MHD*

In the single-fluid approach employed in the previous section, the inertia of the charged particles in the gas-phase (free electrons and ions) is negligible. In the frame co-moving with the neutrals (where the electric field is $\vec{E}$), the equation of motion for the charged particles in the gas-phase (Eqs. 17 and 18) is set by the balance between the Lorentz force density and the collision term due to neutral drag[4]. For the free electrons and ions, respectively, one thus has

$$-e n_e \left(\vec{E} + \frac{\vec{v}_e \times \vec{B}}{c} \right) - \vec{p}_{e \leftrightarrow n} \approx \vec{0}, \quad (26)$$

and

$$eZ n_i \left(\vec{E} + \frac{\vec{v}_i \times \vec{B}}{c} \right) - \vec{p}_{i \leftrightarrow n} \approx \vec{0}. \quad (27)$$

Let us now specify the form for the collisional terms $\vec{p}_{e \leftrightarrow n}$ and $\vec{p}_{i \leftrightarrow n}$. They are intrinsically related to the drift velocities between the neutrals and charged particles. The rate of momentum exchange due to collisions between a charged particle j and the neutrals, $\vec{p}_{j \leftrightarrow n}$, can be written as

$$\vec{p}_{j \leftrightarrow n} = \gamma_j \rho_j \rho_n \left(\vec{v}_j - \vec{v}_n\right). \quad (28)$$

---

[4] drag due to collisions between the charged particle j and the neutrals

Here γ_j is the neutral drag coefficient on charged particle j defined as

$$\gamma_j = \frac{\langle \sigma v \rangle_{j \leftrightarrow n}}{m_n + m_j}, \tag{29}$$

where $\langle \sigma v \rangle_{j \leftrightarrow n}$ is the rate coefficient for momentum transfer in collisions by elastic scattering between species j and neutrals (defined in Sect. 3.5.1), and $m_n = \mu m_H$ is the mean molecular mass. In general, the relative importance for a charged particle j between the Lorentz force density and the neutral drag is characterized by the ratio between the gyrofrequency and the rate of momentum exchange due to collisions, called the Hall parameter. For a charged particle j, the Hall parameter[5] β_j is defined as

$$\beta_j = \frac{|Z_j| e B}{m_j c} \frac{1}{\gamma_j \rho_n}, \tag{30}$$

with $B = |\vec{B}|$ the r.m.s. strength of the magnetic field. Remembering that $\rho_n \approx \rho_{gas}$ for the single-fluid approach, ρ_n is computed using Eq. (66) in this thesis. When $\beta_j \ll 1$ the charged particle j is strongly coupled with the neutrals and collisions dominate, whereas it is strongly coupled to the magnetic field and the magnetic force dominates when $\beta_j \gg 1$. One should note that $\beta_e \gg \beta_i$, since the free electrons are much more mobile than the ions ($m_e \ll m_i$). Consequently, the free electrons generally dominate the electric conduction of the gas, and magnetic fields are effectively carried by them.

To further proceed and obtain the induction equation for the magnetic field $\vec{B}$, let us make the great following simplifications: (1) the magnetic force must dominate over the collisional term for both free electrons and ions, hence $\beta_i, \beta_e \gg 1$ (i.e., the drift velocities $|\vec{v}_i - \vec{v}_n|$ and $|\vec{v}_e - \vec{v}_n|$ are small enough or the magnetic field is strong enough); and (2) the free electrons and ions must be tightly coupled (i.e., their drift velocity $|\vec{v}_i - \vec{v}_e|$ is small enough but not zero to have currents and magnetic fields). In this case, $\vec{v}_j \approx \vec{v}_e \approx \vec{v}_n \approx \vec{v}_{gas}$ (the equality comes from the single-fluid approach) and both Eqs. (26), (27) give

$$\vec{E} \approx -\frac{\vec{v}_{gas} \times \vec{B}}{c}. \tag{31}$$

This case is called the ideal MHD regime, and the ideal induction equation is obtained by simply combining Eq. (31) and the third equation of Eq. (7). It reads

$$\frac{\partial \vec{B}}{\partial t} = \vec{\nabla} \times \left(\vec{v}_{gas} \times \vec{B} \right). \tag{32}$$

One should note that the ideal induction equation implies that the magnetic field lines are "frozen-in", namely there is no diffusion of the magnetic field with respect to the gas. This is known as the Alfvén's theorem.

By using the conservation of mass and momentum equations for the gas in the single-fluid approach (Eqs. 19 and 25) and the ideal induction equation (Eq. 32),

---

5 caution not to confuse it with the plasma-β parameter, which is the ratio between the gas thermal pressure and the magnetic pressure

it can be shown [e.g., 88, 114, 115] that the differentially rotating gas component of the protoplanetary disk, threaded by a weak magnetic field[6], is unstable to an infinitesimal perturbation of the field lines if

$$\frac{\partial \Omega^2}{\partial r} < 0, \tag{33}$$

with Ω the angular velocity of the gas. In protoplanetary disks the angular velocity is almost the Keplerian angular velocity, which decreases outward (See Sect. 2.2). Consequently, the differentially rotating gas component of the protoplanetary disk is unstable to an infinitesimal perturbation of the field lines everywhere, except in the boundary layer of the disk near the star. This is the simplest manifestation of the MRI.

The basic physical mechanism of the MRI in its ideal MHD version is illustrated in Fig. 9. Let us consider two gas parcels located at the same distance from the central star and linked by a magnetic field line that is purely vertical when unperturbed. When that field line is slightly perturbed radially (possible only if the field is weak enough for magnetic tension not to be dominant initially), these two gas parcels are displaced by perfectly following the field line perturbation (ideal MHD regime). They thus move at different radial locations. Due to the resulting difference in their angular velocities (shear in the disk), with the inner gas parcel rotating faster than the outer one (the angular velocity decreases outward in accretion disks such as protoplanetary disks), the gas parcels move apart azimuthally. This stretches the magnetic field line coupled to the two gas parcels. Magnetic tension[7] then acts to reduce this stretch by imparting forces to both the inner gas parcel (in the direction opposite to its orbital motion) and the outer gas parcel (in the direction along its orbital motion). Magnetic tension thus slows down the inner gas parcel (reducing its angular momentum) while it accelerates the outer one (increasing its angular momentum). The inner gas parcel moves further inward while the outer one moves outward because the angular momentum increases outward in accretion disks such as protoplanetary disks. The magnetic field line becomes even more stretched, leading to a runaway process. As a result, the MRI grows and at the same time generates MHD turbulence as well as transports angular momentum radially outward, which is needed for accretion (see Fig. 10). For the instability to develop, the magnetic field can be arbitrarily weak but not arbitrarily strong as I mentioned above. Roughly speaking, the magnetic pressure needs to be smaller than the gas thermal pressure. Furthermore, one should note that the MRI grows quickly, with the growth timescale being of order of the local orbital period in the linear regime.

---

6 the magnetic field needs to be in sub-equipartition
7 which can be thought of as being analogous to a stretched spring

perturb initially
vertical magnetic field

shear leads to
azimuthal displacement

magnetic tension
transfers angular
momentum

fluid elements separate
radially ⟶ instability
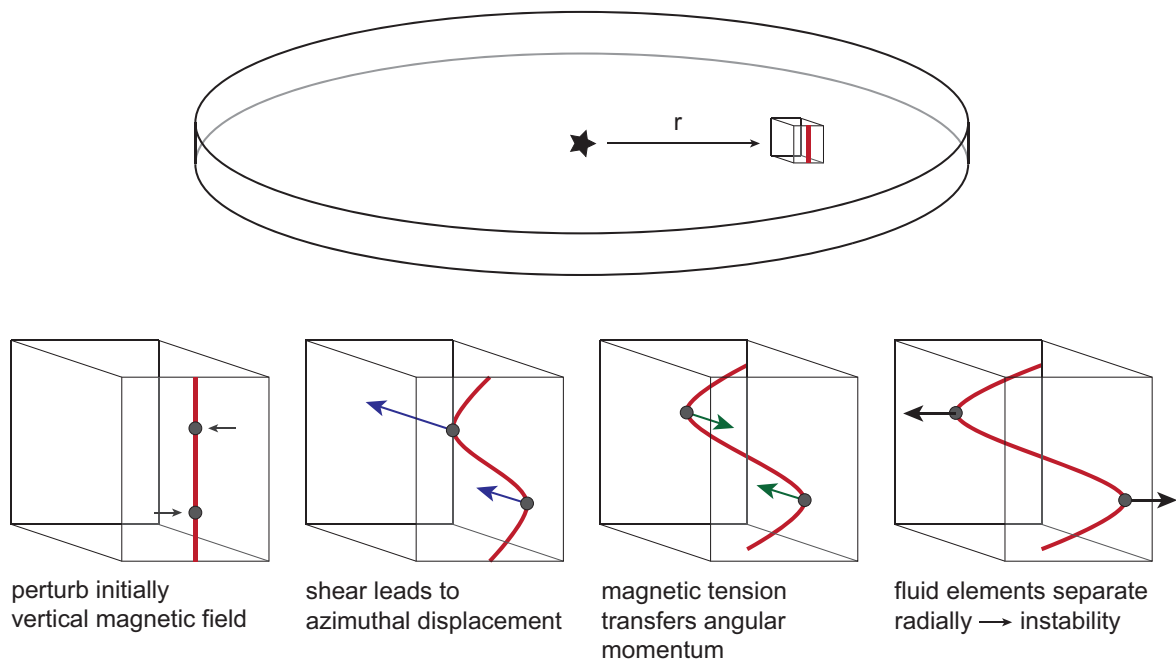
Figure 9: Cartoon illustrating why a weak magnetic field destabilizes a Keplerian disk, leading to the magnetorotational instability (MRI). See the main text in Sect. 2.1.3 for a description. Figure taken from Armitage [116].
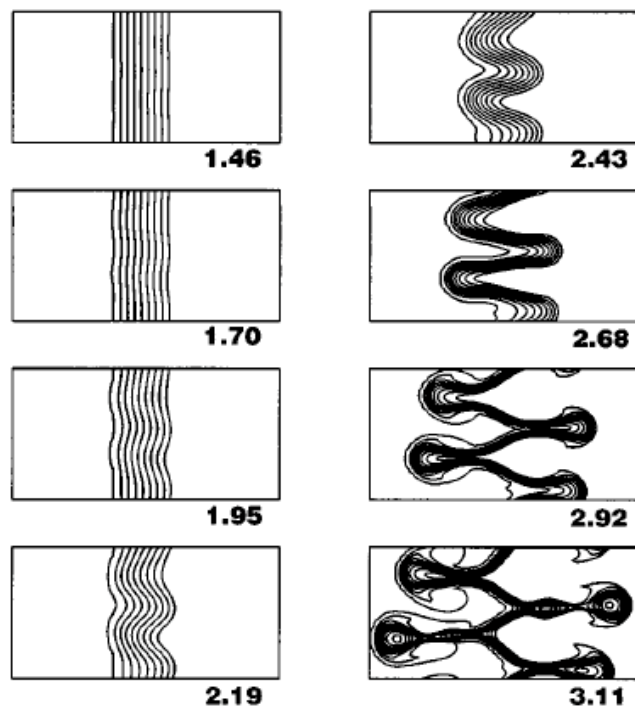
Figure 10: Ideal MHD simulation showing that the growth of the MRI is intricately related to MHD turbulence and angular momentum transport. Figure taken from Balbus and Hawley [117].

2.1.4 *MRI in nonideal MHD*

In the previous section, the ideal MHD regime has been employed in order to un-veil the nature of the MRI in its ideal MHD version. For this regime to be valid, I showed that: (1) the magnetic force must dominate over the collisional term for both the free electrons and ions; and (2) the free electrons and ions must be tightly coupled. In practice, the quasi-ideal MHD version of the MRI can thus arise when the protoplanetary disk is ionized enough[8]. This is possible in regions where ther-mal ionization or thermionic emission are efficient. The former is important for producing free electrons and ions in the gas-phase when the gas temperature be-comes high enough to start ionizing alkali metals present in the gas-phase. For example, the ionization potential of potassium is 4.34 eV, which leads to temper-atures higher than $\sim 800\,\mathrm{K}$ for appreciable gas ionization relevant for sustaining the MRI in its ideal MHD version. The latter also becomes important for similar gas temperatures due to electrons on the dust grains obtaining a finite probabil-ity of leaving the grain to produce free electrons. As a result, the gas is ionized enough to sustain the MRI in its ideal MHD version only in the very inner regions of the protoplanetary disks ($\lesssim 1\,\mathrm{au}$). It implies that, in most of the protoplanetary disk, the gas is very weakly ionized with the ionization process being initiated by nonthermal ionization of molecular hydrogen and helium (see Sect. 3.3). When the very weakly ionized gas is imperfectly coupled to the magnetic field lines, non-ideal MHD effects can stabilize the disk against the MRI and completely modify the onset of its behavior, as I show below.

Let us go back to the balance between the Lorentz force density and the collision term due to neutral drag for the free electrons (Eq. 26), obtained in the single-fluid approach. Let us attempt to re-write this equation in terms of the current density. Let us start with the mathematically equivalent expression, using the definition of $\vec{p}_{e\leftrightarrow n}$ and introducing the various drift velocities between each particles present in the gas-phase (free electrons, ions, and neutrals)

$$\vec{E} + \frac{1}{c}\left[\vec{v}_n + (\vec{v}_e - \vec{v}_i) + (\vec{v}_i - \vec{v}_n)\right] \times \vec{B} + \frac{m_e \gamma_e \rho_n}{e}\left[(\vec{v}_e - \vec{v}_i) + (\vec{v}_i - \vec{v}_n)\right] = \vec{0}. \quad (34)$$

The two terms that involve $(\vec{v}_e - \vec{v}_i)$ can be replaced with the current density, since

$$(\vec{v}_e - \vec{v}_i) = -\frac{\vec{J}}{e n_e}. \quad (35)$$

By definition of the rate momentum exchange due to collisions between ions and neutrals ($\vec{p}_{i\leftrightarrow n}$), $(\vec{v}_i - \vec{v}_n) = \vec{p}_{i\leftrightarrow n}/(\gamma_i \rho_i \rho_n)$. Furthermore, adding up Eqs. (26) and (27), leads to $\vec{p}_{i\leftrightarrow n} + \vec{p}_{e\leftrightarrow n} = \left(\vec{J} \times \vec{B}\right)/c$. Noting that $|\vec{p}_{e\leftrightarrow n}|$ is small compared to $|\vec{p}_{i\leftrightarrow n}|$, provided that the drift velocity $|\vec{v}_e - \vec{v}_n|$ is not much larger than $|\vec{v}_i - \vec{v}_n|$ [for a discussion, see Appendix A of 114],

$$(\vec{v}_i - \vec{v}_n) \approx \frac{1}{c \gamma_i \rho_i \rho_n}\left(\vec{J} \times \vec{B}\right). \quad (36)$$

---

8 but still weakly ionized in comparison to other astrophysical objects

Inserting the drift velocities re-written in terms of the current density into Eq. (34), one has

$$\vec{E} + \frac{\vec{v}_n \times \vec{B}}{c} - \frac{m_e \gamma_e \rho_n}{e^2 n_e}\vec{J} + \frac{1}{c^2 \gamma_i \rho_i \rho_n}\left(\vec{J} \times \vec{B}\right) \times \vec{B} - \frac{1}{e n_e c}\left[1 - \frac{Z m_e \gamma_e}{m_i \gamma_i}\right]\left(\vec{J} \times \vec{B}\right) = \vec{0}.$$
(37)

In order to obtain the term $[1 - (Z m_e \gamma_e) / (m_i \gamma_i)]$, I used $\rho_i = m_i n_i$ and $n_e = Z n_i$ (charge neutrality condition). Noting that Z is of order of $\mathcal{O}(1)$ in weakly ionized protoplanetary disks, $m_e \ll m_i$ and $\gamma_e \ll \gamma_i$ (for the same reasons why $|\vec{p}_{e\leftrightarrow n}|$ is small compared to $|\vec{p}_{i\leftrightarrow n}|$), one has $[1 - (Z m_e \gamma_e) / (m_i \gamma_i)] \approx 1$. Introducing the unitary vector $\hat{\vec{B}}$, such that $\vec{B} = B\hat{\vec{B}}$ with B the r.m.s. strength of the magnetic field, and remembering that $\vec{v}_n \approx \vec{v}_{gas}$ as well as $\rho_n \approx \rho_{gas}$ for the single-fluid approach employed, Eq. (37) can be re-written as

$$\vec{E} = -\frac{\vec{v}_{gas} \times \vec{B}}{c} + \frac{m_e \gamma_e \rho_{gas}}{e^2 n_e}\vec{J} - \frac{B^2}{c^2 \gamma_i \rho_i \rho_{gas}}\left(\vec{J} \times \hat{\vec{B}}\right) \times \hat{\vec{B}} + \frac{B}{e n_e c}\left(\vec{J} \times \hat{\vec{B}}\right).$$
(38)

One should note that inverting this expression leads to a generalized Ohm's law that is applicable *only when* the mobile charged particles are free electrons and ions.

Combining Eq. (38) with the third equation of Eq. (7), one can finally obtain the nonideal induction equation for the magnetic field $\vec{B}$

$$\frac{\partial \vec{B}}{\partial t} = \underbrace{\vec{\nabla} \times \left(\vec{v}_{gas} \times \vec{B}\right)}_{\text{ideal MHD term}} - \underbrace{\frac{4\pi}{c}\vec{\nabla} \times \left[\eta_O \vec{J} + \eta_{AD} \vec{J}_\perp + \eta_H \left(\vec{J} \times \hat{\vec{B}}\right)\right]}_{\text{nonideal MHD term}},$$
(39)

where the current density $\vec{J}$ is given by the fourth equation of Eq. (7). Here I have introduced $\vec{J}_\perp = \hat{\vec{B}} \times \left(\vec{J} \times \hat{\vec{B}}\right)$, which is the component of $\vec{J}$ perpendicular to the magnetic field $\vec{B}$. Furthermore, $\eta_O, \eta_{AD}, \eta_H$ have the dimension of diffusion coefficients. They are called the Ohmic, ambipolar diffusion and Hall magnetic diffusivity, respectively, and are defined as

$$\eta_O = \frac{c^2 m_e \gamma_e \rho_{gas}}{4\pi e^2 n_e}, \qquad \eta_{AD} = \frac{B^2}{4\pi \gamma_i \rho_i \rho_{gas}}, \qquad \eta_H = \frac{cB}{4\pi e n_e}.$$
(40)

Taking a closer look at Eq. (39), one can notice that the new induction equation for the magnetic field $\vec{B}$ is the ideal induction equation modified by nonideal MHD terms. Going from left to right in Eq. (40), the nonideal MHD terms are called Ohmic resistivity, ambipolar diffusion and the Hall effect. Their strength is controlled by their respective magnetic diffusivities η_O, η_{AD} and η_H. Looking back at the derivation conducted so far, one can easily understand that Ohmic resistivity mainly originates from the collisions between free electrons and neutrals, creating the free electron-neutral drift. Ambipolar diffusion mainly arises due to the collisions between ions and neutrals, creating the ion-neutral drift. Finally, the Hall effect mainly appears due to the free electron-ion drift.

When comparing the relative strength of a nonideal MHD term with respect to another, it is convenient to notice that

$$\frac{\eta_H}{\eta_O} = \beta_e, \qquad \frac{\eta_{AD}}{\eta_H} = \beta_i, \qquad \frac{\eta_{AD}}{\eta_O} = \beta_e\beta_i, \tag{41}$$

where β_e and β_i are the Hall parameter for free electrons and ions, respectively, with $\beta_e \gg \beta_i$ as I already mentioned in the previous section. As a result, Ohmic resistivity is the dominant nonideal MHD term when $\beta_i \ll \beta_e \ll 1$, namely both the free electrons and ions are strongly coupled to the neutrals through collisions. Ambipolar diffusion is the dominant nonideal MHD term when $\beta_e \gg \beta_i \gg 1$, namely both the free electrons and ions are strongly coupled to the magnetic field through the Lorentz force density. The Hall effect is the dominant nonideal MHD term when $\beta_e \gg 1 \gg \beta_i$, namely the free electrons are strongly coupled to the magnetic field, but the ions are strongly coupled to the neutrals. Finally, noting that $\beta_j \propto B/\rho_{gas}$ (see Eq. 30), Ohmic resistivity dominates in regions of the protoplanetary disk where the gas density is high and the magnetic field strength is low, which corresponds to the inner regions of the disk near its midplane. Ambipolar diffusion dominates where the gas density is low (the collisions with the neutrals are not enough to couple the whole gas to the magnetic field) and the magnetic field strength is strong, which corresponds to the outer regions of the disk and its surface layers. The Hall effect dominates for regions that lie in-between.

While Eq. (39) corresponds to the nonideal induction for the magnetic field $\vec{B}$ that is widely used for protoplanetary disks, one should note that the exact expressions for the magnetic diffusivities given in Eq. (40) or their ratios in Eq. (41) are applicable *only when* the mobile charged particles are exclusively free electrons and ions. In Sect. 3.5.1, I provide more general expressions that can incorporate an arbitrary number of positively and negatively charged particles. In particular, the eager reader may have already realized that including the dust component of the protoplanetary disk in these calculations is crucial, and will complicate the picture drawn here.

The nonideal MHD effects affect the propagation of MHD waves, and lead to energy dissipation. Without loss of generality[9], the energy dissipation rate associated with the nonideal MHD terms is given by

$$\dot{\epsilon}_{\text{nonideal MHD}} = \frac{1}{c}\vec{J}\cdot\left\{\frac{4\pi}{c}\left[\eta_O\vec{J} + \eta_{AD}\vec{J}_\perp + \eta_H\left(\vec{J}\times\hat{B}\right)\right]\right\} = \frac{4\pi}{c^2}\left[\eta_O|\vec{J}|^2 + \eta_{AD}|\vec{J}_\perp|^2\right]. \tag{42}$$

It is clear that Ohmic resistivity dissipates the total current density (leading to magnetic reconnection), whereas ambipolar diffusion only dissipates the current density perpendicular to the magnetic field. In the linear regime, Ohmic resistivity and ambipolar diffusion damps all three families of MHD waves (Alfvén, slow and fast), although in different ways. The Hall effect, though, is *not* dissipative. It describes magnetic diffusion without breaking the magnetic field lines, which is

---

9 the mathematical expression of the energy dissipation rate is correct even when other charged particles than free electrons and ions are included

in some way a similar behavior of the ideal MHD term $\vec{\nabla} \times \left(\vec{v}_{gas} \times \vec{B} \right)$. Due to its non-dissipative character, the Hall effect does not damp MHD waves, but it breaks the degeneracy between the left- and right- handed Alfvén waves. Furthermore, the Hall effect is the only nonideal MHD effect that depends on the polarity of the magnetic field. Indeed, the nonideal MHD equation (Eq. 39) is not invariant when flipping the direction of $\vec{B}$ because $\eta_H \propto B$, whereas η_O is independent of the magnetic field strength B and $\eta_{AD} \propto B^2$. Since the origin of the Hall effect is the drift between free electrons and ions, one should note that it is present even in fully ionized plasma, unlike the two other nonideal MHD effects.

What about the MRI in all of this?, the eager reader may ask. In the previous section, I discussed that the magnetic field lines need to be sufficiently coupled to the gas motion for the MRI to operate. The nonideal MHD effects weaken this coupling by allowing the magnetic field to diffuse with respect to the gas motion, which can stabilize the magnetized protoplanetary disk against the MRI (Ohmic resistivity and ambipolar diffusion) and even generate new MHD instabilities (the Hall effect). In the case of Ohmic resistivity, for example, I showed that η_O is independent of the magnetic field strength, $\eta_O \propto \gamma_e \propto T$ with T the gas temperature, and $\eta_O \propto n_{gas}/n_e$ which is the inverse of the gas ionization degree (tells how well the gas is ionized). As a result, Ohmic resistivity only depends on how well the gas is ionized and how hot it is. The gas ionization degree at which Ohmic resistivity suppresses the MRI is of the order $n_e/n_{gas} \sim 10^{-13}$ [e.g., 115]. Since protoplanetary disks mostly rely on nonthermal ionization sources to ionize the gas, the gas ionzation degree can be even lower in the cold dense regions of the disk. In such regions, the so-called "dead zone" [118], the MRI cannot operate.

The nonideal MHD effects, especially Ohmic resisitivity and ambipolar diffusion, thus lead to the very interesting concept of layered accretion in protoplanetary disks (see Fig. 16 for a picture), since they can suppress the MRI in some regions of the disk but not others[10]. In the dead zone, the gas flow is largely laminar potentially dominated by hydrodynamic instabilities. In contrast, the immediate surface layers of the disk above the dead zone as well as the regions beyond the dead zone are sufficiently ionized for the MRI to operate. These regions are called the "MRI active layer", and the gas is turbulent there. In the surface layers of the disk located even higher and the regions located even further from the central star, ambipolar diffusion suppresses the MRI and the gas flow becomes once again laminar, potentially dominated by hydrodynamic instabilities. One should note that the Hall effect could modify this layered accretion picture due to the new MHD effects it introduces. The fact that protoplanetary disk might be layered accretion disks is very important for planet formation, due to the ability of causing jumps in turbulence at the transitions between MRI and non-MRI regions. At these transitions the gas might accumulate and form a pressure maximum, where dust particles might be trapped. Some of the observed dust substructures (Sect. 1.3) might thus be explained by invoking no other processes than MRI-driven accretion itself. Fur-

---

10 I provide, in Sect. 3.5.1, criteria that depend on the nonideal MHD terms in order to know where the MRI can operate in the disk

thermore, locally trapped dust particles can more efficiently coagulate and grow in size, which in turn might explain the formation of the building blocks of planets (pebbles and planetesimals). Although such an idea has become very popular in the recent years [e.g., 108–110, 119], no framework has had all the necessary physical ingredients to properly investigate it. The main goal of this thesis is to provide such a framework for the first time.

2.2   PROTOPLANETARY DISK GAS STRUCTURE AND EVOLUTION

The fact that protoplanetary disks are actively accreting requires transport and loss of angular momentum. Angular momentum transport is the most fundamental problem in the theory of accretion disks, which is determined by the internal gas dynamics in the disk, and largely governs the secular evolution of the disk. There are two ways for the angular momentum to be transported in accretions disks: Radial transport (local redistribution due to gas turbulence) within the disk, and vertical transport (loss) from the disk. The radial transport of angular momentum generally requires MHD and/or hydrodynamic and/or gravitational turbulence, whereas the vertical transport generally requires MHD disk winds (Sect. 1.4).

As I already mentioned in Sect. 1.6, the aim of this thesis is to specifically investigate how the interplay of gas, dust and MRI shapes the secular evolution of protoplanetary disks. Since protoplanetary disks spend most of their lifetime in the Class II phase (Sect. 1.3), the disk gas mass is not large enough compared to the mass of the central star for significant self-gravitating interactions, hence gravitational turbulence, to be driven. The radial transport for angular momentum that I thus considered in this thesis are the MHD turbulence driven by the MRI (important in the MRI active layer of the disk) and hydrodynamic instabilities (important in the non-MRI regions of the disk such as the dead zone). In order to solely focus on the interplay of gas, dust and MRI, I will further neglect the vertical transport driven by the MHD disk winds. One should note, though, that the latter are very important for the accretion process. Indeed, the nonideal MHD effects such as Ohmic resistivity or ambipolar diffusion can severely modify the onset of the MRI, which makes it hard for the MRI to explain alone the observed disk accretion rates. Nonetheless, I defer the inclusion of MHD disk winds to future work in order to avoid the kitchen-sink approach where everything is included but nothing is understood.

When the MRI operates in some regions of the protoplanetary disk, the local radial redistribution of angular momentum originates from the shear stress produced between two adjacent gas bands rotating at different angular velocities, where the inner gas band rotates faster than the outer one (see Sect. 2.1.3). Such a process is called a "viscous" process. The general theory for the evolution of viscously accreting disks was set out by Shakura and Sunyaev [120] and Lynden-Bell and Pringle [121], in the so-called α-disk model. The α parameter characterizes both the effi-

ciency of radial angular momentum transport and the turbulence strength. One way to define it is as

$$T_{r\phi} = \frac{3}{2}\alpha P_{gas} = \frac{3}{2}\alpha \rho_{gas} c_s^2,$$ (43)

where α is a dimensionless quantity such that $0 < \alpha < 1$, P_{gas} is the local thermal gas pressure, ρ_{gas} is the local gas mass density, c_s is the local sound speed, and $T_{r\phi}$ is the sum of the Reynolds and Maxwell component of the shear stress tensor between the radial direction and azimuthal direction, as I will introduce in Eq. (71). Here I have used the cylindrical coordinate system centered on the star (r, ϕ, z) with the basis $(\vec{e}_r, \vec{e}_\phi, \vec{e}_z)$, respectively the radial, azimuthal and vertical direction. The idea of the α parameter is that the turbulent velocities, whose correlation determines $T_{r\phi}$ as I will show in Sect. 2.2.3, would be limited by the local sound speed. Indeed, velocities in excess would create shocks and quickly drop to below the sound speed, hence killing the turbulence and radial angular momentum transport.

Although most works studying the secular evolution of protoplanetary disks assume constant value for α and treat it as a free parameter, I want to emphasize that the α parameter is actually determined by the microphysics in the accretion disk. In the context of this thesis, the origin of α is the MRI. Numerical simulations have shown that the saturation of the MRI leads to strong MHD turbulence and efficient outward transport of angular momentum, where the MRI-induced viscosity α parameter has been found to be variable over space with values in the range 10^{-3}–10^{-1} [e.g., 122–127]. In general, the MRI-induced turbulence is highly dependent on the magnetic field topology and the detailed microphysics, the latter lacking in most of these simulations. One of the main achievements of this thesis is the fact that an accretion model has been built in order to compute self-consistently this MRI-induced α given gas, dust and stellar properties of the disk (see Chapter 3).

The timescale associated with viscous accretion can be roughly estimated by dividing the measured disk gas masses by the observed accretion rates, which gives a timescale of order of $\mathcal{O}(Myrs)$ for typical disk values [e.g., 18]. Furthermore, protoplanetary disks are observed to be geometrically thin (i.e., their height is much smaller than their radius). Consequently, the secular evolution timescale is much longer than the timescale associated with obtaining dynamical equilibrium in the protoplanetary disk. I will thus consider the structure and evolution of the protoplanetary disk as two separate problems. Before diving into these topics, let us talk about the thermal structure of the disk.

2.2.1   *Thermal structure*

In this thesis I focus on the outer regions ($r \gtrsim 1\,au$) of Class II protoplanetary disks because such regions are believed to be where planets form (Sect. 1.2). I discussed earlier that the MRI activity is quenched due to nonideal MHD effects there. This implies that the MRI-driven turbulence is weakened, and viscous heating is not efficient [128–130]. Instead, protoplanetary disks are closer to "passive disks",

where the thermal structure is mainly set by the radiation field of the central star [e.g., 131]. One should note that heating by the nonideal MHD effects can also be significant [e.g., 129, 132], although it is beyond the scope of this thesis.

In order to simplify the problem even further I assume the protoplanetary disk to be axisymmetric (invariance of the physical quantities with respect to the azimuthal direction), and the gas to be vertically isothermal following the ideal gas law. This is a fairly good approximation if most of the gas in either very optically thick or very optically thin to its own heating/cooling radiation. The thermal gas pressure P_{gas}, the gas mass density ρ_{gas} (which is the mass density of the neutrals in the single-fluid approach employed), and the gas temperature T are then related by

$$P_{gas}(t,r,z) = \frac{\rho_{gas}(t,r,z)k_B T(t,r)}{m_n} = \rho_{gas}(t,r,z)c_s^2(t,r), \tag{44}$$

where t is the time variable, k_B is the Boltzmann constant, and $m_n = \mu m_H$ is the mean molecular mass of the neutral particles in the gas-phase, with $\mu = 2.34$ the mean molecular weight (assuming solar abundances for the neutrals) and m_H the atomic mass of hydrogen. The isothermal sound speed, c_s, is defined as

$$c_s(t,r) = \sqrt{\frac{k_B T(t,r)}{m_n}}. \tag{45}$$

Across the Chapters of this thesis, I will consider two options to compute T:

- OPTION A (Chapters 4 and 5). The gas is optically thin to stellar radiation, leading to

$$T(t,r) = \left[T_{1\,au}^4 \left(\frac{r}{1\,au} \right)^{-2} \left(\frac{L_\star(t)}{L_\odot} \right) + T_{bkg}^4 \right]^{\frac{1}{4}}, \tag{46}$$

  where $T_{1\,au} = 280\,K$ is the gas temperature at $1\,au$ for $L_\star(t) = L_\odot$, and $T_{bkg} = 10\,K$ is the background gas temperature corresponding to the primordial temperature of the cloud prior to the collapse. Any extra projection factors arising from the relative inclination between the disk surface and incident stellar irradiation are not included here.

- OPTION B (Chapters 4 and 6). The gas is optically thick to stellar radiation, which gives

$$T(t,r) = \left(\theta \frac{L_\star(t)}{4\pi\sigma_{SB}r^2} + T_{bkg}^4 \right)^{\frac{1}{4}}, \tag{47}$$

  where $\theta = 0.05$ is the grazing angle under which the stellar light can illuminate the surface of the flared disk, σ_{SB} is the Stefan-Boltzmann constant, and $T_{bkg} = 10\,K$ is the background gas temperature corresponding to the primordial temperature of the cloud prior to the collapse. This temperature profile is obtained by assuming that cooling from the two surfaces of the disk radiating as Planck functions can exactly compensate for heating due to stellar irradiation.

The quantity $L_\star$ that appears above is the stellar bolometric luminosity. In this thesis there are two choices for computing it: (1) I assume that it is a constant free parameter of the model (Chapters 4 and 5); (2) I assume the more realistic case where it is a function of time t (Chapter 6) that follows the evolutionary track of Kunitomo et al. [133] (see *top panel* of their Fig. 4).

2.2.2 Dynamical structure

The goal here is to derive the first order gas structure of the protoplanetary disk. Let us begin with the conservation of momentum equations derived in Sect. 2.1.2. One can re-write it in the following way,

$$\frac{\partial}{\partial t}\left(\rho_{gas}\vec{v}_{gas}\right) + \vec{\nabla} \cdot \mathbf{W} = -\vec{\nabla}\left(P_{gas} + \frac{B^2}{8\pi}\right) - \rho_{gas}\vec{\nabla}\Phi, \tag{48}$$

where Φ is the gravitational potential exerted by the central star (the disk is not self-gravitating), which is defined below. I have introduced the vector transpose notation ".$^\mathsf{T}$" and the 3×3 symmetric stress tensor $\mathbf{W}$, the latter being defined as

$$\mathbf{W} = \rho_{gas}\vec{v}_{gas}\vec{v}_{gas}^{\mathsf{T}} - \frac{\vec{B}\vec{B}^{\mathsf{T}}}{4\pi} = \begin{pmatrix} W_{rr} & W_{r\phi} & W_{rz} \\ W_{\phi r} & W_{\phi\phi} & W_{\phi z} \\ W_{zr} & W_{z\phi} & W_{zz} \end{pmatrix}. \tag{49}$$

As I discussed in Sect. 2.1.3, the growth of the MRI comes hand in hand with MHD turbulence and radial transport of angular momentum. If the disk was not accreting the gas motion will be purely azimuthal, and $\vec{v}_{gas} = r\Omega\vec{e}_\phi$ with Ω the angular velocity. Since protoplanetary disks are accretion disks, and the accretion process is assumed to be driven by the MRI in this thesis, the gas motion is not purely azimuthal because the MRI-driven turbulence introduces 3D fluctuations in the gas motion. Let us call $\delta v_{gas,r}$, $\delta v_{gas,\phi}$, and $\delta v_{gas,z}$ these fluctuation velocities in the radial, azimuthal and vertical direction respectively. It is important to note that $\delta v_{gas,r}$, $\delta v_{gas,\phi}$, and $\delta v_{gas,z}$ do not have vanishing mean values. Another crucial comment to make here is that the fluctuation velocities are not instantaneous quantities, but time-averaged ones. Indeed, gas turbulent eddies generated by the MRI develop on a timescale of order the orbital period (see Sect. 2.1.3). The exchange of angular momentum must happen on a timescale of order the orbital period, and the quantities $\delta v_{gas,r}$, $\delta v_{gas,\phi}$, $\delta v_{gas,z}$ or any combinations (e.g., $\delta v_{gas,r}\delta v_{gas,\phi}$) are time-averaged over that timescale. Furthermore, these fluctuations are at most of order the sound speed when the disk is geometrically thin because fluctuations in excess of this form shocks and kill the turbulence. Since $c_s \ll r\Omega$ in a geometrically thin protoplanetary disk, $\delta v_{gas,r}, \delta v_{gas,\phi}, \delta v_{gas,z} \ll r\Omega$.

Consequently, one can decompose the total gas velocity as $\vec{v}_{gas} = \delta v_{gas,r}\vec{e}_r + \left(r\Omega + \delta v_{gas,\phi}\right)\vec{e}_\phi + \delta v_{gas,z}\vec{e}_z$ [134]. Let us also introduce the components of the magnetic field, $\vec{B} = B_r\vec{e}_r + B_\phi\vec{e}_\phi + B_z\vec{e}_z$. The components of $\mathbf{W}$ can then be written as

$$W_{rr} = \rho_{gas}\delta v_{gas,r}\delta v_{gas,r} - \frac{B_r B_r}{4\pi},$$

$$W_{r\phi} = W_{\phi r} = \rho_{gas}\delta v_{gas,r}\left(r\Omega\right) + \rho_{gas}\delta v_{gas,r}\delta v_{gas,\phi} - \frac{B_r B_\phi}{4\pi},$$

$$W_{rz} = W_{zr} = \rho_{gas}\delta v_{gas,r}\delta v_{gas,z} - \frac{B_r B_z}{4\pi},$$

$$W_{\phi\phi} = \rho_{gas}\left(r\Omega\right)^2 + 2\rho_{gas}\left(r\Omega\right)\delta v_{gas,\phi} + \delta v_{gas,\phi}\delta v_{gas,\phi} - \frac{B_\phi B_\phi}{4\pi},$$

$$W_{\phi z} = W_{z\phi} = \rho_{gas}\left(r\Omega\right)\delta v_{gas,z} + \rho_{gas}\delta v_{gas,\phi}\delta v_{gas,z} - \frac{B_\phi B_z}{4\pi},$$

$$W_{zz} = \rho_{gas}\delta v_{gas,z}\delta v_{gas,z} - \frac{B_z B_z}{4\pi}. \tag{50}$$

One should note that the form of the components of the shear stress tensor **W** is very important. The existence of the fluctuation velocities are not responsible for the turbulence and the transport of angular momentum transport in the protoplanetary disk. What causes the accretion is actually the correlation between these fluctuations, namely the fact that time-averaging these quantities or any combinations over an orbital period is not zero.

2.2.2.1 *Along the radial direction*

Using the definition of the tensor divergence $\vec{\nabla}\cdot\mathbf{W}$ in cylindrical coordinates, the component of Eq. (48) along the radial direction $\vec{e}_r$ reads

$$\frac{\partial}{\partial t}\left(\rho_{gas}v_{gas,r}\right) + \left[\frac{1}{r}\frac{\partial}{\partial r}\left(rW_{rr}\right) + \frac{\partial W_{zr}}{\partial z} - \frac{W_{\phi\phi}}{r}\right] = -\frac{\partial}{\partial r}\left(P_{gas} + \frac{B^2}{8\pi}\right) - \rho_{gas}\frac{\partial\Phi}{\partial r}, \tag{51}$$

where I used the assumption that the protoplanetary disk is axisymmetric to neglect any partial derivatives with respect to the variable ϕ.

I have argued above that the timescale associated with the accretion process is much longer that the timescale it takes the disk to reach a dynamical equilibrium, since disks are geometrically thin. One can thus separate Eq. (51) into the part responsible for the radial dynamical equilibrium and the part responsible for the accretion. The components of the stress tensor that encode the accretion process are all the terms that depend on a fluctuation velocity (due to the MRI-driven turbulence) or a magnetic field strength (due to the magnetic tension). It is easy to see that all the terms in the relevant stress tensor components depend on both, except for the first term of the component $W_{\phi\phi}$. Therefore, the term $\rho_{gas}\left(r\Omega\right)^2$ of $W_{\phi\phi}$ is the only term of the stress tensor that intervenes in the radial dynamical equilibrium for the disk. Consequently, the equation that governs the radial dynamical equilibrium of the gas is

$$-\frac{\rho_{gas}\left(r\Omega\right)^2}{r} = -\frac{\partial}{\partial r}\left(P_{gas} + \frac{B^2}{8\pi}\right) - \rho_{gas}\frac{\partial\Phi}{\partial r}. \tag{52}$$

For the MRI to develop, hence the accretion process to take place, the gas thermal pressure must exceed the magnetic pressure (this is the case for the bulk of the disk

near the midplane and not too far from the central star). The term $B^2/8\pi$ can then be neglected in first order approximation. Furthermore, the gravitational potential Φ exerted by the central star is given by

$$\Phi(r,z) = -\frac{GM_\star}{\left(r^2 + z^2\right)^{1/2}}, \tag{53}$$

where G is the gravitational constant. The equation that governs the radial dynamical equilibrium of the gas is thus in first order approximation

$$r\Omega^2 = r\Omega_K^2 + \frac{1}{\rho_{gas}}\frac{\partial P_{gas}}{\partial r}. \tag{54}$$

Here I have introduced the Keplerian angular velocity for a geometrically thin disk (i.e., $z \ll r$), which is defined as

$$\Omega_K(r,z) \approx \sqrt{\frac{GM_\star}{r^3}}. \tag{55}$$

One can write Eq. (54) as

$$r\Omega^2 = r\Omega_K^2 \left(1 - 2\eta_{gas}\right), \tag{56}$$

where η_{gas} is the gas pressure support parameter[11]

$$\eta_{gas} = -\frac{1}{2\rho_{gas}r\Omega_K^2}\frac{\partial P_{gas}}{\partial r}. \tag{57}$$

Finally, the mean velocity of the gas in the azimuthal direction (i.e., without the fluctuation $\delta v_{gas,\phi}$ due to MRI-driven turbulence), that I call $v_{gas,\phi}$, is given by

$$v_{gas,\phi} = r\Omega = v_K\sqrt{1 - 2\eta_{gas}}, \tag{58}$$

where $v_K = r\Omega_K$ is the Keplerian velocity. For the purposes of this thesis, η_{gas} (hence $v_{gas,\phi}$) will be computed near the disk midplane.

The first striking comment that one can make is that the gas component of the protoplanetary disk orbits at speed slightly[12] sub-Keplerian because the radial gradient of the gas thermal pressure is typically negative in most of the protoplanetary disk. However, the gas can become Keplerian (resp. super-Keplerian) at radial locations where the gradient of the gas thermal pressure is zero (resp. strictly positive). A very important concept emerges here. When the gradient of the gas thermal pressure goes from being strictly positive to zero to strictly negative, namely the gas goes from being super-Keplerian to Keplerian to sub-Keplerian, there is a pressure maximum located where the gas becomes Keplerian. This is crucial for dust particles trapping, as I will talk about in Sect. 2.3.3.

---

11 caution not to confuse it with the magnetic diffusivities
12 η_{gas} is small compared to unity in practice

2.2.2.2 *Along the vertical direction*

The component of Eq. (48) along the vertical direction $\vec{e}_z$ reads

$$\frac{\partial}{\partial t}\left(\rho_{gas}v_{gas,z}\right) + \left[\frac{1}{r}\frac{\partial}{\partial r}\left(rW_{rz}\right) + \frac{\partial W_{zz}}{\partial z}\right] = -\frac{\partial}{\partial z}\left(P_{gas} + \frac{B^2}{8\pi}\right) - \rho_{gas}\frac{\partial \Phi}{\partial z}, \qquad (59)$$

where I used the assumption that the protoplanetary disk is axisymmetric to neglect any partial derivatives with respect to the variable ϕ.

Similarly to what has been done for the radial direction above, one can separate Eq. (59) into the part responsible for the vertical dynamical equilibrium (called hydrostratic equilibrium) and the part responsible for the accretion. Looking at all the terms of the stress tensor components (Eq. 50), one can notice that all the terms of the relevant stress tensor depend on both a fluctuation velocity and a magnetic field strength. It means that none of the terms of the relevant stress tensor components intervene in the hydrostatic equilibrium. As a result, the equation that governs the hydrostatic equilibrium of the gas is

$$0 = -\frac{\partial}{\partial z}\left(P_{gas} + \frac{B^2}{8\pi}\right) - \rho_{gas}\frac{\partial \Phi}{\partial z}. \qquad (60)$$

Again noting that the gas thermal pressure dominates over the magnetic pressure for the bulk of the disk, and that disks are geometrically thin, as well as using the isothermal ideal gas law (Eq. 44) and the stellar gravitational potential (Eq. 53), this equation can be written in first order approximation as

$$\frac{\partial P_{gas}}{\partial z} = -\frac{P_{gas}\Omega_K^2}{c_s^2}z. \qquad (61)$$

This can be easily integrated to lead to

$$P_{gas}(t,r,z) = P_{gas}(t,r,z=0)\exp\left(-\frac{z^2}{2H_{gas}^2(t,r)}\right), \qquad (62)$$

where I have introduced the vertical gas scale height given by

$$H_{gas} = \frac{c_s}{\Omega_K}. \qquad (63)$$

Using again the isothermal ideal gas law (Eq. 44) leads to

$$\rho_{gas}(t,r,z) = \rho_{gas}(t,r,z=0)\exp\left(-\frac{z^2}{2H_{gas}^2(t,r)}\right). \qquad (64)$$

Let us now introduce the gas surface density as the following:

$$\Sigma_{gas}(t,r) = \int_{-\infty}^{+\infty}\rho_{gas}(t,r,z)\,dz. \qquad (65)$$

One can thus obtain $\rho_{gas}(t, r, z = 0)$ (hence $P_{gas}(t, r, z = 0)$) by using the definition of $\Sigma_{gas}(t, r)$. Doing so, one can finally get

$$\rho_{gas}(t, r, z) = \frac{\Sigma_{gas}(t, r)}{\sqrt{2\pi}H_{gas}(t, r)} \exp\left(-\frac{z^2}{2H_{gas}^2(t, r)}\right). \tag{66}$$

The number density of the gas is then given by:

$$n_{gas} = \frac{\rho_{gas}}{m_n}. \tag{67}$$

This section provides two important results. First, the mass density of the gas (which is the same as the mass density of the neutrals in the single-fluid approach employed) is Gaussian about the disk midplane. It implies that most of the disk gas mass is contained close to the midplane. Second, the timescale it takes to attain vertical dynamical equilibrium is of order $H_{gas}/c_s \sim 1/\Omega_K$. This is comparable to the timescale to attain radial dynamical equilibrium. The gas component of the protoplanetary disk can thus be considered to be globally in dynamical equilibrium on timescales longer than the disk orbital period. This justifies the fact that, when investigating the secular evolution of protoplanetary disks, dynamical equilibrium of the gas component is always assumed in first order approximation.

2.2.3 Secular evolution

The goal now is to derive an equation that encodes the secular evolution of the gas component of the protoplanetary disk. In this section, I will connect the viscously accreting disk theory (the α-disk model of Shakura and Sunyaev [120] and Lynden-Bell and Pringle [121]) to the MHD turbulence driven by the MRI (dominant mechanism for angular momentum transport considered in this thesis).

Let us consider the component of Eq. (48) along the azimuthal direction $\vec{e}_\phi$, and multiply all the terms by r. Using the axisymmetry assumption to neglect all the partial derivatives with respect to the variable ϕ, one has

$$\frac{\partial}{\partial t}\left(r\rho_{gas}v_{gas,\phi}\right) + \left[\frac{1}{r}\frac{\partial}{\partial r}\left(r^2 W_{r\phi}\right) + r\frac{\partial W_{z\phi}}{\partial z}\right] = 0. \tag{68}$$

The physical interpretation of this equation is the conservation of specific angular momentum $rv_{gas,\phi}$. In this thesis, it is assumed that angular momentum and mechanical energy are solely transported radially through the disk. The component $W_{z\phi}$ of the shear stress tensor can thus be discarded (i.e., the vertical transport of angular momentum by MHD disk winds are neglected by adopting zero shear stress boundary conditions at the disk surface layers). By averaging over azimuth (shown by $\langle . \rangle_\phi$) and integrating vertically, one can obtain for an axisymmetric disk

$$\frac{\partial}{\partial t}\left(r^2 \Omega \Sigma_{gas}\right) + \left[\frac{1}{r}\frac{\partial}{\partial r}\left(r^3 \Omega \Sigma_{gas}\overline{\delta v}_{gas,r} + r^2 \int_{-\infty}^{+\infty} T_{r\phi} dz\right)\right] = 0, \tag{69}$$

where I have introduced the effective radial gas velocity

$$\overline{\delta v}_{gas,r} = \frac{\int_{-\infty}^{+\infty} \rho_{gas}\delta v_{gas,r}dz}{\Sigma_{gas}}, \tag{70}$$

and the $r\phi$ shear stress

$$T_{r\phi} = \langle \rho_{gas}\delta v_{gas,r}\delta v_{gas,\phi}\rangle_\phi - \langle \frac{B_r B_\phi}{4\pi}\rangle_\phi. \tag{71}$$

$T_{r\phi}$ has two components: $\langle \rho_{gas}\delta v_{gas,r}\delta v_{gas,\phi}\rangle_\phi$ is called the turbulent Reynolds stress, and $\langle B_r B_\phi/4\pi\rangle_\phi$ is the Maxwell stress. This is the quantity that is linked to the α parameter in viscously accreting disk theory (see Eq. 43). This is why α quantifies the turbulence strength.

The conservation of mass equation (Eq. 19) in cylindrical coordinates, and assuming axisymmetry, reads

$$\frac{\partial \rho_{gas}}{\partial t} + \frac{1}{r}\frac{\partial}{\partial r}\left(r\rho_{gas}\delta v_{gas,r}\right) + \frac{\partial}{\partial z}\left(\rho_{gas}\delta v_{gas,z}\right) = 0. \tag{72}$$

Vertically integrating this equation, using the fact that $\delta v_{gas,z} \ll \delta v_{gas,r}$ because the transport of angular momentum is assumed to primarily happen radially in this thesis, leads to

$$\frac{\partial \Sigma_{gas}}{\partial t} + \frac{1}{r}\frac{\partial}{\partial r}\left(r\Sigma_{gas}\overline{\delta v}_{gas,r}\right) = 0. \tag{73}$$

Using this equation into Eq. (69), and remembering that $\Omega \approx \Omega_K$ for a protoplanetary disk, leads to

$$\dot{M}_{acc} = -2\pi r\Sigma_{gas}\overline{\delta v}_{gas,r} = \frac{4\pi}{r\Omega}\frac{\partial}{\partial r}\left(r^2\int_{-\infty}^{+\infty} T_{r\phi}dz\right) = 4\pi\sqrt{r}\frac{\partial}{\partial r}\left(\sqrt{r}\frac{1}{\Omega}\int_{-\infty}^{+\infty} T_{r\phi}dz\right), \tag{74}$$

with $\dot{M}_{acc}$ the inward radial gas accretion rate. With this expression, one can see that the coupling between magnetic field and gas motion generates gas accretion through the quantity $T_{r\phi}$. This is why the α parameter quantifies the efficiency of radial angular momentum transport.

Let us now inject the newly found expression for $r\Sigma_{gas}\overline{\delta v}_{gas,r}$ into Eq. (73). One has

$$\frac{\partial \Sigma_{gas}}{\partial t} = \frac{2}{r}\frac{\partial}{\partial r}\left[\sqrt{r}\frac{\partial}{\partial r}\left(\sqrt{r}\frac{1}{\Omega}\int_{-\infty}^{+\infty} T_{r\phi}dz\right)\right]. \tag{75}$$

Using the definition of the local disk viscosity parameter[13] α (Eq. 43), one can write

$$\int_{-\infty}^{+\infty} T_{r\phi}dz = \frac{3}{2}\int_{-\infty}^{+\infty} \alpha P_{gas}dz = \frac{3}{2}\bar{\alpha}\Sigma_{gas}c_s^2, \tag{76}$$

where I have introduced the effective disk viscosity parameter[14] $\bar{\alpha}$ given by

$$\bar{\alpha}(t,r) = \frac{\int_{-\infty}^{+\infty} \alpha(t,r,z) P_{gas}(t,r,z)\,dz}{\int_{-\infty}^{+\infty} P_{gas}(t,r,z)\,dz} = \frac{\int_{-\infty}^{+\infty} \alpha(t,r,z) P_{gas}(t,r,z)\,dz}{\Sigma_{gas}c_s^2}. \tag{77}$$

---

13 also referred to as the local turbulent parameter interchangeably
14 also referred to as the effective turbulent parameter interchangeably

Here I have used the assumption that the protoplanetary disk is vertically isothermal. Furthermore, it is very important to note that α depends on t, r, z. Let us now define one last quantity called the kinematic disk viscosity $\bar{\nu}$, which has dimensions of a diffusion coefficient ($cm^2.s^{-1}$) and is defined by

$$\bar{\nu} = \frac{\bar{\alpha} c_s^2}{\Omega} = \bar{\alpha} c_s H_{gas}, \tag{78}$$

with $\Omega \approx \Omega_K$. The kinematic disk viscosity is a quantity analog to the molecular viscosity of a fluid, but resulting from the turbulence process of accretion disks rather than the gas molecules motion with respect to the mean gas flow. In the same way molecular viscosity can be estimated as the product between the typical distance molecules can travel between collisions (mean free path) and their typical velocities (thermal velocity), the kinematic disk viscosity can be seen as the product between the typical lenthscale of the gas turbulent eddies and their velocity. This product must have an upper bound of order $c_s H_{gas}$ in order to keep the gas motion subsonic and avoid shocks that will quickly damp the turbulence and accretion. Since $0 < \bar{\alpha} < 1$, the quantity $\bar{\alpha}$ can thus be seen as a re-parametrization of the kinematic disk viscosity $\bar{\nu}$ to ensure such a condition.

Introducing these notations in Eq. (75), one can finally obtain the evolution equation for the gas surface density of the protoplanetary disk in the theory of viscously accreting disks. It reads

$$\frac{\partial \Sigma_{gas}}{\partial t} = \frac{3}{r} \frac{\partial}{\partial r} \left[\sqrt{r} \frac{\partial}{\partial r} \left(\sqrt{r} \Sigma_{gas} \bar{\nu} \right) \right]. \tag{79}$$

Also, the gas moves radially at velocity

$$\overline{\delta v}_{gas,r} = -\frac{\dot{M}_{acc}}{2\pi r \Sigma_{gas}} = -\frac{3}{\sqrt{r} \Sigma_{gas}} \frac{\partial}{\partial r} \left(\sqrt{r} \Sigma_{gas} \bar{\nu} \right). \tag{80}$$

The secular evolution of the gas component of the protoplanetary disk (Eq. 79) has the form of a diffusion equation with local diffusion timescale $t_{visc} \sim r^2/(3\bar{\nu})$. This is consistent with the fact that the growth of the MRI leads to *internal redistribution* of angular momentum through radial diffusion. Unlike the classical α-disk model [121], though, the origin of the α parameter is not unknown in this thesis. It directly comes from the MHD turbulence driven by the MRI through the shear stress $T_{r\phi}$ (Eq. 71). Knowing $T_{r\phi}$ thus allows us to obtain the MRI-induced local disk viscosity parameter α, hence the MRI-induced effective disk viscosity parameter $\bar{\alpha}$. This in turn allows us to understand the first order evolution of the gas in the disk on secular timescales. This is the strategy used in this thesis.

Finally, the disk viscosity α controls both the efficiency of the angular momentum transport and the turbulence strength in the theory of viscously accreting disks, which the MRI accretion belongs to. However, it is worth noting that gas turbulence and angular momentum transport do not always come hand in hand. For example, if the MRI is suppressed and the angular momentum transport occurs vertically by MHD disk winds, the gas flow is found to be laminar rather than turbulent [e.g., 87, 91].

2.3 FROM INTERSTELLAR DUST PARTICLES TO THE BUILDING BLOCKS OF PLANETS

Although the dust component of protoplanetary disks only represents around 1% of the total disk mass initially, it plays a crucial role in planet formation for many reasons. First, the dust represents the material out of which planets and minor bodies (e.g., asteroids) are formed, hence it constitutes the building blocks for what currently remains in stellar systems [e.g., 35, 135]. Second, the dust controls the disk opacity, which thus determines the appearance of protoplanetary disks in infrared and millimeter wavelengths (see Sect. 1.3). Finally, the dust provides the surface area for surface chemical reactions, and significantly influence the gas ionization degree by sweeping up free electrons and ions from the gas-phase (See Chapter 3). This in turn dictates how the nonideal MHD effects modify the MRI (See Chapter 5). Clearly, understanding the evolution of the dust component of the protoplanetary disk is a fundamental piece in the puzzle of planet formation.

This evolution is governed by both collisional processes (leading to a change in the dust particle size[15]) and transport processes (leading to a change in the dynamics of the dust). It is important to understand that such processes are strongly interdependent, since transport processes depend on the dust particle size, hence the collisional evolution of the dust, while the collisions between dust particles are driven by their dynamics. Consequently, both collisional processes and transport processes need to be considered simultaneously when solving for the global evolution of dust particles.

In this thesis, one should note that each grain species of the dust component of the protoplanetary disk is assumed to be a perfect compact sphere of intrinsic volume density $\rho_{\text{bulk}} = 1.4\,\text{g.cm}^{-3}$, which is consistent with the solar abundance when H_2O ice is included in grains [e.g., 136]. For a grain of size a, the corresponding mass is then $m(a) = \frac{4}{3}\pi\rho_{\text{bulk}}a^3$.

2.3.1 *Dust dynamics*

Most of the transport and dynamics of dust particles in the protoplanetary disk are regulated by the interactions between them and the surrounding gas component of the disk.

2.3.1.1 *Drag force*

As I discussed in Sect. 2.2.2, the gas orbits at slightly sub-Keplerian velocity due to pressure support. Dust particles, on the contrary, are not pressure supported and try to orbit at Keplerian velocity. However, in the same way there are collisions between neutrals and charged particles in the gas component of the protoplanetary

---

15 also referred to as the grain size interchangeably

disk (see Sect. 2.1.2), there are also collisions between gas particles (neutrals, free electrons or ions) and dust particles. This can be modeled by a drag force density

$$\vec{f}_{\text{drag}} = \rho_{\text{dust}} \frac{(\vec{v}_{\text{dust}} - \vec{v}_{\text{gas}})}{\tau_s}, \tag{81}$$

where $\vec{v}_{\text{gas}}$ is the gas flow velocity that I have mentioned in Sect. 2.1, $\vec{v}_{\text{dust}}$ is the velocity of a dust particle, ρ_{dust} is the mass density of the dust, and τ_s is what is called the dust particle stopping time (or friction time). This is the time it takes a dust particle to decelerate due to the drag force induced by the gas.

Even more useful than the dust particle stopping time is the dimensionless ratio of the stopping-to-dynamical timescale called the Stokes number. It reads

$$\text{St} = \tau_s \Omega_K, \tag{82}$$

with Ω_K the Keplerian angular velocity. The Stokes number is a very useful quantity because two particles of different composition, structure, mass or size behave aerodynamically identical if their Stokes number is identical. It represents the dimensionless timescale over which a dust particle couples to the gas flow, hence capturing both the gas flow properties and the dust particle properties. As a rule of thumb, the smaller the Stokes number, the tighter the dust is coupled to the gas, and vice-versa. For $\text{St} \ll 1$, the dust particle adapts the gas velocity on timescales much shorter than the orbital timescale, while it takes several orbits before the drag force alters the dust particle velocity for $\text{St} \gg 1$. The formulation of the drag force given in Eq. (81) is quite general. In this thesis, two drag regimes are specifically relevant: the Epstein regime and the Stokes I regime. For an azimuthally averaged and vertically integrated disk (same assumptions made to obtain the equation of secular evolution for the gas in Sect. 2.2.3), the Stokes number of a dust particle of size a is given by

$$\text{St}(t, r, a) = \frac{\pi}{2} \frac{a \, \rho_{\text{bulk}}}{\Sigma_{\text{gas}}(t, r)} \cdot \begin{cases} 1 & \lambda_{\text{mfp,mid}}/a \geqslant 4/9 \quad \text{(Epstein regime)} \\ \frac{4}{9} \frac{a}{\lambda_{\text{mfp,mid}}} & \lambda_{\text{mfp,mid}}/a < 4/9 \quad \text{(Stokes I regime)} \end{cases}, \tag{83}$$

where $\lambda_{\text{mfp,mid}} = \left(n_{\text{gas}}(t, r, z = 0)\sigma_{H_2}\right)^{-1}$ is the midplane mean free path of gas particles, with $\sigma_{H_2} = 2 \times 10^{-15} \, \text{cm}^2$ the molecular cross-section for H_2 [e.g., 137, 138]. One should note that this definition is only valid near the disk midplane, where most of the relevant dust evolution processes occur.

It is important to note that the drag force that the gas exerts on a dust particle depends on the stopping time, hence the Stokes number. The velocity and trajectory of a dust particle in the protoplanetary disk are thus size dependent. This implies that dust particles with different Stokes number collide with each other in addition to the gas particles. These collisions can be constructive and lead to grain growth, or destructive and lead to fragmentation. The collisional outcome therefore strongly depends on the relative velocity between two colliding dust particles (see Sect. 2.3.2).

2.3.1.2 *Dust drift*

Since dust particles orbit faster azimuthally compared to the gas, they feel a head wind due to the drag force. As a result, they loose angular momentum, and drift radially inward toward the central star. This phenomenon is termed the "radial drift of dust particles". Radial drift of dust particles is considered as a grain growth barrier [e.g., 11, 139], in the sense that if dust particles do not grow fast enough from sub-micron sizes to planetesimals, the building blocks of planets will be accreted by the central star on very short timescales, and therefore lost. Let us come back to this challenge and how to potentially overcome it in Sect. 2.3.3. Similarly, there is also an azimuthal and vertical drift of dust particles.

Nakagawa, Sekiya, and Hayashi [140] is one of the first studies that actually derived mathematically the expressions for the radial and azimuthal dust velocities. Following their footsteps as well as other studies [e.g., 141], where a azimuthally averaged and vertically integrated disk is assumed, it can be shown that the dust radial velocity for each grain species of size a is

$$v_{\text{dust},r}(t,r,a) = \underbrace{\frac{\overline{\delta v}_{\text{gas},r}(t,r)}{1+\text{St}^2(t,r,a)}}_{\text{radial gas flow}} - \underbrace{\frac{2\eta_{\text{gas}}(t,r,z=0)v_K(r)\text{St}(t,r,a)}{1+\text{St}^2(t,r,a)}}_{\text{radial drift}}, \tag{84}$$

and the dust azimuthal velocity for each grain species of size a is

$$v_{\text{dust},\phi}(t,r,a) = \underbrace{v_K(r)}_{\text{Keplerian velocity}} - \underbrace{\frac{\eta_{\text{gas}}(t,r,z=0)v_K}{1+\text{St}^2(t,r,a)}}_{\text{azimuthal drift}}. \tag{85}$$

Here $\eta_{\text{gas}}(t,r,z=0)$ is the midplane gas pressure support parameter (Eq. 57), v_K is the Keplerian velocity, and $\overline{\delta v}_{\text{gas},r}$ is the effective radial gas velocity (Eq. 80). I also used cylindrical coordinates as in Sect. 2.2. One should note that these formula are valid when dust backreaction onto the gas is not significant [e.g., 142, 143].

The mathematical expression of these velocities have several important consequences. First, dust particles with $\text{St} \ll 1$ primarily follow the gas flow radially, while dust particles with $\text{St} \gg 1$ are almost not moving radially. Second, radial drift is the highest for $\text{St} \approx 1$. For typical disk conditions, η_{gas} is of order a few per mille, which means that the maximum radial drift speed is a few per mille of the Keplerian velocity. In other words, the orbit of a dust particle decays on a timescale of only a few hundred orbits, which is why radial drift is considered as grain growth barrier. Third, the direction of radial drift is toward higher pressure. This information needs to be kept in mind for dust trapping (see Sect. 2.3.3). Finally, dust particles with $\text{St} \ll 1$ can orbit at sub-Keplerian, Keplerian or super-Keplerian velocity depending on the sign of η_{gas}, hence the sign of the gas thermal pressure gradient. When it is negative (resp. positive), the dust orbits at sub-Keplerian (resp. super-Keplerian) velocity. At locations where there is no pressure gradient (pressure maxima or minima), the dust orbits at Keplerian velocity. Dust particles with $\text{St} \gg 1$ always orbit at Keplerian velocity.

For the vertical drift, Dullemond and Dominik [144] constructed detailed models of vertical disk structure describing the depletion of dust particles in the upper layers of the protoplanetary disk. Using their results combined with the argument made by Birnstiel, Dullemond, and Brauer [138], the vertical drift dust velocity (also called the sedimentation velocity) is given by

$$v_{dust,z}(t, z, a) = -z\Omega_K \min\left(St(t, a), \frac{1}{2}\right). \tag{86}$$

Dust particles thus sediment (or settle) toward the disk midplane, which is much faster for particles with larger St. Since the detailed vertical distribution of dust particles is not resolved in this thesis, I will take the scale height of each grain species ($H_{dust}(a)$, which is introduced in the next section) as average height above the midplane. In other words, z should be replaced by $H_{dust}(a)$ in the expression for $v_{dust,z}$.

2.3.1.3 *Turbulent mixing*

When the gas is turbulent, the dust particles are mixed by the random motion induced by the gas turbulent eddies. This will act as a diffusivity on the dust, which means that gas turbulence counteracts gradients in concentration. In other words, turbulent mixing from the gas smears out any local enhancement of dust particles in all directions.

In the radial direction, each dust particle of size a diffuses with a general dust diffusivity approximated by [145]

$$D_{dust}(t, r, a) = \frac{\delta_{rad}(t, r)c_s^2(t, r)}{\Omega_K(r)\left(1 + St^2(t, r, a)\right)}, \tag{87}$$

where δ_{rad} is the parameter that controls the mixing strength of dust particles in the radial direction. Similarly to the local viscous evolution timescale t_{visc} seen in Sect. 2.2.3, one can define a local dust diffusion timescale for each grain species of size a: $t_{dust,diff} \sim r^2/D_{dust}$. In this thesis, the gas turbulence that leads to turbulent mixing comes from the MHD turbulence driven by the MRI (Sect. 2.2.3). Therefore, it will be assumed that $\delta_{rad} = \bar{\alpha}$. In this case, $D_{dust}(t, r, a) = \bar{\nu}(t, r)/1 + St^2(t, r, a)$, with $\bar{\nu}$ given by Eq. (78). For dust particles with $St \ll 1$, one has $D_{dust} \sim \bar{\nu}$ and $t_{dust,diff} \sim t_{visc}$. Dust particles thus diffuse with the gas, over a timescale of viscous evolution. For dust particles with $St \approx 1$, one can already see that they diffuse on a timescale twice longer than the gas. Since the viscous evolution timescale is of order $\mathcal{O}(Myrs)$, it means that dust particles with $St \approx 1$ almost do not diffuse away during the secular evolution of the protoplanetary disk. For dust particles with $St \gg 1$, the diffusion is not efficient at all.

In the vertical direction, dust particles sediment toward the disk midplane (at velocity $v_{dust,z}$), with a settling timescale of order $t_{sett}(a) \sim 2\pi/(\Omega_K St(a))$ for each grain species of size a. However, gas turbulence once again counteracts this concentration effect by stirring up dust particles, until an equilibrium is met. This

equilibrium is actually seen in ALMA observations of edge-on disks [e.g., 146, 147]. As a result, one can expect the number of dust particles to drop significantly above a dust scale height, H_{dust}, that can be much smaller than the gas scale height, H_{gas}, depending on the dust particle size. Following Dubrulle, Morfill, and Sterzik [148], one has for each grain species of size a

$$H_{dust}(t, r, a) = H_{gas}(t, r)\sqrt{\frac{\delta_{vert}(t, r)}{\delta_{vert}(t, r) + St(t, r, a)}}, \tag{88}$$

where δ_{vert} is the parameter that controls the mixing strength of dust particles in the vertical direction. In this thesis, the gas turbulence that leads to turbulent mixing comes from the MHD turbulence driven by the MRI (Sect. 2.2.3). Therefore, it will be assumed that $\delta_{vert} = \bar{\alpha}$.

As I mentioned above, the strength of both the radial and vertical mixing of dust particles are assumed to be characterized by the effective disk viscosity parameter $\bar{\alpha}$. It implicitly means that the dust radial and vertical diffusion coefficients are identical. In other words, it has been implicitly assumed that the dust diffusion is isotropic.

2.3.1.4   *Dust radial transport equation*

Let us consider an azimuthally averaged and vertically integrated protoplanetary disk model. These assumptions are the ones used to obtain the 1D evolution equation for the gas surface density seen in Sect. 2.2.3 (Eq. 79). In the same fashion, the overall evolution of the dust surface density Σ_{dust} can be described by a 1D advection-diffusion equation [e.g., 138, 149]

$$\frac{\partial \Sigma_{dust}(t, r, a)}{\partial t} + \frac{1}{r}\frac{\partial}{\partial r}(rF_{tot}(t, r, a)) = 0, \tag{89}$$

where F_{tot} is the total radial flux. There are no sink terms included in this equation because the potential loss of dust particles through wind entrainment from, for example, internal photoevaporative winds or MHD disk winds have been ignored [see e.g., 52, 53]. Although such processes are crucial for the secular evolution of protoplanetary disks, they are beyond the scope of this thesis.

The total radial flux F_{tot} has contributions from a diffusive flux (F_{diff}) and an advective flux (F_{adv}), namely $F_{tot} = F_{adv} + F_{diff}$. The diffuse part comes from turbulent mixing (Sect. 2.3.1.3), and can be written as [e.g., 138]

$$F_{diff}(t, r, a) = -\Sigma_{gas}(t, r)D_{dust}(t, r, a)\frac{\partial}{\partial r}\left(\frac{\Sigma_{dust}(t, r, a)}{\Sigma_{gas}(t, r)}\right). \tag{90}$$

The advection part comes from the radial velocities of dust particles from the gas flow entertainment and the radial drift (Sect. 2.3.1.2), and can be written as [e.g., 138]

$$F_{adv}(t, r, a) = \Sigma_{dust}(t, r, a)v_{dust,r}(t, r, a). \tag{91}$$

The transport equation for each grain species of size a, that is solved in this thesis, is then

$$\frac{\partial \Sigma_{dust}}{\partial t} + \frac{1}{r}\frac{\partial}{\partial r}\left\{ r\left[\Sigma_{dust}\nu_{dust,r} - \Sigma_{gas}D_{dust}\frac{\partial}{\partial r}\left(\frac{\Sigma_{dust}}{\Sigma_{gas}}\right)\right]\right\} = 0. \tag{92}$$

2.3.1.5 *Dust vertical structure*

In this thesis, the detailed vertical distribution of dust particles is not resolved. For simplicity, and following what we have learned from the vertical structure of the gas component of the protoplanetary disk in Sect. 2.2.2, the vertical dust mass density is assumed to follow a Gaussian distribution. Although this approximation is quite accurate near the disk midplane, one should note that it may not hold in the uppermost layers of the protoplanetary disk [e.g., 150].

For each grain species of size a, the dust mass density is described by

$$\rho_{dust}(t, r, z, a) = \frac{\Sigma_{dust}(t, r, a)}{\sqrt{2\pi}H_{dust}(t, r, a)}\exp\left(-\frac{z^2}{2H_{dust}^2(t, r, a)}\right), \tag{93}$$

where Σ_{dust} is the dust surface density and H_{dust} is the dust scale height, for each grain species of size a. The total dust mass density (accounting for all grain species) is then defined as

$$\rho_{dust,tot}(t, r, z) = \sum_a \rho_{dust}(t, r, z, a). \tag{94}$$

The dust number density for each grain species of size a is given by

$$n_{dust}(t, r, z, a) = \frac{\rho_{dust}(t, r, z, a)}{m(a)}, \tag{95}$$

where $m(a)$ is the corresponding grain mass. It follows that the total dust number density (accounting for all grain species) is determined by

$$n_{dust,tot}(t, r, z) = \sum_a n_{dust}(t, r, z, a). \tag{96}$$

The eager reader can notice that I summed over each grain species instead of integrating. This is because all the dust quantities representing the dust mass in this section are already in mass bins, since I will solve for the discretized Smoluchowski equation to account for grain growth process as I will explain in the next section.

2.3.2 *Grain growth processes*

The dust contained in the prestellar infalling core is generally assumed to have the sizes of the ISM, from 0.005 to 1 µm, depending on the composition of the grain [e.g., 151]. In the classical picture, it is thought that grain growth primarily happens in the Class II phase of the disk, although there is increasing observational evidence

that grains might be already grown past the ISM sizes in the Class I phase [e.g, 20, 21]. Regardless of when exactly grain growth occurs, planet formation requires that the dust grows over twelve orders of magnitude in size to make terrestrial planets or the cores of giant planets (see Fig. 3). Collisional dust growth from interstellar sub-micron to centimeter-sized particles is the first and key step for the bottom-up planet formation scenario via core accretion (See Fig. 3). To understand how dust particles grow, one needs to understand: (1) at which velocities dust particles collide; (2) how often they collide; and (3) what the outcome of each collision is.

2.3.2.1 *Smoluchowski equation*

Since it is computationally unfeasible[16] to simulate every dust particle individually, two main methods have been developed to model the growth of dust particles. First, there is the Monte Carlo method wherein several dust particles are combined into a few representative particles, whose evolution can be simulated [e.g., 152, 153]. The second method is to simulate the evolution of a distribution of dust particles with different sizes instead of individual particles [e.g., 137, 138]. The advantage of the Monte Carlo method is that it is quite easy to include additional dust particle properties (e.g., porisity, complex composition). However, these simulations are computationally expensive, which is a major problem if one wants to study the secular evolution of protoplanetary disks.

For this reason, the second method is employed in this thesis. The dust component of the protoplanetary disk thus consists of a distribution of dust particles with different sizes, which are obtained by solving the Smoluchowski equation. It reads

$$\frac{\partial n(m)}{\partial t} = \int_0^{+\infty} \int_0^{m'} \mathbf{K}(m, m', m'') R(m', m'') n(m') n(m'') dm' dm''$$
$$- n(m) \int_0^{+\infty} R(m, m') n(m') dm'. \tag{97}$$

Here the collisional evolution of a dust mass distribution $n(m)$ of particles with mass m is computed. The first double integral on the right-hand side (RHS) of the equation accounts for all possible collisions of particles with masses m' and m'' with collision rate $R(m', m'')$. The collision Kernel tensor $\mathbf{K}(m, m', m'')$ holds information about the collision outcomes of each collision and describe the amount that gets added into $n(m)$ from a single collision with masses m' and m''. The upper boundary of the inner integral is m' instead of $+\infty$ because collisions of particles with masses m' and m'' are identical to collisions with particles m'' and m', and should not be counted twice. The negative term of the RHS of the equation accounts for the particles that get removed from the distribution $n(m)$ due to collisions with other particles.

---

16 for example, growing a dust particle of size 1 cm out of micrometer sized particles would require to follow 10^{12} dust particles

It is usual to discretize $n(m)$ on a mass grid with N_m mass bins by integrating $n(m)$ over the mass bin width [e.g., 137, 138]. For the kth mass bin, one has the dust mass distribution

$$n_k = \int_{m_{k-\frac{1}{2}}}^{m_{k+\frac{1}{2}}} n(m) dm. \tag{98}$$

The discretized Smoluchowski equation is thus

$$\frac{\partial n_k}{\partial t} = \sum_{l=1}^{N_m} \sum_{p=1}^{l} K_{lpk} R_{lp} n_l n_p - n_k \sum_{q=1}^{N_m} R_{qk} \left(1 + \delta_{qk}\right), \tag{99}$$

where δ_{qk} is the Kronecker quantity. Since it is computationally challenging to solve for the 3D Smoluchowski equation [e.g., 154], and that grain growth mostly happens near the protoplanetary disk midplane, the Smoluchowski equation is often solved for an axisymmetric protoplanetary disk that is vertically integrated [e.g., 137, 138]. This will also be the case in this thesis, where the azimuthally averaged and vertically integrated discretized Smoluchowski equation is solved at each disk radius and time evolution [see Appendix A of 138]. This allows us to trace the size of radial evolution of dust particles (Eq. 92) in a combined way, where both grain growth processes and dust transport processes are expressed in terms of the same quantity $\Sigma_{dust}(t, r, a)$.

2.3.2.2 *Collisional outcomes*

The first crucial ingredient for grain growth models are collisional outcome models. This provides the properties of the resulting particles when two dust particles collide, and is encoded into the collision Kernel ($\mathbf{K}(m, m', m'')$ or K_{lpk}) in the Smoluchowski equation. Collisional outcome models depend on many parameters such as the relative velocities between the two colliding particles, their sizes, or their chemical and structural properties. When two particles collide, the main collisional outcome is unfortunately not necessarily coagulation or sticking. Instead there are many potential collisional outcomes, which are [e.g., 135, 155]:

- Coagulation/Sticking: Hit-and-stick collisions due to electrostatic van der Waals forces, which results is a new particle of larger mass.

- Fragmentation: When the relative velocity between the two dust particles is higher than the fragmentation velocity v_{frag}, the two dust particles are destroyed into lighter fragments which are typically distributed in a power-law fragment size distribution [e.g., 156, 157]. A constant value, which is a free parameter, is usually used for v_{frag}. However, one should note that it actually depends on the properties of the two colliding dust particles such as the composition or porosity [e.g., 158].

- Bouncing: Elastic collisions, which results in the masses of the colliding dust particles to remain unchanged. This leads to no net grain growth. Roughly

speaking, bouncing occur when the relative velocity between the two dust particles is equal to the coagulation speed [e.g., 159], and is more likely to happen for highly compact silicate dust particles [e.g., 160].

- Erosion/Cratering: When the mass of one of the two dust particles is much larger than the other one, the lighter dust particle only excavate a fraction of the mass of the heavier one while possibly shattering itself [e.g., 161]. In this case, the relative velocity between the two dust particles is higher than the fragmentation velocity, but the result is not complete fragmentation although the resulting maximum grain size after collision is still limited.

- Mass transfer: When the mass of one of the two dust particles is much larger than the other one, the lighter one fragments, but also deposit a fraction of its mass.

Figure 11 shows an example of the collisional model of Windmark et al. [162], where the collision outcome is predicted given the relative velocity of two colliding dust particles. One can see that fragmentation, erosion and bouncing *do not* lead to net grain growth. Generally speaking, fragmentation processes occur when the relative velocity between the two colliding particles is too high. Similarly to radial drift of dust particles, these processes are also grain growth barriers, in the sense that they need to be overcome for dust particles to grow into larger bodies as it is needed to form planets. Until now, the discussion assumed that dust particles are purely neutrals. Nonetheless, the dust component of the protoplanetary disk actively interacts with the gas component (hence why there is a drag force as seen in the previous section). Since the gas is weakly ionized, dust particles can actually be charged (see Sect. 3.4 for further details). As a result, another grain growth barrier occurs called the electrostatic barrier. It operates for small particles (micron-sized ones), where the relative velocity between two colliding dust particles is not high enough to overcome the Coulomb repulsion [e.g., 163–166]. Akimkin et al. [167] recently showed that the coagulation-fragmentation equilibrium, accounting for charged dust particles, is characterized by dramatically higher abundances of sub-micron dust particles compared to the case of pure neutral dust. The reason for this is a continuous replenishment of small grain population due to fragmentation of the larger grain population, that is not counteracted by the usual efficient coagulation of small particles by Brownian motion (see bottom-left corner of Fig. 11) due to the electrostatic barrier. Although the effect of charged dust is not yet included when solving for the Smoluchowski equation in this thesis, I wanted to introduce the electrostatic barrier to show the eager reader that collisional outcome models are still under active research.

2.3.2.3 *Relative velocities*

The second crucial ingredient for grain growth models is the relative velocity between two colliding dust particles, which determines both the collision rate (e.g., $R(m, m')$ or R_{qk}) and the collisional outcome in the Smoluchowski equation. The
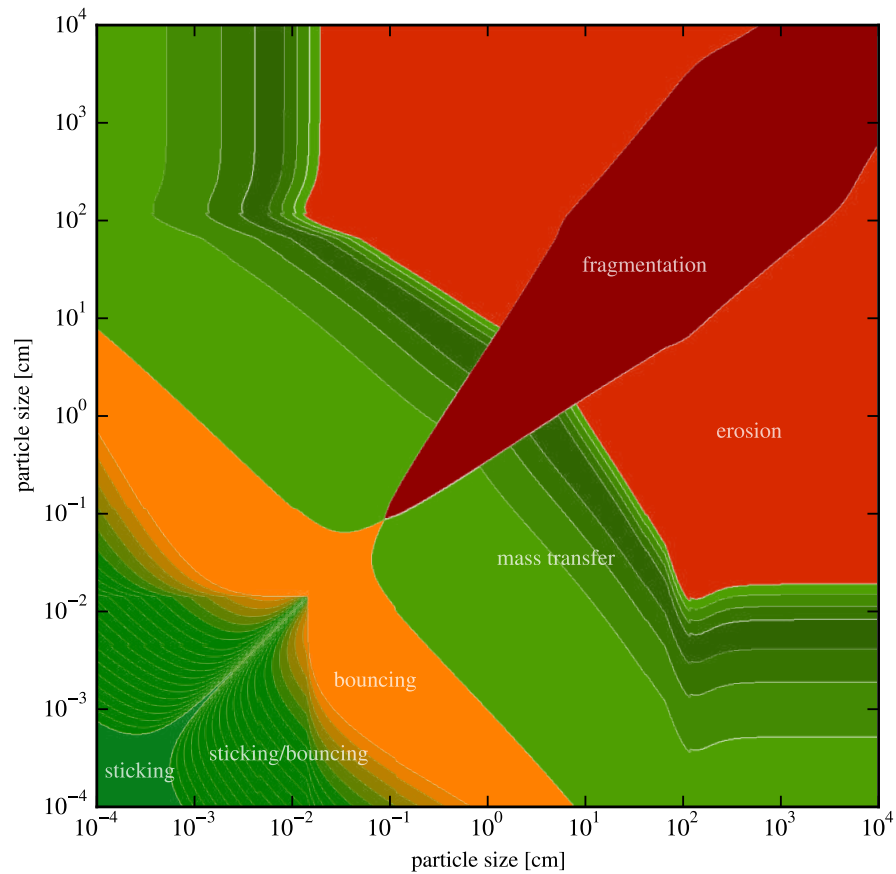
Figure 11: Mean collisional outcomes for silicates grains from the model of Windmark et al. [162]. Green regions denote net growth of the larger collision partner, orange denotes mass neutral bouncing collisions, and red denotes net mass loss. One should note that the exact collisional outcomes are model dependent. This plot is only used to provide the reader a basic picture. In particular such a plot underestimates the outcome of fragmentation and erosion, which are much more observed in laboratory experiments [e.g., 168–170]. Figure taken from Windmark et al. [162].

relative velocity between two dust particles comes from the dust transport processes. There are five sources that induce a relative velocity between two colliding dust particles of size a_1 and a_2: radial, azimuthal and vertical drift (Sect. 2.3.1.2), turbulence (Sect. 2.3.1.3), and Brownian motion. The total relative velocity between two colliding dust particles of size a_1 and a_2 corresponds to the root mean square of all these contributions.

For the relative velocities induced by radial, azimuthal and vertical drift one has respectively

$$\Delta v_{\mathrm{drif},r}(a_1, a_2) = |v_{\mathrm{dust},r}(a_1) - v_{\mathrm{dust},r}(a_2)|, \tag{100}$$

$$\Delta v_{\mathrm{drif},\phi}(a_1, a_2) = |v_{\mathrm{dust},\phi}(a_1) - v_{\mathrm{dust},\phi}(a_2)|, \tag{101}$$

and

$$\Delta v_{\mathrm{drif},z}(a_1, a_2) = |v_{\mathrm{dust},z}(a_1) - v_{\mathrm{dust},z}(a_2)|, \tag{102}$$

where $v_{\mathrm{dust},r}$, $v_{\mathrm{dust},\phi}$ and $v_{\mathrm{dust},z}$ are given in Sect. 2.3.1.2. One can notice that all these relative velocities vanish if the two dust particles have similar Stokes numbers, as it is expected.

For the relative velocity induced by turbulent mixing (Sect. 2.3.1.3), $\Delta v_{\mathrm{turb}}(a_1, a_2)$, I will follow the prescription of Ormel and Cuzzi [e.g., 171], where a general parameter δ_{turb} controls the strength of the turbulent collision velocities. In this thesis, the gas turbulence that leads to turbulent mixing comes from the MHD turbulence driven by the MRI (Sect. 2.2.3). As a result, it will be assumed that $\delta_{\mathrm{turb}} = \bar{\alpha}$.

Finally, the relative velocity induced by random Brownian motion is

$$\Delta v_{\mathrm{BM}}(a_1, a_2) = \sqrt{\frac{8 k_B T\, (m_1 + m_2)}{\pi m_1 m_2}}, \tag{103}$$

where T is the gas temperature, and $m_k = \frac{4}{3} \pi \rho_{\mathrm{bulk}} a_k^3$ is the dust particle mass of size a_k.

It is important to note that the relative velocities due to dust drift (radial, azimuthal, vertical) and turbulent mixing increase with Stokes number, reach a maximum for $St = 1$ and decrease for dust particles with $St > 1$. Furthermore, they vanish for $St \ll 1$, unlike the relative velocity due to Brownian motion. Consequently, grain growth initially starts with random motions of sub-micron dust particles induced by Brownian motion. Once they reach sizes larger than a few micrometers, grain growth proceeds with random motions due to turbulent mixing [e.g., 172]. At even larger sizes, both turbulent mixing and dust drift (radial, azimuthal, vertical) play a role in the growth of dust particles [e.g., 135]. Finally, dust particles are decoupled from the gas motion for the largest sizes, and grain growth is promoted by the collisions induced by dust drift.

2.3.3 Forming the building blocks of planets

In Sects. 2.3.1 and 2.3.2, I have introduced the concept of grain growth barriers, which are: radial drift barrier, fragmentation barrier, and electrostatic barrier (not

included in this thesis). These barriers prevent dust particles from growing monotonically to pebbles and planetesimals, the building blocks of planets. Instead, dust particles continuously coagulate and fragment in the protoplanetary disk, which leads to sizes that range from sub-micron to millimeter and centimeter. These millimeter- and centimeter-sized dust particles are what I refer to as pebbles. They are the most impacted by radial drift, which means they are the ones that are lost from the disk perspective on very short timescales. This in turn hinders the formation of planetesimals (solid bodies of size tens of kilometers) that are made of pebbles. On top of that, the electrostatic barrier complicates the picture further, since it makes initial grain growth of sub-micron dust particles by Brownian motion much less efficient than anticipated [e.g., 167], hence leading to an even lower number of pebbles within the disk. Also, it is worth noting that overcoming the fragmentation barrier requires low relative velocities between colliding dust particles, while overcoming the electrostatic barrier requires high relative velocities. This raises many questions on how these two grain growth barriers can be overcome simultaneously. All in all, it is clear that keeping pebbles and forming planetesimals within the protoplanetary disk is quite challenging. This is quite a paradox because exoplanets are routinely found in our galaxy (see Sect. 1.1). This problem is known as the "meter-size barrier problem": even if direct grain growth from interstellar sub-micron dust particles to planetesimals was theoretically possible with "lucky dust particles" that manage to overcome the electrostatic and fragmentation barriers due to the Stochastic nature of the processes involved, the process would take much longer than it takes the solids to be accreting onto the central star due to radial drift [for a review, see 35].

At this point, the eager reader might ask the natural question: *how can planets form in protoplanetary disks if their building blocks seem to be missing?* To address this question, I will now introduce the concept of dust trapping[17] by axisymmetric pressure maxima (also called pressure bumps). By definition, an axisymmetric pressure maximum (or a pressure bump) is a radial location within the disk where the gas is Keplerian at that location, super-Keplerian before that location (closer to the central star) and sub-Keplerian beyond that location (further away from the central star). As a reminder, to determine how Keplerian the gas component of the protoplanetary disk is, one needs to compute the gas pressure support parameter η_{gas} (Eq. 57). The gas is super-Keplerian when $\eta_{gas} < 0$, Keplerian when $\eta_{gas} = 0$, and sub-Keplerian when $\eta_{gas} > 0$. Dust particles near a pressure maximum migrate toward it because the direction of radial drift is toward regions of higher pressure. At a pressure maximum, the radial drift of dust particles vanishes because $\eta_{gas} = 0$ by definition (see Eq. 84). As a result, dust particles become trapped near a pressure maximum as long as it lasts (diffusion timescale), provided that the pressure gradient is sufficiently steep around this location [e.g., 97]. When a pressure maximum can efficiently trap dust particles, it is called a dust trap. Obviously, such a process can only trap dust particles that are partially or totally decoupled from

---

17 one should note that dust trapping can also occur in the azimuthal direction of the protoplanetary disk due to anticyclonic vortices

the gas, since large enough Stokes numbers are required for radial drift to be significant. This leads to a spatial segregation between dust particles with low Stokes numbers that follow the gas and are barely affected by pressure maxima, and dust particles with large enough Stokes numbers that remain trapped near them. This spatial segregation is actually what is observed in scattered-light and continuum emission of protoplanetary disks (Sect. 1.3).

While the dust particles that are barely affected by the presence of pressure maxima ($\sim$ 0.1–10 µm) ensure the constant replenishment of dust everywhere in the disk, the dust particles trapped near them can grow to pebble size ($\sim$ 100 µm–1 cm) much more efficiently compared to other locations in the disk. This is because there is a local dust enhancement relative to the gas near the pressure maxima, where the collision rates between dust particles increase and their relative velocities decrease. These newly formed pebbles stay trapped near the pressure maxima until these diffuse away, which naturally explains how the radial drift barrier can be overcome and pebbles can be kept within the protoplanetary disk. The efficient grain growth near the pressure maxima is still regulated by fragmentation, though, which means that the formation of planetesimals via direct subsequent collisions is unlikely. However, planetesimals can be formed out of pebbles through a combination of two instabilities: the Streaming Instability (SI) and the *dust* GI [e.g., 173–178]. The SI is a complex mechanism, based on the interplay between the dust and gas, where an asymmetric cloud of pebbles can dynamically drive gas and dust flows that subsequently enhance the density of the cloud itself [see Figure 2 of 87]. For a given radial location (not necessarily near a pressure maximum), the SI is thought to arise if the local pebbles have large Stokes numbers (St $\gtrsim 10^{-2}$) and if their midplane local dust-to-gas mass density ratios is high enough ($\rho_{\mathrm{dust}}/\rho_{\mathrm{gas}} \gtrsim 1$), although the exact criteria are still under intensive research [for a review, see 87]. These conditions can be satisfied near a pressure maximum. It is worth noting, thought, that the SI has long been thought to require the drag force between the dust and gas to be triggered. Consequently, it was believed until recently that it cannot occur at the exact location of a pressure maximum. Nonetheless, some recent studies show that the SI or a version of it might actually be triggered there [e.g., 179]. Since it is still not fully clear, it is assumed in this thesis that the SI can indeed be successfully triggered at the exact location of a pressure maximum. When this is the case, the SI leads to the concentration of pebbles into dense filaments within it. The local dust-to-gas mass density ratios there may reach values that exceeds the Roche limit, thus leading to the contraction and gravitational collapse of the pebble cloud due its own gravity (the dust GI mechanism) [e.g., 27, 180, 181]. This leads to the formation of planetesimals of size a few kilometers, although the exact properties, timing and location of the resulting planetesimals are still under active research [e.g., 35, 87, 182]. These uncertainties constitute a major obstacle in our understanding of how, where, and what type of planets emerge within protoplanetary disks.

Clearly, the disk regions near the pressure maxima are keys in order to keep pebbles within the disk and most likely form planetesimals. One of the main goals of

this thesis is to investigate if the interplay of gas, dust and MRI can create such pressure maxima, hence dust traps, during the secular evolution of the protoplanetary disk. If so, these dust traps would naturally explain some of the current disk dust observations, and could represent potential initial conditions for planet formation by being the birth-sites of soon-to-be planets (see Chapter 6 for further details).

2.3.4   *DustPy and mhdpy codes*

According to what has been seen so far in this Foundation Chapter, there are three main evolutionary equations that need to be solved when the secular evolution of the protoplanetary disk is investigated: the gas transport equation (Eq. 79), the dust transport equation (Eq. 92), and the discretized Smoluchowski coagulation–fragmentation equation (Eq. 99). For this purpose, I will use the code `DustPy`[18] [183] in this thesis, which can solve for these three equations simultaneously.

One should remember that the goal of this thesis is to study how the interplay of gas, dust and MRI shapes the secular evolution of protoplanetary disks. Solely using the code `DustPy` is therefore not enough, since it assumes the effective disk viscosity parameter $\bar{\alpha}$ to be a constant free parameter by default. As I discussed earlier, this parameter is what controls the gas turbulence and angular momentum transport. Furthermore, it also plays a crucial role in dust evolution because the strength of the radial and vertical mixing of the dust as well as the strength of the turbulent collision velocities are assumed to be determined by $\bar{\alpha}$ in this thesis ($\delta_{\text{turb}} = \delta_{\text{vert}} = \delta_{\text{rad}} = \bar{\alpha}$). However, as I discussed in Sect. 2.2, the disk viscosity is actually entirely described by the accretion process. In this thesis, it is assumed that the accretion is driven by the MRI and hydrodynamic instabilities. Consequently, the code `DustPy` needs to be complemented by another model that can compute, at each time-step, a self-consistent MRI-induced disk viscosity parameter $\bar{\alpha}$ that uses the gas and dust outputs of `DustPy` itself.

In Chapter 3, I will build a global MRI-driven disk accretion model that performs such a task. This model is implemented in a newly developed code called `mhdpy`, that will be publicly available soon. When the secular evolution of the protoplanetary disk will be investigated in this thesis (Chapters 5 and 6), the codes `DustPy` and `mhdpy` will be coupled to each other. It will then be possible, for the first time, to study how the interplay of gas, dust and MRI shapes the disk secular evolution. I invite the eager reader to go to the method sections of Chapters 5 and 6 to have further details about how the coupling between the two codes is achieved.

GLOBAL MRI-DRIVEN DISK ACCRETION MODEL

*The 1+1D global MRI-driven magnetized disk accretion model described in this Chapter is based on the published research articles **Delage T. N.**, Okuzumi S., Flock M., Pinilla P., & Dzyurkevich N.; "Steady-state accretion in magnetized protoplanetary disks", A&A (2022), vol. 658, A97 [184], and **Delage T. N.**, Gárate M., Okuzumi S., Yang C.C., Pinilla P., Flock M., Stamler S. M., & Birnstiel T.; "The impact of dust evolution on the dead zone outer edge in magnetized protoplanetary disks"; A&A (2023), vol. 674, A190 [185].*

3.1 MOTIVATION

As I discussed in Sect. 1.6, the ultimate goal of this thesis is to understand how the interplay of gas, dust and MRI activity shapes the protoplanetary disk secular evolution in the context of planet formation. A time-dependent disk model where nonideal MHD calculations[1] are self-consistently coupled with gas and dust (dynamics and grain growth processes combined) evolution on million-year timescales is thus required. This is indeed the only way if one wants to achieve a meaningful comparison between the post-processed[2] outputs of such a model and the current dust continuum and gas observations of million-year-old Class II protoplanetary disks. Furthermore, since most of the disk observations are sensitive to the outer region of disks ($r \gtrsim 1\,\mathrm{au}$, where r is the distance from the central star), the global MRI-driven disk accretion model built in this thesis solely focuses on these regions. Should one want to include the disk inner region, one could extend the model by following the methodology described in Jankovic et al. [186, 187], for example.

In a world with infinite computational power, the way to go would be to run 3D global nonideal MHD simulations to model the full extent of protoplanetary disks where the following key processes are implemented: thermo-chemistry (with the relevant ionization sources), simultaneous transport of gas and dust, grain growth processes from interstellar micron-sized particles to planetesimals, and induction equation for the magnetic fields. It is because protoplanetary disks are, by nature, 3D weakly ionized and magnetized objects made of gas and dust (See Chapter 2). Nevertheless, we are not leaving in such a word yet. Although one could achieve very detailed 3D nonideal MHD simulations [e.g., 188–190], it is always for a subset of the full extent of the disk and without considering grain growth processes. What make it so challenging computationally are the very different timescales at play. For example, turbulent gas eddies grow and decay on a timescale of one orbital

---

1 hence the underlying physics and chemistry
2 by radiative transfer calculations

period [e.g., 191], while dust particles grow to macroscopic sizes and settle to the midplane on a timescale of a few orbital periods depending on the grain size [e.g., 137, 154, 192]. Consequently, the time-step needed in these simulations has to be "small enough" (of order an orbital period), which makes difficult to evolve the disk on secular timescales. Even though some theoretical works have studied the detailed behavior of the MRI activity in disks by performing 3D local shearing box or global simulations [e.g., 109, 112, 113, 193–196], they suffer from this challenge, hence preventing any meaningful comparisons with disk observations. Conversely, some other works have used the Shakura-Sunyaev α-disk model[3] (see Sect. 2.2) to simulate the protoplanetary secular evolution where viscous gas evolution and dust evolution (dynamics and grain growth processes combined) can be coupled. However, they most of the time use a constant or, at best *ad hoc* prescriptions, for the α parameter [e.g., 110] in order to describe the MRI-driven disk turbulence. As a result, the detailed physics of the MRI is ignored in such works.

To date, a disk model that can properly capture the interplay of gas, dust and MRI activity for the secular evolution of protoplanetary disks remains to be built. One way to achieve it could be by building what I call a "trade-off" model, where the Shakura-Sunyaev α-disk model is complemented with self-consistent nonideal MHD calculations: At each gas and dust evolution time-steps, the α parameter is self-consistently computed by a global MRI-driven disk accretion model that can capture the essence of the MRI-driven accretion in a computationally inexpensive way, so that the implementation into viscous gas and dust (dynamics and grain growth processes combined) evolution models is feasible on million-year timescales, unlike the 3D global nonideal MHD simulations. Some previous studies attempted to make such trade-off models [e.g., 197–200]. However, they did not include all the necessary physics to capture the MRI-driven turbulence in protoplanetary disks (e.g., ambipolar diffusion is omitted).

In this Chapter, I make the necessary preparations for our quest by presenting a theoretical groundwork which explains how to derive a self-consistent MRI-induced Shakura-Sunyaev disk viscosity α parameter for the outer region of Class II protoplanetary disks ($r \gtrsim 1\,\mathrm{au}$). This new global MRI-driven disk accretion model is an essential tool at the core of this thesis. It is implemented in a newly developed code called `mhdpy`, which will be publicly available soon. Below I provide a road map that explains the main methodology adopted to build the global MRI-driven disk accretion model.

3.2   ROAD-MAP FOR A SELF-CONSISTENT MRI-INDUCED DISK VISCOSITY PARAMETER

In this thesis the angular momentum transport and disk turbulence are assumed to be solely controlled by both the MRI and hydrodynamic instabilities, implying that the origin of the local disk viscosity α that goes into Eq. (77) is the MHD turbulence driven by the MRI. It means that I do not consider other processes that could

---

3 wherein the quantity α (disk viscosity parameter) encodes the disk turbulence level

drive angular momentum transport such as MHD disk winds or gravitoturbulence (Sect. 1.4). The total disk gas mass chosen for all the simulations of this thesis is such that $Q > 2$ everywhere in the disk, so that that the latter should be negligible compared to the MHD turbulence driven by the MRI.

It is important to note that considering the MRI to be the dominant magnetically controlled mechanism for turbulence requires the solution for vertical stratification[4], since the MRI activity (hence the local disk viscosity α of Eq. 77) changes with disk height. Consequently, the global MRI-driven disk accretion model that I need in order to start our quest has to derive a self-consistent local disk viscosity α in the $r - z$ plane, given the radial and vertical structure of the gas (Sect. 2.2) and dust (Sect. 2.3) components of the protoplanetary disk as well as the central star properties (mass $M_\star$, bolometric luminosity $L_\star$, and total stellar X-rays (XR) luminosity L_{XR}). By assuming the disk to be geometrically thin ($H_{gas} \ll r$), axisymmetric and symmetric about the midplane, the vertical and radial dimensions of the model can be decoupled into a 1+1D (r, z) framework, where each radial grid-point contains an independent vertical grid. Furthermore, it is enough to compute the domain $z \geqslant 0$ to obtain the full solution.

For the global MRI-driven disk accretion model to compute such a self-consistent local disk viscosity α, whilst capturing the essence of the MRI-driven accretion without resorting to computationally expensive 3D global nonideal MHD simulations, it needs to include the key following physical processes: (1) disk heating by passively absorbing stellar irradiation; (2) nonthermal ionization sources (Sect. 3.3); (3) ionization chemistry that captures the charge state of the disk dust–gas mixture, hence carefully modeling the gas ionization degree (Sect. 3.4); and (4) nonideal MHD calculations (Sect. 3.5). In order to know where the MRI can operate in the disk, under the framework of viscously driven accretion, the general methodology is to compute the magnetic diffusivities of the nonideal MHD effects as well as their corresponding Elsasser numbers from the ionization chemistry and the magnetic field (Sect. 4.3.2.3), then apply a set of conditions for sustaining active MRI derived from 3D numerical simulations. In the non-MRI regions (where the MRI is suppressed), it is further assumed that the gas can still accrete due to a small constant hydrodynamic turbulent parameter α_{hydro} (model parameter), induced by hydrodynamic instabilities such as the VSI. For given stellar, gas and dust properties, the local disk viscosity α parameter can thus be determined self-consistently from detailed considerations of the nonideal MHD version of the MRI, both as a function of radius and height. Finally, the effective disk viscosity $\bar{\alpha}$ parameter (Eq. 77) can be derived, which is the key output of the model. Figure 12 summarizes, in a nutshell, the interactions between each ingredient required to capture the essence of the MRI-driven turbulence.

The next sections provide more details about each ingredient of the global MRI-driven disk accretion model. Table 1 summarizes the constant parameters used in this model throughout the thesis.

---

4 protoplanetary disks are layered accretion disk as seen in Sect. 2.1.4

Constant parameters	Symbol [Units]	Value
Direct X-ray amplitude	$\zeta_{1,XR}$ [s^{-1}]	6×10^{-12}
Direct X-ray penetration depth	$\Sigma_{1,XR}$ [g.cm^{-2}]	0.0035
Scattered X-ray amplitude	$\zeta_{2,XR}$ [s^{-1}]	10^{-15}
Scattered X-ray penetration depth	$\Sigma_{2,XR}$ [g.cm^{-2}]	1.64
Galactic cosmic ray amplitude	$\zeta_{CR,ISM}$ [s^{-1}]	10^{-17}
Galactic cosmic ray penetration depth	Σ_{CR} [g.cm^{-2}]	96
Radionuclide ionization rate for ^{26}Al	$\zeta_{RA,^{26}Al}$ [s^{-1}]	7.6×10^{-19}
Half-decay time for ^{26}Al	$t_{half,^{26}Al}$ [years]	7.4×10^{5}
Radionuclide ionization rate for ^{60}Fe	$\zeta_{RA,^{60}Fe}$ [s^{-1}]	4×10^{-20}
Half-decay time for ^{60}Fe	$t_{half,^{60}Fe}$ [years]	1.5×10^{6}
Radionuclide ionization rate for ^{40}K	$\zeta_{RA,^{40}K}$ [s^{-1}]	1.1×10^{-22}
Half-decay time for ^{40}K	$t_{half,^{40}K}$ [years]	1.28×10^{9}
Ion mass (HCO^{+})	m_i [g]	$29 \times m_H$
Ion sticking coefficient	s_i	1
Electron sticking coefficient	s_e	0.3, 0.6
Hydrodynamic turbulent parameter	α_{hydro}	10^{-4}

Table 1: Summary of the constant parameters used in the global MRI-driven disk accretion model of this Chapter. One should note that $s_e = 0.3$ is used in Chapter 4, whereas $s_e = 0.6$ is used in Chapters 5 and 6. Furthermore, $\alpha_{hydro} = 10^{-4}$ except in Sect. 4.4.5. Here m_H corresponds to the atomic mass of hydrogen.
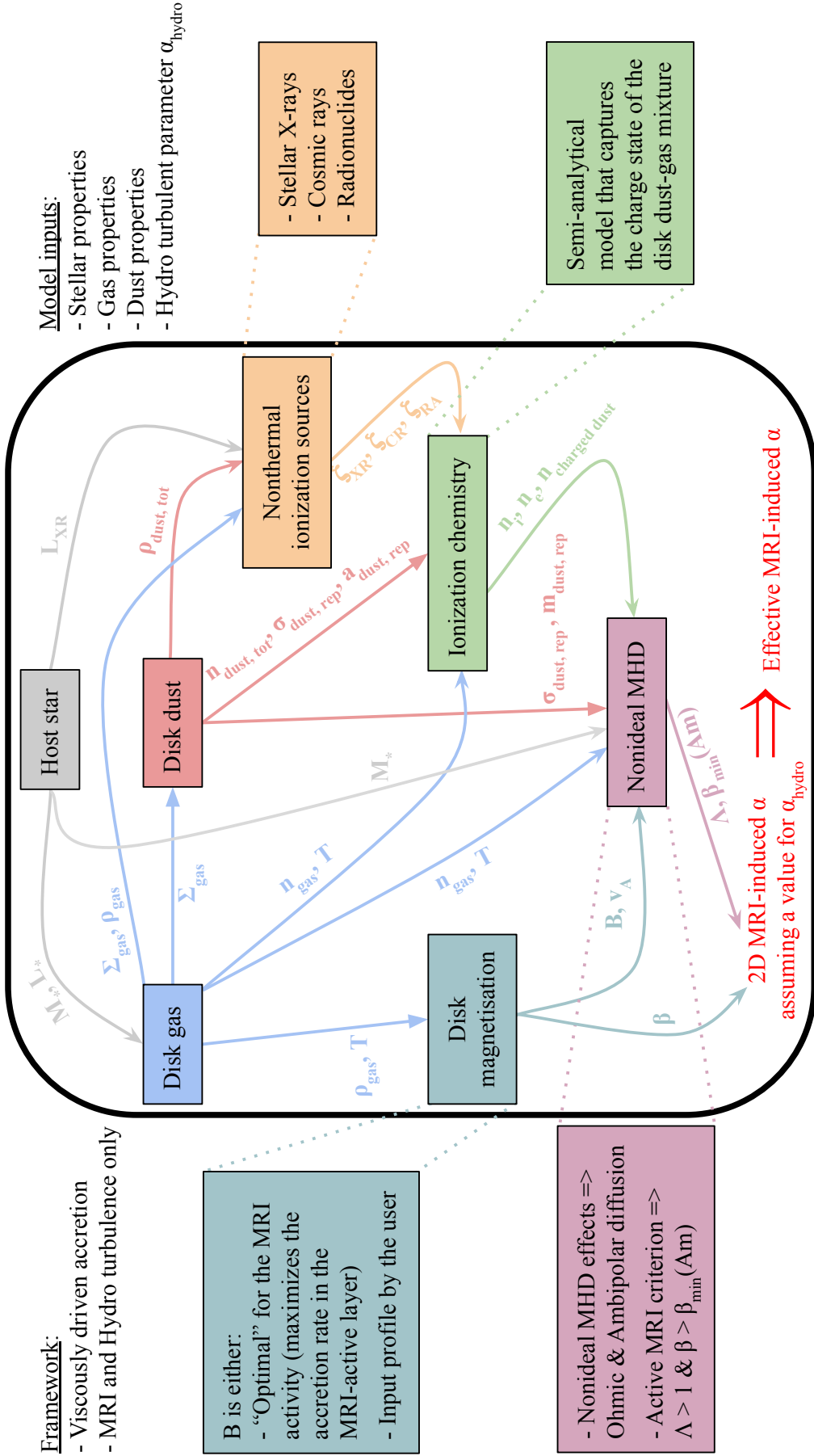
Figure 12: Flowchart of the new global MRI-driven disk accretion model used throughout the thesis. This model captures the essence of the MRI-driven turbulence in a 1+1D framework, accounting for the following: stellar properties (gray symbols), disk gas properties (blue symbols), disk dust properties (red symbols), nonthermal ionization sources (yellow symbols), ionization chemistry modeling the gas ionization degree (green symbols), disk magnetization properties (powder blue symbols), and nonideal MHD calculations (dark pink symbols). The main output of the model is an effective radial profile for the MRI-induced viscosity parameter, $\bar{\alpha}$ (Eq. 77).

3.3   NONTHERMAL IONIZATION SOURCES

As I discussed in Sect. 2.1, the MRI can operate only if the mobile charged particles in the gas-phase of the protoplanetary disk are well enough[5] coupled to the magnetic field lines. The more charged particles are in the gas-phase with respect to the neutrals (i.e., the more the gas component of the disk is ionized), the weaker the nonideal MHD effects are and the better the coupling is. In the outer regions of the disk ($r \gtrsim 1\,au$) –which is the main focus of this thesis– thermal ionization and thermionic emission are inefficient. The gas is thus very weakly ionized and the ionization process is primarily initiated by nonthermal ionization of molecular hydrogen (H_2) and helium (He). In order to derive the relative proportion of all charged carriers in the gas-phase, one needs to explicitly balance the rate of ionization from the relevant nonthermal sources against the rate of recombination within the gas. Consequently, one needs first to identify the relevant nonthermal ionization sources that can initiate the ionization process.

In general, the most important nonthermal ionization sources for isolated[6] protoplanetary disks are stellar X-rays, stellar energetic particles (SPs), stellar far-ultraviolet (FUV) radiation, all of them emanating from the central star as well as galactic cosmic rays (CR), and the decay of short- and long-lived radionuclides (RA) [e.g., 201–205]. Here I would like to make two comments: (1) FUV can fully ionize atomic carbon and sulfur. Perez-Becker and Chiang [206] showed that FUV can penetrate a vertical gas column density $\Sigma_{FUV} \in [0.01 - 0.1]$ g.cm^{-2}, and produce much higher ionization than other sources. Additionally, Simon et al. [207] found that the MRI is the most effective in the FUV layer of the outer disk. Depending at exactly which disk height the penetration depth Σ_{FUV} is reached, FUV may be important close to the disk midplane. Nonetheless, it is more likely that it will only dominate the very upper layers of the disk, hence have a moderate impact of the effective MRI-induced disk viscosity $\bar{\alpha}$ (since it is a pressure-weighted vertically averaged quantity). (2) Stellar energetic particles become the dominant H_2 ionization source in the warm molecular layer of the disk above the CO ice line, and can increase the column densities of HCO^+ by a factor in the range $3 - 10$ for disk radii $r \lesssim 200\,au$, with a higher impact in the disk regions with low cosmic ray ionization [see 205]. The inclusion of the SPs may be of importance, but more work is needed to really understand their ionizing power. Due to the uncertainties about stellar FUV radiation and SPs for ionizing the bulk of the disk gas, I only consider the nonthermal ionization driven by stellar X-rays, galactic cosmic rays and radionuclides in the present global MRI-driven disk accretion model. Figure 13 provides the reader an idea of what nonthermal ionization source is expected to dominate at various locations in the protoplanetary disk for the assumptions made (obtained for the fiducial model of Chapter 4).

Since the ionization rate for He is related to the one for H_2 by $\zeta^{(He)} = 0.84 \times \zeta^{(H_2)}$ [see 204, 208], it is enough to know $\zeta^{(H_2)}$ to compute the total ionization

---

5 "well enough" is discussed in Sect. 3.5
6 namely, far enough from any other stars

rate required for the ionization chemistry. The total ionization rate, ζ, is given by $\zeta = \zeta^{(H_2)}x_{H_2} + \zeta^{(He)}x_{He}$, where $x_{H_2} = \frac{n_{H_2}}{n_{gas}}$ and $x_{He} = \frac{n_{He}}{n_{gas}}$ are the factional abundances of H_2 and He, respectively. x_{H_2} and x_{He} are calculated from the solar system abundance by Anders and Grevesse [209]: $x_{H_2} = \frac{n_{H_2}}{n_{gas}} = \frac{n_{H_2}}{n_H} \times \frac{n_H}{n_{gas}}$, with $\frac{n_{H_2}}{n_H} = 0.5$ (all H nuclei are in the form of H_2), and $x_{He} = \frac{n_{He}}{n_{gas}} = \frac{n_{He}}{n_H} \times \frac{n_H}{n_{gas}}$, with $\frac{n_{He}}{n_H} = 0.0975$. Here, n_H is the number density of hydrogen nucleus, which can be estimated as $n_H = \rho_{gas}/(1.4 m_H)$ for the solar abundance [e.g., 210]. In total, it leads to

$$\zeta(t, r, z) = 0.97 \times \zeta^{(H_2)}(t, r, z). \tag{104}$$

In order to compute $\zeta^{(H_2)}$, the stellar X-ray (Sect. 3.3.1), the galactic cosmic ray (Sect. 3.3.2), and the radionuclide (Sect. 3.3.3) contribution are summed up as

$$\zeta^{(H_2)} = \zeta^{(H_2)}_{XR} + \zeta^{(H_2)}_{CR} + \zeta^{(H_2)}_{RA}. \tag{105}$$

Besides, I follow standard prescriptions where the previous ionization rates are given as a function of vertical gas column densities: $\Sigma^+_{gas}(t, r, z) = \int_z^{+\infty} \rho_{gas}(t, r, z')dz'$ and $\Sigma^-_{gas}(t, r, z) = \Sigma_{gas}(t, r) - \Sigma^+_{gas}(t, r, z)$, where $\Sigma^+_{gas}(t, r, z)$ and $\Sigma^-_{gas}(t, r, z)$ represent the vertical gas column density measured from above and below a height of interest z, respectively, at a given radius r. The underlying assumption is that the nonthermal ionization source penetrate the gas in the vertical direction, at any distance from the star. Although this approximation is good enough for galactic cosmic rays that originate from outside the protoplanetary disk, stellar X-rays are launched from around the central star and the use of vertical gas column densities might become invalid. Indeed, stellar X-rays that reach the outer regions of the disk need to travel first within the dense inner regions. If the densities are high enough, "self-shadowing" can occur and the stellar X-rays may be fully or partially absorbed. This self-shadowing event could thus result in an overall lower effective stellar X-ray ionization rate.

A way to alleviate such an issue and properly deduce the ionization rate within the disk is by performing radiative transfer calculations. However, doing so would greatly increase the computational complexity of the whole problem. Since the ultimate goal of this thesis is to couple self-consistently a global MRI-driven disk accretion model to gas and dust evolution models (dynamics and growth processes combined), the implementation of fast radiative transfer calculations is not treated here. Nonetheless, if one would want to do so, the global two-layer radiative transfer model put forward by Okuzumi, Ueda, and Turner [211] may be a good starting point.

3.3.1 *Stellar X-ray ionization*

The coronae of typical T Tauri stars are powerful sources of keV X-rays [212]. The typical total stellar X-rays luminosity, L_{XR}, is time-dependent and in the range $\approx 10^{28}$–10^{32} erg.s^{-1} depending on the stellar type, with temperatures $k_B T_{XR}$ of a few keV. The physics of the interaction of these stellar X-rays with the gas component
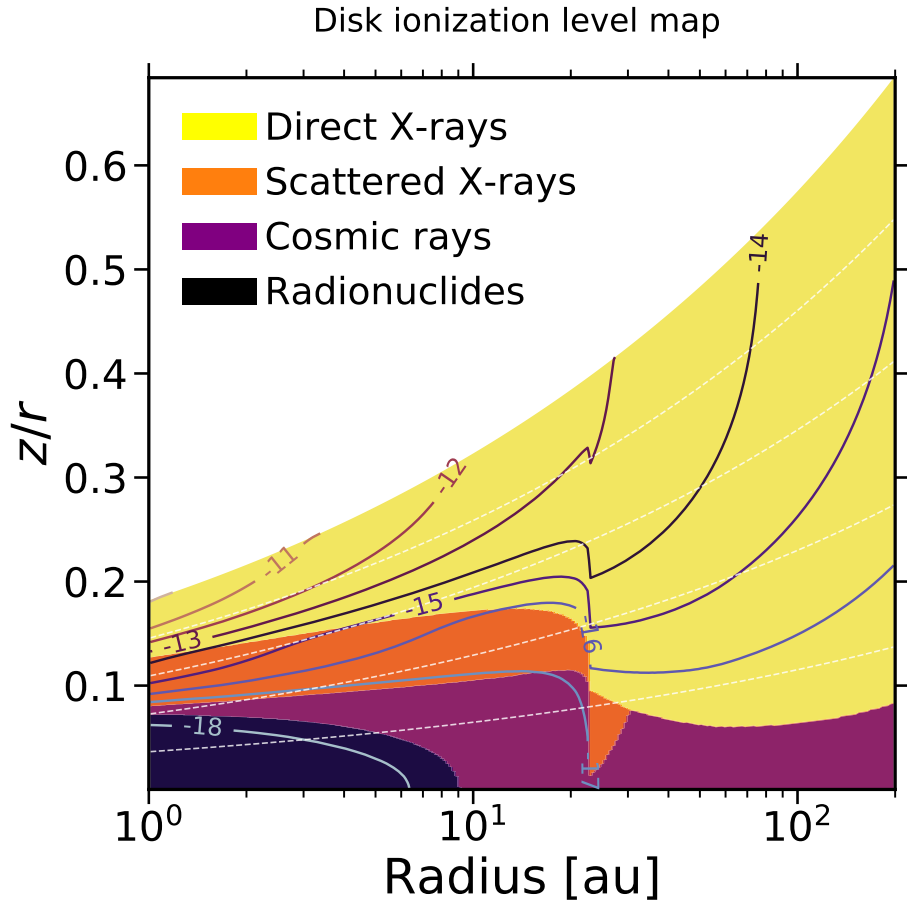
Figure 13: Ionization rate for H_2 $\zeta^{(H_2)}$ (defined in Sect. 3.3) and its different contributions, as a function of location in the disk, obtained for the fiducial model of Chapter 4. For each color, the following nonthermal ionization source dominates: decay from short- and long-lived radionuclides (black), galactic cosmic rays (purple), or stellar X-rays (orange and yellow for the scattered and direct contribution, respectively). The solid colored contour lines correspond to the surfaces of constant total ionization rate, $\zeta^{(H_2)}$, ranging from $7.6 \times 10^{-19}\,\mathrm{s}^{-1}$ to $1.8 \times 10^{-10}\,\mathrm{s}^{-1}$. The dashed white lines correspond to the surfaces $z = 1\,\mathrm{H_{gas}}$, $z = 2\,\mathrm{H_{gas}}$, $z = 3\,\mathrm{H_{gas}}$, and $z = 4\,\mathrm{H_{gas}}$, from bottom to top, respectively.

of the protoplanetary disk involves Compton scattering and absorption by photo-ionization.

To compute the stellar X-ray ionization rate $\zeta_{XR}^{(H_2)}$ for H_2, I adopt the fitting formula of Bai and Goodman [213] at X-ray temperature $T_{XR} = 3\,keV$, based on the Monte Carlo simulations from Igea and Glassgold [210]. It reads:

$$\zeta_{XR}^{(H_2)} = \zeta_{XR,\,direct}^{(H_2)} + \zeta_{XR,\,scattered}^{(H_2)},\tag{106}$$

where

$$\zeta_{XR,\,direct}^{(H_2)}(t,r,z) = \left(\frac{L_{XR}(t)}{10^{29}\,erg.s^{-1}}\right)\left(\frac{r}{1\,au}\right)^{-2.2} \times$$
$$\zeta_{1,XR}\left[\exp\left(-\left(\frac{\Sigma_{gas}^{+}(t,r,z)}{\Sigma_{1,XR}}\right)^{0.4}\right) + \exp\left(-\left(\frac{\Sigma_{gas}^{-}(t,r,z)}{\Sigma_{1,XR}}\right)^{0.4}\right)\right],\tag{107}$$

and

$$\zeta_{XR,\,scattered}^{(H_2)}(t,r,z) = \left(\frac{L_{XR}(t)}{10^{29}\,erg.s^{-1}}\right)\left(\frac{r}{1\,au}\right)^{-2.2} \times$$
$$\zeta_{2,XR}\left[\exp\left(-\left(\frac{\Sigma_{gas}^{+}(t,r,z)}{\Sigma_{2,XR}}\right)^{0.65}\right) + \exp\left(-\left(\frac{\Sigma_{gas}^{-}(t,r,z)}{\Sigma_{2,XR}}\right)^{0.65}\right)\right].\tag{108}$$

The first term of Eq. (106) corresponds to the direct X-ray contribution of the total stellar X-ray ionization rate, whereas the second term corresponds to its scattered X-ray contribution. $\zeta_{XR,\,direct}^{(H_2)}$ describes the attenuation of X-rays photons by absorption, with the unattenuated coefficient $\zeta_{1,XR} = 6 \times 10^{-12}\,s^{-1}$ and the penetration depth $\Sigma_{1,XR} \approx 0.0035\,g.cm^{-2}$. $\zeta_{XR,\,scattered}^{(H_2)}$ describes the contribution from scattering, with the unattenuated coefficient $\zeta_{2,XR} = 10^{-15}\,s^{-1}$ and the penetration depth $\Sigma_{2,XR} \approx 1.64\,g.cm^{-2}$. Here I recalculated the penetration depths given by Bai and Goodman [213] in terms of hydrogen nucleus into the corresponding gas surface density penetration depths ($\Sigma_{1,XR}$ and $\Sigma_{2,XR}$).

There are two options for computing the total stellar X-rays luminosity, L_{XR}, in this thesis: (1) I assume that $L_{XR} = 10^{-3.5} \times L_\star$ [214], with $L_\star$ the stellar bolometric luminosity being a constant free parameter of the model (Chapters 4 and 5); (2) I assume the more realistic case where it is a function of time t (Chapter 6) that follows the evolutionary track of Kunitomo et al. [133] (see their Fig. 5).

3.3.2 *Galactic cosmic ray ionization*

Galactic cosmic rays are another potential source of disk ionization. To compute the galactic cosmic ray ionization rate $\zeta_{CR}^{(H_2)}$ for H_2, I adopt the standard description of

the galactic (i.e., interstellar) cosmic ray flux which is encapsulated in the fitting formula given by Umebayashi and Nakano [204]:

$$
\zeta_{CR}^{(H_2)}(t,r,z) = \frac{\zeta_{CR,ISM}}{2} \times
$$

$$
\left\{ \exp\left(-\frac{\Sigma_{gas}^+(t,r,z)}{\Sigma_{CR}}\right) \left[1 + \left(\frac{\Sigma_{gas}^+(t,r,z)}{\Sigma_{CR}}\right)^{\frac{3}{4}}\right]^{-\frac{4}{3}} + \right.
$$

$$
\left. \exp\left(-\frac{\Sigma_{gas}^-(t,r,z)}{\Sigma_{CR}}\right) \left[1 + \left(\frac{\Sigma_{gas}^-(t,r,z)}{\Sigma_{CR}}\right)^{\frac{3}{4}}\right]^{-\frac{4}{3}} \right\}, \quad (109)
$$

where the unattenuated galactic cosmic ray ionization rate is $\zeta_{CR,ISM} = 10^{-17}\,\mathrm{s}^{-1}$, and the galactic cosmic ray penetration depth is $\Sigma_{CR} = 96\,\mathrm{g.cm}^{-2}$. Nevertheless, it is important to note that the galactic cosmic ray ionization rate suffers from large uncertainties, since it is unclear whether or not the unattenuated interstellar medium flux of cosmic rays can reach the surfaces of protoplanetary disks. Indeed, the magnetic fields embedded in the stellar wind (equivalent to the solar wind from the Sun) can form a partial barrier to incoming cosmic ray particles (called the Heliosphere in our solar system). Consequently, the unattenuated galactic cosmic ray ionization rate could become as low as $\zeta_{CR,ISM} \approx 10^{-19}\,\mathrm{s}^{-1}$ [e.g., 215, 216].

3.3.3 Radionuclide ionization

In the high-density regions of protoplanetary disks, the dominating ionization source is the decay of radionuclides contained in dust particles. There is significant evidence in meteorites that these radionuclides existed in the formation stage of the Sun and the solar system [e.g., 217]. For example, Lee, Papanastassiou, and Wasserburg [218] found excesses of ^{26}Mg of up to 10% in Ca–Al-rich inclusions (CAIs) in the Allende meteorite, and showed that the correlation of these excesses with the Al/Mg ratio can be interpreted as the evidence for the existence of the short-lived radionuclide ^{26}Al in the past. Also, over 1500 Mg-isotopic analyses of Al-rich material in meteorites clearly showed that excesses of ^{26}Mg in refractory inclusions are the result of the decay of ^{26}Al [see 219]. The other extinct short-lived radionuclides such as ^{60}Fe have also been found to have existed in the early solar system [e.g., 217, 220]. From these evidence, it is very tentative to think that these short-lived radionuclides have been continuously generated by nucleosynthesis in the Galaxy and have existed universally in the ISM [e.g., 221, 222]. Furthermore, the ionization rate by the long-lived radionuclide ^{40}K has been investigated by Cameron [223] and Nakano and Tademaru [224].

The ionization rate by a radionuclide X depends on its abundance $x(X)$ relative to hydrogen nucleus by number, its decay rate constant $w(X) = \ln 2/t_{1/2}(X)$ with $t_{half}(X)$ its half-decay time, and the average energy $\bar{E}_{em}(X)$ emitted by its decay which is released in the form of kinetic energies of electrons (resulting from nuclear

β-decay), α-particle and photons. I define the total radionuclide ionization rate $\zeta_{RA}^{(H_2)}$ for H_2 as it follows

$$\zeta_{RA}^{(H_2)}(t, r, z) = \zeta_{RA}(t) \times \frac{(\rho_{dust,tot}(t, r, z)/\rho_{gas}(t, r, z))}{10^{-2}}, \tag{110}$$

with ρ_{gas} defined in Eq. (66) and $\rho_{dust,tot}$ defined in Eq. (94). Here $\zeta_{RA}(t)$ is the radionuclide ionization rate that depends on the short- and long-lived radionuclides chosen. Across the Chapters of this thesis, I will consider two options to compute $\zeta_{RA}(t)$:

- OPTION A (Chapters 4 and 5). I assume a simple prescription for the radionuclide ionization rate where it is time-independent (no decay of radionuclides accounted for) and is solely given by the short-lived radionuclide ^{26}Al. It reads

$$\zeta_{RA}(t) = \zeta_{RA,^{26}Al} = 7.6 \times 10^{-19}\,s^{-1}. \tag{111}$$

- OPTION B (Chapter 6). I assume a more complex time-dependent prescription for the radionuclide ionization rate where the short-lived radionuclides ^{26}Al, ^{60}Fe and the long-lived radionuclide ^{40}K, as well as their decay, are accounted for. It reads

$$\zeta_{RA}(t) = \zeta_{RA,^{26}Al} \left(\frac{1}{2}\right)^{t/t_{half,^{26}Al}} + \zeta_{RA,^{60}Fe} \left(\frac{1}{2}\right)^{t/t_{half,^{60}Fe}} + \zeta_{RA,^{40}K} \left(\frac{1}{2}\right)^{t/t_{half,^{40}K}}, \tag{112}$$

with $\zeta_{RA,^{26}Al} = 7.6 \times 10^{-19}\,s^{-1}$ and $t_{half,^{26}Al} = 7.4 \times 10^5$ years, $\zeta_{RA,^{60}Fe} = 4 \times 10^{-20}\,s^{-1}$ and $t_{half,^{60}Fe} = 1.5 \times 10^6$ years, $\zeta_{RA,^{40}K} = 1.1 \times 10^{-22}\,s^{-1}$ and $t_{half,^{40}K} = 1.28 \times 10^9$ years [see Tables 1 and 2 of 204].

In Eq. (110), one can notice that the total radionuclide ionization rate is obtained by scaling $\zeta_{RA}(t)$ with the local dust-to-gas mass ratio $\rho_{dust,tot}/\rho_{gas}$, normalized by the ISM value 10^{-2}. Since radionuclides are refractory and locked into dust particles, a change in the local dust-to-gas mass ratio is expected to induce a local change in the number of radionuclides locally available to ionize the gas. One should also note that Eq. (110) does not account for the escape of decay products, and therefore overestimates radionuclide ionization rates in low gas column density regions ($\Sigma_{gas} \lesssim 10\,g\,cm^{-2}$). Nevertheless, radionuclide ionization does not dominate the nonthermal ionization for such low gas surface densities reached in the outer disk region. In practice, this inconsistency is thus not an issue.

3.4 IONIZATION CHEMISTRY

Armed with the total ionization rate driven by the nonthermal ionization sources, the goal is now to derive the abundance of all mobile charge carriers in the gas-phase of the protoplanetary disk. This is a necessary step to quantify the strength

of the nonideal MHD effects, hence knowing where the MRI can operate and what turbulence it can drive.

It is very important to remember that disks also contain dust particles. The small grains of the dust distribution can efficiently remove away charged particles from the gas-phase due to their large total grain surface area [e.g., 74, 225, 226], although some laboratory experiments may have found that dust particles could also be source of gas ionization through mutual collisions [227] (not included in this thesis because it is not yet well constrained quantitatively). This implies that the MRI activity in disks is crucially controlled by the concentration and properties of dust particles since they modify the gas ionization degree, hence the strength of the nonideal MHD effects. Furthermore, the net charge of dust particles does not vanish due to the presence of the weakly ionized ambient gas [e.g., 228]. There are thus charged dust particles that directly intervene in the calculations of the magnetic diffusivities for the nonideal MHD effects. Consequently, one needs to account for the charge state of the dust–gas mixture altogether in order to properly derive the abundance of all charge carriers in the disk. Figure 14 summarizes the ionization–recombination reactions in a disk dust–gas mixture.

3.4.1 *Semi-analytical chemical model*

By assuming that local ionization–recombination equilibrium is reached at every locations of the protoplanetary disk, the abundance of all charge carriers (free electrons, ions and charged dust particles) initiated by the ionization process can be obtained. When the nonthermal sources ionize molecular hydrogen (H_2) and helium (He), the charge is quickly transferred to other abundant gas species through collisions, producing molecular and atomic ions (e.g. HCO^+, Mg^+). In the context of the MRI, the exact composition of the gas that this leads to is unimportant in the presence of dust particles [see Sect. 4.2 of 229, for a discussion], and simple chemical networks reproduce the gas ionization level well [e.g., 226]. As a result, it is assumed that the gas always exists mainly as H_2 and He and their ionization at a rate ζ directly produces ions and free electrons at a volumetric rate ζn_{gas}.

In the present global MRI-driven disk accretion model, I do not implement a chemical reaction network [e.g., 112, 213, 226, 230]. Instead, I implement a semi-analytical chemical model based on Okuzumi [163]. The main motivation behind this choice is the need of a chemical model that carefully captures the charge state of the disk dust–gas mixture, without greatly enhancing the computational complexity of the whole problem[7]. The difference between the semi-analytical chemical model presented here and the one described in Okuzumi [163] is the fact that compact rather than fluffy grains are considered.

Similarly to Okuzumi [163], I make the following approximations: (1) the ions species can be represented by a single dominant ion species; (2) the grain charge distribution can be approximated as a continuous function of Z. Here the dominant

---

7 requirement for a self-consistently coupling between the global MRI-driven disk accretion model and gas/dust evolution models
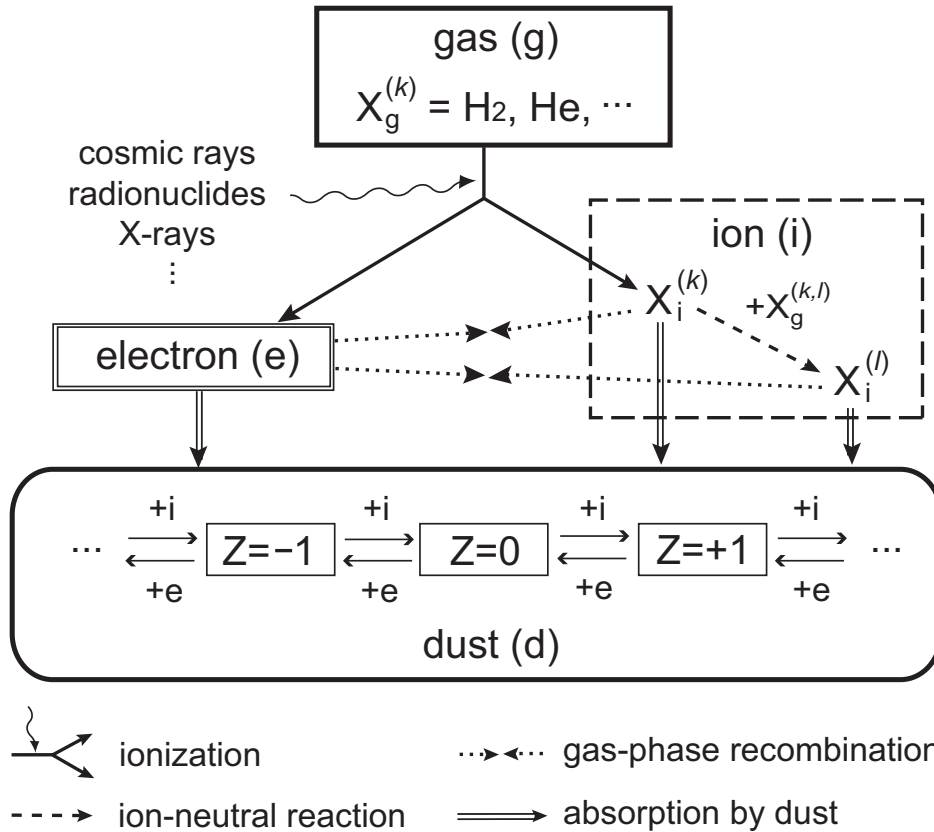
Figure 14: Schematic diagram of the ionization–recombination reactions in a disk dust–gas mixture. Free electrons and ions are created (solid arrows) by the nonthermal ionizations sources and removed from the gas-phase by gas-phase recombination (dotted arrows) and the adsorption onto dust particles (double line arrows). Some ion species can react with neutral gas particles to create different species of ions (dashed arrows). Since dust particles interact with free electrons and ions, they can be charged themselves. The abundance of all charge carriers is determined by the balance between all these reactions. Figure taken from Okuzumi [163].

ion species is assumed to be the molecular ion HCO^+, with mass $m_i = 29\,m_H$ and rate coefficient for the gas-phase recombination $k = 2.4 \times 10^{-7}\,(T/300\,K)^{-0.69}\,cm^3.s^{-1}$ [see 231]. This choice reflects the fact that CO is the most abundant molecule after H_2. It is worth noting that the choice of the dominant ion species does not strongly affect the outcome of the semi-analytical chemical model as long as the dominant ion species in the disk are molecular ions that recombine with free electrons dissociatively, and therefore at similar recombination rates [e.g., 232]. One should note that atomic metal ion species that can desorb from the dust particles (e.g., Mg^+) are ignored for simplicity here (it implicitly means that all metal elements are assumed locked into grains). In reality, they are the dominant ion species for $r \lesssim$ 1–5 au rather than molecular ion species such as HCO^+. Their implementation might slightly impact the results of this thesis, but only for the very inner regions of the disk [e.g., 200]. Similarly, the dominant ion species are NH_x^+ (with $x = 1, 2, 3$) for the very outer regions of the disk with temperatures below 25 K (CO freeze-out). Their inclusion might sightly impact the results of this thesis, but only for the very outer regions of the disk. Since this thesis focuses on the bulk of the protoplanetary disk, these are not major problems in practice.

The key parameter in the semi-analytical chemical model is the dimensionless parameter, Γ, that measures the ratio of the electrostatic attraction or repulsion energy between a charged dust particle and an incident ion or free electron, respectively, to the thermal kinetic energy. It is defined as

$$\Gamma = \frac{\left(-\langle Z \rangle\, e^2/a_{dust,rep}\right)}{k_B T} = \frac{-\langle Z \rangle\, \lambda_O}{a_{dust,rep}} = \frac{-\langle Z \rangle}{\tau}. \tag{113}$$

In the first equality, $\langle Z \rangle$ is the mean charge carried by dust particles at a given location in the disk (r, z), and λ_O is given by $\lambda_O = e^2/k_B T$; with e the elementary charge, and T the gas temperature. In the second equality, the dimensionless parameter τ is given by $\tau = a_{dust,rep}/\lambda_O$. Here $a_{dust,rep}$ corresponds to the representative grain size of the dust distribution at location (r, z) of the protoplanetary disk and time t of its evolution. It reads

$$a_{dust,rep}(t, r, z) = \frac{1}{n_{dust,tot}(t, r, z)} \sum_a a\, n_{dust}(t, r, z, a), \tag{114}$$

with $n_{dust}(t, r, z, a)$ the dust number density for each grain species of size a defined in Eq. (95), and $n_{dust,tot}(t, r, z)$ the total dust number density (accounting for all grain species) defined in Eq. (96). In the simple case of a mono-disperse grain size distribution[8] (i.e., all the grains in the disk are of same size a_{dust}), $a_{dust,rep} = a_{dust}$. One should note that the representative grain size is related to the total grain size per unit volume called "C_{tot}" in [164, 165, 199]. Indeed, one can write $a_{dust,rep} = C_{tot}/n_{dust,tot}$.

The forms of the effective collision cross-sections between ions/dust particles $(\sigma_{d\leftrightarrow i}(\Gamma))$ and free electrons/dust particles $(\sigma_{d\leftrightarrow e}(\Gamma))$ need to be further specified to

---

8 single grain size assumption

properly account for grain surface chemistry. Without loss of generality, they can be written as

$$\sigma_{d\leftrightarrow i}(\Gamma) = s_i \sigma_{dust,rep} P_i(\Gamma), \tag{115}$$

and

$$\sigma_{d\leftrightarrow e}(\Gamma) = s_e \sigma_{dust,rep} P_e(\Gamma), \tag{116}$$

where s_i and s_e are the sticking coefficients for ions and free electrons, respectively. One should note that $s_i = 1$ is used everywhere across this thesis, whereas $s_e = 0.3$ is used for Chapter 4 and $s_e = 0.6$ is used for Chapters 5 and 6. $P_i(\Gamma)$ and $P_e(\Gamma)$ are dimensionless factors determined by the electrostatic interactions between ions/dust particles and free electrons/dust particles, respectively (see below for their definition). $\sigma_{dust,rep}$ is the representative grain geometric cross-section of the dust distribution at location (r, z) of the protoplanetary disk and time t of its evolution. It reads

$$\sigma_{dust,rep}(t, r, z) = \frac{1}{n_{dust,tot}(t, r, z)} \sum_a \pi a^2 n_{dust}(t, r, z, a), \tag{117}$$

with $n_{dust}(t, r, z, a)$ and $n_{dust,tot}(t, r, z)$ defined in Eq. (95) and Eq. (96), respectively. In the simple case of a mono-disperse grain size distribution of size a_{dust}, $\sigma_{dust,rep} = \pi a_{dust}^2$. One should note that the representative grain geometric cross-section is related to the total grain surface area called "A_{tot}" in [164, 165, 199]. Indeed, one can write $\sigma_{dust,rep} = A_{tot}/n_{dust,tot}$. It is important to understand that what truly matters for the ionization chemistry are the quantities C_{tot} and A_{tot}. The dust mainly affects the ionization chemistry (hence the MRI-driven turbulence) by A_{tot}, and weakly by C_{tot}.

In this thesis, dust particles are considered compact. I thus need to account for their induced electric polarization forces. Since free electrons collide with neutral grains much faster, hence more frequently than ions [e.g., 74, 233], one can assume that grains are negatively charged (i.e., $\langle Z \rangle < 0$, hence $\Gamma > 0$). Consequently, $P_i(\Gamma)$ and $P_e(\Gamma)$ are functions of Γ that can be written as

$$P_i(\Gamma) = (1 + \Gamma) \left(1 + \sqrt{\frac{2}{\tau (1 + 2\Gamma)}} \right) \tag{118}$$

and

$$P_e(\Gamma) = \exp\left(-\frac{\Gamma}{1 + (\tau\Gamma)^{-\frac{1}{2}}} \right) \left(1 + \sqrt{\frac{1}{\tau (4 + 3\Gamma)}} \right)^2, \tag{119}$$

where Eqs. (118) and (119) are directly obtained from Eqs. (3.4) and (3.5) of Draine and Sutin [228], respectively (see Sect. 3.4.2 for further details).

For a successful implementation of ionization chemistry in protoplanetary disks, charge neutrality needs to be reached at every location[9]

$$n_i(t, r, z) - n_e(t, r, z) + \int_{Z_{min}}^{Z_{max}} Z\, n_{dust}(t, r, z, Z)\, dZ = 0, \tag{120}$$

---

[9] implied by non-relativistic MHD theory as seen in Sect. 2.1.1

where n_i is the total number density of ions, n_e is the total number density of free electrons, and $n_{dust}(t, r, z, Z)$ is the number density of dust particles of net charge Z at location (r, z) of the protoplanetary disk and time t of its evolution.

For $\tau \gtrsim 1$, the ionization–recombination equilibrium grain charge distribution can be well approximated by a Gaussian distribution resulting in (see Sect. 3.4.2 for further details)

$$n_{dust}(t, r, z, Z) = \frac{n_{dust,tot}(t, r, z)}{\sqrt{2\pi \langle \Delta Z^2 \rangle}} \exp \left[-\frac{(Z - \langle Z \rangle)^2}{2 \langle \Delta Z^2 \rangle} \right], \tag{121}$$

where $n_{dust,tot}(t, r, z) = \int_{Z_{min}}^{Z_{max}} n_{dust}(t, r, z, Z) \, dZ$ is the same as Eq. (96). The mean grain charge $\langle Z \rangle$ is defined as

$$\langle Z \rangle = \frac{1}{n_{dust,tot}(t, r, z)} \int_{Z_{min}}^{Z_{max}} Z \, n_{dust}(t, r, z, Z) \, dZ = -\Gamma \tau, \tag{122}$$

and the grain charge dispersion $\sqrt{\langle \Delta Z^2 \rangle}$ is defined as

$$\left(\sqrt{\langle \Delta Z^2 \rangle} \right)^2 = \frac{1}{n_{dust,tot}(t, r, z)} \int_{Z_{min}}^{Z_{max}} (Z - \langle Z \rangle)^2 \, n_{dust}(t, r, z, Z) \, dZ \tag{123}$$

A complete expression of the previous equation is given by the following (see Sect. 3.4.2 for further details)

$$\left(\sqrt{\langle \Delta Z^2 \rangle} \right)^2 = \tau \left[\frac{2\Gamma\tau + 3\sqrt{\Gamma\tau}}{2 \left(\sqrt{\Gamma\tau} + 1 \right)^2} + \frac{1}{\Gamma + 1} \right.$$
$$- \frac{\sqrt{2}}{(2\Gamma + 1) \left((2\Gamma + 1)\sqrt{\frac{\tau}{2\Gamma+1}} + \sqrt{2} \right)}$$
$$\left. + \frac{3}{(3\Gamma + 4)^2 \sqrt{\frac{1}{3\Gamma+4}} \left(\sqrt{\frac{1}{3\Gamma+4}} + \sqrt{\tau} \right)} \right]^{-1}. \tag{124}$$

Since the grain charge distribution is solely parameterized by Γ, n_i and n_e can be written as a function of that single parameter in the ionization–recombination equilibrium state. Specifically, the balance between ionization and recombination yields (see Sect. 3.4.2 for further details)

$$n_i = \frac{2\zeta n_{gas}}{s_i u_i \sigma_{dust,rep} n_{dust,tot}} \frac{1}{P_i(\Gamma) \left(1 + \sqrt{1 + 2g(\Gamma)} \right)} \tag{125}$$

and

$$n_e = \frac{2\zeta n_{gas}}{s_e u_e \sigma_{dust,rep} n_{dust,tot}} \frac{1}{P_e(\Gamma) \left(1 + \sqrt{1 + 2g(\Gamma)} \right)}, \tag{126}$$

where

$$g(\Gamma) = \frac{2k\zeta n_{gas}}{s_i u_i s_e u_e \left(\sigma_{dust,rep} n_{dust,tot}\right)^2} \frac{1}{P_i(\Gamma) P_e(\Gamma)}. \tag{127}$$

If $g(\Gamma) \gtrsim 1$ the recombination process is dominated by gas-phase recombination; otherwise, it is dominated by charge adsorption onto grains. k is the rate coefficient for the gas-phase recombination defined above, ζ is the total ionization rate determined by Eq. (104), n_{gas} is the total number density of gas particles given by Eq. (67), and u_i, u_e are the mean thermal velocities of the dominant ion species and free electrons, respectively, given by $u_{i(e)} = \sqrt{8k_B T/\pi m_{i(e)}}$ with m_i being the mass of the dominant ion species define above and m_e the electron mass.

The only remaining unknown of the problem is the key parameter Γ. Equation (120) with Eqs. (122), (125), and (126) leads to the following equation whose root is Γ:

$$\frac{1}{P_i(\Gamma)} - \left[\frac{s_i u_i}{s_e u_e} \frac{1}{P_e(\Gamma)} + \frac{\Gamma}{\Theta} \frac{\left(1 + \sqrt{1 + 2g(\Gamma)}\right)}{2} \right] = 0, \tag{128}$$

where Θ is a dimensionless parameter that quantifies which of the free electrons and dust particles are the dominant carriers of negative charge. It is defined by

$$\Theta = \frac{\zeta n_{gas} \lambda_O}{s_i u_i \sigma_{dust,rep} a_{dust,rep} n_{dust,tot}^2}. \tag{129}$$

To summarize, the abundance of all mobile charge carriers in the protoplanetary disk are written as analytical functions of the single key parameter Γ. By numerically solving Eq. (128) with the classic Brent's method (see Brent [234] for the original description of the algorithm and Press [235] for a more recent description), one can obtain Γ and thus those abundances. In Sect. 3.4.3, I check the validity of the outcome from the semi-analytical chemical model by comparing to the outcome of a commonly used chemical reaction network.

3.4.2 *Derivation of the equations for the dust–gas charge reaction equilibrium*

In this section, I derive the equations that describe the dust–gas charge reaction ionization–recombination equilibrium, Eqs. (121)–(126). I follow the derivation by Okuzumi [163], but take the induced polarization force between ions/free electrons with charged grains into account since I assume the dust particles to be compact rather than fluffy. I begin with the equations describing the time evolution of n_i and n_e due to ionization of molecular hydrogen (H_2) and helium (He) at rate ζ producing ions and free electrons at volumetric rate ζn_{gas} (first term in the two equations below), and recombination onto the grains (second term in the two equations below) or in the gas-phase (third term in the two equations below):

$$\frac{dn_i}{dt} = \zeta n_{gas} - s_i u_i \sigma_{dust,rep} n_{dust,tot} P_i n_i - k n_i n_e, \tag{130}$$

$$\frac{dn_e}{dt} = \zeta n_{gas} - s_e u_e \sigma_{dust,rep} n_{dust,tot} P_e n_e - k n_i n_e, \tag{131}$$

where $P_{i(e)}$ is the effective cross-section averaged over grain charge Z and normalized by $s_{i(e)}\sigma_{dust,rep}$,

$$P_{i(e)} = \langle \tilde{J}_{i(e)}(Z) \rangle, \tag{132}$$

with $\tilde{J}_{i(e)}$ being the normalized effective cross sections for grains of charge Z and the brackets denote an average over Z. Accounting for the induced polarization forces and assuming $Z < 0$ (see previous section), I use Eqs. (3.4) and (3.5) of Draine and Sutin [228] and obtain

$$\tilde{J}_i = \left(1 - \frac{Z}{\tau}\right)\left(1 + \sqrt{\frac{2}{\tau - 2Z}}\right), \tag{133}$$

$$\tilde{J}_e = \exp\left(\frac{Z/\tau}{1 + (-Z)^{-\frac{1}{2}}}\right)\left(1 + \sqrt{\frac{1}{4\tau - 3Z}}\right)^2. \tag{134}$$

In comparison, one should note that Okuzumi [163] adopted $\tilde{J}_i = 1 - Z/\tau$ and $\tilde{J}_e = \exp(Z/\tau)$ for $Z < 0$ by neglecting the induced polarization forces, as the author was considering fluffy grains.

Assuming local ionization–recombination equilibrium means that $dn_i/dt = 0$ and $dn_e/dt = 0$. Equations (130) and (131) thus reduce to two algebraic equations for n_i and n_e that can be easily solved to yield Eqs. (125) and (126) [see 163, for a similar calculation].

Furthermore, the ionization–recombination equilibrium grain charge distribution is derived by following the Appendix of Okuzumi [163] and writing down the detailed balance equation

$$s_i u_i n_i \tilde{J}_i(Z) n_{dust}(Z) = s_e u_e n_e \tilde{J}_e(Z+1) n_{dust}(Z+1). \tag{135}$$

The grain charge distribution satisfies $\sqrt{\langle \Delta Z^2 \rangle} \gtrsim 1$ for $\tau \gtrsim 1$, and hence can be viewed as a continuous function of Z. In this case, $\tilde{J}_e(Z+1) \approx \tilde{J}_e(Z)$ and $n_{dust}(Z+1) \approx n_{dust}(Z) + dn_{dust}/dZ$. Consequently, Eq. (135) approximately reduces to

$$\frac{dn_{dust}(Z)}{dZ} + W(Z)n_{dust}(Z) = 0, \tag{136}$$

with

$$W(Z) = 1 - \frac{s_i u_i n_i \tilde{J}_i(Z)}{s_e u_e n_e \tilde{J}_e(Z)}. \tag{137}$$

To derive an approximate solution for Eq. (136), Z_0 is defined such that $W(Z_0) = 0$ (i.e., $s_i u_i n_i \tilde{J}_i(Z_0) = s_e u_e n_e \tilde{J}_e(Z_0)$) and $\delta Z = Z - Z_0$. To the first order in δZ, one has

$$
\begin{aligned}
W(Z) &\approx -\frac{s_i u_i n_i}{s_e u_e n_e}\frac{d}{dZ_0}\left(\frac{\tilde{J}_i(Z_0)}{\tilde{J}_e(Z_0)}\right)\delta Z \\
&= -\frac{\tilde{J}_e(Z_0)}{\tilde{J}_i(Z_0)}\frac{d}{dZ_0}\left(\frac{\tilde{J}_i(Z_0)}{\tilde{J}_e(Z_0)}\right)\delta Z \\
&= -\left(\frac{d\ln\tilde{J}_i(Z_0)}{dZ_0} - \frac{d\ln\tilde{J}_e(Z_0)}{dZ_0}\right)\delta Z.
\end{aligned}
\tag{138}
$$

With Eq. (138), one can solve analytically Eq. (136). This yields $n_{dust}(Z)$ to be the Gaussian distribution given by Eq. (121), with average $\langle Z \rangle = Z_0$ and variance

$$\left(\sqrt{\langle \Delta Z^2 \rangle} \right)^2 = - \left(\frac{d \ln \tilde{J}_i(\langle Z \rangle)}{d \langle Z \rangle} - \frac{d \ln \tilde{J}_e(\langle Z \rangle)}{d \langle Z \rangle} \right)^{-1}. \tag{139}$$

By approximating $\tilde{J}_{i(e)}(\langle Z \rangle) \approx \langle \tilde{J}_{i(e)}(Z) \rangle = P_{i(e)}$ and using $\langle Z \rangle = -\Gamma \tau$, the expression seen in Eq. (124) for the grain charge dispersion $\sqrt{\langle \Delta Z^2 \rangle}$ can be obtained.

3.4.3 *Semi-analytical chemical model validation*

In this section, the goal is to validate the semi-analytical chemical model by comparing with a chemical reaction network. Particularly, I use the chemical reaction network from Umebayashi and Nakano [236] where the following charged species are included: free electrons, five ion species (H^+, H_3^+, HCO^+, He^+, and C^+) and charged grains. Among these, HCO^+ represents heavy molecular ion species (e.g., H_3O^+) that recombine with free electrons dissociatively, and therefore at similar recombination rates. I neglect atomic metal ion species, assuming that all metal elements are locked into grains. The grains are allowed for a discrete charge distribution $Z \in [Z_{min}, Z_{max}]$ with $Z_{min} = \lfloor \langle Z \rangle - 4\sqrt{\langle \Delta Z^2 \rangle} \rfloor$ and $Z_{max} = \lceil \langle Z \rangle + 4\sqrt{\langle \Delta Z^2 \rangle} \rceil$, where $\langle Z \rangle$ and $\sqrt{\langle \Delta Z^2 \rangle}$ are the mean grain charge and the grain charge dispersion predicted from the semi-analytical model given by Eqs. (122) and (124), respectively. The radial and vertical profiles for the temperature, gas and dust densities as well as the total ionization rate are taken from the equilibrium solution obtained for the fiducial model of Chapter 4.

I calculate the abundances of the various charged species in local ionization–recombination equilibrium for $0 \leqslant z/H_{gas} \leqslant 5$, at $r = 5$ au and $r = 100$ au. Figure 15 shows the results of the chemical network calculations where the vertical profiles of the free electron abundance, total ion abundance, and the abundances of individual ion species are plotted. The results show that the dissociatively recombining molecular ions HCO^+ are the dominant ions at all locations in the disk, except in the upper layers ($z \gtrsim 4\,H_{gas}$) of the disk outer regions. In such high-altitude regions, though, the gas density is so low that it does not impact the results of this thesis ($\bar{\alpha}$ is a pressure-weighted vertically averaged quantity). Consequently, the assumption that HCO^+ is the dominant ion species in most of the protoplanetary disk is a good approximation. Figure 15 also displays the free electron and total ion abundances from the semi-analytical chemical model. At $r = 5$ au (resp. $r = 100$ au), the semi-analytical calculations are in good agreement with the chemical reaction network for all $z \lesssim 5\,H_{gas}$ (resp. $z \lesssim 4\,H_{gas}$). At $r = 100$ au and for $z \approx 4\,H_{gas}$, the semi-analytical calculations slightly underestimate the free electron and total ion abundances, since the slowly recombining ion species H_3^+ and C^+ become as important as the fast recombining HCO^+. However, the relative error between the outcome of the chemical reaction network and the semi-analytical chemical model is no larger than 40%. This discrepancy becomes larger for $4 < z/H_{gas} \lesssim 5$ because HCO^+ are no longer the dominant ions species. In these regions, the semi-analytical calcula-

tions can underestimate the free electron and total ion abundances up to a factor of ≈ 5 (at $z = 5\,H_{gas}$). Nevertheless, the gas density is very low there, which means that the results of this thesis are not sensitive to this discrepancy ($\bar{\alpha}$ is a pressure-weighted vertically averaged quantity).

3.5   MRI-DRIVEN TURBULENCE

The mass and angular momentum transport of weakly ionized protoplanetary disks is governed by MRI magnetic torques only if the coupling between the mobile charged particles in the gas-phase and the magnetic field is sufficient; namely, the gas motion induced by those torques can generate magnetic stresses (due to orbital shear) faster than they can diffuse away due to nonideal MHD effects. Now that the abundance of all mobile charge carriers in the protoplanetary disk have been derived, the last step is to compute the MRI-driven turbulence that will be encoded into the effective disk viscosity parameter $\bar{\alpha}$ (Eq. 77). To do so, one needs to know where the MRI can operate in the protoplanetary disk, to link the MRI stress to the disk turbulence state, and to specify the magnetic field strength and topology.

3.5.1   *Criteria for active MRI*

The turbulence that the MRI can induce depends on, first of all, if a certain region of the protoplanetary disk is unstable to the MRI. As I discussed in Sect. 2.1.4, there are three nonideal MHD effects that can modify the evolution of the magnetic field in the protoplanetary disk, hence the behavior of the MRI: Ohmic resistivity, ambipolar diffusion, and the Hall effect. Their strength are encoded into their respective magnetic diffusivity. Mathematically speaking, the expressions of the magnetic diffusivities given in Eq. (40) are valid *only when* the mobile charged particles are exclusively free electrons and ions. In Sect. 2.1.4, I deliberately omitted the presence of charged grains from the dust component of the protoplanetary disk as other mobile charged carriers. I did so to provide the eager reader the basic nature of the MRI, and show how the nonideal MHD effects arising in weakly ionized gas can modify its behavior. Considering the dust component of the protoplanetary disk complicates the picture depicted until now, since dust can impact the gas ionization degree (Sect. 3.4) and charged grains can contribute to the current density (they are mobile charged particles affected by the Lorentz force density).

Taking now into account all the mobile charged carriers present in the disk (free electrons, ions and charged grains), the general expressions for the Ohmic, ambipolar and Hall magnetic diffusivities that go into the nonideal induction equation (Eq. 39) and are used in this thesis are respectively given by [e.g., 74]

$$\eta_O = \frac{c^2}{4\pi\sigma_O}, \qquad \eta_{AD} = \frac{c^2}{4\pi\sigma_\perp}\frac{\sigma_P}{\sigma_\perp} - \eta_O, \qquad \eta_H = \frac{c^2}{4\pi\sigma_\perp}\frac{\sigma_H}{\sigma_\perp}, \qquad (140)$$
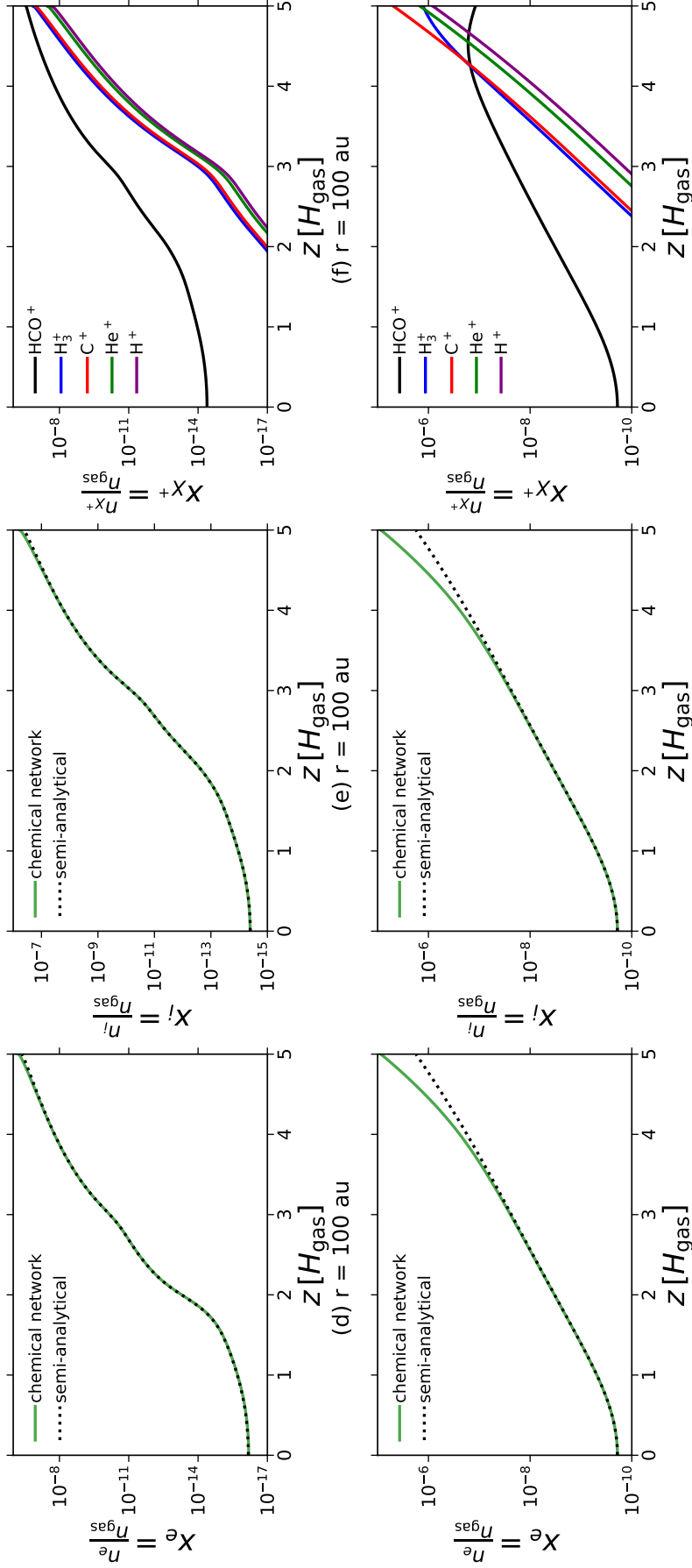
Figure 15: Comparison between the semi-analytical chemical model and a chemical reaction network, for the fiducial model of Chapter 4. The panels show various species abundances as a function of height, z, at $r = 5$ au and $r = 100$ au (upper and lower rows, respectively). *Left Panels*: Free electron abundance from the chemical reaction network (solid green lines) and the semi-analytical chemical model (dotted black lines). *Central Panels*: Total ion abundance from the chemical reaction network (solid green lines) and the semi-analytical chemical model (dotted black lines). *Right Panels*: Abundances of individual ion species from the chemical reaction network. The solid black line corresponds to HCO$^+$, the solid blue line to H$_3^+$, the solid red line to C$^+$, the solid green line to He$^+$, and the solid purple line to H$^+$.

where $\sigma_\perp = \sqrt{\sigma_H^2 + \sigma_P^2}$, and the Ohmic, Hall and Perdersen conductivities are respectively [e.g., 74]

$$\sigma_O = \frac{ec}{B}\sum_j n_j |Z_j| \beta_j, \qquad \sigma_H = -\frac{ec}{B}\sum_j \frac{n_j Z_j \beta_j^2}{1+\beta_j^2}, \qquad \sigma_P = \frac{ec}{B}\sum_j \frac{n_j |Z_j| \beta_j}{1+\beta_j^2}. \quad (141)$$

Here the summation goes over all mobile charged species (free electrons $j = e$, ions $j = i$, and grains $j = \mathrm{dust}$). One should note that the Hall conductivity depends on the sign of the charge of species j, Z_j, whereas the Ohmic and Pedersen conductivities are always positive. β_j is the Hall parameter for mobile charged species j defined in Eq. (30), with $\beta_e \gg \beta_i \gg \beta_{\mathrm{dust}}$. As seen in Sect. 2.1.3, the Hall parameter for a charged particle j depends on the neutral drag coefficient γ_j (Eq. 29), which in turn depends on $\langle \sigma v \rangle_{j \leftrightarrow n}$. In this thesis, I adopt the formulation from Draine [237] (see their Table 2.1 and Eq. 2.34), Bai [112] (see their Eq. 15), and Wardle and Ng [238] (see their Eq. 21); respectively for $\langle \sigma v \rangle_{i \leftrightarrow n}$, $\langle \sigma v \rangle_{e \leftrightarrow n}$, and $\langle \sigma v \rangle_{\mathrm{dust} \leftrightarrow n}$:

$$\langle \sigma v \rangle_{i \leftrightarrow n} = 2.0 \times 10^{-9} \sqrt{\frac{m_H}{\delta}} \, \mathrm{cm}^3.\mathrm{s}^{-1}, \quad (142)$$

$$\langle \sigma v \rangle_{e \leftrightarrow n} = 8.3 \times 10^{-9} \times \max\left[1, \sqrt{\frac{T}{100\,\mathrm{K}}}\right] \mathrm{cm}^3.\mathrm{s}^{-1} \quad (143)$$

and

$$\langle \sigma v \rangle_{\mathrm{dust} \leftrightarrow n} = \sigma_{\mathrm{dust,rep}} \sqrt{\frac{128 k_B T}{9\pi m_n}}, \quad (144)$$

where $\delta = m_i m_n / (m_i + m_n)$ is the reduced mass in a typical ion-neutral collision, T is the gas temperature defined in Sect. 2.2, and $\sigma_{\mathrm{dust,rep}}$ is the representative grain geometric cross-section of the dust distribution defined in Sect. 3.4 (Eq. 117). One should note that a dust mass is needed to compute the dust Hall parameter. In general, the dust component of the protoplanetary disk is made of grains following a size distribution. I thus assume that the dust mass needed to compute the dust Hall parameter is the representative dust mass of the dust distribution. At location (r, z) of the protoplanetary disk and time t of its evolution, it reads

$$m_{\mathrm{dust,rep}}(t, r, z) = \frac{1}{\rho_{\mathrm{dust,tot}}(t, r, z)} \sum_a \frac{4}{3}\pi \rho_{\mathrm{bulk}} a^3 \rho_{\mathrm{dust}}(t, r, z, a), \quad (145)$$

where $\rho_{\mathrm{dust}}(t, r, z, a)$ is the dust volume density for each grain species of size a defined in Eq. (93), and $\rho_{\mathrm{dust,tot}}(t, r, z)$ is the total dust volume density (accounting for all grain species) defined in Eq. (94). In the simple case of a mono-disperse grain size distribution of size a_{dust}, $m_{\mathrm{dust,rep}} = \frac{4}{3}\pi \rho_{\mathrm{bulk}} a_{\mathrm{dust}}^3$. It is worth noting that the definition of $m_{\mathrm{dust,rep}}$ does not really matter here. This is because the dust Hall parameter is actually quasi-independent of it when the grain mass is much larger than the mass of the neutral gas particles (m_n), which is always the case for any grains of size $a \geqslant 0.1\,\mu\mathrm{m}$ (minimum grain size considered in this thesis).

The strength of the nonideal MHD effects, the magnetic diffusivities, can be conveniently measured in dimensionless quantities called the Elsasser numbers. The Elssaser numbers for Ohmic resistivity, ambipolar diffusion, and the Hall effect are defined respectively as

$$\Lambda = \frac{v_{Az}^2}{\eta_O \Omega_K}, \tag{146}$$

$$Am = \frac{v_A^2}{\eta_{AD} \Omega_K}, \tag{147}$$

and

$$\chi = \frac{v_A^2}{|\eta_H| \Omega_K}. \tag{148}$$

The total Alfvén velocity, v_A, is defined as

$$v_A = \frac{B}{\sqrt{4\pi\rho_{gas}}} \tag{149}$$

and $v_{Az} = B_z/\sqrt{4\pi\rho_{gas}}$ is its vertical component. B_z corresponds to the strength of the vertical component of the magnetic field, and B is its r.m.s. strength. These two quantities are not independent, and numerical simulations show a correlation between them as I will discuss in the next section. One should note that the Elsasser numbers are determined by both the detailed microphysics of the disk and the r.m.s. magnetic field strength through their corresponding magnetic diffusivities and the Alfvén velocity.

With the Elssaser numbers, I can now explain how the nonideal MHD effects impact the MRI, accounting for the dust component of the protoplanetary disk. Ohmic resistivity can suppress the MRI entirely by decoupling the magnetic field from the mobile charged carriers. Numerical simulations [e.g., 239, 240] show that it does *not* suppress the MRI if

$$\Lambda > 1. \tag{150}$$

It expresses the requirement that for the MRI to operate, the MRI growth rate must be larger than the diffusion caused by Ohmic resistivity [e.g., 241]. The growth rate of the fastest growing mode is $\sim \Omega_K$ and the wavenumber of that mode is $k \sim \Omega_K/v_{Az}$ [e.g., 242]. From the nonideal induction equation (Eq. 39), the diffusion rate of this wavenumber k due to Ohmic resistivity is $\sim \eta_O k^2$. The comparison of the two rates yields Eq. (150). One should note that the dependence on the vertical component of the Alfvén velocity v_{Az} (hence B_z) rather than the total velocity v_A (hence B) comes from the fact that Ohmic resistivity affects smaller lengthscale perturbations most easily. In a thin protoplanetary disk (assumption that is used in this thesis), those are in the vertical direction [e.g., 240]. A region where Ohmic resistivity suppresses the MRI, and thus the condition (150) is *not* satisfied (i.e., $\Lambda \leqslant 1$), is called a "dead zone". Since all the mobile charged carriers are included here, the notion of dead zone is an extension of the classical dead zone by Gammie [118] (see Sect. 2.1.4).

Ambipolar diffusion can also suppress the MRI. A similar criterion to the above has been investigated using the ambipolar Elssaser number. Wardle [243] argued that an appropriate criterion for efficient MRI when ambipolar diffusion dominates should mirror Eq. (150), namely Am > 1. When free electrons and ions are the only mobile charged carriers, the latter conditions reduces to $\gamma_i \rho_i / \Omega_K > 1$, where γ_i is the drag coefficient between ions and neutrals (Eq. 29) and $\rho_i = n_i m_i$ the ion volume density. Such a condition would then mean that ambipolar diffusion does *not* suppress the MRI if ions and neutrals collide a least once per orbit. However, Hawley and Stone [244] suggested that Am > 1 is too lenient. Their 3D local shearing-box simulations, using an idealized two-fluid approach (ions and neutrals, where ionization and recombination are not considered), indicates that the efficient MRI with ambipolar diffusion requires much more frequent collisions between ions and neutrals ($\gamma_i \rho_i / \Omega_K \gtrsim 100$). However, as I already mentioned in Sect. 2.1, the single-fluid approach is used in this thesis. In this context, Bai and Stone [113] have showed that the MRI can still operate even though Am < 1, provided that the magnetic pressure is sufficiently weak compared to the gas pressure. Let us now introduce the plasma-β parameter, defined as the ratio between the gas pressure $P_{gas} = \rho_{gas} c_s^2$ and the r.m.s. magnetic pressure $P_B = B^2/8\pi$, with B the r.m.s. magnetic field strength. It reads

$$\beta = \frac{P_{gas}}{P_{magnetic}} = \frac{8\pi \rho_{gas} c_s^2}{B^2} \tag{151}$$

The MRI is *not* suppressed by ambipolar diffusion if

$$\beta > \beta_{min}(Am). \tag{152}$$

The minimum threshold β_{min} is a function of the ambipolar Elsasser number given by [113]

$$\beta_{min}(Am) = \sqrt{\left(\frac{50}{Am^{1.2}}\right)^2 + \left(\frac{8}{Am^{0.3}} + 1\right)^2}. \tag{153}$$

One should note that $\lim_{Am \to +\infty} \beta_{min}(Am) = 1$, which is a requirement for magnetic tension not to be too strong so that the gas motion can bend the magnetic field lines. The fact that $\beta \gg 1$ when the MRI operates thus imposes that $c_s \gg v_A/2$, which is why one can link the α-disk model to MHD turbulence as it was done in Sect. 2.2. A region where ambipolar diffusion suppresses the MRI, and thus the condition (152) is *not* satisfied (i.e., $\beta \leqslant \beta_{min}(Am)$), is called a "zombie zone" following Mohanty, Ercolano, and Turner [229]. For the single-fluid (of neutrals) approach to be valid, it is required that the density of free electrons and ions be much lower than the density of neutrals, and that the recombination timescales t_{rcb} be much shorter than the dynamical timescale t_{dyn} (see Sect. 2.1.2). When complex chemical networks are used and dust particles are abundant, Bai and Stone [113] showed that this approach is valid in protoplanetary disks. However, this limit may not always hold in simple chemical models such as the one employed in this thesis, due to the limited number of recombination pathways. I proceed by first assuming

that the single-fluid approach holds, and then check *a posteriori* that it is indeed true (see Sect. 4.5.4).

The non-dissipative Hall effect is also very important for the MRI. A useful way of quantifying the Hall effect, independently of the magnetic field strength, is by introducing the Hall lengthscale defined as

$$l_H = \frac{v_A}{\Omega_K \chi}. \tag{154}$$

When $l_H \gtrsim 0.2 H_{gas}$, Kunz and Lesur [245] found that the Hall effect severely changes the MRI activity in protoplanetary disks. The impact of the Hall effect on the MRI, however, is very different from Ohmic resistivity and ambipolar diffusion as I discussed in Sect. 2.1.4. In the presence of a net magnetic field, the Hall effect depends on whether the field is aligned or anti-aligned with the rotation axis of the disk. In the aligned case, the Hall effect does not directly modify the MRI, but rather generates a new MHD instability called the Hall Shear instability (HSI). Unlike the MRI, the HSI does not depend on the Coriolis force, and is indifferent to the sign of the angular velocity gradient. It has been shown that it reactivates the dead zone by producing large-scale and ordered magnetic fields transporting angular momentum radially with little turbulent motion through laminar shear stresses [e.g., 246–248]. In the anti-aligned case, the Hall effect has been shown to substantially reduce the level of MRI-driven turbulence [e.g., 245, 248–250]. Furthermore, the Hall effect supports a mean-field disk dynamo cycle (it is a battery mechanism) provided the presence of a net magnetic field [e.g, 247]. This behavior is completely different from anything possible with the MRI in its ideal MHD version. It is clear that the impact of the Hall effect on protoplanetary disks is absolutely nontrival, and its exact impact on the MRI-driven turbulence is still under intensive research. I will thus neglect it in this thesis.

Finally I further impose that the fastest growing modes of the MRI must develop in the MRI active layer. This requirement is to ensure that the MRI active layer does not have an infinitesimally small vertical thickness, given the magnetic field strength and topology adopted. In the upper layers of the MRI active layer, the MRI behavior is marginally close to its ideal MHD limit (Am ∼ 1; see Fig. 40a). In this regime, the wavelength of the fastest growing modes is defined as $\lambda_m = 2\pi v_{Az}/\Omega_K$ [e.g., 242]. Here I demand, at each disk radius and each time, that the longest wavelength of the fastest growing modes in the MRI active layer fits within both the vertical gas scale height H_{gas} and the MRI active layer thickness h_{MRI}. At each disk radius and each time, this condition can be mathematically written as

$$\lambda_{MRI}(t, r) \leqslant H_{gas}(t, r) \text{ and } \lambda_{MRI}(t, r) \leqslant h_{MRI}(t, r), \tag{155}$$

where $\lambda_{MRI}(t, r) = \max_{z \in \text{MRI layer}} \left\{ \lambda_m(t, r, z) \right\}$ is the longest wavelength of the fastest growing modes in the MRI active layer, at disk radius r and time t. One should note that h_{MRI} implicitly depends on the r.m.s. magnetic field strength B.

In summary, I use the abundance of all mobile charged carriers n_j (Sect. 3.4) as well as the magnetic field strengths adopted B, B_z (as explained in Sect. 3.5.3) to

compute η_O, η_{AD}, and then Λ, Am, $\beta_{\min}(Am)$ at every locations of the protoplanetary disk. If conditions (150)[10], (152)[11], and (155) are fulfilled at some location in the disk, it is assumed that the MRI can operate there. With these conditions for active MRI, the underlying assumption is that the MRI is either in a saturation level allowed by the nonideal MHD effects considered or completely damped at any locations in the disk. Fundamentally, this assumption comes down to the fact that the MRI growth timescale is short ($\propto \Omega_K^{-1}$) compared to viscous evolution timescales or dust evolution timescales. One should thus note that a zombie zone is qualitatively the same as a dead zone, since in both regions the MRI is fully suppressed.

3.5.2 *From the MRI accretion formulation to MRI-driven turbulence*

A key ingredient that the present global MRI-driven disk accretion model requires is the MRI-induced local disk viscosity parameter α that goes into Eq. (77).

In non-MRI regions (dead or zombie zone), the source of disk viscosity is thought to be mainly from hydrodynamic instabilities that can produce non-MRI turbulent Reynolds shear stress (see Sect. 1.4). The turbulence in all non-MRI regions can thus be encoded into a single hydrodynamic turbulent parameter, α_{hydro}, which depends on the disk location and evolution state in general. Since I do not implement a model to compute such a parameter in a self-consistent way (beyond the scope of this thesis), I assume α_{hydro} to be a constant that is an input parameter of the model. This constant is assumed to be the same across a given non-MRI region regardless of whether the region is a dead or zombie zone. Motivated by the results from 3D global hydrodynamic simulations of the VSI [e.g., 84, 251], which is believed to lead to the highest turbulence from hydrodynamic instabilities, I choose $\alpha_{\mathrm{hydro}} = 10^{-4}$ everywhere in this thesis[12].

In the regions of the disk where the MRI can operate (following our criteria in Sect. 3.5.1), a variety of numerical simulations show that there exists a tight correlation between $T_{r\phi}$ (Eq. 71) and the magnetic pressure, since $T_{r\phi}$ is dominated by the Maxwell shear stress for MRI-driven turbulence [e.g., 252, 253]. This correlation can be represented by

$$T_{r\phi} \approx \frac{P_B}{2}, \tag{156}$$

with $P_B = B^2/8\pi$ the magnetic pressure. Remembering that the MRI-induced local disk viscosity parameter α_{MRI} and $T_{r\phi}$ are connected by Eq. (43), one has

$$\alpha_{\mathrm{MRI}} = \begin{cases} \frac{1}{3\beta} & \text{if } \frac{1}{3\beta} > \alpha_{\mathrm{hydro}} \\ \alpha_{\mathrm{hydro}} & \text{otherwise} \end{cases}. \tag{157}$$

where β is the plasma-β parameter (Eq. 151). One can notice that Eq. (157) displays a condition that depends on α_{hydro}. It is because the MRI-driven turbulence must

---

10 referred to as Ohmic condition in this thesis
11 referred to as ambipolar condition in this thesis
12 expect in Sect. 4.4.5 where I explore the effect of this parameter on the MRI activity

dominate over the hydrodynamic instabilities-driven turbulence in the MRI active regions. If not, such regions are considered as non-MRI regions in the sense that the dominant source of turbulence is not the MRI, even though the set of conditions for active MRI is satisfied.

To summarize, the local disk viscosity parameter α that goes into Eq. (77) is calculated as follows

$$\alpha(t,r,z) = \begin{cases} \alpha_{DZ}(t,r,z) & \text{in the dead zone} \\ \alpha_{ZZ}(t,r,z) & \text{in the zombie zone} \\ \alpha_{MRI}(t,r,z) & \text{in the MRI active layer} \end{cases} \tag{158}$$

with $\forall t,r,z\ \alpha_{DZ}(t,r,z) = \alpha_{ZZ}(t,r,z) = \alpha_{hydro}$, and $\alpha_{MRI}(t,r,z)$ is given by Eq. (157).

3.5.3 *Magnetic field strength*

Once the gas component of the protoplanetary disk is coupled to magnetic field lines (through its mobile charged particles), the strength and topology of the net vertical magnetic field threading the disk become key control parameters to the MHD turbulence driven by the MRI. Indeed, there is ample evidence from numerical simulations that the saturation level of the MRI is controlled by the strength of the net vertical magnetic field [e.g., 122, 195, 207, 254, 255]. The poloidal component of the magnetic flux (hence the poloidal magnetic field) inherited from the molecular cloud during the disk formation can subsequently by advected radially due to accretion of the gas, diffuse relative to the gas due to the nonideal MHD effects, or reconnect if the flux has varying sign across the disk. Nonetheless, such complexities are ignored in the present global MRI-driven disk accretion model, since the details behind the evolution and transport of large-scale magnetic field lines are yet to be fully understood [e.g., 256–261]. I invite the eager reader to go to Sect. 7.2.1 for further discussion about this exciting topic.

In this section, I thus explain how the magnetic field strength and topology is set for the global MRI-driven disk accretion model to be complete. As I showed in Sects. 3.5.1 and 3.5.2, the criteria for the MRI to operate in the protoplanetary disk, the value of the MRI-induced local disk viscosity parameter, all depend on the magnetic field strength. Specifically, the Ohmic condition (Eq. 150) and the ambipolar condition (Eq. 152) are functions of the vertical component of the magnetic field strength B_z as well as the r.m.s. strength B respectively, and the value of α where the MRI operates (Eq. 157) is also a function of the r.m.s. strength B (through the plasma-β parameter). Since I do not solve for the evolution or the generation of magnetic fields here, I make the assumption that

$$B^2 \approx 25B_z^2 \tag{159}$$

(i.e., $\beta \approx \beta_z/25$), which is supported by MRI simulations [e.g., 252]. As a result, it is sufficient to know one to get the other. Here β and β_z are the plasma-β parameters of B and B_z, respectively. Furthermore, I assume the magnetic field to be vertically

constant. This comes from the fact that MRI simulations found the field to be constant with height within the MRI active layer [e.g., 122, 252, 262–266]. It means that, $\forall t, r, z\ B_z(t, r, z) = B_z(t, r, z = 0)$ and $B(t, r, z) = B(t, r, z = 0)$. It is thus enough to know the radial profile of the field at time t to reconstruct it in the plane (r, z). Across the Chapters of this thesis, I will consider three options to compute such radial profiles:

- OPTION A (Chapters 4 and 5). The radial profile of B is numerically constrained by the global MRI-driven disk accretion model itself, such that the MRI activity is at the maximal efficiency as permitted by Ohmic resistivity and ambipolar diffusion. In other words, the r.m.s. magnetic field is found such that it maximizes the accretion rate in the MRI active region ($\dot{M}_{acc, MRI}$) at any disk radii. I use Eq. (24) of Bai [112] to write $\dot{M}_{acc, MRI} \propto h_{MRI}B^2/\Omega$, where h_{MRI} is the MRI active layer thickness and $\Omega \approx \Omega_K$ is the Keplerian angular velocity. This formula is derived assuming that $\alpha \propto \beta^{-1}$, which is the case in this thesis (see Sect. 3.5.2). The goal here is to maximize the quantity $h_{MRI}B^2$ with B as high as possibly allowed for the MRI to still operate, namely β as low as possible while satisfying both Eqs. (150) and (152). One should note that h_{MRI} implicitly depends on B. Since ambipolar diffusion prohibits the MRI-driven turbulence with too strong magnetic fields (see Eqs. 152 and 153), maximizing B alone formally leads to an infinitesimal h_{MRI}, hence $\dot{M}_{acc, MRI} \to 0$. In practice I adopt a similar procedure as described in Mohanty, Ercolano, and Turner [229] to compute the radial profile of B, such that the MRI activity is at the maximal efficiency as permitted by Ohmic resistivity and ambipolar diffusion. For a specified disk radius r, I loop through a range of r.m.s. field strengths $B \in \left[10^{-5} - 10^3\right]$ Gauss, which covers the plausible range in stellar accretion disks. For a given value of that range, I determine the MRI active layer thickness h_{MRI} given the criteria for the MRI to operate. I then check that the longest wavelength of the fastest growing modes in the MRI active layer fits within both the vertical gas scale height (H_{gas}) and the MRI active layer thickness (condition 155). If it does, I compute the quantity $h_{MRI}B^2$. If not, I automatically discard this magnetic field strength value by setting the quantity $h_{MRI}B^2$ to 0. I then reiterate the previous steps for the different field strength values in the range, and finally choose the final value B for this specific disk radius r such that the quantity $h_{MRI}B^2$ is the highest. I repeat the steps above to cover the whole radial extent of the protoplanetary disk, which leads to B as a function of disk radius r. I finally obtain $B(t, r, z)$ by assuming the field to be vertically constant, and then $B_z(t, r, z)$ given Eq. (159). I want to emphasize that such a choice for the magnetic field offers a very optimistic view of the MRI activity which may not be fulfilled in reality.

- OPTION B (Chapters 4 and 6). I assume the vertical plasma-β parameter β_z to have a constant *midplane* component (hence the *midplane* r.m.s. β also constant). It implies that, $\forall t, r\ \beta_z(t, r, z = 0) = \beta_{z,mid}$, where $\beta_{z,mid}$ is a constant

free parameter of the model. The radial profile of B_z is then obtained by remembering that $B_z(t, r, z = 0) = \sqrt{8\pi\rho_{gas}(t, r, z = 0)c_s^2(t, r)/\beta_{z,mid}}$ (rearranging Eq. 151). I finally obtain $B_z(t, r, z)$ by assuming the field to be vertically constant, and then $B(t, r, z)$ given Eq. (159). One should note that $B_z(t, r, z)$ and $B(t, r, z)$ are *not* radially constant and *not* stationary (time-independent) in this case.

- OPTION C (Chapter 6). I assume the radial profile of the vertical component of the magnetic field to be constant. It means that, $\forall t, r$ $B_z(t, r, z = 0) = B_z$, where B_z is a constant free parameter of the model. I finally obtain $B_z(t, r, z)$ by assuming the field to be vertically constant, and then $B(t, r, z)$ given Eq. (159). One should note that $B_z(t, r, z)$ and $B(t, r, z)$ are radially constant and stationary in this case.

STEADY-STATE MRI-DRIVEN ACCRETION

---

*This Chapter is an adapted version of the published research articles **Delage T. N.**, Okuzumi S., Flock M., Pinilla P., & Dzyurkevich N.; "Steady-state accretion in magnetized protoplanetary disks", A&A (2022), vol. 658, A97 [184], and **Delage T. N.**, Gárate M., Okuzumi S., Yang C.C., Pinilla P., Flock M., Stamler S. M., & Birnstiel T.; "The impact of dust evolution on the dead zone outer edge in magnetized protoplanetary disks"; A&A (2023), vol. 674, A190 [185].*

4.1 MOTIVATION

As I discussed in Sect. 2.1, the ideal MHD version (magnetic field perfectly coupled to the gas) of the MRI applies only in the thermally ionized region very close to the star. In most of the protoplanetary disk, though, the gas ionization degree is low and the MRI activity is substantially modified due to the nonideal MHD effects (Sects. 2.1.4 and 3.5.1). In general, quantifying the local turbulence induced by the MRI-driven accretion is a complex problem that significantly depends on the local dust and gas properties, the magnetic field strength, as well as the complex ionization chemistry.

Armed with the global MRI-driven disk accretion model of Chapter 3, we can finally start our adventure toward understanding how the interplay of gas, dust and MRI activity shapes the protoplanetary disk secular evolution in the context of planet formation. Since this interplay has a lot of intricacies, it is obviously not a good idea to directly dive into it. Let us progressively gather the necessary knowledge that will pave the way to a better understanding of this full picture.

The first detour of our adventure is to get an idea about how the MRI activity is shaped by the various protoplanetary disk components (stellar, gas and dust). This is very important if one wants to really understand what physical processes need to be accounted for in order to complement the global MRI-driven disk accretion model. In this Chapter, I thus want to understand better the MRI activity by specifically investigating the case of steady-state MRI-driven accretion. Although simple, this case proves itself invaluable. It allows one to really understand what disk parameters crucially set the MRI activity by varying them one at a time, without falling for the kitchen-sink approach where everything is included but nothing is understood. This is possible because the steady-state accretion involves no evolutionary equations, which is then very fast to solve for. Here I am particularly interested in describing the overall structure of a fiducial steadily MRI-driven accreting disk (turbulence level, gas surface density, ionization level, magnetic field

strength required to satisfy maximal efficiency for the MRI activity, accretion rate, and the dead zone outer edge location), to then conduct a detailed parameter study in order to better quantify the importance of each disk parameters.

4.2   METHOD

Table 2 summarizes all the models considered in this Chapter. Below I present the methodology employed to study steady-state MRI-driven accretion.

4.2.1   *Approach*

In this Chapter, the gas and dust components of the protoplanetary disk are assumed to be in steady-state, namely the gas surface density Σ_{gas} and the dust surface density Σ_{dust} are not evolving in time. It means that the gas and dust transport equations (Eqs. 79 and 92, respectively) as well as the discretized Smoluchowski equation (Eq. 99) are not considered. Furthermore, the stellar bolometric and total X-rays luminosity are also assumed stationary (time-independent). Essentially it implies that, $\forall t \ L_\star(t) = L_\star$ and $L_{XR}(t) = L_{XR}$, where $L_\star$ as well as L_{XR} are constant free parameters of the model.

Here the general methodology is to seek for a steady-state MRI-driven accretion for the gas (i.e., the gas accretion rate is radially constant) using the global MRI-driven disk accretion model described in Chapter 3. To do so I self-consistently solve for the gas surface density through an iterative process (see Sect. 4.2.2), alongside the appropriate effective turbulent parameter $\bar{\alpha}$, to ensure the accretion rate $\dot{M}_{acc}$ to be radially constant in the outer regions of the disk ($r \gtrsim 1$ au). In practice, for each step of the iteration process, I solve the coupled set of equations for both the gas surface density and the MRI-driven turbulence. These equations are coupled because: (1) $\bar{\alpha}$ and $\dot{M}_{acc}$ are constrained by the MRI accretion, which depends on the disk structure; (2) the disk structure in steady-state accretion is determined by $\bar{\alpha}$, $\dot{M}_{acc}$, and stellar parameters. In other words, I derive Σ_{gas} alongside $\bar{\alpha}$ so that they satisfy the equilibrium solution for the steady-state MRI-driven accretion, given the total disk gas mass M_{disk} as well as the dust and stellar properties. Although the detailed procedure is different, one should note that the overall methodology used in this Chapter is similar to the one adopted in Mohanty et al. [267]. In this study the authors focus on regions around the dead zone inner edge ($r < 1$ au) by presenting a semi-analytical steady-state dust-free model in which the disk structure, thermal ionization and the viscosity due to the MRI are determined self-consistently. Among the key differences, the numerical model of this Chapter focuses on regions beyond 1 au (including the dead zone outer edge), includes the relevant nonthermal ionization sources at those locations in the disk, and employs a semi-analytical chemical model to capture the charge state of the disk dust–gas mixture.

In the model, I choose M_{disk} as a free input parameter and self-consistently obtain the corresponding $\dot{M}_{acc}$, rather than choosing $\dot{M}_{acc}$ as the free parameter. This

Model	$M_\star$ [$M_\odot$]	$L_\star$ [$L_\odot$]	M_{disk} [$M_\star$]^a	a_{dust} [μm]	f_{dg}	B & B_z [Gauss]	α_{hydro}	T [K]	a_{min} [μm]	$a_{\mathrm{dist,max}}$ [μm]	$p_{\mathrm{dist,max}}$
Fiducial	1	2	0.05	1	10^{-2}	MRI-optimal	10^{-4}	Thin	–	–	–
I	1	2	Sect. 4.4.1	1	10^{-2}	MRI-optimal	10^{-4}	Thin	–	–	–
II	1	2	0.05	Sect. 4.4.2	10^{-2}	MRI-optimal	10^{-4}	Thin	–	–	–
III	1	2	0.05	1	Sect. 4.4.3.1	MRI-optimal	10^{-4}	Thin	–	–	–
IV	1	2	0.05	1	Sect. 4.4.3.2	MRI-optimal	10^{-4}	Thin	–	–	–
V	1	2	0.05	1	10^{-2}	Sect. 4.4.4	10^{-4}	Thin	–	–	–
VI	1	2	0.05	1	10–2	MRI-optimal	Sect. 4.4.5	Thin	–	–	–
VII	1	2	0.05	1	10^{-2}	MRI-optimal	10^{-4}	Sect. 4.4.6	–	–	–
VIII	Sect. 4.4.7.1	Sect. 4.4.7.1	0.01	1	10^{-2}	MRI-optimal	10^{-4}	Thin	–	–	–
IX	Sect. 4.4.7.2	Sect. 4.4.7.2	0.05	1	10^{-2}	MRI-optimal	10^{-4}	Thin	–	–	–
X	1	2	0.05	–	10^{-2}	MRI-optimal	10^{-4}	Thin	0.1	Sect. 4.4.8	−3.5
XI	1	2	0.05	–	10^{-2}	MRI-optimal	10^{-4}	Thin	Sect. 4.7.1.1	1	−3.5
XII	1	2	0.05	–	10^{-2}	MRI-optimal	10^{-4}	Thin	0.1	1	Sect. 4.7.1.2

Table 2: Summary of the parameters used in each model of this Chapter. Model Fiducial refers to the fiducial model (Sect. 4.3) and Models I–XII correspond to the models of the parameter study conducted (Sect. 4.4). One should note that a_{dust} is only defined for models using the single grain size assumption (Models Fiducial and Models I–IX), whereas a_{min}, $a_{\mathrm{dist,max}}$ and $p_{\mathrm{dist,max}}$ are only defined for the models describing the dust as a power-law grain size distribution (Models X–XII). Furthermore, "Thin" means that the gas temperature model follows Eq. (46), and "MRI-optimal" means that the r.m.s. magnetic field B and the vertical magnetic field B_z are derived following option A of Sect. 3.5.3. Finally, I assume the total stellar X-rays luminosity to follow $L_{\mathrm{XR}} = 10^{-3.5} \times L_\star$. For a detailed description of the various models, see the dedicated sections.

a but for Model VIII of the parameter study, where it is in units of $M_\odot$

choice is particularly interesting if one wants to compare the effective turbulent parameter $\bar{\alpha}$ obtained for a steady-state accretion disk with a disk that would be out of equilibrium but with the same total disk gas mass; or if one wants to compare the equilibrium solutions obtained for different stellar masses, where the total disk gas mass is fixed. Setting either $\dot{M}_{acc}$ or M_{disk} as the free input parameter of the model is equivalent and lead to the same results.

While the steady-state solution describes the inner inward-accreting region ($r \lesssim R_t$) of viscously evolving disks well, it cannot treat the outer viscously expanding region ($r \gtrsim R_t$). Here R_t corresponds to the transition radius at which the gas motion changes from inward to outward in a viscously evolving disk [e.g., 268]. Ignoring this outer region, the steady model underestimates the real total disk gas mass. However, if one regards the outer boundary r_{max} of the disk model as the transition radius R_t, the neglected mass is at worst comparable to the mass within the model[1].

4.2.2   *The equilibrium solution*

In the classical 1D viscous disk model, the steady-state accretion rate can be written as [for a derivation, see Appendix B of 267]:

$$\dot{M}_{acc} = \frac{3\pi c_s^2 \bar{\alpha} \Sigma_{gas}}{f_r \Omega_K} \approx \frac{3\pi c_s^2 \bar{\alpha} \Sigma_{gas}}{\Omega_K}, \tag{160}$$

where $f_r = \left(1 - \sqrt{\frac{R_{in}}{r}}\right)$ comes from the thin boundary-layer condition at the inner edge of the disk, assuming a zero-torque inner boundary condition [e.g., 269]. In the α-disk model, R_{in} is by definition the location where the Keplerian angular velocity Ω_K plateaus and turns over. For instance, if the disk extends up to the stellar surface, $R_{in} = R_\star$ with $R_\star$ the stellar radius. In any case $R_{in} \ll 1\,au$, justifying the second equality in Eq. (160) that I shall use in this Chapter, since I study the structure of the outer disk ($r \gtrsim 1\,au$).

Solving for Σ_{gas} by rearranging Eq. (160), one can obtain the self-consistent steady-state gas surface density under the framework of viscously driven accretion

$$\Sigma_{gas} \approx \frac{\dot{M}_{acc} \Omega_K}{3\pi c_s^2 \bar{\alpha}}. \tag{161}$$

---

1 For instance, the self-similar α-constant disk model has a gas mass distribution given by $M_<(r) = M_{tot,self-similar}[1 - \exp(-r/(2R_t))]$, where $M_<(r)$ is the disk gas mass within disk radius, r, and $M_{tot,self-similar}$ is the total gas mass of the whole self-similar disk [e.g., 268]. For this specific model, the inner inward-accreting region ($r \lesssim R_t$) comprises $\approx 40\%$ of the total disk gas mass. Neglecting the gas mass within the outer viscously expanding region ($r \gtrsim R_t$) thus underestimates the total disk gas mass by only $\approx 60\%$.

When multiplying Eq. (161) by $2\pi r$, integrating over the radius and using the fact that $\dot{M}_{acc}$ is radially constant for steady-state accretion, one can find the relation between the accretion rate and the total disk gas mass M_{disk}

$$\dot{M}_{acc} \approx \frac{3M_{disk}}{2 \int_{r_{min}}^{r_{max}} \frac{r\Omega_K}{\bar{\alpha}c_s^2} \, dr}, \tag{162}$$

where r_{min} and r_{max} are the inner and outer boundary of the radial grid, respectively. Equation (162) is another way of expressing the dependence of the accretion rate on the disk structure. It allows us to compute $\dot{M}_{acc}$ accordingly to the chosen free input parameter M_{disk}, and ensure that the calculated Σ_{gas} is such that $M_{disk} = \int_{r_{min}}^{r_{max}} 2\pi r \Sigma_{gas}(r) \, dr$. Here I want to emphasize that the total disk gas mass M_{disk} is defined as the gas mass enclosed between r_{min} and r_{max}, and does not account for the mass residing beyond the outer boundary r_{max} (M_{disk} is equal to the real total disk gas mass within a factor of two; see Sect. 4.2.1). Once the free input parameter M_{disk} is chosen, I always compute $\dot{M}_{acc}$ using Eq. (162) and Σ_{gas} using Eq. (161), if not stated otherwise.

The steady-state Σ_{gas} and $\bar{\alpha}$ are obtained by iterating through the following steps (those two quantities utterly determine the equilibrium solution):

- Step 1. Compute the accretion rate $\dot{M}_{acc}$ (Eq. 162) for a given fixed total disk gas mass M_{disk} and stellar properties.

- Step 2. Derive the steady-state gas structure by computing the gas surface density Σ_{gas} and by reconstructing the gas volume density distribution ρ_{gas}.

- Step 3. Derive the steady-state dust structure by computing the dust surface density $\Sigma_{dust} = f_{dg}\Sigma_{gas}$, with f_{dg} the vertically integrated dust-to-gas mass ratio being an input parameter of the model, and by reconstructing the dust volume density distribution ρ_{dust}.

- Step 4. Compute the total ionization rate, ζ, as in Sect. 3.3.

- Step 5. Derive the number densities of free electrons, ions, and charged dust particles by using the semi-analytical chemical model described in Sect. 3.4.

- Step 6. Derive the Ohmic and ambipolar magnetic diffusivities (η_O and η_{AD}), and compute their corresponding Elsasser numbers from which a set of conditions for active MRI can be derived as in Sect. 3.5.1.

- Step 7. Derive the local turbulent parameter α by connecting the MRI formulation of accretion to the α-disk model (Eq. 158), and finally compute the effective turbulent parameter $\bar{\alpha}$ (Eq. 77).

After each Step 7, I check that Σ_{gas} and $\bar{\alpha}$ are such that the right-hand side of Eq. (160) is radially constant and equal to $\dot{M}_{acc}$ at any disk radii, which is given by Eq. (162). If not, I keep on iterating from Step 1 to Step 7 with the updated Σ_{gas} and $\bar{\alpha}$ from the previous iteration. The equilibrium solution is reached once the three

following convergence conditions are met for the last 15 consecutive iterations: (1) $\dot{M}_{acc}$ is constant from iteration i-1 to iteration i within a 5% error; (2) the right-hand side of Eq. (160) is radially constant and equal to $\dot{M}_{acc}$ within a 5% error; and (3) Σ_{gas} is constant from iteration i-1 to iteration i within a 5% error.

This iteration process converges toward a solution for the following reason. For a given fixed total disk gas mass, gas temperature profile, stellar properties, and dust properties, $\dot{M}_{acc}$ varies from iteration i-1 to iteration i only if $\bar{\alpha}$ varies (see Eq. 162). Once $\bar{\alpha}$ is constant from iteration i-1 to iteration i, $\dot{M}_{acc}$ becomes constant as well, and so does Σ_{gas} (Eq. 161). In this Chapter (except in Sect. 4.4.4), I constrain and choose the r.m.s. magnetic field strength such that the MRI activity is at the maximal efficiency as permitted by the nonideal MHD effects considered (see option A of Sect. 3.5.3). Consequently, $\bar{\alpha}$ converges through iterations for the steady-state accretion solution that satisfies this condition.

I initially assume that the protoplanetary disk is fully turbulent, and arbitrarily set $\bar{\alpha}$ to be radially constant and equal to $\bar{\alpha}_{init} = 0.1$ (in order to obtain the first $\dot{M}_{acc}$ and Σ_{gas}, required to initiate the iteration process). I have checked that this choice does not affect the equilibrium solutions found in this Chapter.

4.2.3 *Numerical implementation*

The parameters used to run the global MRI-driven disk accretion model of Chapter 3 are taken from Table 1. One should note that the electron sticking coefficient, s_e, is chosen equal to 0.3. If not stated otherwise the fiducial model of this Chapter has the following parameters definition:

- STELLAR PROPERTIES. Stellar mass $M_\star = 1\,M_\odot$, stellar bolometric luminosity $L_\star = 2\,L_\odot$, and total stellar X-rays luminosity $L_{XR} = 10^{-3.5} \times L_\star$.

- GAS PROPERTIES. Total disk gas mass $M_{disk} = 0.05\,M_\star$ (where the relation $M_{disk} \propto M_\star$ is commonly used [e.g., 270, 271]). Furthermore, the gas is assumed vertically isothermal with a radial temperature profile following Eq. (46).

- DUST PROPERTIES. I consider the dust particles as a mono-disperse population of perfect compact spheres of radius $a_{dust} = 1\,\mu m$ (standard ISM value), intrinsic volume density $\rho_{bulk} = 1.4\,g.cm^{-3}$ and mass $m_{dust} = \frac{4}{3}\pi\rho_{bulk}a_{dust}^3$. Furthermore, I assume that $\Sigma_{dust} = f_{dg}\Sigma_{gas}$, with the vertically integrated dust-to-gas mass ratio $f_{dg} = 10^{-2}$ (standard ISM value).

- IONIZATION CHEMISTRY. When the single grain size assumption is made, the dust quantities that come into play in the semi-analytical chemical model and nonideal MHD calculations of the global MRI-driven disk accretion model ($a_{dust,rep}$, $\sigma_{dust,rep}$ and $m_{dust,rep}$) become $a_{dust,rep} = a_{dust}$, $\sigma_{dust,rep} = \pi a_{dust}^2$ and $m_{dust,rep} = m_{dust}$. Furthermore, the radionuclide ionization rate $\zeta_{RA}^{(H_2)}$ for H_2 is computed following option A of Sect. 3.3.3.

- MAGNETIC FIELD. The magnetic field strength and topology are set by following option A of Sect. 3.5.3.

By assuming the protoplanetary disk to be geometrically thin, the vertical and radial dimensions can be decoupled into a 1+1D (r, z) problem, where each radial grid-point contains an independent vertical grid. Furthermore, by assuming the disk to be axisymmetric and symmetric about the midplane, it is enough to compute the domain $z \geqslant 0$ to obtain the full solution. The radial grid is computed from r_{min} to r_{max}, with N_r cells logarithmically spaced. For every radial grid-point $r \in [r_{min}, r_{max}]$, the corresponding vertical grid is computed from the disk midplane ($z = 0$) to z_{max}, with N_z cells linearly spaced. In all the simulations of this Chapter, I chose the following general setup: $r_{min} = 1$ au, $r_{max} = 200$ au, $N_r = 256$ cells, $z_{max} = 5\,H_{gas}(r)$ for every radial grid-points $r \in [r_{min}, r_{max}]$, and $N_z = 512$ cells. Here H_{gas} corresponds to the vertical gas scale height defined in Eq. (63).

The next sections are organized as follows: In Sect. 4.3 I explore the properties of the steady-MRI driven accretion for the fiducial model considered. In Sect. 4.4 I perform a comprehensive parameter study to determine the key parameters shaping the equilibrium solution. In Sect. 4.5 I discuss the implications of the results. Finally Sect. 4.6 summarizes the findings.

4.3 RESULTS—FIDUCIAL MODEL

Now that I have set the stage for obtaining steady-state MRI-driven accretion with the global disk accretion model of Chapter 3, I can now investigate the outer region structure ($r \gtrsim 1$ au) of steadily viscously accreting protoplanetary disks. I first present a detailed description of the equilibrium solution obtained for the fiducial model: the different accretion layers (Sect. 4.3.1); the disk structure (Sect. 4.3.2); and the disk turbulence level (Sect. 4.3.3).

4.3.1 *MRI active layer, dead zone, and zombie zone*

When Ohmic resistivity and ambipolar diffusion are the only nonideal MHD effects considered, the MRI active layer is sandwiched between two inactive regions: the dead and the zombie zone.

Figure 16a shows the stratification of the disk with the three different accretion layers. First, one can notice that the dead zone sits in the innermost regions where the gas density is the highest, whereas the zombie zone is located in the disk atmosphere where the gas density is low. Second, the MRI active layer only develops in the upper layers for $r \lesssim 23$ au, whereas the MRI operates from the midplane for $r \gtrsim 23$ au. As I discuss in Sect. 4.3.2.2, the ionization level is high enough only in the upper layers sitting right above the dead zone so that the MRI can only develop in a thin layer for $r \lesssim 23$ au; until ambipolar diffusion prohibits it in the very upper layers. Conversely, for $r \gtrsim 23$ au, the ionization level is high enough right from the midplane so that the magnetic field can efficiently couple to the charged particles

in the gas-phase to trigger the MRI. Third, in Fig. 16a, the region in between the dash-dotted magenta lines defines where the ambipolar condition ($\beta > \beta_{min}$) is satisfied in the disk, whereas the region above the dashed cyan line defines where the Ohmic condition ($\Lambda > 1$) is fulfilled. I want to emphasis that: (1) the upper envelope of the MRI active layer is utterly set by the ambipolar condition; (2) its lower envelope is mainly determined by the Ohmic condition (although the ambipolar condition plays a role for $2\,\mathrm{au} \lesssim r \lesssim 9\,\mathrm{au}$). The latter result is different from previous studies [e.g., 229], where they find that both the upper and lower envelope of the MRI active layer are completely set by the ambipolar condition around a Sun-like star. This difference can be explained as follows: First, they did not describe the steady-state accretion solution, resulting in a disk structure different from what is presented here. Second and most importantly, they used the total Alfvén velocity in their Ohmic condition, whereas I used its vertical component. Since the vertical component is assumed five times less than the total quantity in the global MRI-driven disk accretion model of Chapter 3 ($B^2 \approx 25 B_z^2$), the Ohmic Elsasser number found here is lower, resulting in a more stringent Ohmic condition, and thus a more extended dead zone (both radially and vertically).

Figure 16b shows which one of the nonideal MHD effects dominates the magnetic diffusivities in the disk. The MRI active layer is overplotted and shown by the black hatched area. One can notice that ambipolar diffusion dominates in most regions of the protoplanetary disk (especially the zombie zone), followed by the Hall effect, and finally the Ohmic resistivity. As expected, ambipolar diffusion dominates the low-density regions such as the upper layers or the outermost regions (midplane included), Ohmic resistivity dominates the innermost and densest regions, and the Hall effect comes into play for intermediate regions. Furthermore, most of the MRI active layer sits in the ambipolar-dominated region of the disk, implying that the MRI can be sustained there but it is weakened compared to its ideal limit ($0.1 \lesssim \mathrm{Am} \lesssim 10$ in the MRI active layer, as shown in Fig. 40a). Particularly, the upper envelope of the MRI active layer sits well within the region where the ambipolar magnetic diffusivity dominates; confirming that ambipolar diffusion sets it as seen above. On the other hand, Ohmic resistivity does not dominate the magnetic diffusivities where the lower envelope for the MRI active layer sits. This result seems different from what I said above, where I showed that mainly Ohmic resistivity is important to determine the lower envelope of the MRI active layer. This shows that Ohmic resistivity is the most stringent nonideal MHD effect to overcome for the MRI to operate, and does not need to dominate the magnetic diffusivities to have a strong impact on it.

Finally, it is quite striking that the Hall effect dominates the magnetic diffusivities in most of the dead zone as well as the inner regions of the MRI active layer. Particularly, Figure 16b shows that the lower envelope of the MRI active layer sits in the Hall-dominated region. I further discuss the implications in Sect. 4.5.5.
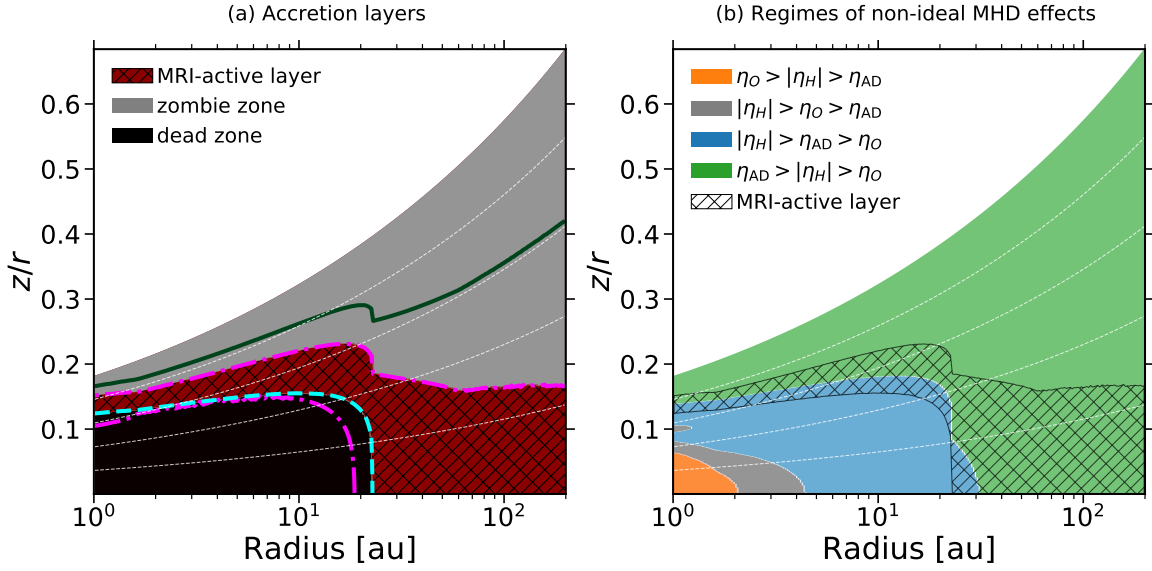
Figure 16: *Panel a*: Steady-state accretion layers, as a function of location in the disk, for the fiducial model. The black colored area corresponds to the dead zone. The gray colored area corresponds to the zombie zone. The red and black hatched area corresponds to the MRI active layer. The region within the dash-dotted magenta lines defines where the ambipolar condition ($\beta > \beta_{min}$) is satisfied in the disk, while the region above the dashed cyan line defines where the Ohmic condition ($\Lambda > 1$) is fulfilled. The region above the solid green line corresponds to where $\beta > 1$. The dashed white lines correspond to the surfaces $z = 1\,H_{gas}$, $z = 2\,H_{gas}$, $z = 3\,H_{gas}$, and $z = 4\,H_{gas}$, from bottom to top, respectively. *Panel b*: Regimes of the nonideal MHD effects by showing the dominant magnetic diffusivities as a function of location in the disk. In the orange colored region the Ohmic resistivity dominates (η_O is the highest magnetic diffusivity), in the gray and blue colored regions the Hall effect dominates ($|\eta_H|$ is the highest magnetic diffusivity), and in the green colored regions ambipolar diffusion dominates (η_{AD} is the highest magnetic diffusivity). The MRI active layer is shown by the black hatched area. The dashed white lines are the same as in *Panel a*.

4.3.2   *Disk structure*

4.3.2.1   *Gas*

The gas surface density is self-consistently derived -alongside the effective turbulence $\bar{\alpha}$- to ensure steady-state accretion (Eq. (161)). Figure 17 shows the steady-state radial profile (dotted red line) obtained through iterations.

It can be divided into two regions: a high-density region for $r \lesssim 23\,\mathrm{au}$ (midplane dead zone), and a low-density region for $r \gtrsim 23\,\mathrm{au}$ (midplane MRI active layer), where $r = 23\,\mathrm{au}$ corresponds to the midplane dead zone outer edge. One should note that the transition at the dead zone outer edge is sharp, and appears as a discontinuity. As I will discuss in Sect. 4.3.3, the effective turbulent parameter $\bar{\alpha}$ sharply increases by jumping from a low turbulence state in the non-MRI regions to a high turbulence state in the MRI active layer at $r = 23\,\mathrm{au}$. Since the accretion rate must be kept radially constant to ensure steady-state accretion, the gas surface density has to compensate by sharply decreasing at that location.

The profile displayed in Fig. 17 is actually expected. Indeed, if one initially assumes the disk to be out of equilibrium with its gas surface density following, for example, the self-similar solution from [121], the accretion rate is radially variable, where the outer regions (MRI active layer) accrete more than the inner ones (dead zone) on average. Consequently, by letting viscously evolving the gas, one will find that the gas is depleted from the MRI active layer to be accumulated into the dead zone.

4.3.2.2   *Ionization level*

Since the gas content is mostly located within the dead zone, the ionization level is highly heterogeneous across the protoplanetary disk. Figures 18 and 19 show the steady-state total ionization rates for H_2 for the different nonthermal ionization sources considered (stellar X-rays, galactic cosmic rays, radionuclides) and the steady-state gas ionization fraction[2], respectively. Here the gas ionization fraction corresponds to the free electrons abundance with respect to the neutrals abundance, and it is defined as follows

$$x_e = \frac{n_e}{n_n} \approx \frac{n_e}{n_{gas}}, \tag{163}$$

where n_e is the free electron number density and n_n is the neutral species number density. Here $n_n \approx n_{gas}$ because the gas is almost entirely neutral with only a small admixture of charged particles (See Sect. 2.1.2).

Deep inside the dead zone ($r \lesssim 5\,\mathrm{au}$ and $z \lesssim 1.5\,H_{gas}$), the ionization solely comes from the decay of short- and long-lived radionuclides (Figs. 18a and 18b). In those innermost regions, the gas surface density is so high that the other nonthermal ionization sources cannot penetrate at all, resulting in a very low gas ionization fraction (Fig. 19a). For $9\,\mathrm{au} \lesssim r \lesssim 23\,\mathrm{au}$ and $z \lesssim 1.5\,H_{gas}$, galactic cosmic rays can penetrate deep enough to dominate the ionization process, leading to an

---

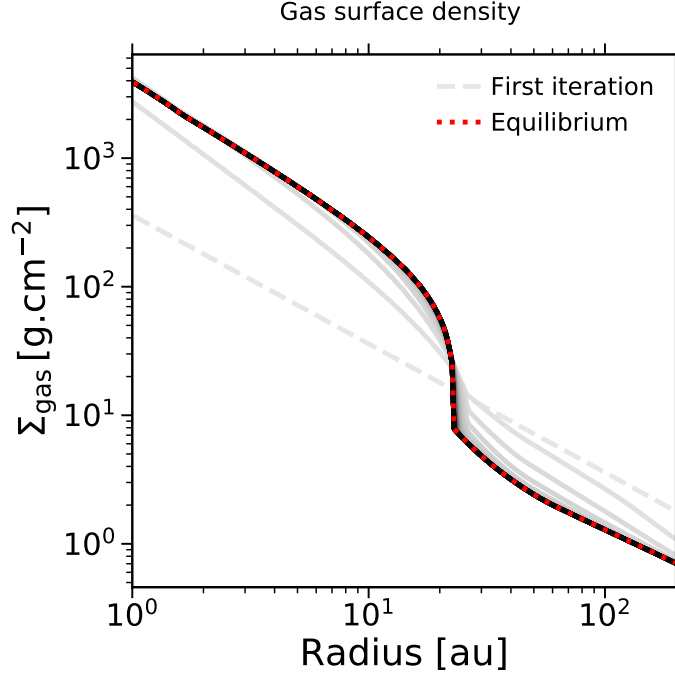2   also referred to as gas ionization degree interchangeably

Figure 17: Steady-state gas surface density, Σ_{gas} (Eq. 161), as a function of radius, for the fiducial model. The dashed gray line shows the initial gas surface density by initially assuming that the effective turbulent parameter, $\bar{\alpha}$, is radially constant and equal to $\bar{\alpha}_{init} = 0.1$. From light-colored solid lines to dark ones, I show how the gas surface density converges through iterations until the equilibrium solution is reached (dotted red line).

increase in the gas ionization fraction (Figs. 19a and 19b). Right at the midplane dead zone outer edge ($r = 23$ au), the gas becomes tenuous enough for scattered stellar X-rays to come into play and contribute as much as the galactic cosmic rays (Fig. 18a). As a result, the total ionization rate for H_2 gets a "boost" at the transition between the midplane dead zone and the midplane MRI active layer (comparing the black solid curves in Figs. 18c and 18d). One can further notice that stellar X-rays (both the scattered and direct contributions) can overall penetrate deeper for $r \gtrsim 23$ au due to lower gas column densities. Consequently, the gas ionization fraction sharply increases at the transition between the midplane dead zone and the midplane MRI active layer (comparing the red and blue curves of Fig. 19b), resulting in enough charged particles in the gas-phase for the magnetic field to couple with and triggering the MRI from the midplane (not only in the surface layers as it is the case for $r \lesssim 23$ au). Although the total ionization rate for H_2 is utterly dominated by stellar X-rays in the disk atmosphere (either through the scattered or direct contribution), Fig. 18a shows that galactic comic rays always dominate at the midplane for $r \gtrsim 23$ au. This behavior can be understood as follows: On one hand, the total stellar X-ray ionization rate (sum of the scattered and direct contribution) decreases over radius ($\propto r^{-2.2}$) unlike the ionization rate from galactic cosmic rays. Even though the gas is tenuous enough for the stellar scattered X-rays to penetrate deep enough, this emission has already lost most of its energy by traveling up to those regions. On the other hand, the stellar direct X-rays have a very

small penetration depth -although they are the most energetic source of ionization considered here. The gas is thus not tenuous enough for them to efficiently ionize the midplane. Interestingly, the total ionization rate for H_2 roughly saturates at a value equal to $\zeta^{(H_2)} \approx 1.5 \times 10^{-17}\,s^{-1}$ in the midplane MRI active layer (Fig. 18a): the galactic cosmic ray ionization rate saturates at its unattenuated value $10^{-17}\,s^{-1}$, and the total stellar X-ray ionization rate roughly adds up $0.5 \times 10^{-17}\,s^{-1}$). Consequently, the gas ionization fraction monotonously increases in the midplane MRI active layer (Fig. 19a).

In summary, I find that (see Fig. 13): (1) the decay of short- and long-lived radionuclides dominates the ionization process in the innermost regions of the dead zone; (2) galactic cosmic rays dominate the outermost regions of the dead zone, the whole midplane MRI active layer, and most of the regions right about the midplane MRI active layer; (3) stellar scattered X-rays dominate the lower layers of the disk atmosphere that sit right above the dead zone, and contribute as much as galactic cosmic rays right at the midplane dead zone outer edge; (4) stellar direct X-rays dominate the ionization process in the upper layers of the disk atmosphere, including the lower layers of the outermost regions; (5) the MRI is mainly driven by stellar X-rays, except close to the midplane where it is primarily driven by galactic cosmic rays.

4.3.2.3 *Magnetic field strength*

A lower limit on the magnetic field strength is the mean galactic field, which is roughly equal to 10^{-5} Gauss [e.g., 272], whereas an upper limit is the equipartition field (field such that the gas thermal pressure and the magnetic pressure are equal), which makes the shortest unstable MRI mode no longer fit within the vertical gas scale height (hence, no MRI activity possible at all). In the fiducial model, I numerically constrained the magnetic field strength, B, such that the MRI activity is at the maximal efficiency as permitted by Ohmic resistivity and ambipolar diffusion at any locations in the disk.

Figure 20a shows the various midplane fields of interest as a function of distance from the star. As expected, the highest value for B is well below the equipartition field $B_{equi} = \sqrt{8\pi\rho_{gas}c_s^2}$, while its lowest value is well above the mean galactic field. One can notice that the MRI-optimal r.m.s. magnetic field B displays a small discontinuity located at the midplane dead zone outer edge ($r = 23$ au). Although nonphysical, this mathematical discontinuity expresses the fact that B jumps from a solution in the dead zone where the turbulence is weak to another in the MRI active layer where the turbulence is stronger. In the midplane MRI layer ($r \gtrsim 23$ au), B is very close (but strictly lower) to $B_{max} = \sqrt{\frac{8\pi\rho_{gas}c_s^2}{\beta_{min}}}$, which corresponds to the maximal field strength from and above which the MRI-driven turbulence with such a field strength is prohibited by ambipolar diffusion (see Eqs. 152 and 153). This is expected since I constructed the field strength such that the MRI operates at maximal efficiency. One can further notice that the MRI-optimal r.m.s. magnetic field B is higher than B_{max} for $r \lesssim 18$ au. It thus implies that the ambipolar condition is
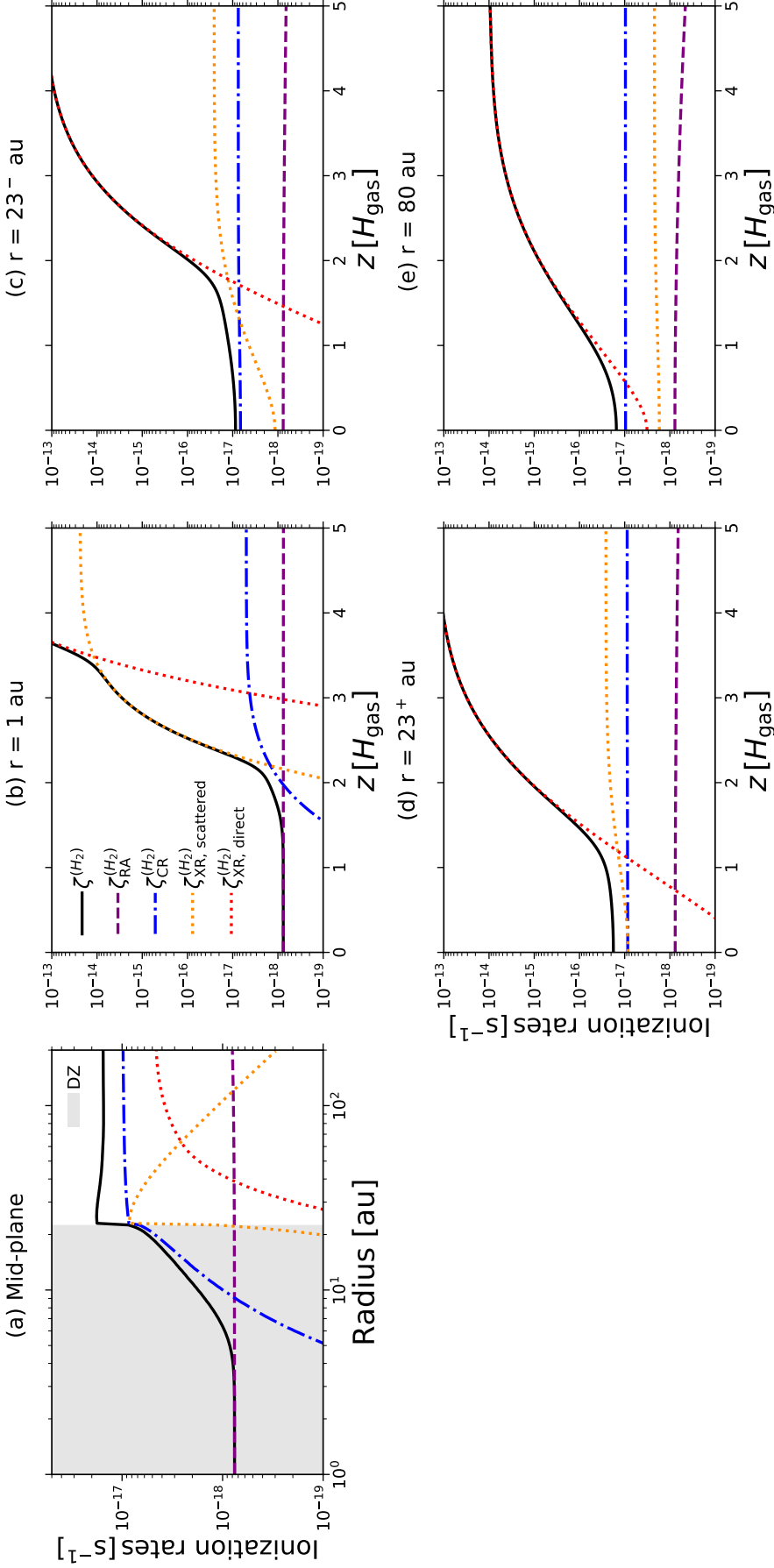
Figure 18: Steady-state ionization rates for the fiducial model. The total ionization rate for H_2 ($\zeta^{(H_2)}$; solid black line) is the sum of the following contributions: the radionuclides ionization rate for H_2 ($\zeta_{RA}^{(H_2)}$; dashed purple line) defined by Eq. (110); the galactic cosmic ray ionization rate for H_2 ($\zeta_{CR}^{(H_2)}$; dash-dotted blue line) defined by Eq. (109); the scattered X-ray contribution of the X-ray ionization rate for H_2 ($\zeta_{XR,scattered}^{(H_2)}$; dotted dark orange line) defined by Eq. (108); and its direct X-ray contribution ($\zeta_{XR,direct}^{(H_2)}$; dotted red line) defined by Eq. (107). *Panel a*: Midplane ionization rates as a function of radius. The gray shaded area corresponds to the radial locations within the midplane dead zone. *Panel b*: Ionization rates computed at $r = 1\,au$ (a radial location well within the dead zone) as a function of height, z. *Panel c*: Same as *Panel b* but for $r = 23^-\,au$, corresponding to the radial location right before the midplane dead zone outer edge. *Panel d*: Same as *Panel b* but for $r = 23^+\,au$, corresponding to the radial location right after the midplane dead zone outer edge. *Panel e*: Same as *Panel b* but for $r = 80\,au$, corresponding to a radial location well within the MRI active layer. A 2D map of the total ionization rate for H_2 ($\zeta^{(H_2)}$) and its different contributions can be found in Fig. 13.

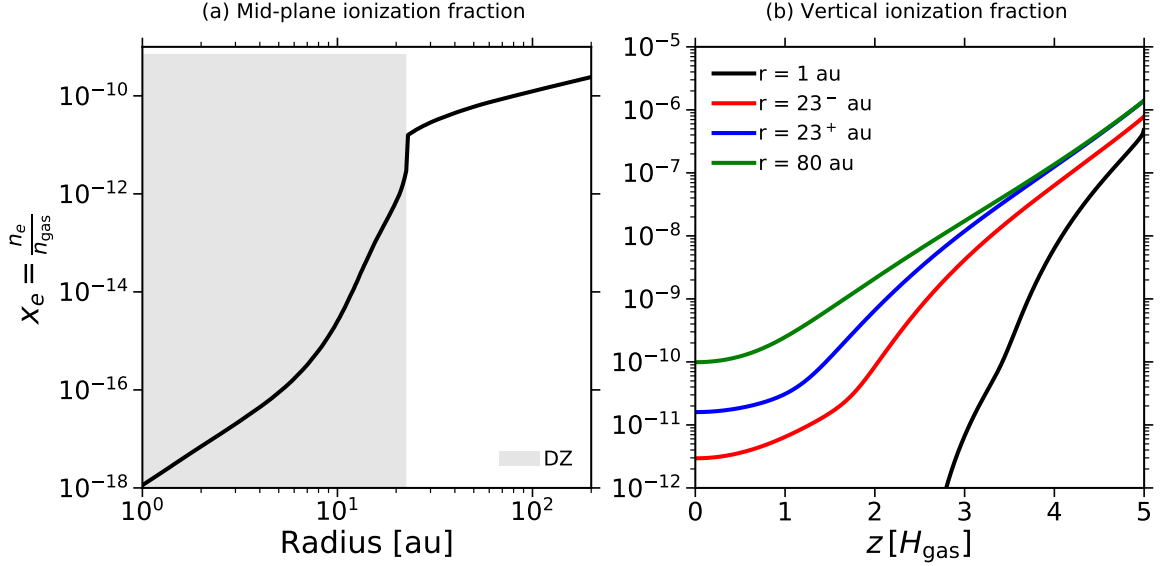Figure 19: Steady-state gas ionization fraction, x_e (n_e is defined by Eq. (126)), for the fiducial model. *Panel a*: Midplane gas ionization fraction as a function of radius. The gray shaded area corresponds to the radial locations within the midplane dead zone. *Panel b*: Vertical profiles for the gas ionization fraction at the same radial locations as in Fig. 18. The solid black line corresponds to $r = 1$ au. The solid red line corresponds to $r = 23^-$ au. The solid blue line corresponds to $r = 23^+$ au. The solid green line corresponds to $r = 80$ au.

also not met in most of the midplane dead zone where the MRI is suppressed by Ohmic resistivity, as I showed in Sect. 4.3.1

Figure 20b shows the r.m.s. plasma-β parameter (β) radial profiles at various heights in the disk. Since the MRI-optimal r.m.s. magnetic field B is assumed to be vertically constant, the r.m.s. plasma-β parameter decreases exponentially with increasing height; hence, the radial profiles at different vertical gas scale heights are rescaled versions of the midplane profile (solid line). In the midplane dead zone ($r \lesssim 23$ au), the midplane r.m.s. plasma-β parameter has a mean value of roughly 8×10^3. As expected, the midplane dead zone is thus weakly magnetized, since the MRI cannot operate. In the midplane MRI active layer ($r \gtrsim 23$ au), the midplane r.m.s. plasma-β parameter has a mean value of roughly 142, implying that these regions are moderately magnetized. One can further notice that the midplane r.m.s. plasma-β saturates in the MRI active layer from $r \gtrsim 60$ au. This behavior can be understood as follows: As seen in the last section, the midplane gas ionization fraction increases with radius (Fig. 19a; this results in the magnetic field being more efficiently couple to the gas in these regions, which leads to a possible stronger MRI-driven local turbulence. However, ambipolar diffusion is the dominant non-ideal MHD effect in the regions where the gas is scarce, as I showed in Sect. 4.3.1. In such regions, a stronger local MRI-driven turbulence implies a stronger field strength ($\alpha \propto \beta^{-1}$), resulting in this stronger local turbulence being prohibited by ambipolar diffusion. Consequently, the midplane r.m.s. plasma-β parameter saturating in the MRI active layer from $r \gtrsim 60$ au expresses that the positive feedback on the MRI from a higher gas ionization degree is compensated for by the neg-
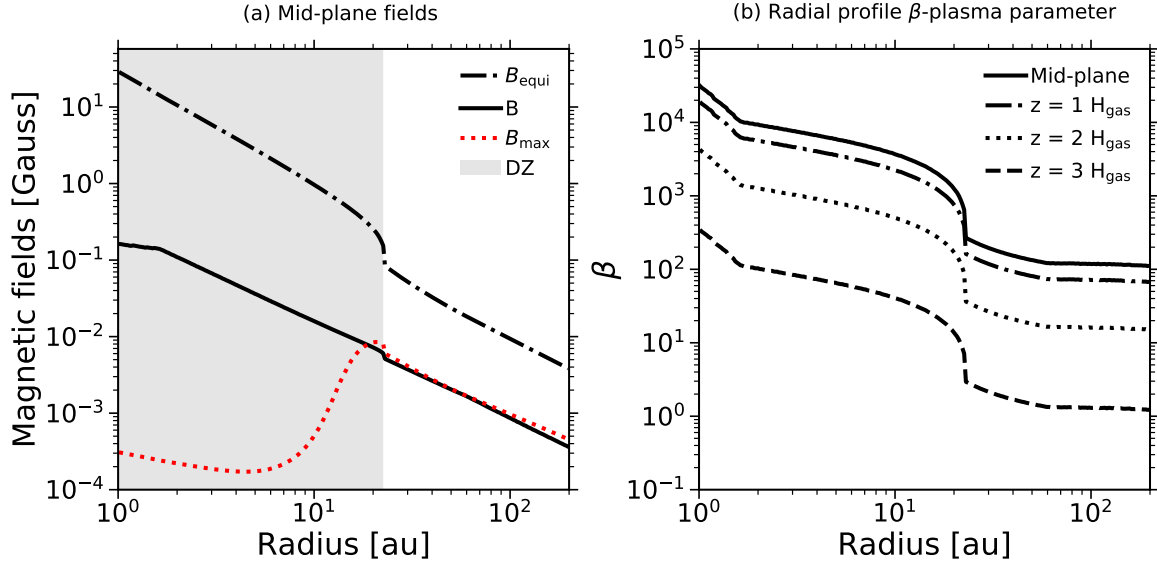
Figure 20: Steady-state quantities describing the disk magnetization for the fiducial model. *Panel a*: Midplane magnetic fields strength as a function of radius. The solid black line corresponds to B, the MRI-optimal r.m.s. magnetic field strength that is required for the MRI activity to be at the maximal efficiency as permitted by Ohmic resistivity and ambipolar diffusion (Sect. 3.5.3). The dotted red line corresponds to $B_{max} = \sqrt{\frac{8\pi\rho_{gas}c_s^2}{\beta_{min}}}$, the threshold for the magnetic field strength from and above which the MRI-driven turbulence with such a field strength is prohibited by ambipolar diffusion, given the ambipolar condition ($\beta > \beta_{min}$) of the active MRI criteria (Sect. 3.5.1). The dash-dotted black line corresponds to $B_{equi} = \sqrt{8\pi\rho_{gas}c_s^2}$, the equipartition field. The gray shaded area corresponds to the radial locations within the midplane dead zone. *Panel b*: Radial profiles for the r.m.s. plasma-β parameter (β) derived from the MRI-optimal r.m.s. magnetic field strength B (Sect. 3.5.1), for the midplane (solid line), $z = 1\,H_{gas}$ (dash-dotted line), $z = 2\,H_{gas}$ (dotted line), and $z = 3\,H_{gas}$ (dashed line).

ative feedback from ambipolar diffusion that prohibits turbulence with stronger magnetic fields.

4.3.3 *Turbulence*

In this thesis, it is assumed that the origin of turbulence is the radial transport of angular momentum redistributed within the protoplanetary disk by standard viscous torques: MRI magnetic torques in the active regions, and hydrodynamic torques in the nonactive regions. Figure 21 shows various quantities of interest describing the properties of the steady-state disk turbulence.

As expected, the disk is significantly more turbulent in the MRI active layer than it is in the dead or zombie zone. From Figs. 21a and 21b, one can notice that the local turbulent parameter α is higher at large radii and heights, in the MRI active layer. Indeed, the ionization level is higher in these regions because the gas surface densities are lower, leading to more penetration by the nonthermal ionization sources (stellar X-rays in the disk atmosphere, and galactic cosmic rays at the

disk midplane) as well as slower recombination. At the midplane dead zone outer edge ($r = 23$ au), the turbulence jumps from a low regime in the midplane dead zone to a high regime in the midplane MRI active layer. More generally, this very steep transition happens at the boundaries between active and nonactive regions; namely, at the upper and lower envelopes of the MRI active layer. I obtain such a behavior due to the assumption made on the MRI activity: either in a saturation level allowed by the nonideal MHD effects, or completely shut off (see criteria in Sect. 3.5.1). Figure 21d shows that, due to this sharp change, the effective turbulent parameter $\bar{\alpha}$ displays a small discontinuity at the midplane dead zone outer edge ($r = 23$ au), resulting in the discontinuity seen in the steady-state gas surface density (Fig. 17). I further discuss such a sharp transition in the gas surface density profile in Sect. 4.5.1.

Since there is a thin turbulent MRI active layer that sits right above the dead zone for $r \lesssim 23$ au, the effective turbulent parameter $\bar{\alpha}$ is higher than the minimum value $\alpha_{hydro} = 10^{-4}$ in the dead zone, and increases toward the dead zone outer edge (see dotted red line in Fig. 21d). If not located too high above the dead zone, active regions can indeed make the dead zone effectively more turbulent by launching turbulent waves [e.g., 193, 195, 273, 274]. Although such waves are not described by the global MRI-driven disk accretion model of Chapter 3, the effective turbulent parameter $\bar{\alpha}$ encodes the influence of the upper layers on the turbulence, since this quantity is the pressure-weighted vertical average of the local turbulence. In the innermost regions of the dead zone, $\bar{\alpha} \approx \alpha_{hydro}$ because the MRI active layer represents a very small fraction of the gas column densities. Since the vertical extent of the dead zone diminishes for larger radii, the active regions right above the dead zone increasingly represent a higher fraction of the gas column densities toward the dead zone outer edge; meaning that the contribution from the MRI active layer on the effective turbulent parameter $\bar{\alpha}$ increasingly becomes larger. Overall, though, I find that the mean value of $\bar{\alpha}$ is roughly 1.7×10^{-4} in the dead zone. Therefore, the general behavior of the turbulence in these regions is a low regime, as expected.

Conversely, the dotted red line in Fig. 21d shows that the mean value of $\bar{\alpha}$ in the outer region of the MRI active layer ($r \gtrsim 23$ au) is roughly 3.1×10^{-3}, which is 19 times higher than the mean value stated above for the dead zone. Interestingly, the effective turbulent parameter $\bar{\alpha}$ decreases for $r \gtrsim 60$ au. This seems to be at odds with the fact that the local turbulent parameter α saturates and is roughly constant for a given height at those radii (because $\alpha \propto \beta^{-1}$ and the r.m.s. plasma-β parameter is roughly constant for a given height at those radii, as seen in Fig. 20b). To better understand this behavior, the MRI active layer thickness h_{MRI} is shown in Fig. 21c. One can notice that it diminishes comparatively to H_{gas} for $r \gtrsim 23$ au. Indeed, h_{MRI} increases toward larger radii, but slowly since local turbulence with stronger than permitted magnetic fields would be considered if the active layer was thicker at a given r, which is prohibited by ambipolar diffusion. As a result, the quantity h_{MRI}/H_{gas} slowly decreasing for $r \gtrsim 23$ au implying that the MRI active layer increasingly represents a lower fraction of the gas column densities for increasing radii from $r \gtrsim 23$ au. For a local turbulent parameter α roughly constant

for $r \gtrsim 60\,au$ and a reduction in how much the MRI active layer contributes to the gas column densities, the effective turbulent parameter $\bar{\alpha}$ decreases for $r \gtrsim 60\,au$.

In summary, I find that the effective turbulent parameter $\bar{\alpha}$ is strong when both the local MRI-driven turbulence α and the MRI active layer thickness h_{MRI} (comparatively to H_{gas}) are significant: The former tells us how much turbulence can be locally driven by the MRI, whereas the latter describes how much the MRI active layer contributes to the gas column density at a given radius.

I want to emphasize that the accretion rate $\dot{M}_{acc}$ presented in Fig. 21e represents the highest value possibly reachable given the set of criteria for active MRI employed, since I have adopted the required magnetic field strength such that the MRI activity is at maximal efficiency (see Sect. 3.5.3). In Sect. 4.4.4, I explore what would be the derived accretion rates for either weaker or stronger magnetic field strengths, and show that the choice made for the magnetic field strength leads to the highest value for the accretion rate as expected.

4.4 RESULTS—PARAMETER STUDY

Here I perform a series of simulations exploring the effect of various parameters on the equilibrium solution of the fiducial model described in the last section. Particularly, I vary the total disk gas mass (Sect. 4.4.1), the representative grain size (Sect. 4.4.2), the vertically integrated dust-to-gas mass ratio (Sect. 4.4.3), the magnetic field strength and topology (Sect. 4.4.4), the hydrodynamic turbulent parameter (Sect. 4.4.5), the gas temperature model (Sect. 4.4.6), the stellar properties – mass and luminosity – (Sect. 4.4.7), and I implement a grain size distribution (Sect. 4.4.8). In each series, I derive the radial profile of key quantities reached by the equilibrium solution. These quantities are: (a) the pressure-weighted vertically integrated turbulent parameter $\bar{\alpha}$; (b) the gas surface density Σ_{gas}; (c) the midplane total ionization rate ζ; (d) the midplane MRI-optimal r.m.s. magnetic field strength B required for the MRI activity to be at maximal efficiency; (e) the gas accretion rate $\dot{M}_{acc}$; (f) the midplane location of the dead zone outer edge R_{DZ} (corresponding to the dead zone maximal radial extent). A detailed description of the results are given in the following sections. Table 2 summarizes the parameters used in each model.

4.4.1 *Effect of disk mass*

The amount of gas enclosed within the protoplanetary disk sets many of the disk structure properties (e.g., ionization level). It is then expected that the variation in total disk gas mass significantly impacts the equilibrium solution. To quantify this further, I run a set of simulations where M_{disk} varies from a gas-poor disk motivated by ALMA observations in the thermal continuum [e.g., 275, assuming a gas-to-dust ratio of 100] to a gas-rich disk close to the GI limit. The turbulence model of Chapter 3 does not treat gravitoturbulence, hence why the GI limit sets the upper limit for the total disk gas mass. I determine such an upper limit by
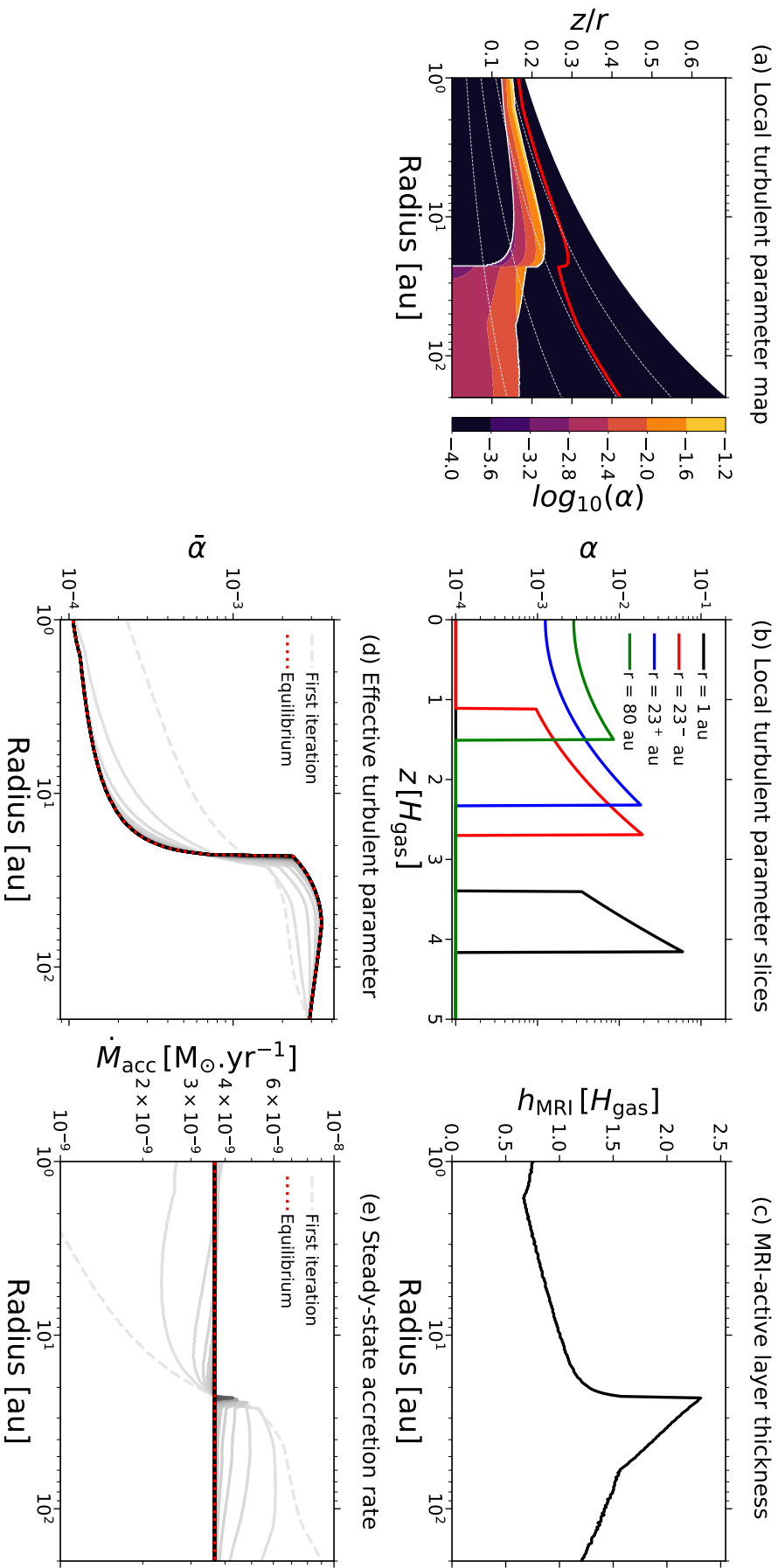
Figure 21: Steady-state quantities describing the turbulence state in the disk for the fiducial model. *Panel a*: Local turbulence parameter, α (Eq. 158), as a function of location in the disk. The region above the solid red line corresponds to where β > 1. The dashed white lines correspond to the surfaces z = 1 H$_{gas}$, z = 2 H$_{gas}$, z = 3 H$_{gas}$, and z = 4 H$_{gas}$, from bottom to top, respectively. *Panel b*: Vertical profiles for the local turbulent parameter, α, at various radial locations, with color codes as in Fig. 19. *Panel c*: MRI active layer thickness, h$_{MRI}$, as a function of radius, expressed in terms of the vertical gas scale height, H$_{gas}$. The dashed gray line shows the profile after the first iteration. *Panel d*: Pressure-weighted vertically integrated turbulent parameter, ᾱ (Eq. 77), as a function of radius. The dashed gray line shows the profile after the first iteration. From light-colored solid lines to dark ones, I show how the pressure-weighted vertically integrated turbulent parameter converges through iterations until the equilibrium solution is reached (dotted red line). *Panel e*: Same as in *Panel d*, but for the accretion rate, Ṁ$_{acc}$ (Eq. 162).

choosing a total disk gas mass value so that $Q \gtrsim 2$ is satisfied at every radii r, where Q is the Toomre parameter [29] defined as $Q = (c_s \Omega_K) / (\pi G \Sigma_{gas})$. In practice, I choose M_{disk} in the list $\{0.005, 0.01, 0.05, 0.10\} M_\star$ with $M_\star = 1 M_\odot$. This set of simulations corresponds to Model I, and the results are presented in Fig. 22.

As expected for a steady-state viscously accreting protoplanetary disk, the accretion rate and total disk gas mass follow a tight correlation (Fig. 22e). Particularly, I find that $\dot{M}_{acc} \propto M_{disk}^{0.54}$. In the disk model employed, $c_s^2 \propto T \propto r^{-1/2}$. Consequently, Eq. (162) gives:

$$\dot{M}_{acc} \propto \frac{L_\star^{1/4} M_{disk}}{\sqrt{M_\star} \int_{r_{min}}^{r_{max}} \bar{\alpha}^{-1} dr}.$$

For fixed $L_\star$ and $M_\star$, the quantity $\dot{M}_{acc}/M_{disk}$ is entirely determined by the integral $\int_{r_{min}}^{r_{max}} \bar{\alpha}^{-1} dr$. I find that $\left[\int_{r_{min}}^{r_{max}} \bar{\alpha}^{-1} dr \right] \propto M_{disk}^{0.46}$, hence the relation between $\dot{M}_{acc}$ and R_{DZ}. Physically, this relation can be simply understood as follows: a higher total disk gas mass implies more gas available to be accreted onto the central star, hence a higher accretion rate.

Additionally, a similar correlation between the dead zone maximal radial extent and the total disk gas mass $R_{DZ} \propto M_{disk}^{0.64}$ can be found. Figure 22f shows that the dead zone maximal radial extent (corresponding to the midplane dead zone outer edge) can be as small as ≈ 4 au for low total disk gas masses, and as large as ≈ 31 au for high total disk gas masses. For a massive disk, the gas surface density is higher at every radii; leading to a lower ionization state compared to a low total disk gas mass (Fig. 22c). Since the gas ionization fraction is lower, there are less charged particles in the gas-phase for the magnetic field to couple with. Consequently, the midplane dead zone outer edge is located further away because the location where the ionization level is enough to trigger the MRI is reached further away. With the same argument on the overall lower gas ionization degree, one can understand why the mean value of the overall effective turbulent parameter $\bar{\alpha}$ is lower for disks with a higher total disk gas mass.

Interestingly, $\bar{\alpha}$ displays a different shape for the two less massive disks. Instead of only steeply increasing right at the dead zone outer edge, it also displays a second shallow but significant increase in the MRI active layer. One can explain the shape displayed for the two less massive disks by looking at their midplane total ionization rate (Fig. 22c): For such low total disk gas masses, the ionization process (midplane included) is dominated by stellar X-rays. The scattered X-ray contribution dominates right at the dead zone outer edge (first steep increase in ζ) but quickly decreases for larger radii, while the direct X-ray contribution increases from the dead zone outer edge but cannot penetrate deep enough yet. As a result, the midplane total ionization rate immediately decreases beyond the dead zone outer edge, until the direct X-ray contribution can finally penetrate deep enough to compensate for the decrease in the scattered X-ray contribution and provide another boost to the midplane ionization (second shallow increase in ζ).

Furthermore, the MRI-optimal r.m.s. magnetic field strength B is weaker for a lower total disk gas mass once the midplane MRI active layer is reached due to am-

bipolar diffusion (Fig. 22d). Since a lower total disk gas mass implies a higher gas ionization degree at the midplane, the ambipolar Elsasser number Am is slightly higher once the midplane MRI active layer is reached (for example, Am can be up to three times higher for $M_{disk} = 0.005\,M_\star$ compared to $M_{disk} = 0.05\,M_\star$). This implies that $\beta_{min}(Am)$ is slightly lower for a lower total disk gas mass in such regions (it can be up to four times lower for $M_{disk} = 0.005\,M_\star$ compared to $M_{disk} = 0.05\,M_\star$). However, the gas surface densities are much lower across the disk for a lower total disk gas mass, leading to an overall lower gas volume density ρ_{gas} (it is at best four times lower for $M_{disk} = 0.005\,M_\star$ compared to $M_{disk} = 0.05\,M_\star$). Since the threshold for the magnetic field strength from and above which the MRI-driven turbulence with such a field strength is prohibited by ambipolar diffusion (B_{max}) is such that $B_{max} \propto \sqrt{\frac{\rho_{gas}}{\beta_{min}(Am)}}$, and ρ_{gas} decreases faster than $\beta_{min}(Am)$ does for a lower total disk gas mass, one can conclude that B_{max} is lower, hence a lower B.

Finally, a striking result is that the effective turbulence level roughly becomes independent of the total disk gas mass considered at $r \approx 200\,au$ (all the $\bar{\alpha}$ converge toward the same value $\approx 3 \times 10^{-3}$). This shows how ambipolar diffusion operates as a regulator to compensate for the positive feedback on the MRI from a higher gas ionization degree for a lower total disk gas mass, as explained in the previous paragraph.

4.4.2   *Effect of representative grain size*

The representative grain size at a given location in the disk is subject to significant change over time due to processes such as coagulation, fragmentation or radial drift. Depending on whether the representative grain size is skewed toward small or large dust particles, the equilibrium solution is expected to be very different. In first order, the importance of representative grain size on the equilibrium solution can be assessed using the single grain size assumption, that is assuming all dust particles to be of size a_{dust} anywhere in the protoplanetary disk. In practice, I run a set of simulations where the dust particles size, a_{dust}, varies from submicron to millimeter with values in the list $\{10^{-5}, 10^{-4}, 10^{-3}, 10^{-2}, 10^{-1}\}$ cm. This set of simulations corresponds to Model II, and the results are presented in Fig. 23.

A smaller grain size implies a lower accretion rate and a more extended dead zone (Figs. 23e and 23f). Smaller dust particles have indeed higher cross-section areas allowing them to efficiently capture free electrons or ions (overall lower ionization level, Fig. 23c). Since there are less charged particles in the gas-phase for the magnetic field to couple with, the MRI cannot be triggered easily and can even be shut off in most of the disk by strong Ohmic resistivity and ambipolar diffusion. Particularly, for submicron grains and at the midplane, the MRI can develop in the outermost regions of the disk only ($r \gtrsim 92\,au$, Fig. 23a). For $r \lesssim 92\,au$, the MRI can only operate in the surface layers, since the effect of grains on the ionization chemistry is diminished and stellar X-rays can more efficiently ionize the gas. Nonetheless, it is not enough to compensate for the fact that most of the disk is
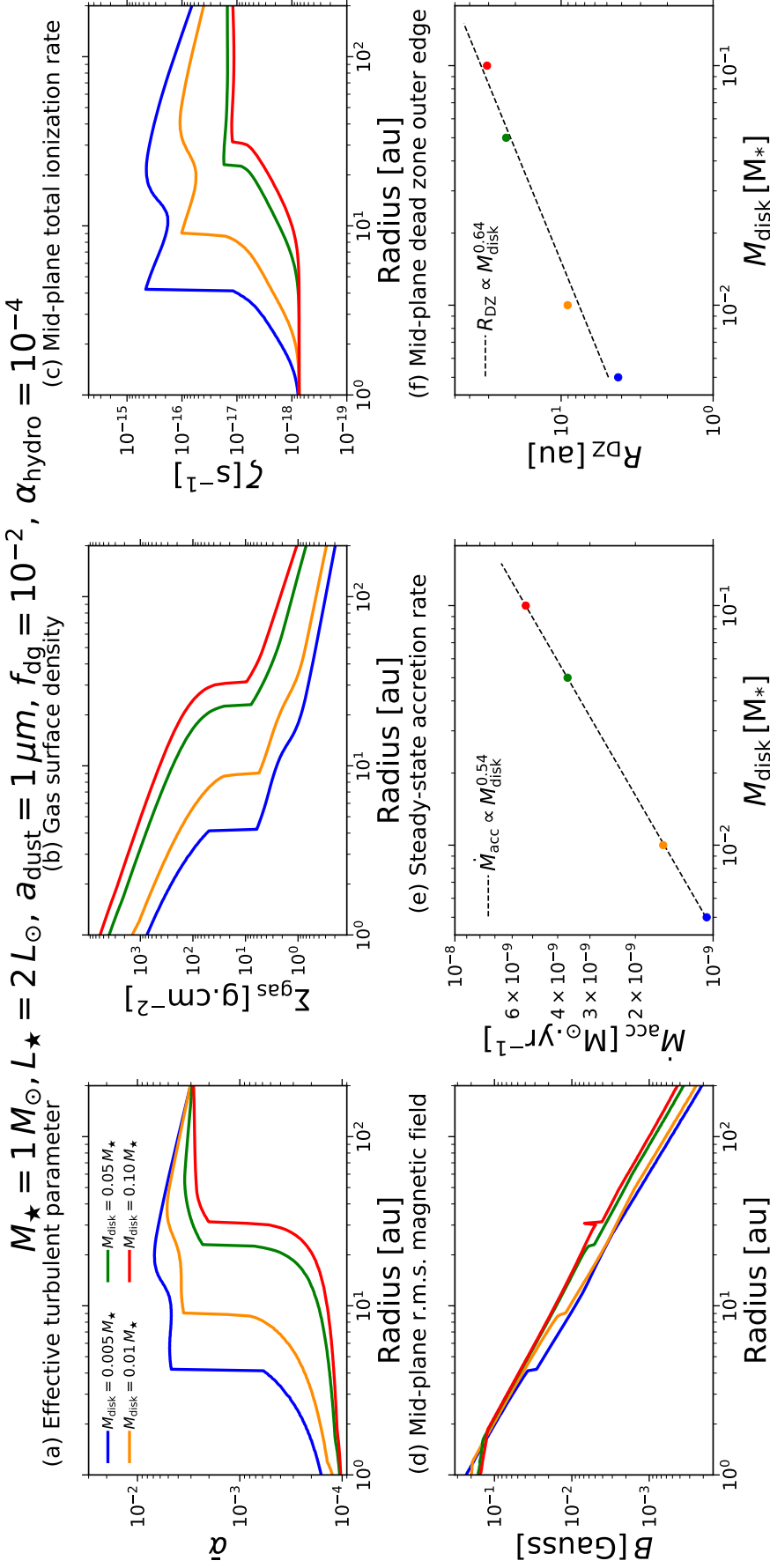
Figure 22: Model I. Effect of the total disk gas mass on the equilibrium solution when varying the parameter M_{disk} from $0.005\,M_\star$ (gas-poor disk) to $0.10\,M_\star$ (gas-rich disk close to the GI limit): The case $M_{\text{disk}} = 0.005\,M_\star$ is shown in blue, $M_{\text{disk}} = 0.01\,M_\star$ in dark orange, $M_{\text{disk}} = 0.05\,M_\star$ in green (fiducial model), and $M_{\text{disk}} = 0.10\,M_\star$ in red. The panels show the steady-state radial profiles of some key quantities, for the model parameters $M_\star = 1\,M_\odot$, $L_\star = 2\,L_\odot$, $a_{\text{dust}} = 1\,\mu m$, $f_{\text{dg}} = 10^{-2}$, and $\alpha_{\text{hydro}} = 10^{-4}$. *Panel a*: Pressure-weighted vertically integrated turbulent parameter, $\bar{\alpha}$ (Eq. 77). *Panel b*: Gas surface density, Σ_{gas} (Eq. 161). *Panel c*: Midplane total ionization rate, ζ (Eq. 104). *Panel d*: Midplane MRI-optimal r.m.s. magnetic field strength, B, that is required for the MRI activity to be at the maximal efficiency as permitted by Ohmic resistivity and ambipolar diffusion (option A of Sect. 3.5.3. *Panel e*: Gas accretion rate, $\dot{M}_{\text{acc}}$ (Eq. 162). *Panel f*: Midplane radial dead zone outer edge location, R_{DZ}, defined as the midplane radial location where both the Ohmic and ambipolar condition are met for the first time (Sect. 3.5.1). The dashed black lines in *Panels e,f* correspond to a power-law fit of $\dot{M}_{\text{acc}}$ and R_{DZ} as a function of M_{disk} respectively.

MRI-dead; leading to a mean value of a few times 10^{-4} for $\bar{\alpha}$. Overall the accretion rate is thus much lower for submicron grains.

For larger grain sizes, the overall ionization level in the disk becomes higher for two reasons: The cross-section is significantly reduced, resulting in the gas-phase recombination more easily dominating the recombination process, and dust settling becomes important. Regarding the latter, larger dust particles easily decouple from the gas in the upper layers of the disk atmosphere, where the turbulence level is low due to ambipolar diffusion (see Sect. 4.3.3). Consequently, settling can overcome vertical stirring, resulting in the dust being concentrated in regions closer to the midplane. Dust settling thus implies a higher local dust-to-gas ratio closer to the midplane, hence a higher midplane radionuclides ionization rate since the ionization from radionuclides is mainly due to ^{26}Al locked into grains. The effect of dust settling can be seen in Fig. 23c, where the total midplane ionization rate is the highest for $a_{dust} = 1\,mm$, for $r \lesssim 4\,au$.

Another salient result is that the steady-state accretion solution becomes independent of the grain size choice for $a_{dust} \gtrsim 100\,\mu m$. One can thus infer that there exists a threshold for the grain size above which the grains have little impact on the ionization chemistry, hence on the ionization level, and ultimately on the MRI. This threshold marks the regime in which the dust–gas mixture behaves as a grain-free plasma due to the recombination process primarily occurring in the gas-phase rather than onto the grains surface.

Finally, once the midplane MRI active layer is reached, one can notice that the corresponding mean value of $\bar{\alpha}$ is roughly independent of the grain size, in the range $2 \times 10^{-3} - 3 \times 10^{-3}$ (Fig. 23a). I showed previously that the disk becomes more MRI-dead when smaller grain sizes are considered, implying that the gas surface densities in the MRI active layer are lower compared to the ones for larger grain sizes (required to preserve the total disk gas mass constant). Since the gas surface densities are lower in the MRI active layer for smaller grain sizes (Fig. 23b), one would expect more charged particles available in the gas-phase (due to stronger ionization) in such regions compared to the case of larger grain sizes. However, these charged particles are more efficiently captured when the dust grains are small, implying that the effective ionization level is actually not higher than the ones for larger grain sizes. Once the MRI active layer is reached, its mean effective turbulence level is thus roughly constant regardless of the grain size.

4.4.3 *Effect of dust-to-gas mass ratio*

Whether small dust particles are depleted or accumulated is expected to be crucial for the equilibrium solution, since the higher the concentration of those is, the harder it is for the MRI to operate. I run two sets of simulations where: (1) I consider an overall change in the vertically averaged dust-to-gas mass ratio from 10^{-5} (99.9% depletion of dust particles relative to standard ISM) to 10^{-1}; (2) I impose local dust enhancements either at the expected dead zone outer edge location for the fiducial model ($r = 23\,au$) or at two locations in the disk, respectively, $r = 5\,au$, which is
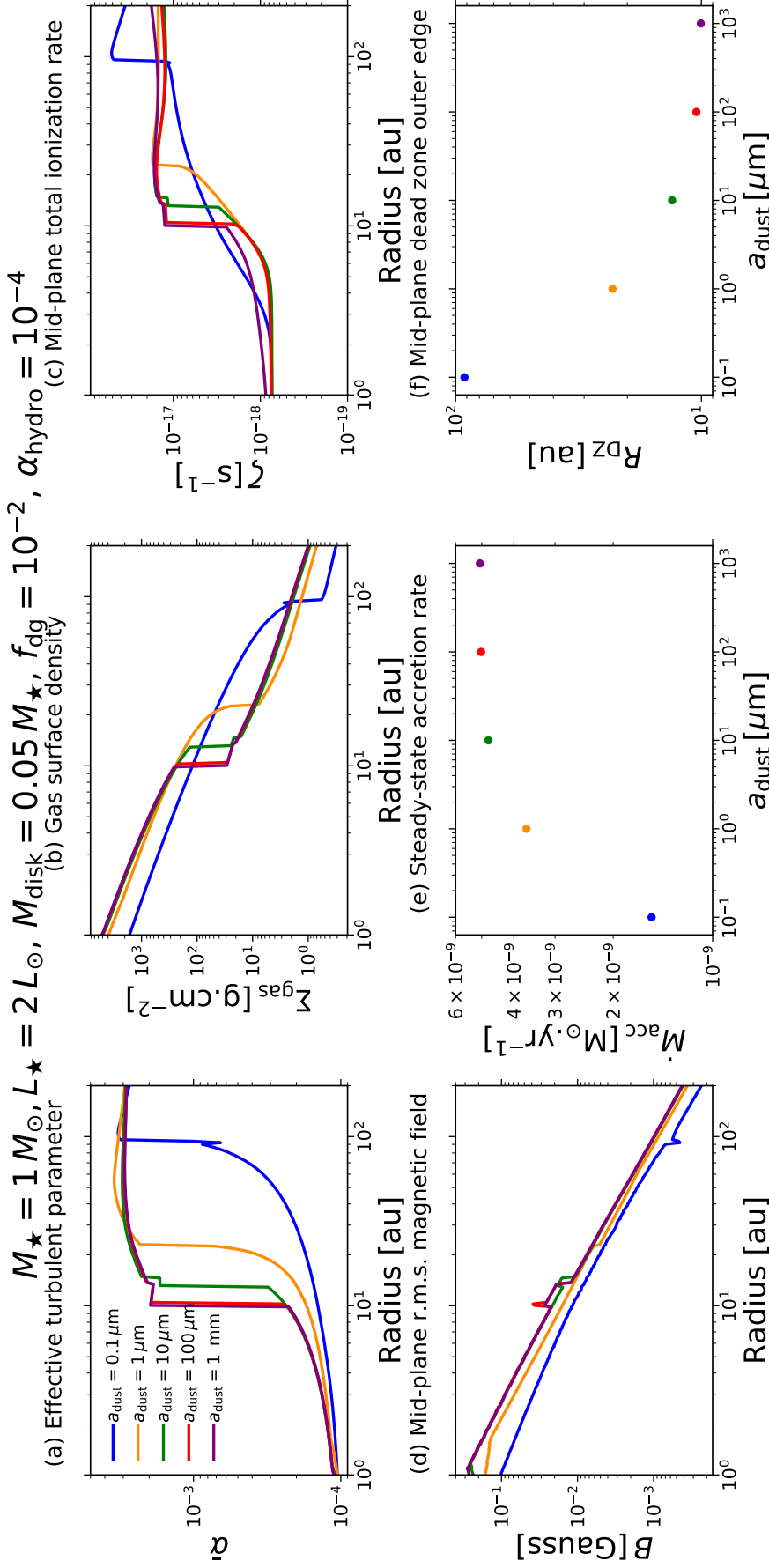
Figure 23: Model II. Effect of the representative grain size on the equilibrium solution when varying the parameter a_{dust} from $0.1\,\mu m$ to $1\,mm$: The case $a_{dust} = 0.1\,\mu m$ is shown in blue, $a_{dust} = 1\,\mu m$ in dark orange (fiducial model), $a_{dust} = 10\,\mu m$ in green, $a_{dust} = 100\,\mu m$ in red, and $a_{dust} = 1\,mm$ in purple. *Panels a–f* show the steady-state radial profiles of the same key quantities as in Fig. 22, but for the model parameters $M_\star = 1\,M_\odot$, $L_\star = 2\,L_\odot$, $M_{disk} = 0.05\,M_\star$, $f_{dg} = 10^{-2}$, and $\alpha_{hydro} = 10^{-4}$.

within the midplane dead zone, and $r = 60\,\mathrm{au}$, which is within the midplane MRI active layer.

4.4.3.1 *Overall change*

For this set of simulations, the vertically averaged dust-to-gas mass ratio f_{dg} is chosen to be radially constant and equal to a value in the list $\{10^{-5}, 10^{-4}, 10^{-3}, 10^{-2}, 10^{-1}\}$. This set of simulations corresponds to Model III, and the results are presented in Fig. 24.

Figures 24e and 24f show that protoplanetary disks with an overall higher depletion of micron-sized dust particles have a higher accretion rate and a more compact dead zone. For a disk poor in micron-sized grains, Ohmic resistivity and ambipolar diffusion are less stringent on the MRI activity because the amount of small grains is not enough to significantly impact the recombination process, happening then mostly in the gas-phase; although the overall ionization level in the innermost regions is lower compared to less depleted disks due to fewer radionuclides being available (Fig. 24c).

For a disk rich in micron-sized grains, the ionization from the decay of short- and long-lived radionuclides is stronger. However, it is not enough to compensate for the more stringent nonideal MHD effects on the MRI-driven turbulence, since a higher number of grains can more efficiently sweep up free electrons and ions from the gas-phase. Particularly, the case $f_{dg} = 10^{-1}$ leads to the lowest accretion rate ($\approx 2 \times 10^{-9}\,\mathrm{M_\odot.yr^{-1}}$) and the largest dead zone maximal radial extent ($\approx 47\,\mathrm{au}$).

One can notice that the steady-state accretion solution becomes independent of the vertically averaged dust-to-gas mass ratio choice for $f_{dg} \lesssim 10^{-4}$. Similarly to what I showed for the effect of representative grain size, there exists a threshold below which the dust depletion is so high that the grains barely have an impact on the ionization chemistry. Once again, this threshold marks the regime in which the dust–gas mixture behaves as a grain-free plasma due to the recombination process primarily occurring in the gas-phase rather than onto the grains surface. Consequently, an even higher depletion would not change the ionization level, and ultimately the MRI.

Finally, the mean effective turbulence level is roughly independent of the vertically averaged dust-to-gas mass ratio once the MRI active layer is reached (Fig. 24a). This can be explained by a similar argument used in the previous section: Although the gas surface densities in the MRI active layer are lower for higher f_{dg} (which is expected to result in more charged particles available in the gas-phase due to stronger ionization), these charged particles are more efficiently captured by the dust for higher f_{dg}. It implies that the effective ionization level is actually not higher than the ones for lower f_{dg}; hence, the mean effective turbulence level in the MRI active layer is roughly constant regardless of f_{dg}.
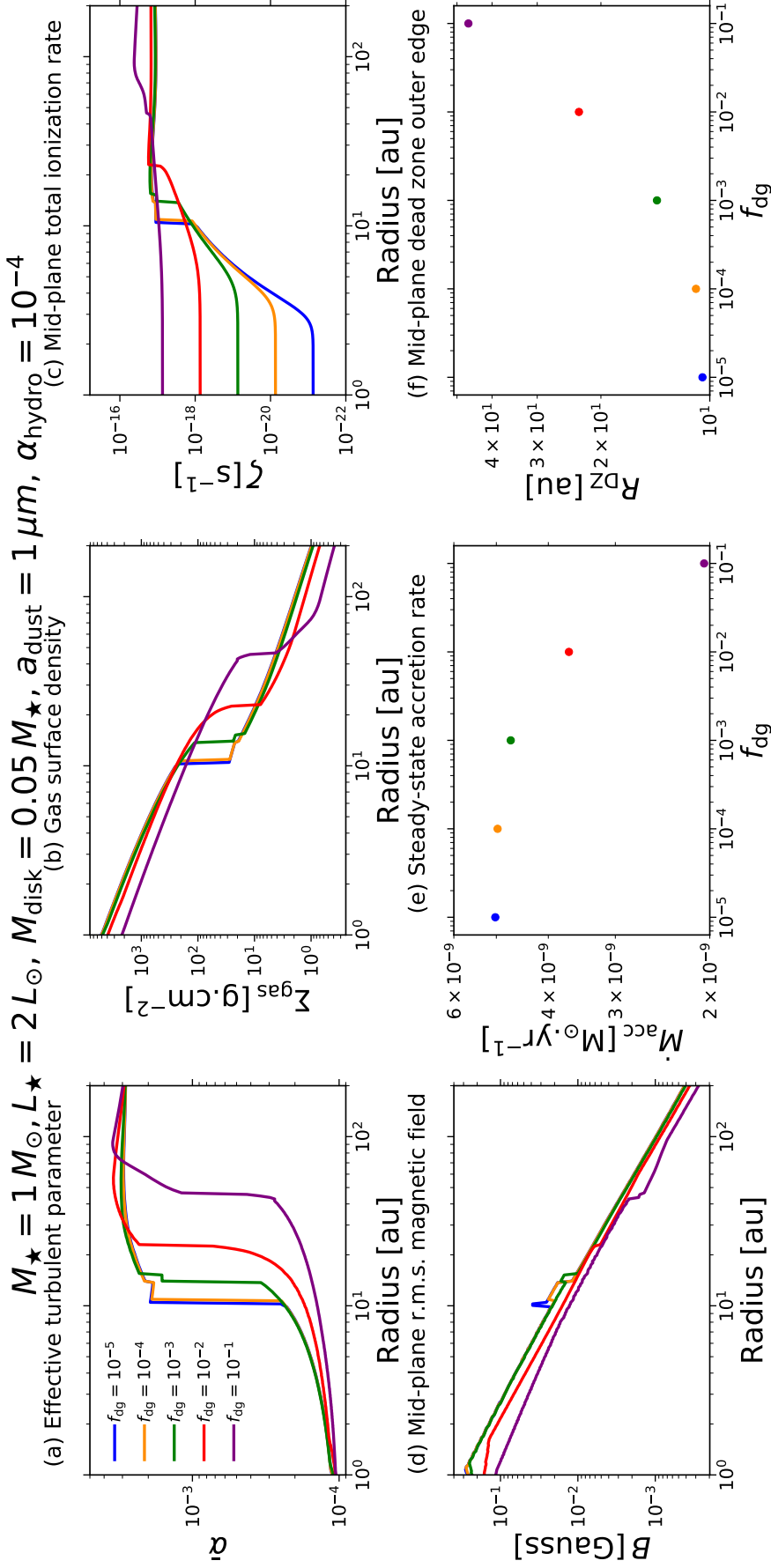
Figure 24: Model III. Effect of overall change in the vertically integrated dust-to-gas mass ratio on the equilibrium solution when varying the radially constant parameter f_{dg} from 10^{-5} (99.9 dust depletion relative to standard ISM) to 10^{-1} (dust-rich disk): The case $f_{dg} = 10^{-5}$ is shown in blue, $f_{dg} = 10^{-4}$ in dark orange, $f_{dg} = 10^{-3}$ in green, $f_{dg} = 10^{-2}$ in red (fiducial model), and $f_{dg} = 10^{-1}$ in purple. *Panels a–f* show the steady-state radial profiles of the same key quantities as in Fig. 22, but for the model parameters $M_\star = 1\,M_\odot$, $L_\star = 2\,L_\odot$, $M_{disk} = 0.05\,M_\star$, $a_{dust} = 1\,\mu m$, and $\alpha_{hydro} = 10^{-4}$.

4.4.3.2   *Local enhancements*

In the first scenario, a fixed local dust enhancement (either moderate or strong) is imposed at the expected dead zone outer edge location for the fiducial model ($r = 23$ au). By doing so, I investigate how the equilibrium solution changes if dust particles have accumulated at the dead zone outer edge before the steady-state accretion regime is reached. In the second scenario, a fixed local dust enhancement (either moderate or strong) is imposed at either $r = 5$ au or $r = 60$ au. Here the goal is to study how local dust enhancements due to, for example, spontaneous traffic jams can impact the steady-state accretion solution if they occur before the steady-state accretion regime is reached. Such traffic jams can form at locations where the gas pressure is enhanced (without the gas pressure gradient to necessarily flip of sign). This set of simulations corresponds to Model IV, and the results are presented in Fig. 26.

For both scenarios, a moderate local dust enhancement refers to a local change in the vertically averaged dust-to-gas mass ratio from 10^{-2} to 5×10^{-2} (referred to as "$5\times$ enhancement"), whereas a strong one refers to a local change from 10^{-2} to 10^{-1} (referred to as "$10\times$ enhancement"). Local dust enhancements are implemented by adding up Gaussian perturbations to a background vertically integrated dust-to-gas mass ratio:

$$B_i(r) = A \exp\left[-\frac{(r - r_{p,i})^2}{2\omega_i^2}\right], \tag{164}$$

where A is the dust enhancement level (either $A = 4$ for a moderate $5\times$ enhancement or $A = 9$ for a strong $10\times$ enhancement), and $r_{p,i}$, ω_i are the center and the width of the Gaussian perturbation, respectively. $r_{p,i} = 23$ au for the first scenario, whereas $r_{p,i} = 5$ au or $r_{p,i} = 60$ au for the second scenario. In all cases, $\omega_i = H_{gas}$ where H_{gas} is the vertical gas scale height defined in Eq. (63). The effective vertically averaged dust-to-gas mass ratio is thus defined as

$$f_{dg}(r) = f_{dg,bkg}\left[1 + B_i(r)\right], \tag{165}$$

where I choose the background value $f_{dg,bkg} = 10^{-2}$ to be the standard ISM value. The different profiles considered for the vertically averaged dust-to-gas mass ratio can be found in Fig. 25.

Figure 26 shows that imposing local dust enhancements before the steady-state accretion regime is reached can lead to the formation of steady-state pressure maxima close to the locations where dust has locally accumulated.

A local enhancement of dust implies a local increase in: (1) ^{26}Al locked into grains; and (2) the number of grains that can efficiently sweep up free electrons and ions. The former induces a local increase in the radionuclides ionization rate ("bumps" in Fig. 26c), hence a local increase in the gas ionization fraction in the gas-phase. The latter leads to a weaker MRI-driven turbulence where dust has accumulated. Figure 26a shows that a lower value for $\bar{\alpha}$ (i.e., a dip) is found at the locations where the dust has accumulated. It thus means that the local increase in the gas ionization fraction due to the decay of short- and long-lived radionuclides

is not enough to balance the decrease in the MRI activity due to stronger nonideal MHD effects. To maintain steady-state accretion ($\dot{M}_{acc}$ = cst), a dip in $\bar{\alpha}$ must be compensated by a bump in Σ_{gas}, hence in the gas pressure. If the perturbation (bump) in the gas pressure profile is significant enough, it can become a local pressure maximum (see Sect. 4.3.2.1).

The nature of such gas pressure perturbations (bumps) imposed by local dust enhancements depends on where and how much the dust has accumulated compared to the background value. Indeed, the effective turbulent parameter $\bar{\alpha}$ is much higher than the lower limit $\alpha_{hydro} = 10^{-4}$ in the MRI active layer, whereas $\bar{\alpha}$ is closer to α_{hydro} in the dead zone (see the fiducial model in Sect. 4.3.3). Additionally, the more dust particles accumulate at a given location in the disk, the deeper the dip in $\bar{\alpha}$ is, regardless of the location. Consequently, it is expected that local dust enhancements in the MRI active layer can generate deeper dips in $\bar{\alpha}$ compared to the ones in the dead zone, hence possibly producing stronger perturbations in the gas pressure profile, all in all depending on the enhancement level. Figure 26f shows that the perturbation in the gas pressure profile at $r = 5$ au (within the dead zone) – caused by the local dust enhancement at that location – does not correspond to a pressure maximum, regardless of the dust enhancement level (5× or 10×). Here I want to emphasize that this could change if the turbulence driven by hydrodynamic instabilities would be lower (e.g., $\alpha_{hydro} = 10^{-5}$), since a lower α_{hydro} value implies a possible deeper dip in $\bar{\alpha}$. Conversely, at $r = 60$ au (within the MRI active layer), one can clearly see that whether the perturbation corresponds to a pressure maximum or not depends on how much dust has locally accumulated. Interestingly, dust accumulation at the dead zone outer edge forms a pressure maximum there for both a 5× and 10× enhancement. This suggests that a spontaneous steady-state pressure maximum can be generated at the dead zone outer edge, even from a moderate amount of dust accumulation. Whether such a steady-state solution is actually reached everywhere in the disk is investigated in Chapter 6.

Such spontaneous steady-state pressure maxima are formed over a viscous evolution timescale $t_{visc,bump} \sim \Delta r^2 / \left[3\bar{\nu}(r = r_{bump}) \right]$ (see Sect. 2.2.3), where r_{bump} is the location of the pressure maximum, and $\Delta r = H_{gas}(r_{bump})$ is the width of the bump (assumed to be the width of the local dust accumulation producing such a pressure maximum). Table 3 summarizes the viscous formation timescales for the potential steady-state pressure maxima formed by the various local dust enhancement scenarios. One can conclude that when steady-state pressure maxima can form, they do so within the typical disk lifetime [5 − 10 Myrs; e.g., 276].

In summary, I find that: (1) no steady-state pressure maxima are expected to be formed in the dead zone except if the turbulence driven by hydrodynamic instabilities is lower than $\alpha_{hydro} = 10^{-4}$; (2) steady-state pressure maxima are expected to be formed in the MRI active layer only if the local dust enhancement level is strong (10×); (3) a steady-state pressure maximum can be formed at the dead zone outer edge, even for a moderate local dust enhancement (5× is enough); (4) steady-state pressure maxima are formed within the disk lifetime, hence promoting further dust trapping and inducing a self-increase in their trapping strength.
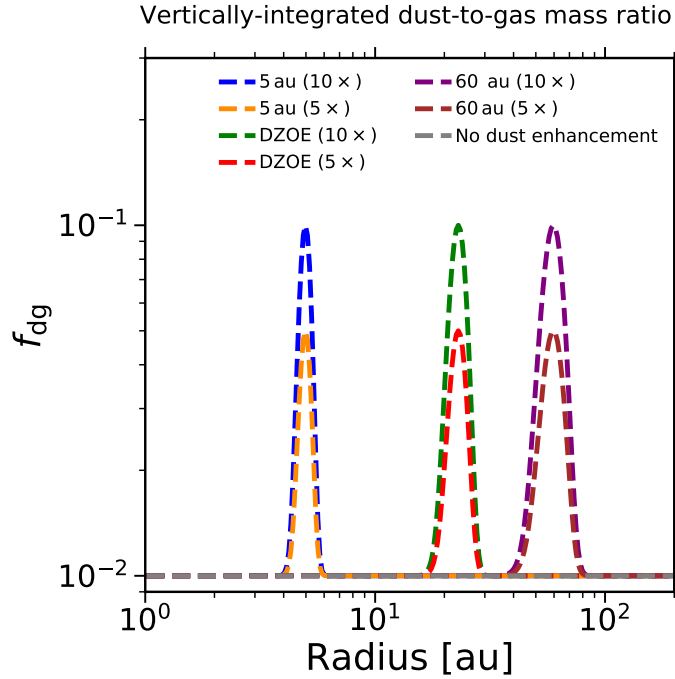
Figure 25: Vertically integrated dust-to-gas mass ratio profiles for different local dust enhancement scenarios.

$r_{p,i}$ [au]	5	23	60
Pressure maximum? (5× enhancement)	✗	✓	✗
Formation timescale [Kyrs]	–	37	–
Pressure maximum? (10× enhancement)	✗	✓	✓
Formation timescale [Kyrs]	–	41	18

Table 3: Summary of the viscous formation timescale of the steady-state pressure maxima formed by local dust enhancement at various locations in the protoplanetary disk. One should note that $r = 23$ au corresponds to the midplane dead zone outer edge location for the fiducial model described in Sect. 4.3.
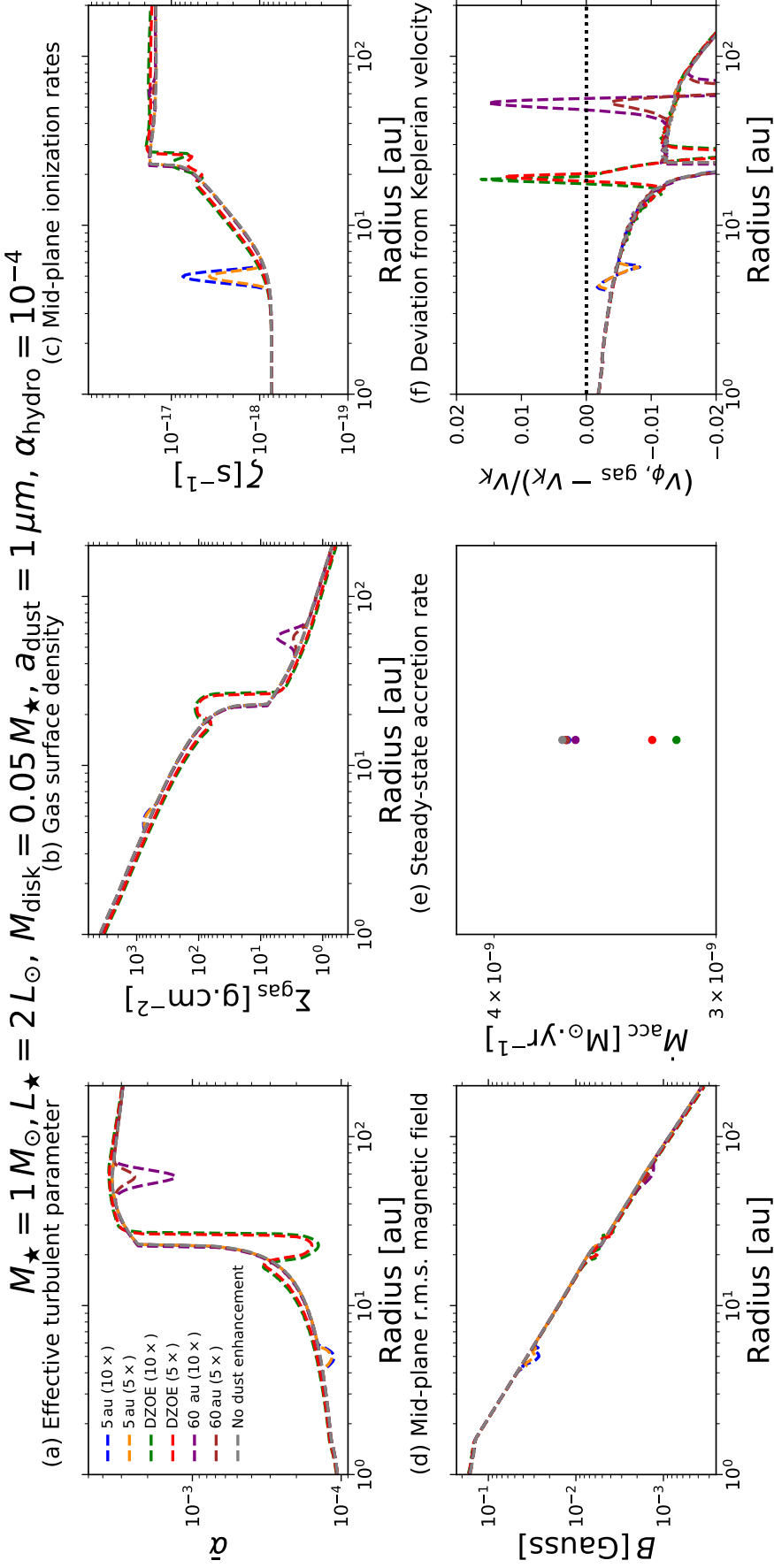
Figure 26: Model IV. Effect of local enhancements in the vertically integrated dust-to-gas mass ratio on the equilibrium solution by imposing f_{dg} to be radially variable with a local Gaussian perturbation at various locations (see the dust-to-gas mass ratio profiles in Fig. 25). The unperturbed value of f_{dg} is the same for all the simulations, equal to 10^{-2}. The "5 au (10×)" case (blue) corresponds to dust enhancement at r = 5 au, where f_{dg} varies from its unperturbed value to 10^{-1}. The "5 au (5×)" case (dark orange) is similar to the previous case, but f_{dg} goes up to 5×10^{-2} instead. The "DZOE (10×)" case (green) corresponds to dust enhancement at the expected dead zone outer edge (DZOE) location for the fiducial model (r = 23 au), where f_{dg} varies from its unperturbed value to 10^{-1}. The "DZOE (5×)" case (red) is similar to the previous case, but f_{dg} goes up to 5×10^{-2} instead. The "60 au (10×)" case (purple) corresponds to dust enhancement at r = 60 au, where f_{dg} varies from its unperturbed value to 10^{-1}. The "60 au (5×)" case (brown) is similar to the previous case, but f_{dg} goes up to 5×10^{-2} instead. The "No dust enhancement" case (gray) corresponds to the fiducial model. Panels a–e show the steady-state radial profiles of the same key quantities as in Fig. 22, but for the model parameters $M_\star = 1\,M_\odot$, $L_\star = 2\,L_\odot$, $M_{disk} = 0.05\,M_\star$, $a_{dust} = 1\,\mu m$, and $\alpha_{hydro} = 10^{-4}$. Panel f): Deviation from Keplerian velocity, where the dotted black line corresponds to $v_{gas,\phi} = v_K$.

4.4.4   *Effect of magnetic field strength*

In the fiducial model, I adopted the magnetic field strength required for the MRI activity to be at maximal efficiency (see Option A of Sect. 3.5.3). Here I explore how assuming either weaker or stronger magnetic field strengths change the equilibrium solution, and show that Option A of Sect. 3.5.3 for the magnetic field strength leads to the highest value for the accretion rate possibly reachable by the equilibrium solution given the set of criteria for active MRI employed in the global MRI-driven disk accretion model of Chapter 3. To do so, I assume various constant midplane r.m.s. plasma-β parameters, β_{mid}, such that $\beta_{mid} \in \{10, 10^2, 10^3, 10^4, 10^5\}$. Then I calculate the corresponding r.m.s. midplane magnetic field strength with $B_{mid} = \sqrt{(8\pi\rho_{gas}c_s^2)/\beta_{mid}}$, and finally obtain B by assuming the magnetic field is vertically constant ($B(r,z) = B(r,z=0) = B_{mid}$). This set of simulations corresponds to Model V, and the results are presented in Fig. 27.

For $\beta_{mid} = 10$, ambipolar diffusion utterly prohibits any MRI-driven turbulence at any locations in the disk because the magnetic field strength is too strong; leading to $\bar{\alpha} = \alpha_{hydro} = 10^{-4}$ at every radii, hence to the lowest accretion rate. For $\beta_{mid} = 10^2$, the MRI can only operate in regions beyond 54 au (there is no MRI active layer sitting above the dead zone for $r \lesssim 54$ au). Although the effective turbulence is higher in such regions for this scenario compared to the MRI-optimal one, the midplane dead zone outer edge is roughly located as twice as far, implying that the accretion rate is overall lower. For $\beta_{mid} = 10^3$, the field strength is such that the MRI can only operate in the upper layers for $r \gtrsim 10$ au, and from the midplane for $r \gtrsim 30$ au. Since this field strength is overall lower than the one constrained for the MRI-optimal scenario in the MRI active layer, the local MRI-driven turbulence is weaker (hence lower $\bar{\alpha}$). Finally, for $\beta_{mid} = 10^4$ and $\beta_{mid} = 10^5$, the MRI can only effectively operate in the surface layers (there is no longer a midplane MRI active layer). On one hand, for $\beta_{mid} = 10^4$, the MRI could in theory develop at the midplane for $r \gtrsim 100$ au. In practice, though, the induced midplane $\alpha_{MRI} = 3.3 \times 10^{-5}$ (radially constant) is less than $\alpha_{hydro} = 10^{-4}$. As a result, I consider such regions as dead by fiat (see Eq. 157). On the other hand, for $\beta_{mid} = 10^5$, the MRI cannot operate at the midplane because Eq. (150) is not fulfilled. Consequently, the midplane is weakly turbulent for both cases ($\bar{\alpha} \approx \alpha_{hydro}$), since the MRI active layer is located too high in the disk atmosphere to significantly contribute to the effective turbulence level.

4.4.5   *Effect of hydrodynamic turbulent parameter*

Previous work on hydrodynamic instabilities suggest that α_{hydro} could approximately range from 10^{-5} to 10^{-3} [e.g., 80–86, 251]. In the global MRI-driven disk accretion model of Chapter 3, I always choose the fiducial value $\alpha_{hydro} = 10^{-4}$ motivated by the most recent studies on the VSI. Here I investigate how the variation in this parameter could potentially change the equilibrium solution by running a
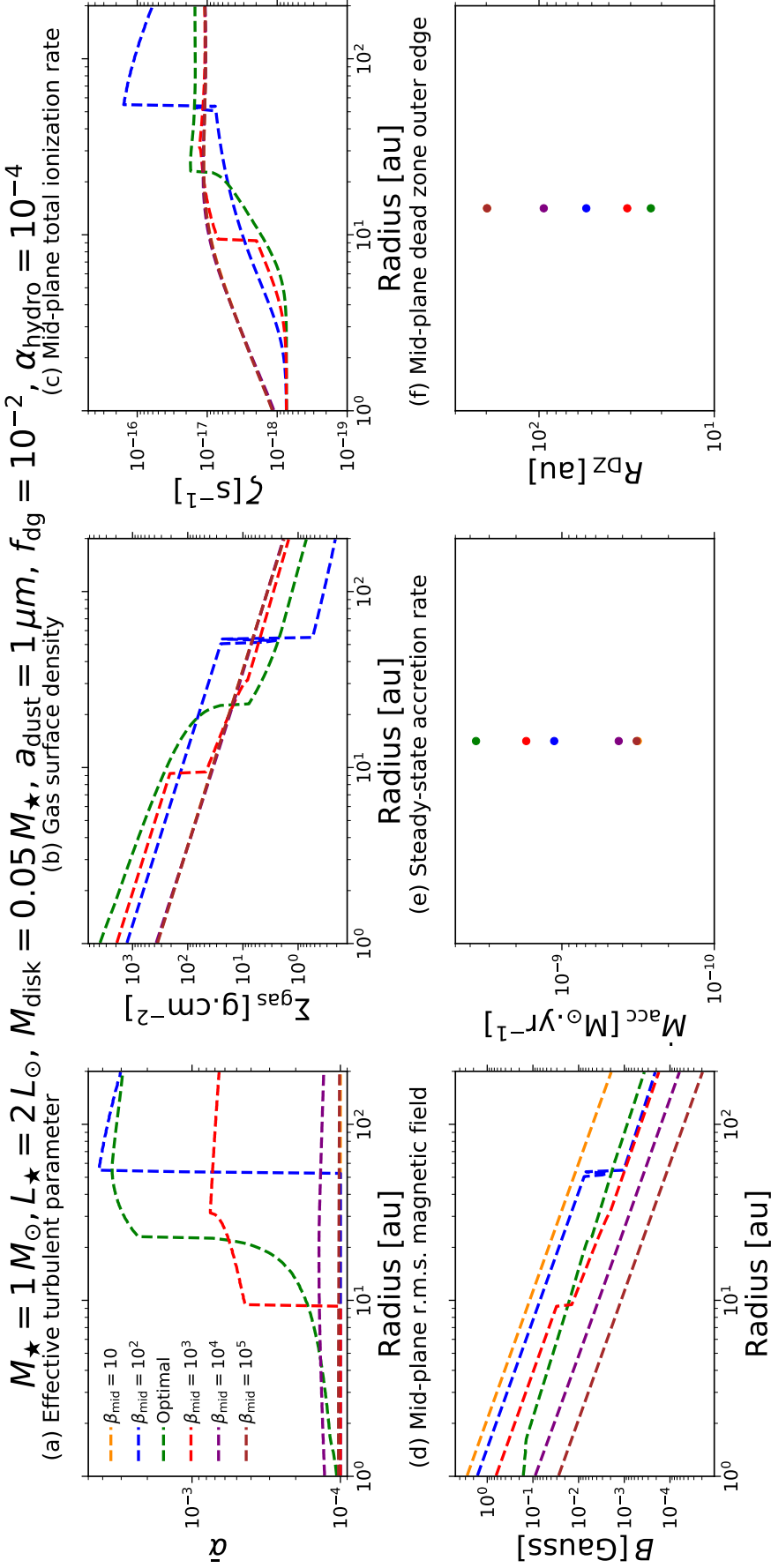
Figure 27: Model V. Effect of the magnetic field on the equilibrium solution when exploring weaker and stronger scenarios compared to the MRI-optimal field. Various constant midplane r.m.s. plasma-β parameters, β_{mid}, were considered such that $\beta_{mid} \in \{10, 10^2, 10^3, 10^4, 10^5\}$. The "optimal" case (green) corresponds to the field strength used in the fiducial model, namely, the field strength that is required for the MRI activity to be at the maximal efficiency as permitted by Ohmic resistivity and ambipolar diffusion. Panels a, b, c, e, f show the steady-state radial profiles of the same key quantities as in Fig. 22, but for the model parameters $M_\star = 1\,M_\odot$, $L_\star = 2\,L_\odot$, $M_{disk} = 0.05\,M_\star$, $a_{dust} = 1\,\mu m$, $f_{dg} = 10^{-2}$, and $\alpha_{hydro} = 10^{-4}$. Panel d: Midplane r.m.s. magnetic field strengths corresponding to the various β_{mid} as well as the MRI-optimal r.m.s. magnetic field strength (green).

set of simulations where α_{hydro} is taken in the list $\{10^{-5}, 10^{-4}, 10^{-3}\}$. This set of simulations corresponds to Model VI, and the results are presented in Fig. 28.

The stronger the hydrodynamic-driven turbulence is, the higher the overall effective turbulence level is, resulting in a shorter timescale for accretion to occur. Consequently, a larger α_{hydro} value induces a larger accretion rate (Fig. 28e). Overall, though, I find a weak dependence of $\dot{M}_{acc}$ on α_{hydro} ($\dot{M}_{acc} \propto \alpha_{hydro}^{0.31}$).

In the global turbulence model, it is a requirement for any potential MRI active regions to have a turbulence level that exceeds the turbulence set by hydrodynamic stresses. For higher α_{hydro}, the MRI needs to generate stronger turbulence to fulfill this requirement. The dead zone maximal radial extent is thus larger (Fig. 28f), since the gas is more ionized in the outer regions of the protoplanetary disk where this can happen. Similarly to what I discussed in the previous paragraph, I find a weak dependence of R_{DZ} on α_{hydro} ($R_{DZ} \propto \alpha_{hydro}^{0.22}$).

Finally, I showed that the effective turbulence level in the MRI active layer is quenched by ambipolar diffusion to $\langle \bar{\alpha} \rangle_{MRI} \approx 3 \times 10^{-3}$ for the fiducial model. It implies that the profile for the effective turbulent parameter, $\bar{\alpha}$, is the smoothest for $\alpha_{hydro} = 10^{-3}$ (Fig. 28a). Consequently, the corresponding steady-state gas surface density displays a much smoother profile $\Sigma_{gas} \propto r^{-1.22}$ compared to the others obtained for lower α_{hydro}, which is close to the constant-α model solution $\Sigma_{gas} \propto r^{-1}$ (Fig. 28b). Knowing how the gas is distributed across the protoplanetary disk could thus provide hints on the overall turbulence set by hydrodynamic instabilities such as the VSI.

4.4.6 *Effect of gas temperature model*

There are a number of uncertainties in determining what the real gas temperature is in protoplanetary disks. To explore the impact of such uncertainties on the equilibrium solution, I run two simulations where the gas temperature model is adopted from either the optically thin approximation (T follows Eq. 46) or optically thick approximation (T follows Eq. 47). This set of simulations corresponds to Model VII, and the results are presented in Fig. 30. The two profiles for the gas temperature model can be found in Fig. 29, obtained for $L_\star = 2\,L_\odot$.

Overall, one can notice that the choice made for the gas temperature model has very little impact on the equilibrium solution. This can be simply explained by noting that the optical thick model is only 1.5 times colder than the thin model. Additionally, most of the disk parameters only weakly depend on the gas temperature profile T. For instance, the vertical gas scale height scales as $H_{gas} \propto \sqrt{T}$, the gas-phase recombination rate scales as $k \propto T^{-0.69}$, and the rate for the adsorption rate onto the grains scales as $\propto \sqrt{T}$. Consequently, the ionization chemistry is barely modified by the variation from optically thick to optically thin.
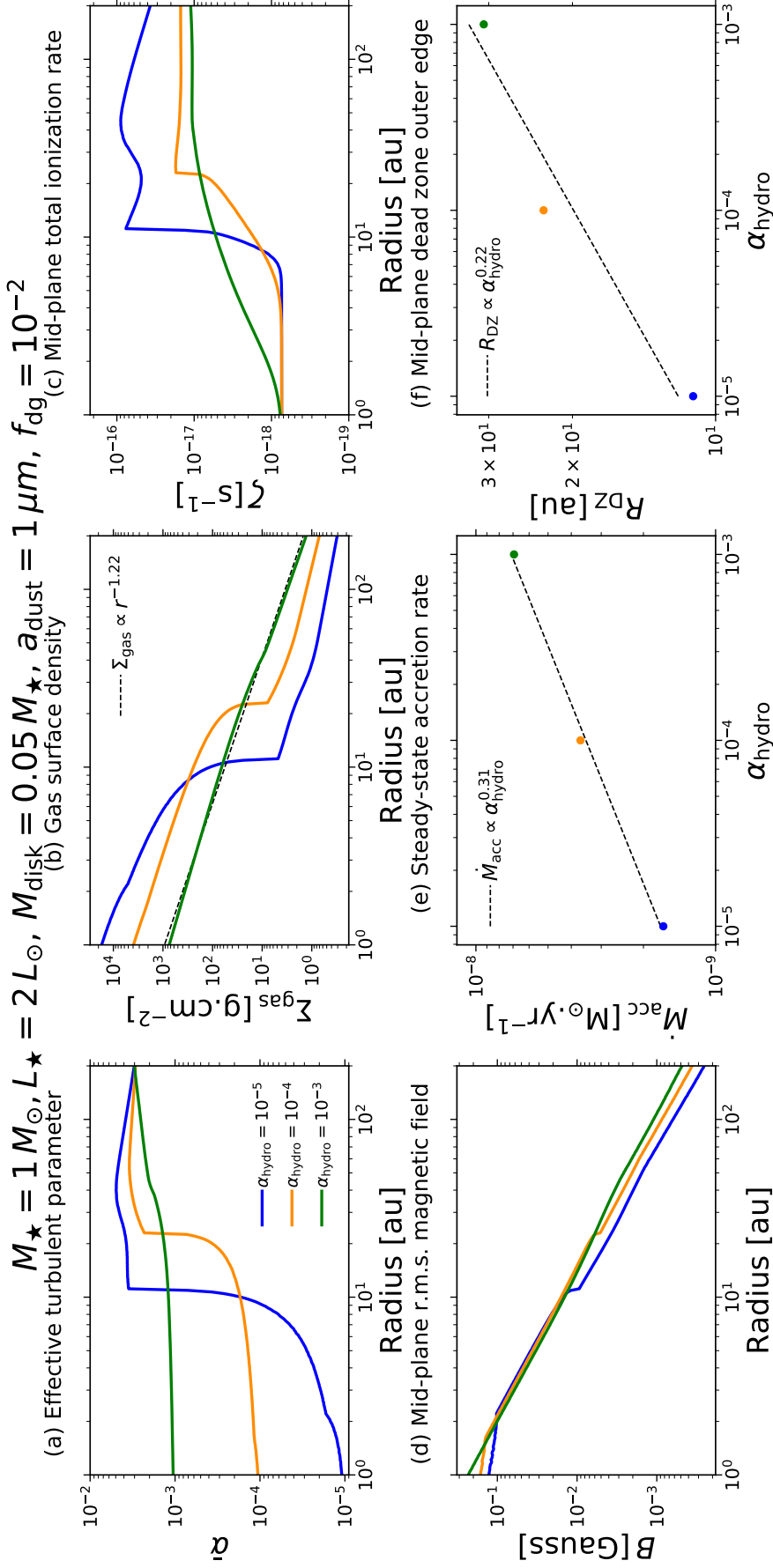
Figure 28: Model VI. Effect of the hydrodynamic turbulent parameter on the equilibrium solution when varying α_{hydro} from 10^{-5} to 10^{-3}: The case $\alpha_{hydro} = 10^{-5}$ is shown in blue, $\alpha_{hydro} = 10^{-4}$ in dark orange (fiducial model), and $\alpha_{hydro} = 10^{-3}$ in green. Panels a–f show the steady-state radial profiles of the same key quantities as in Fig. 22, but for the model parameters $M_\star = 1\,M_\odot$, $L_\star = 2\,L_\odot$, $M_{disk} = 0.05\,M_\star$, $a_{dust} = 1\,\mu m$, and $f_{dg} = 10^{-2}$. The dashed black line in Panel b corresponds to a power-law fit of Σ_{gas} as a function of distance from the star, r. The dashed black lines in Panels e, f correspond to a power-law fit of $\dot{M}_{acc}$ and R_{DZ} as a function of α_{hydro}, respectively.
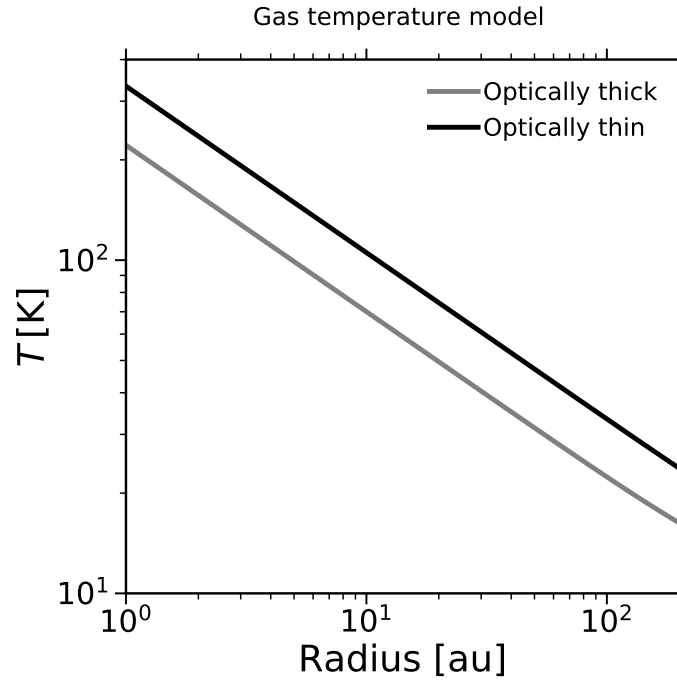
Figure 29: Gas temperature profiles in the optically thin and thick approximation, obtained for $L_\star = 2\,L_\odot$.

Stellar model	$M_\star\,[M_\odot]$	$L_\star\,[L_\odot]$
Star 1	0.05	2×10^{-3}
Star 2	0.1	8×10^{-2}
Star 3	0.3	0.2
Star 4	1	2
Star 5	2	20

Table 4: Summary of the stellar parameters (mass, $M_\star$, and luminosity, $L_\star$) used to investigate the effect of stellar properties on the equilibrium solution. The star 4 model corresponds to the Sun-like star used in the fiducial model described in Sect. 4.3.
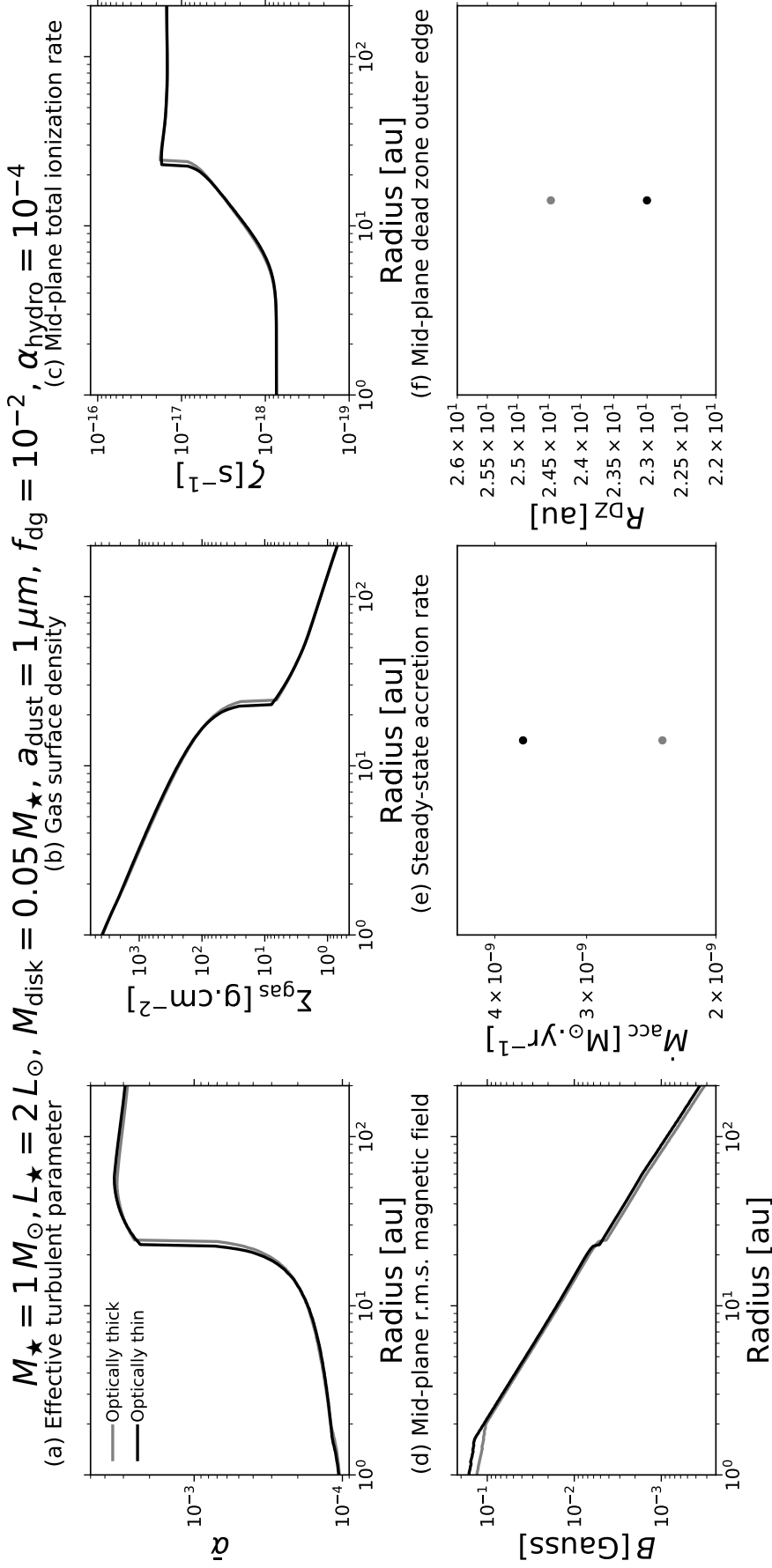
$M_\star = 1\,M_\odot,\ L_\star = 2\,L_\odot,\ M_{\mathrm{disk}} = 0.05\,M_\star,\ a_{\mathrm{dust}} = 1\,\mu m,\ f_{\mathrm{dg}} = 10^{-2},\ \alpha_{\mathrm{hydro}} = 10^{-4}$

Figure 30: Model VII. Effect of the gas temperature model on the equilibrium solution by varying the radial profile T(r). The "optically thick" case (gray) and the "optically thin" case (black) correspond to the gas temperature profiles displayed in Fig. 29. The optically thin case corresponds to the gas temperature profile used in the fiducial model described in Sect. 4.3. Panels a–f show the steady-state radial profiles of the same key quantities as in Fig. 22, but for the model parameters $M_\star = 1\,M_\odot$, $L_\star = 2\,L_\odot$, $M_{\mathrm{disk}} = 0.05\,M_\star$, $a_{\mathrm{dust}} = 1\,\mu m$, $f_{\mathrm{dg}} = 10^{-2}$, and $\alpha_{\mathrm{hydro}} = 10^{-4}$.

4.4.7 *Effect of stellar properties*

4.4.7.1 *Total disk gas mass independent of stellar mass*

Finally, I explore how the stellar properties impact the equilibrium solution by running five simulations, covering the possible range from very low-mass to Herbiglike stars. For each star of interest, both the stellar mass and bolometric luminosity change and are taken from Table 4. Moreover, I avoid the effect of total disk gas mass on the equilibrium solution (see Sect. 4.4.1) by setting the total disk gas mass independent of stellar mass and equal to $0.01\,M_\odot$. This set of simulations corresponds to Model VIII, and the results are presented in Fig. 31.

Going from star 1 to star 5 model, both the stellar mass and bolometric luminosity increase (the latter way faster than the former). A higher bolometric luminosity leads to (slightly) higher gas temperature (see Eqs. 46 and 47), and higher total stellar X-rays luminosity ($L_{XR} \propto L_\star$). Since the effect of gas temperature is weak and barely impacts on the MRI activity (see Sect. 4.4.6), a higher bolometric luminosity implies a positive feedback on the MRI because it produces a higher total stellar X-rays luminosity, generating more charged particles in the gas-phase.

Figures 31e and 31f show that star 4 and 5 models have a higher accretion rate and a more compact dead zone compared to star 1-3 models (the highest accretion rate and most compact dead zone are obtained for the star 5 model). One way to understand this result is by looking at Fig. 31c. One can notice that the midplane ionization rate is much higher for star 4 and 5 models compared to star 1-3 models, with the distinctive shape seen in Sect. 4.4.1 for $M_{disk} = 0.005\,M_\star$ or $M_{disk} = 0.01, M_\star$. Such a shape indicates that stellar X-rays utterly dominate the ionization process in most of the disk, included at the midplane. Since the ionization level is much higher for star 4 and 5 models, the nonideal effects are less stringent (Fig. 31d, where the MRI-optimal r.m.s. magnetic field strength is higher for star 4 and 5 models). As a result, the MRI can be more easily triggered (more compact dead zones) and the MRI-driven turbulence is stronger (higher accretion rates) for high-mass and more luminous stars.

Conversely, I find a weaker dependence of R_{DZ} and $\dot{M}_{acc}$ on $M_\star$ for star 1-3 models. With a subdominant ionization from stellar X-rays at the midplane, the significant increase in $L_\star$ (hence L_{XR}) from star 1 to 3 model does not have as much impact as seen for star 4 and 5 models, since galactic cosmic rays dominate the ionization process at the midplane. As a result, R_{DZ} and $\dot{M}_{acc}$ primarily depends on $M_\star$, and not on $M_\star$ and $L_\star$, as it is the case for star 4 and 5 models (R_{DZ} depends on $L_\star$ only weakly through T for low-mass and less luminous stars). Since $M_\star$ weakly increases from star 1 to 3 model, one can understand the weaker dependence of R_{DZ} and $\dot{M}_{acc}$ on $M_\star$ for low-mass and less luminous stars.

Finally, one should note that the aspect ratio can be as large as 0.4 in the disk outer regions for star 1 and 2 models. I thus caution the reader that the profiles shown for these stars may not be valid for $r \gtrsim 40\,au$, where the thin disk approximation reaches its limit (the aspect ratio is < 1, but not $\ll 1$). Nevertheless,

the global picture for the effect of stellar properties is expected to still hold as described.

Here I investigated the effect of stellar properties alone by setting the total disk gas mass to the fixed stellar-independent value, $M_{disk} = 0.01 \, M_{\odot}$. However, this choice leads to very peculiar total disk gas masses relative to their stellar mass for the star 1 model ($M_{disk} = 0.2 \, M_{\star}$) and the star 5 model ($M_{disk} = 0.005 \, M_{\star}$). Although $M_{disk} = 0.2 \, M_{\star}$ for the star 1 model, one should note that the corresponding Toomre parameter Q is still higher than 2 at all radii, implying that the disk around this star is not self-gravitating. In the next section, I present a set of simulations with a stellar-dependent total disk gas mass ($M_{disk} = 0.05 \, M_{\star}$), which represents a more realistic choice for the gas component of protoplanetary disks.

4.4.7.2 *Total disk gas mass dependent on stellar mass*

For each star model in Table 4, I now run a simulation with a more realistic choice for the total disk gas mass relative to the stellar mass ($M_{disk} = 0.05 \, M_{\star}$, stellar-dependent choice). These simulations thus encapsulate the combined effect of stellar properties and total disk gas mass on the MRI-driven turbulence. This set of simulations corresponds to Model IX, and the results are presented in Fig. 32.

The trend seen in Sect. 4.4.7 where high-mass and more luminous stars generate higher accretion rates still holds, which is expected because a higher total disk gas mass has a higher gas content that can be accreted onto the central star.

The dead zone maximal radial extent now displays a different trend compared to what I showed for the effect of stellar properties alone (see previous section). Indeed, a high-mass and more luminous star has a more massive disk, hence higher gas surface densities. The effect of total disk gas mass can thus compensate for the effect of stellar properties by significantly reducing the overall ionization level, resulting in a more extended dead zone. Nonetheless, Fig. 32f displays the interesting feature that the dead zone maximal radial extent (R_{DZ}) saturates for star 4 model. This saturation can be attributed to stellar X-rays that dominates the midplane ionization process for stars more massive and luminous that star 4 model, as showed by Fig. 32c. The high total stellar X-rays luminosity (L_{XR}) produced by such stars regulates the radial extent of the dead zone. Consequently, it seems that dead zones cannot become indefinitely large for high-mass and more luminous stars. To validate this idea, I run six additional simulations for each star model in Table 4, varying the total disk gas mass from $M_{disk} = 0.001 \, M_{\star}$ to $M_{disk} = 0.10 \, M_{\star}$. For all the total disk gas masses considered, I confirm that the dead zone maximal radial extent saturates for stars more massive and luminous than star 4 model. Similarly, I find that the dead zone maximal radial extent cannot become indefinitely small for stars less massive and luminous than star 2 model due their too low total stellar X-rays luminosity (Fig. 32f shows that the dead zone maximal radial extent is higher for star 1 than star 2 model).
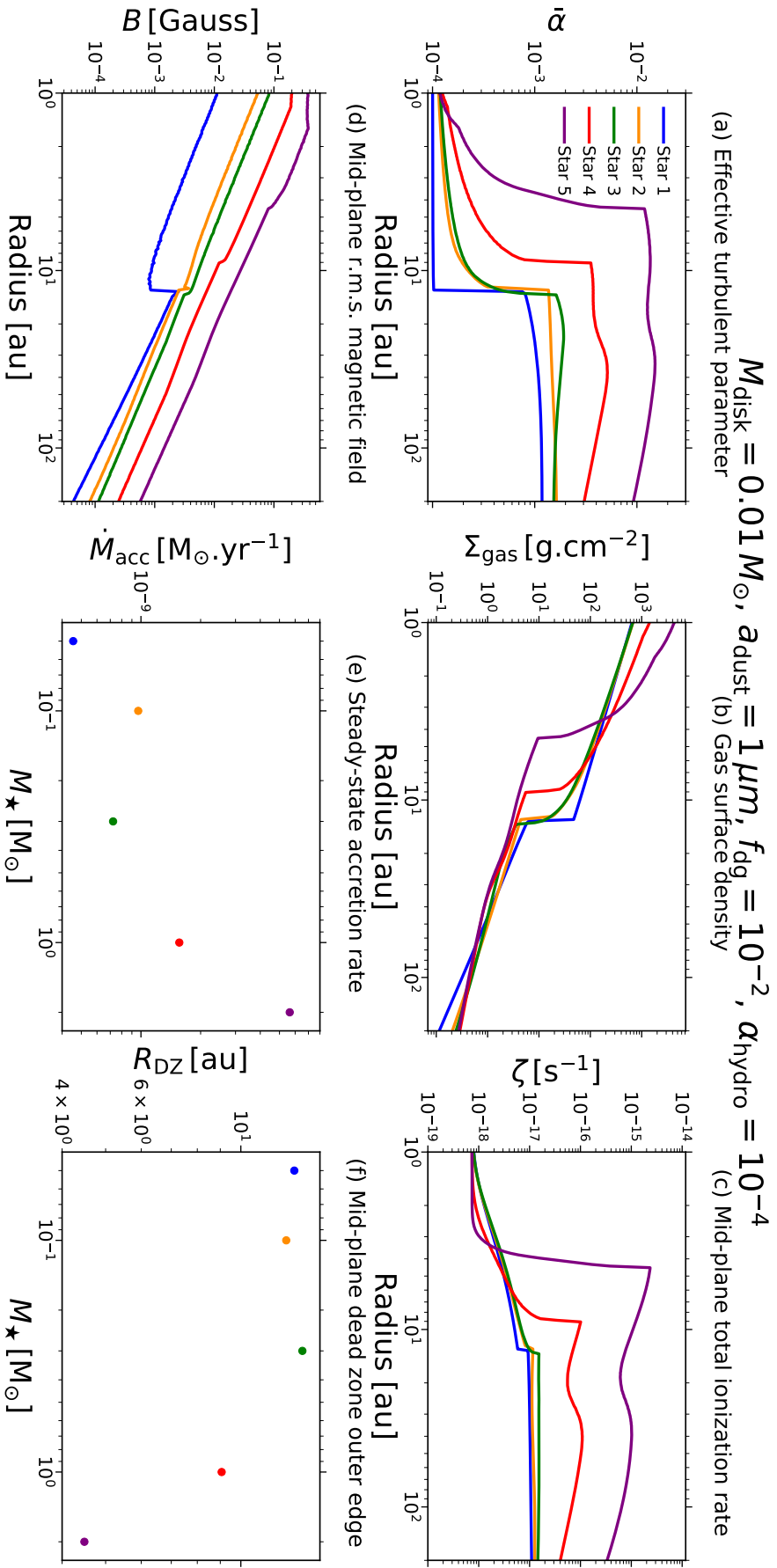
Figure 31: Model VIII. Effect of stellar properties on the equilibrium solution when varying the parameters $M_\star$ and $L_\star$ together, all the way from accreting brown dwarfs to Herbig stars. The total disk gas mass does not depend on stellar mass and is such that $M_{disk} = 0.01\,M_\odot$. The "star 1" case (blue) corresponds to a star of mass $M_\star = 0.05\,M_\odot$ and bolometric luminosity $L_\star = 2 \times 10^{-3}\,L_\odot$. The "star 2" case (dark orange) corresponds to a star of mass $M_\star = 0.1\,M_\odot$ and bolometric luminosity $L_\star = 8 \times 10^{-2}\,L_\odot$. The "star 3" case (green) corresponds to a star of mass $M_\star = 0.3\,M_\odot$ and bolometric luminosity $L_\star = 0.2\,L_\odot$. The "star 4" case (red) corresponds to the fiducial model where the stellar mass is $M_\star = 1\,M_\odot$ and the bolometric luminosity is $L_\star = 2\,L_\odot$. The "star 5" case (purple) corresponds to a star of mass $M_\star = 2\,M_\odot$ and bolometric luminosity $L_\star = 20\,L_\odot$. Panels a–f show the steady-state radial profiles of the same key quantities as in Fig. 22, but for the model parameters $\alpha_{dust} = 1\,\mu m$, $f_{dg} = 10^{-2}$, and $\alpha_{hydro} = 10^{-4}$.
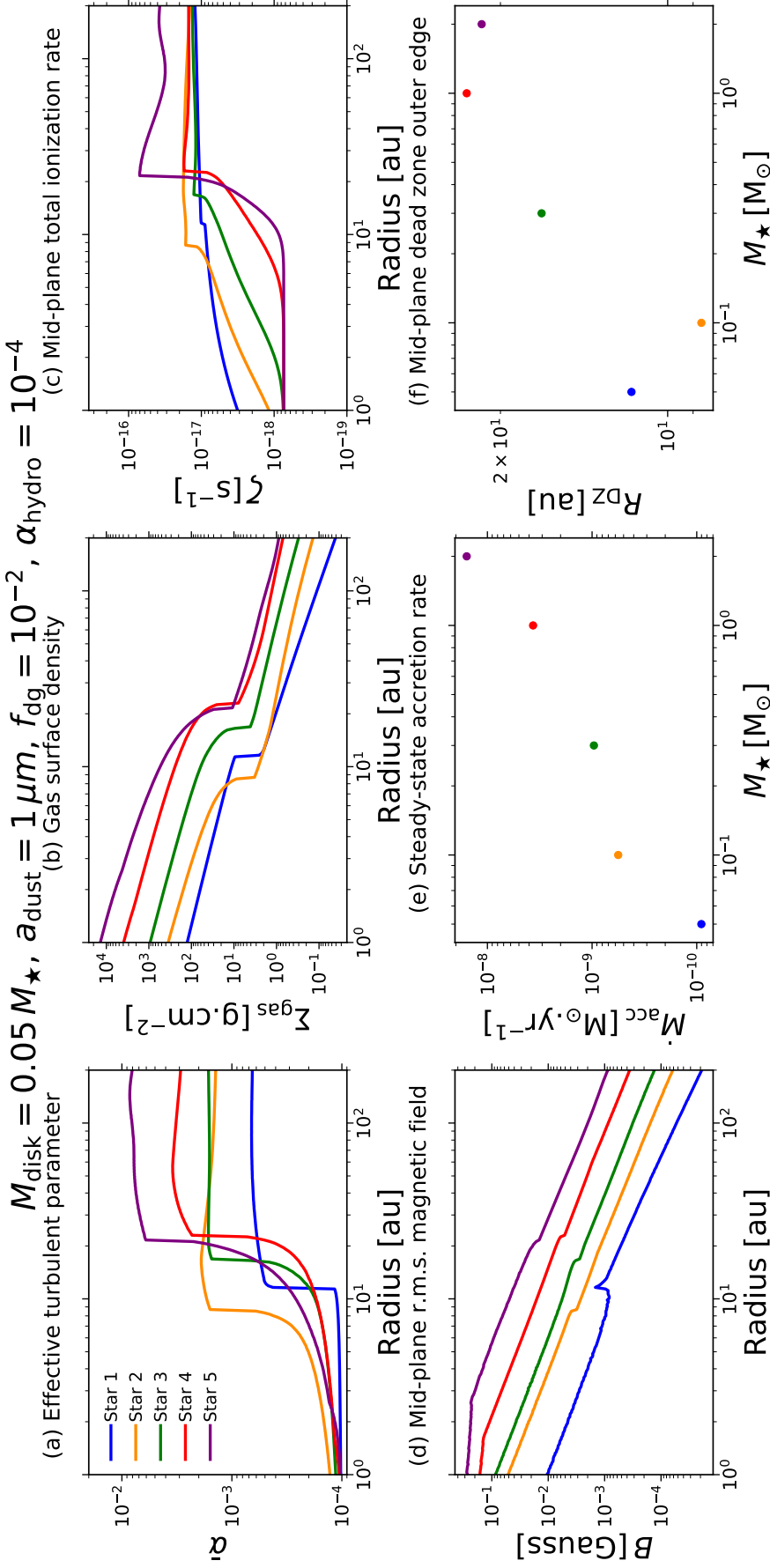
Figure 32: Model IX. Combined effect of stellar properties and total disk gas mass on the equilibrium solution when varying the parameters $M_\star$ and $L_\star$ together, all the way from accreting brown dwarfs to Herbig stars. The total disk gas mass depends on the stellar mass and is such that $M_{\mathrm{disk}} = 0.05\,M_\star$. The "star 1" case (blue) corresponds to a star of mass $M_\star = 0.05\,M_\odot$ and bolometric luminosity $L_\star = 2 \times 10^{-3}\,L_\odot$. The "star 2" case (dark orange) corresponds to a star of mass $M_\star = 0.1\,M_\odot$ and bolometric luminosity $L_\star = 8 \times 10^{-2}\,L_\odot$. The "star 3" case (green) corresponds to a star of mass $M_\star = 0.3\,M_\odot$ and bolometric luminosity $L_\star = 0.2\,L_\odot$. The "star 4" case (red) corresponds to the fiducial model where the stellar mass is $M_\star = 1\,M_\odot$ and the bolometric luminosity is $L_\star = 2\,L_\odot$. The "star 5" case (purple) corresponds to a star of mass $M_\star = 2\,M_\odot$ and bolometric luminosity $L_\star = 20\,L_\odot$. *Panels a–f* show the steady-state radial profiles of the same key quantities as in Fig. 22, but for the model parameters $a_{\mathrm{dust}} = 1\,\mu m$, $f_{\mathrm{dg}} = 10^{-2}$, and $\alpha_{\mathrm{hydro}} = 10^{-4}$.

4.4.8   *Effect of grain size distribution*

In the fiducial model, I used the single grain size approximation to describe the dust component of the protoplanetary disk. I explore now how the equilibrium solution is impacted when accounting for a grain size distribution, which is a much more realistic choice supported by observations. In practice, I assume the grain size distribution to follow a power-law that is determined by the three parameters a_{min}, $a_{dist,Max}$, and $p_{dist,Exp}$; respectively the distribution minimum grain size, maximum grain size, and exponent (based on the distribution of interstellar grains [151]). In the grain size range $[a, a + da]$, it reads as follows:

$$n'_{dust}(a)\,da \propto \begin{cases} a^{p_{dist,Exp}}\,da & \text{if } a_{min} \leqslant a \leqslant a_{dist,Max} \\ 0 & \text{otherwise} \end{cases} , \qquad (166)$$

where $n'_{dust}(a)$ refers to the dust number density per grain size, and is a distribution function over a. It differs from $n_{dust}(a)$ of Sect. 2.3, which is already the quantity integrated over the bin size around grain size a (following the code `DustPy`). The dust surface density for each grain species of size a, $\Sigma_{dust}(r, a)$, then follows from the conservation of the total dust mass: The quantity $\Sigma_{dust,tot}(r) = \sum_a \Sigma_{dust}(r, a)$ must be equal to $f_{dg,tot}(r)\Sigma_{gas}(r)$, where $f_{dg,tot}(r)$ is the vertically integrated total dust-to-gas mass ratio (accounting for all grain species) at radius r. For Models X–XII, I take $f_{dg,tot} = 10^{-2}$ and radially constant.

I run three sets of simulations where the effect of each parameter of the grain size distribution (a_{min}, $a_{dist,Max}$, and $p_{dist,Exp}$) is studied by varying them one at a time. In the following, I present the impact of a variation in $a_{dist,Max}$, while fixing $a_{min} = 0.1\,\mu m$ and $p_{dist,Exp} = -3.5$. This set of simulations corresponds to Model X, and the results are presented in Fig. 33.

Figures 33a, 33e and 33f show that a higher $a_{dist,Max}$ leads to stronger MRI-driven turbulence overall, a higher gas accretion rate, and a more compact dead zone. When larger grain sizes are included in the dust distribution, the overall ionization level becomes higher (Fig. 33c), leading to enough charged particles in the gas-phase for the magnetic field to couple with, mainly due to two reasons: (1) Dust settling becomes more important, which locally leads to an increase in the dust-to-gas mass ratio at the midplane, hence promoting the ionization power of radionuclides (dominating the ionization process in the inner regions of the dead zone). (2) The total grain surface area, A_{tot}, decreases (i.e., grains can less efficiently adsorbe free electrons or ions onto their surfaces), resulting in the gas-phase recombination more easily dominating the recombination process over grain surface adsorption. A_{tot} decreases because a fraction of the smaller sizes in the dust distribution is replaced by larger sizes, implying that charged particles in the gas-phase encounter, per unit volume and on average, less small dust particles.

Consequently, the MRI can operate with stronger magnetic field strengths on average (Fig. 33d). Finding stronger B overall for increasing $a_{dist,Max}$ means that ambipolar diffusion becomes less stringent, allowing for MRI-driven turbulence with stronger magnetic field strengths. Furthermore, the MRI can operate closer

to the central star, leading the dead zone outer edge to be almost located as twice as close for $a_{\mathrm{dist,Max}} = 10\,\mu\mathrm{m}$ compared to $a_{\mathrm{dist,Max}} = 1\,\mu\mathrm{m}$. Interestingly, one can notice that the dead zone outer edge is within 10–50 au, and even 10–20 au for $a_{\mathrm{dist,Max}} \geqslant 100\,\mu\mathrm{m}$, for the given model parameters. The situation in which the midplane would be almost entirely MRI-dead (gray dashed line in Fig. 33a), obtained assuming a mono-disperse dust distribution of fixed size $a_{\mathrm{mono}} = 0.1\,\mu\mathrm{m}$, is thus greatly mitigated when a dust distribution with different sizes is taken into account. I find that the presence of micron-sized particles in the dust size distribution, on top of the submicron-sized particles, prevents the dead zone from extending up to ~ 100 au for the choice made for the magnetic field strength and configuration.

Figure 33a shows that the solid colored lines lie within the dashed gray and black lines, representing the two limiting scenarios for $\bar{\alpha}$ in which all the dust would be either in the form of grains of size $a_{\mathrm{mono}} = 0.1\,\mu\mathrm{m}$ or $a_{\mathrm{mono}} = 1\,\mathrm{cm}$, respectively. Since the minimum grain size of Model I is $a_{\mathrm{min}} = 0.1\,\mu\mathrm{m}$ and its maximum grain size is $a_{\mathrm{dist,Max}} = 1\,\mathrm{cm}$, it is expected that the $\bar{\alpha}$ obtained from such dust distributions with different grain sizes can neither represent a less MRI active scenario than the dashed gray line, nor a more MRI active scenario than the dashed black line. It is worth mentioning that the models with growth (solid colored lines) converge toward the grain-free scenario for the model parameters considered, corresponding to the dashed black line. The dashed black line mimics the grain-free scenario because the recombination process occurs in the gas-phase rather than onto the grains surface when all grains are of size 1 cm. Indeed, the dashed black line of Fig. 33a is identical to the red and purple lines of Fig. 8a of [184] as well as their blue and yellow lines of Fig. 9a, implying that this is the grain-free steady-state solution because it is independent of the dust properties considered.

From Fig. 33, one can infer that the presence of larger sizes in the dust distribution (due to dust growth) substantially impacts the MRI-driven turbulence. Particularly, one can expect dust growth to have a major positive impact on the MRI activity in regions where grain surface absorption is the main process for recombination (this recombination regime is highly sensitive to the dust properties), whereas such impact is expected to be weak in regions where the recombination process is dominated by gas-phase recombination (this recombination regime is weakly dependent of the dust properties). Figure 33a even shows that the overall effective turbulence level in the inner regions of the dead zone ($\bar{\alpha}$ for $r \lesssim 10$ au) is noticeably different depending on $a_{\mathrm{dist,Max}}$. This suggests that dust growth is able to change the activity in the MRI active layer sitting above the dead zone such that the effective turbulence level in the dead zone increases. Furthermore, it seems that dust growth does not need to be very efficient to generate a significant boost in the MRI-driven turbulence. Indeed, the positive feedback obtained from the presence of larger grain sizes on the MRI activity is getting less noticeable once the maximum grain size is larger than 100 μm. For example, the gas accretion rate

and the dead zone outer edge do not change as much for $a_{dist,Max} \geqslant 100\,\mu m$ as $1\,\mu m \leqslant a_{dist,Max} \leqslant 100\,\mu m$ (Figs. 33e and 33f).

Here I have only presented the effect of the variation in $a_{dist,Max}$ on the equilibrium solution. In Sect. 4.7.1, I also present the results for the variation in the two remaining parameters a_{min} (Model XI) and $p_{dist,Exp}$ (Model XII), respectively. The main conclusion is that increasing any of these three parameters leads to a decrease in the total grain surface area, A_{tot}; hence stronger MRI-driven turbulence overall, a higher accretion rate, and a more compact dead zone. In other words, one can expect that any changes occurring in the dust size distribution due to the evolution of the dust phase should impact the MRI-driven turbulence mainly through the quantity A_{tot}.

4.5 DISCUSSION

4.5.1 *Gas structure*

For steady-state accretion, the mass flow through the disk is expected to be uniform only if the disk is more massive at radii where the effective turbulent parameter $\bar{\alpha}$ is lower (see Eq. 160); namely, where the dead zone sits. For the fiducial model, I find that the dead zone indeed contains most of the gas content enclosed in the domain considered (67%). This has been previously seen by studies such as [197]. Here I confirm their result with a more consistent steady-state model that accounts for detailed considerations of the MRI with nonideal MHD effects (Ohmic resistivity and ambipolar diffusion), instead of a parametric version.

It has also been showed by [197] that no steady-state pressure maximum at the dead zone outer edge is expected in a 1+1D approach (see their Fig. 3). I have extended their study by showing that it holds only if dust accumulation has been inefficient at the dead zone outer edge before the disk reaches its steady-state accretion regime. The formation of a pressure bump at that location is indeed expected to be a transient phenomenon, since the gas pileup would be smeared out by density waves or Reynolds stress driven by the turbulent layers [e.g., 110]. However, if a sufficient amount of dust particles accumulate at the dead zone outer edge before the steady-state accretion regime is reached, the gas structure might display a steady-state pressure bump at that location, which can be formed within the disk lifetime (see Sect. 4.4.3), hence promoting further dust trapping.

A striking feature of the steady-state gas surface density profiles seen in this Chapter is the discontinuity at the dead zone outer edge ($r = 23\,au$ for the fiducial model). As mentioned in Sect. 4.3, this discontinuity arises from the on/off criteria for active MRI in the global disk accretion model, inducing a steep change in the local turbulent parameter α at each transition from low to high turbulence regime. To confirm whether this is a real discontinuity in the mathematical sense or a numerical artifact due to a lack of resolution, I have rerun the fiducial model with a refined radial grid around the midplane dead zone outer edge ($r = 23\,au$). With the much higher resolution that provides the refined radial grid (259 cells to

$M_\star = 1\,M_\odot, L_\star = 2\,L_\odot, M_{\text{disk}} = 0.05\,M_\star, f_{\text{dg, tot}} = 10^{-2}, \alpha_{\text{hydro}} = 10^{-4}, a_{\text{min}} = 0.1\,\mu m, p_{\text{dist, Exp}} = -3.5$
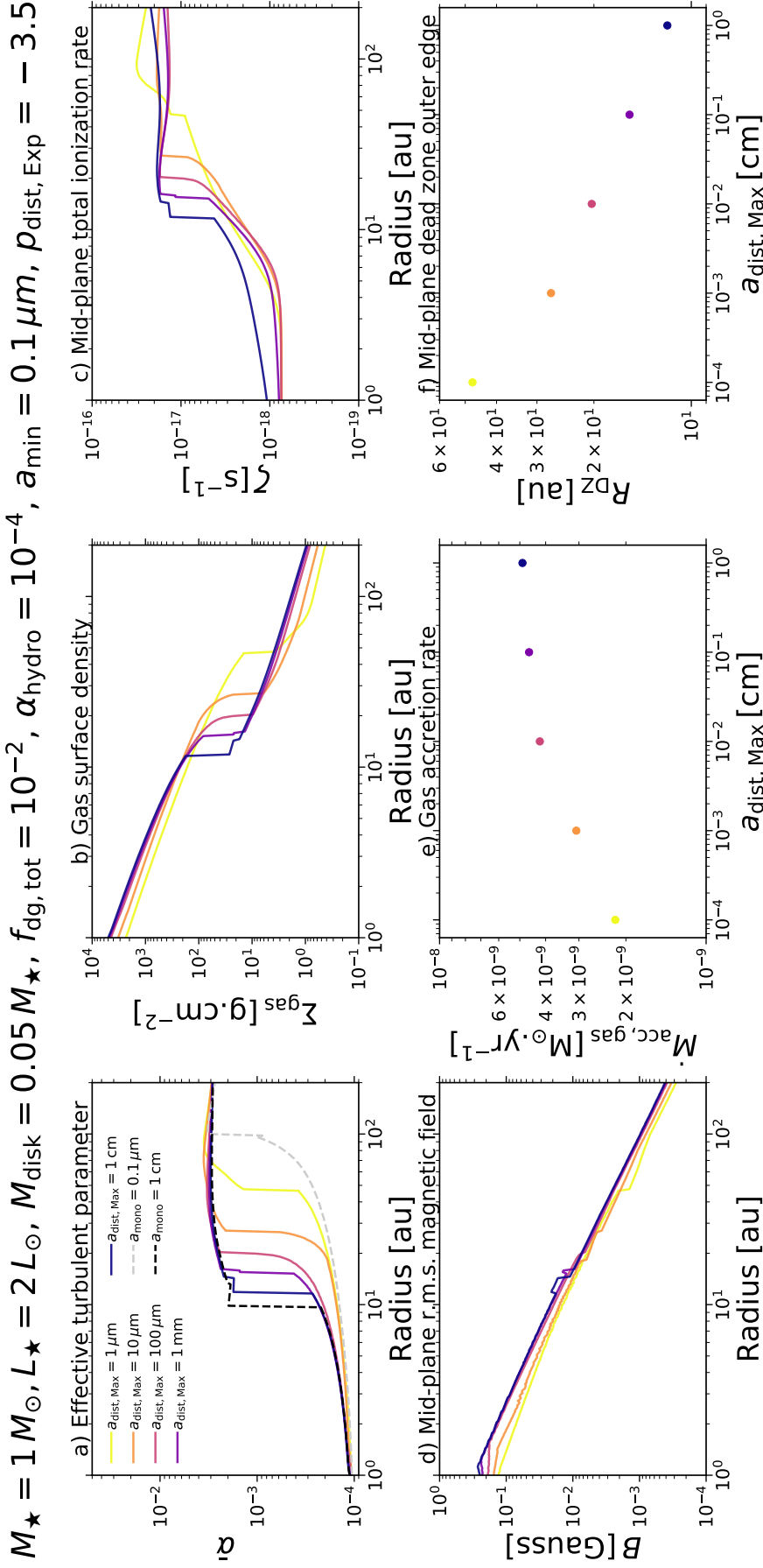

Figure 33: Model X. Effect of the maximum grain size of a fixed power-law grain size distribution on the equilibrium solution. Going from solid light-colored to dark-colored lines, $a_{\text{dist, Max}}$ spans the range from 1 µm to 1 cm. *Panels a–f* show the steady-state radial profiles of the same key quantities as in Fig. 22, but for the model parameters $M_\star = 1\,M_\odot$, $L_\star = 2\,L_\odot$, $M_{\text{disk}} = 0.05\,M_\star$, $f_{\text{dg,tot}} = 10^{-2}$, $\alpha_{\text{hydro}} = 10^{-4}$, $a_{\text{min}} = 0.1\,\mu m$, and $p_{\text{dist, Exp}} = -3.5$. For comparison, the dashed gray and black lines in *Panel a* display the steady-state quantity $\bar{\alpha}$ obtained assuming the limiting case of a mono-disperse population of dust with size $a_{\text{mono}} = 0.1\,\mu m$ and $a_{\text{mono}} = 1\,cm$ (equivalent to the grain-free scenario), respectively.

describe the region $r \in [21, 25]$ au, instead of 9 cells for the fiducial radial grid), I still find that Σ_{gas} is discontinuous at that location. In reality, though, such a steep transition in the gas surface density would not happen: as proposed by [277], the gas would rearrange itself triggered by, for example, Rayleigh adjustment on a timescale shorter (close to the dynamical timescale) than the disk takes to reach its steady-state accretion regime (viscous evolution timescale). Consequently, the steady-state accretion solutions found is this Chapter are expected to be valid everywhere but at the transition between the dead zone and MRI active layer, where the transition should be a smoother version of the present solution. This discrepancy does not change the qualitative results drawn in this Chapter.

As shown by [267] (see their Appendix B), the total inward accretion rate $\dot{M}_{acc}$ can always be decomposed, at each radius, as the sum of the accretion rates within the individual vertical layers of the disk (MRI active layer, dead and zombie zone). Since I impose steady-state accretion, $\dot{M}_{acc}$ is radially constant in the equilibrium solutions. Doing so, though, means that the accretion rates within the individual layers are unavoidably radially variable, as there are no separate conditions to demand invariance. For example, I find for the fiducial model that the accretion rate within the dead zone is negative for $r \gtrsim 10$ au to compensate for the accretion within the MRI active layer that exceeds the total value, hence ensuring that the total inward accretion rate, $\dot{M}_{acc}$, is radially constant (see Fig. 41). Consequently, one could expect the gas to build up at some locations or excavate at others (e.g., $r = 10$ au), hence driving the disk away from the equilibrium solution. To confirm that the present equilibrium solution is valid in a dynamical time-averaged sense, the local viscous evolution timescale – over which the buildup or excavation of gas changes the vertical density structure – must be much longer than the local dynamical timescale needed for the disk to relax back to a hydrostatic equilibrium vertical profile. In Fig. 34, I show the local viscous evolution timescale ($t_{visc} \sim r^2/(3\bar{\nu})$, see Sect. 2.2.3) as well as the local dynamical timescale ($t_{dyn} \sim (2\pi)/\Omega_K$). Since $t_{dyn} \ll t_{visc}$ everywhere, I can thus conclude that the gas volume density perturbations – induced by the variable accretion rates in the individual layers – are vertically smoothed out much more rapidly than they can grow and drive away the disk from the steady-state accretion solution. I confirm that it is the case for all equilibrium solutions presented in this work.

If the protoplanetary disk is at some stage of its evolution out of equilibrium, the gas surface density changes so that the disk evolves toward a steady-state (the equilibrium solutions presented in this Chapter). The local viscous evolution timescale t_{visc} tells us in how much time the steady-state accretion is reached, at a given radius, assuming that the disk is purely viscously evolving. For the fiducial model, I find that t_{visc} is in the range $0.4 - 2.7$ Myrs; with a mean value of 1.5 Myrs in the dead zone and 1 Myr in the MRI active layer (see Fig. 34, where the longest viscous evolution timescale is reached in the dead zone at $r \approx 15$ au). The steady-state accretion regime can thus be established, at most radii, within the disk lifetime, particularly before the disk dispersal phase by, for example, internal photoevaporation that can disperse the gas content after $1 - 4$ Myrs of evolution [e.g., 133, 278].
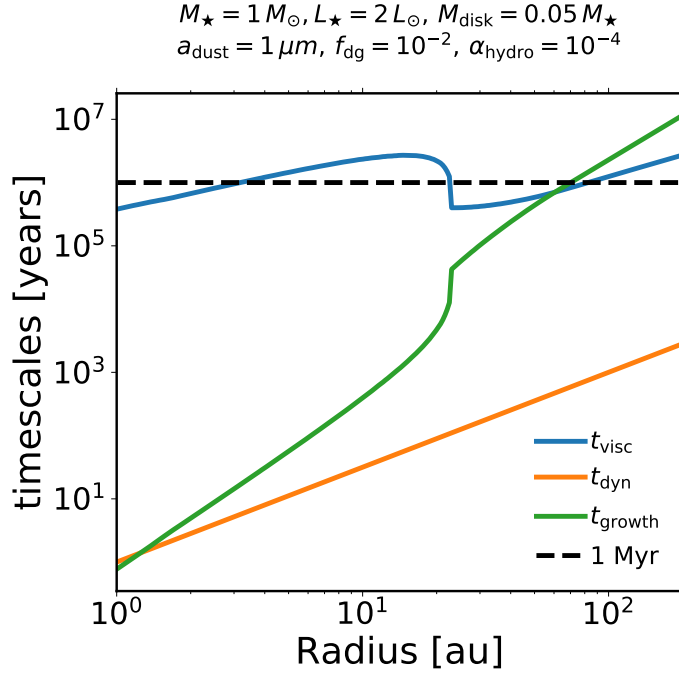
Figure 34: Various local timescales, as a function of radius, for the fiducial model described in Sect. 4.3. The solid blue line (t_{visc}) corresponds to the viscous evolution timescale. The solid orange line (t_{dyn}) corresponds to the dynamical timescale. The solid green line (t_{growth}) corresponds to the growth timescale for the case of micron-sized particles. The dashed black line corresponds to 1 Myr.

Consequently, the protoplanetary disk could accumulate a spatially extended long-lived inner disk gas reservoir (the dead zone) accreting a few times $10^{-9}\,\mathrm{M_\odot.yr^{-1}}$, before photoevaporation starts carving a hole; possibly resulting in transition disks with large gaps and high accretion rates once photoevaporation starts being at play [52]. Whether the steady-state is actually reached everywhere in the protoplanetary disk is investigated in Chapter 6.

4.5.2 *Accretion rates for different stellar masses*

In steady-state viscously-driven accretion, there is a tight correlation between the total disk gas mass and the accretion rate (see Fig. 22e). In principle, for given stellar and dust properties, one could estimate the total disk gas mass from an observed accretion rate (assuming that the disk has reached a steady-state MRI-driven accretion regime).

I perform this exercise with the results reported in [48]. In their work, the authors present a study of a sample of 94 young stars with disks in the Chamaeleon I star-forming regions [1 − 6 Myr; see 279, their Table 1 and references therein]. They analyze the spectra of those objects obtained with the ESO VLT/X-shooter to derive, among others, the $\dot{M}_{\mathrm{acc}} − M_\star$ relation. [48] show that this relation could be better described with a model more complex than a "single-line" fit (although the single-line fit is not statistically excluded): a "segmented-line" fit with a break at $M_\star \approx$

$0.3\,M_\odot$, delimiting a linear relation at higher $M_\star$ and steeper relation at lower $M_\star$. I present the single-line as well as the segmented-line best-fit models in Fig. 35, with the 1σ dispersion around the former (gray area). Furthermore, I run six simulations corresponding to a total disk gas mass $M_{disk} \in \{0.001, 0.002, 0.005, 0.01, 0.05, 0.10\}\,M_\star$, for each stars taken from Table 4. The results are shown in Fig. 35.

To quantitatively match the accretion rates of very low-mass and less luminous stars (star 1 and 2 models) obtained from the [48] $\dot{M}_{acc} - M_\star$ relation, I find that their total disk gas mass must be lower compared to the more massive and luminous counterparts (star 3-5 models). For star 1 and 2 models, Fig. 35 shows that the two best-fit models from [48] are consistent with a total disk gas mass that is roughly in the range $0.002\,M_\star - 0.005\,M_\star$. Conversely, for star 3 and 4 models, the two best-fit models are consistent with a total disk gas mass that is roughly in the range $0.01\,M_\star - 0.05\,M_\star$, whereas they are consistent with a total disk gas mass that is roughly in the range $0.01\,M_\star - 0.10\,M_\star$ for the star 5 model. The results reported in this section support the ideas that the steeper relation seen in the accretion rates for very low-mass and less luminous stars may be caused by: (1) a faster evolution, since I need total disk gas mass values that are lower nowadays to match the observations; or (2) the fact that very low-mass and less luminous stars initially form with a low total disk gas mass (relative to their stellar mass). Previous studies suggest that the faster evolution of disk around very low-mass stars could be explained by faster accretion, since these disks could potentially be entirely MRI active [e.g., 18]. However, as seen in Sect. 4.4.7 [also see, 229], this idea seems unlikely because ambipolar diffusion becomes stronger at the low densities expected for the disk around those stars, hence preventing the MRI from easily operating everywhere. Without any other mechanisms to explain faster evolution in the context of MRI-driven accretion, the idea of very low-mass and less luminous stars being initially formed with a lower total disk gas mass compared to high-mass and more luminous stars seems more probable.

One should note that the accretion rates presented in Fig. 35 depend on the choice made for r_{max}, the outer boundary of the radial grid ($r_{max} = 200\,au$ in this Chapter). For fixed model parameters and given a field strength, the steady-state accretion solution is unique. By solely varying r_{max}, the spatial gas mass distribution is changed: a lower r_{max} implies higher gas surface densities (since the same amount of gas is now distributed across a more confined domain), whereas a higher r_{max} leads to lower ones. I find that both the accretion rate and the dead zone maximal radial extent increase with decreasing r_{max} (not shown here). The former dependence can be explained by the fact that a lower r_{max} means less distance for the gas to travel before being accreted onto the central star. The latter dependence is justified by the fact that a lower r_{max} implies an overall lower ionization level in the disk. Consequently, all the accretion rates presented in Fig. 35 are expected to increase if $r_{max} < 200\,au$, and decrease if $r_{max} > 200\,au$. Additionally, I find that the effect of r_{max} is more prominent for lower total disk gas masses (not shown here). Nonetheless, the main conclusions of this section do not change. Indeed, the gas radius for a disk around a very low-mass and less luminous star is more likely to
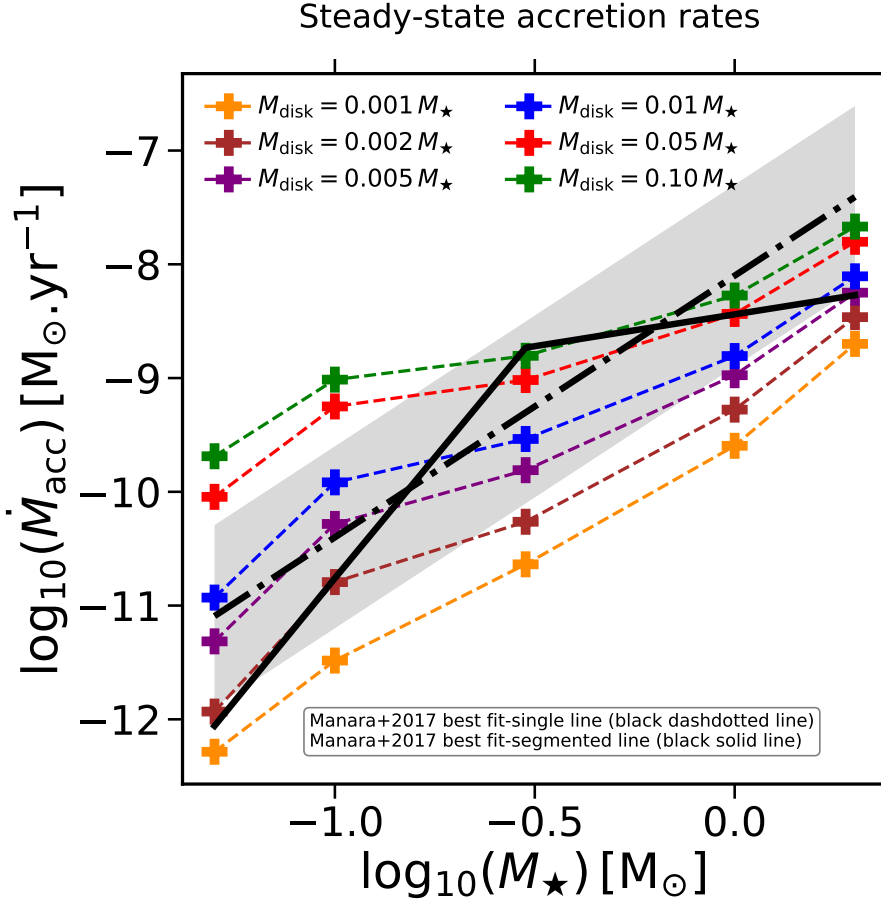
Steady-state accretion rates

Figure 35: Accretion rate as a function of stellar mass. The dash-dotted and solid black lines correspond to the single-line and segmented-line best-fit models, respectively, from [48]. The 1σ dispersion around the single-line best-fit model is shown by the gray area. The "+" symbols represent the accretion rates obtained for various total disk gas masses and for each star taken from Table 4, using the steady-state accretion model. Here I assume that $a_{dust} = 1\,\mu m$, $f_{dg} = 10^{-2}$, and $\alpha_{hydro} = 10^{-4}$.

be lower than the fiducial 200 au [e.g., 66], and also lower than the gas radius for a disk around a high-mass and more luminous star. As a result, the accretion rate of a very low-mass and less luminous stars is expected to increase compared to what is displayed in Fig. 35, implying that even lower total disk gas masses are needed to explain the steeper relation seen in the accretion rates.

4.5.3 *The need for gas, dust, and stellar evolution*

The detailed parameter study conducted in Sect. 4.4 shows that the following parameters play a crucial role in shaping the steady-state accretion solution: (1) the total disk gas mass; (2) the representative grain size; (3) the vertically averaged dust-to-gas mass ratio; and (4) the total stellar X-rays luminosity. In general, those parameters may change during the secular evolution of the protoplanetary disk.

One will thus need to relax the steady-state accretion assumption in future studies by implementing the following ingredients.

First, gas evolution needs to be considered. During the evolution of Class II proto-planetary disks, the gas content is removed from the disk due to accretion onto the star and winds (e.g., magnetocentrifugal or photoevaporative). Additionally, there is no source term as in Class 0/I disks, where the envelope in-fall can feed in gas. In general, the total disk gas mass thus inevitably decreases over time. In Sect. 4.4.1, I showed that the equilibrium solution strongly depends on the total disk gas mass with which the disk reaches its steady-state accretion regime: a lower total disk gas mass implies a lower accretion rate, and a more compact dead zone. Consequently, for a given initial total disk gas mass, the gas surface density is expected to start evolving toward the equilibrium solution corresponding to this total disk gas mass. Since the total disk gas mass decreases over time, the gas surface density readjusts by evolving toward a new steady-state solution corresponding to that new total disk gas mass. Gas evolution is crucial here since it tells us how the gas structure changes over time and, hence, from what steady-state solution to another the disk tends, assuming pure viscous evolution.

Second, dust evolution needs to be implemented, including both dynamics and growth processes. In the fiducial model, I assumed a vertically averaged dust-to-gas mass ratio of 10^{-2} and small dust grains of constant size $1\,\mu m$. Such values may be expected in the very early stages of dust evolution in the disk. However, dust particles grow, fragment, drift, stir and settle during the evolution of protoplanetary disks leading to a grain size distribution. Fig. 34 shows that micron-sized grains grow on a timescale (t_{growth}) that is shorter than the timescale the gas needs to evolve on large scales (viscous evolution timescale t_{visc}) in most of the disk, implying that dust growth processes need to be accounted for. Here t_{growth} is computed using the midplane value of Eq. (30) from [135], where I take the relative velocity Δv to be the Brownian relative velocity defined as $\Delta v = \sqrt{8 k_B T / \pi m_{\mathrm{red}}}$, with m_{red} the reduced mass ($m_{\mathrm{red}} = m_{\mathrm{dust}}/2$ for a collision of equal micron-sized grains. In Sects. 4.4.2 and 4.4.3, I found that both a larger grain size and a higher dust depletion imply a higher accretion rate, a higher $\bar{\alpha}$ overall, and a more compact dead zone. I then confirmed such results by implementing a grain size distribution, which is a much more realistic way to describe the dust (Sect. 4.4.8). Consequently, the following cycle might happen, where the disk turbulence state oscillates between a low and high regime. For the initial conditions $M_{\mathrm{disk}} = 0.05\,M_\star$, $a_{\mathrm{dust}} = 1\,\mu m$ and $f_{\mathrm{dg}} = 10^{-2}$, the gas starts evolving toward the corresponding equilibrium solution. Since $t_{\mathrm{growth}} \lesssim t_{\mathrm{visc}}$ for $r \lesssim 60\,\mathrm{au}$, the dust can efficiently grow by coagulation to representative grain sizes skewed toward larger sizes in such regions, and the vertically averaged dust-to-gas mass ratio of micron-sized grains can substantially drop before this steady-state accretion solution can actually be reached. As a result, the gas evolves toward a new equilibrium solution corresponding to a disk with a higher $\bar{\alpha}$ overall. A higher $\bar{\alpha}$ in the disk implies a more efficient fragmentation that can replenish micron-sized grains. The representative grain sizes can thus be skewed toward micron-sized particles again, and the

vertically averaged dust-to-gas mass ratio of micron-sized grains can re-increase, resulting in the gas evolving toward a steady-state solution close to the initial one, corresponding to a less turbulent disk. Due to a low disk turbulence level, the dust can effectively grow and less frequently fragment again, hence looping the cycle. A similar cycle has been reported in [198] where growth, settling and fragmentation were considered alongside Ohmic resistivity (see their Fig. 3). The authors find that this cycle is actually a "damped oscillation," that is to say, the disk turbulence state and grain size distribution converge and stop oscillating rather than indefinitely oscillating. The equilibrium solution corresponding to $M_{disk} = 0.05\,M_{\star}$, $a_{dust} = 1\,\mu m$, and $f_{dg} = 10^{-2}$ is thus physically motivated if the cycle mentioned above can be completed on a timescale shorter than the viscous evolution timescale (otherwise the total disk gas mass decreases) and the drift timescale (otherwise dust particles are removed from the disk, and the overall dust content drops), and if the grain size distribution at the end of the cycle is comparable to the one at the beginning of the cycle (i.e., the grain size distribution is skewed toward micron-sized grains). Additionally, one should note that such a cycle is also likely to happen in the steady-state pressure maxima generated by local dust enhancements (see Sect. 4.4.3), possibly generating pressure maxima that could "come and go" over time. In order to provide a more consistent picture for this cycle, a time-dependent framework with dust evolution included is required.

Finally, stellar evolution needs to be accounted for. As I showed in Sect. 4.4.7, the total stellar X-rays luminosity L_{XR} plays a fundamental role because it quantifies how much the gas can be ionized by stellar X-rays: the higher the total stellar X-rays luminosity is, the more turbulent the disk is overall. Depending on the stellar type, this quantity is more or less constant over time [e.g., 133, their Fig. 5]. As a result, a time-dependent framework needs to consider the time-dependence of L_{XR}. I want to emphasize that all the effects described above are accounted for in Chapter 6. I thus invite the eager reader to check it out in order to see how the interplay of gas, dust and MRI evolution shape the protoplanetary disk in secular timescales.

4.5.4 *Ambipolar diffusion in the strong-coupling limit*

In the global MRI-driven disk accretion model of Chapter 3, I employ the criterion from Bai and Stone [113] to account for the effect of ambipolar diffusion on the MRI (see Eqs. 152 and 153). The underlying idea behind this criterion is that the disk is in the strong-coupling limit [111] (i.e., the single fluid regime of neutrals). In this limit, local ionization equilibrium is a good enough approximation, and the magnetic diffusion coefficients can be directly evaluated from the total ionization rate and local thermodynamic quantities such as density and temperature. It requires that: (1) the ion inertia is negligible compared to the inertia of the neutrals, so that the ion density is entirely controlled by ionization equilibrium with the neutrals; (2) the ionization equilibrium is achieved on a timescale t_{rcb} shorter than the dynamical timescale $t_{dyn} = 2\pi/\Omega_K$, implying that the ions are continuously

created and destroyed on a timescale that is shorter than the timescale for the MRI to grow.

It is clear that the gas ionization fraction is extremely small in the models presented, and even so in the uppermost layers (Fig. 19b). Hence, the inertia of charged particles is negligible compared to the inertia of neutrals, justifying the first requirement of the strong-coupling limit.

Since I directly solve for the equilibrium ionization state, I do not have access to the recombination timescale t_{rcb}. Nonetheless, I can estimate it as follows: Given the first term of Eqs. (130) and (131), the ionization timescale for ions and free electrons can be respectively written as $t_i = n_i / (\zeta n_{gas})$ and $t_e = n_e / (\zeta n_{gas})$. Since $n_i \geqslant n_e$ (free electrons collide more frequently with grains), $t_i \geqslant t_e$, and hence the overall relaxation timescale of the gas-phase being given by t_i. Assuming local ionization–recombination equilibrium (as it is the case in the semi-analytical chemical model of the global disk accretion model), the ionization timescale (t_i) equals the recombination timescale (t_{rcb}). Therefore, $t_{rcb} \approx n_i / (\zeta n_{gas}) \approx 1 / (s_i u_i \sigma_{dust} n_{dust} P_i + k n_e)$, where the second equality is found by equating Eq. (130) to zero. Figure 36 shows, for the fiducial model, that the recombination timescale is shorter than the dynamical timescale ($t_{rcb}/t_{dyn} < 1$) everywhere. As a result, the second requirement of the strong-coupling limit is also justified.

One can thus conclude that the strong-coupling limit holds for the fiducial model, justifying the use of the criterion from Bai and Stone [113] to describe the effect of ambipolar diffusion on the MRI. I verified that it holds for all the models shown in this Chapter.

4.5.5   *The Hall effect*

In this section, I discuss the potential impact that the Hall effect could have on the equilibrium solutions. As I discussed in Sect. 3.5.1, the impact of the Hall effect on the MRI is nontrivial. In Sect. 4.3.1, I showed that the Hall effect dominates the nonideal MHD terms in most of the dead zone, as well as in the inner regions of the MRI active layer (Fig. 16b). Although I have ignored the Hall effect when deriving the self-consistent MRI-induced disk viscosity parameter, I can investigate *a posteriori* its potential impact on the present results by plotting the Hall Elsasser number χ (Eq. 148) in Fig. 37.

If the magnetic field is anti-aligned with the rotation axis of the disk, the Hall effect could substantially reduce the amount of MRI-driven turbulent transport in the MRI active layer where it dominates the nonideal MHD terms [e.g., 245, 248–250]. In the fiducial model, the MRI at the midplane would thus only develop from ≈ 50 au instead of ≈ 23 au, implying that a significant part of the midplane would be laminar driven by non-MRI stresses. A laminar midplane would have significant impact on the dust dynamics and the growth process, since lower turbulence implies effective coagulation and less effective fragmentation. It would suggest that the dust at the midplane could grow to larger sizes, where the typical grain size reached at a given location in the disk would depend on how much the MRI is
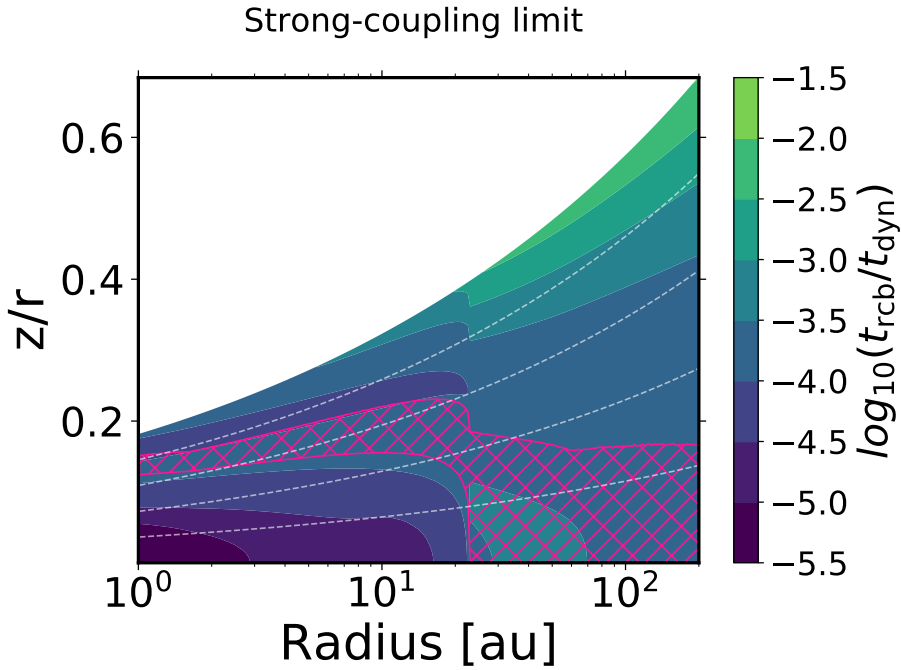
Figure 36: Ratio of the recombination timescale (t_{rcb}) to the dynamical timescale (t_{dyn}), as a function of location in the disk, for the fiducial model described in Sect. 4.3. The pink hatched area corresponds to the MRI active layer. The dashed white lines correspond to the surfaces $z = 1\,H_{gas}$, $z = 2\,H_{gas}$, $z = 3\,H_{gas}$, and $z = 4\,H_{gas}$, from bottom to top, respectively.

suppressed by the Hall effect, as well as how strong the turbulence from non-MRI stresses is.

Conversely, if the magnetic field is aligned with the rotation axis of the protoplanetary disk, the HSI could reactivate the dead zone by producing large-scale and ordered magnetic fields transporting angular momentum radially with little turbulent motion through laminar viscous stresses [e.g., 246–248]. As such, the steady-state pressure maximum at the dead zone outer edge seen in Sect. 4.4.3 could thus be removed.

4.6 SUMMARY AND CONCLUSIONS

In this Chapter, I have employed the global MRI-driven disk accretion model of Chapter 3 to investigate the structure of a steadily accreting protoplanetary disk. To obtain the steady-state MRI-driven accretion solution (referred as equilibrium solution) corresponding to the MRI activity at maximal efficiency, the gas surface density, gas ionization state, magnetic field, viscosity, and accretion rate are calculated self-consistently. For the fiducial protoplanetary disk model considered, the key findings can be summarized as follows:

- The accretion rate reached by this disk model is $\dot{M}_{acc} \approx 3.7 \times 10^{-9}\,M_{\odot}.yr^{-1}$, the mean effective turbulence level in the MRI active layer is $\langle \bar{\alpha} \rangle_{MRI} \approx 3 \times 10^{-3}$, and the dead zone maximal radial extent is $R_{DZ} = 23\,au$. For studies
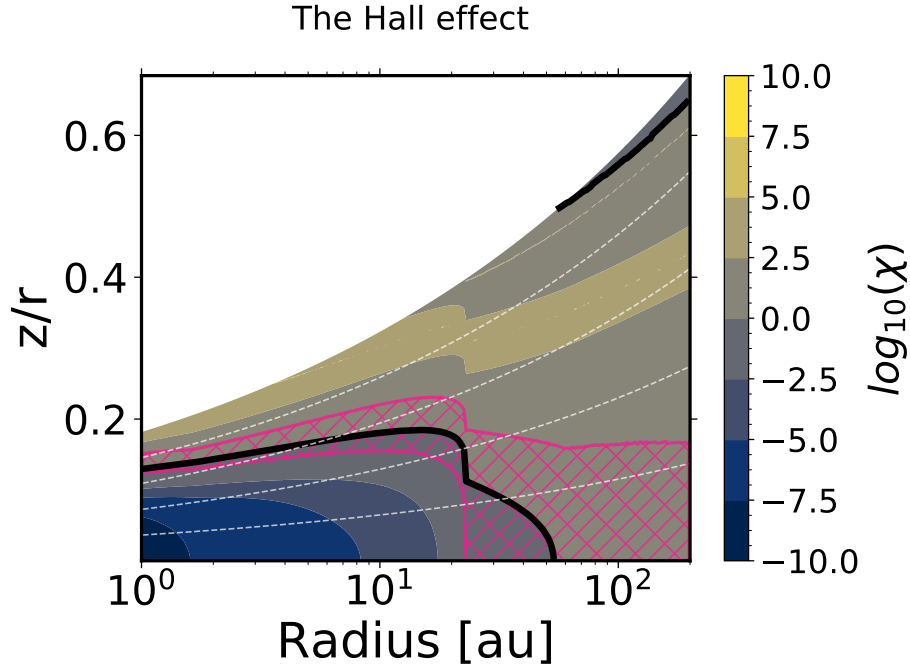
Figure 37: Steady-state Hall Elsasser number, as a function of location in the disk, for the fiducial model described in Sect. 4.3. The pink hatched area corresponds to the MRI active layer. The solid black lines indicate where $\chi = 1$. Everywhere between these lines, $\chi > 1$. The dashed white lines correspond to the surfaces $z = 1\,H_{gas}$, $z = 2\,H_{gas}$, $z = 3\,H_{gas}$, and $z = 4\,H_{gas}$, from bottom to top, respectively.

using an ad hoc prescription for the Shakura-Sunyaev viscosity parameter α, a value of a few times 10^{-3} is found to be more appropriate for describing the viscosity in the MRI active layer, accounting for ambipolar diffusion.

- The steady-state accretion regime of such a disk is reached within the disk lifetime, particularly before the disk dispersal phase. The disk could thus accumulate a spatially extended long-lived inner disk gas reservoir before internal photoevaporation starts carving a hole.

- A steady-state pressure maximum does not form at the dead zone outer edge.

- Ambipolar diffusion quenches the MRI activity over most of the disk. The upper envelope of the MRI active layer is set by ambipolar diffusion, whereas Ohmic resistivity primarily sets its lower envelope.

Additionally, I have performed an exhaustive parameter study to investigate what model parameters are crucial to the MRI-driven accretion in protoplanetary disks, as well as the extent to which the accretion is efficient (namely, the location of the dead zone outer edge and the value of the accretion rate). I have adopted the fiducial parameters but vary some of the model parameters one at a time (see Table 2). The key findings can be summarized as follows:

- The accretion rate and dead zone outer edge location as a function of the total disk gas mass are approximately power-laws: $\dot{M}_{acc} \propto M_{disk}^{0.54}$ and $R_{DZ} \propto M_{disk}^{0.64}$.

A more massive disk implies a higher accretion rate and a more extended dead zone (both radially and vertically).

- A smaller grain size leads to a smaller accretion rate and a more extended dead zone. When submicron dust particles are considered ($a_{dust} = 0.1\,\mu m$), the disk midplane is mainly MRI-dead and accretes much more slowly. Furthermore, the steady-state solution remains unchanged regardless of the grain size for $a_{dust} \gtrsim 100\,\mu m$. There exists a threshold for the grain size above which the grains have little impact on the ionization chemistry, and hence little impact on the MRI. This threshold marks the regime in which the dust–gas mixture behaves as a grain-free plasma due to the recombination process primarily occurring in the gas-phase rather than onto the grains surface.

- An overall higher depletion of micron-sized grains leads to a higher accretion rate and a more compact dead zone. Dust enhancement ($f_{dg} = 10^{-1}$) compared to the standard ISM value strongly damps the MRI-driven accretion. Additionally, the steady-state accretion solution is independent of the vertically integrated dust-to-gas mass ratio choice for $f_{dg} \lesssim 10^{-4}$. As a result, there exists a threshold for the depletion of micron-sized grains below which the grains have little impact on the ionization chemistry, and hence little impact on the MRI. Once again, this threshold marks the regime in which the dust–gas mixture behaves as a grain-free plasma.

- If a sufficient amount of dust particles has locally accumulated in a region where the MRI can operate before the disk reaches its steady-state accretion regime, the gas structure might adjust to form a steady-state pressure maximum close to the location of dust enhancement. These spontaneous steady-state pressure maxima can be formed within the disk lifetime, which might have direct consequences for planet formation by promoting further dust trapping.

- For a fixed stellar-independent total disk gas mass, a more massive and luminous star implies a higher accretion rate and a more compact dead zone.

- The accretion rate and dead zone outer edge location as a function of the hydrodynamic turbulent parameter are approximately power-laws: $\dot{M}_{acc} \propto \alpha_{hydro}^{0.31}$ and $R_{DZ} \propto \alpha_{hydro}^{0.22}$. A higher α_{hydro} leads to a higher accretion rate and a more extended dead zone. For $\alpha_{hydro} = 10^{-3}$, the gas surface density profile is much smoother ($\Sigma_{gas} \propto r^{-1.22}$) than the profiles obtained for lower α_{hydro} values and is actually close to the constant-α model solution ($\Sigma_{gas} \propto r^{-1}$).

- The choice for either an optically thin or thick radial gas temperature model has little impact on the accretion rate, dead zone size, or the overall equilibrium solution.

Finally, I have investigated in more depth the effect of stellar properties by considering more realistic models in which the total disk gas mass is stellar-dependent. I find that:

- For a fixed stellar-dependent total disk gas mass, a more massive and luminous star implies a higher accretion rate and a more extended dead zone.

- The dead zone cannot become indefinitely large for high-mass and more luminous stars, since their high total stellar X-rays luminosity regulates its radial extent. Similarly, the dead zone cannot become indefinitely small for low-mass and less luminous stars due to their too low total stellar X-rays luminosity.

- For the range of stars considered ($0.05\,M_\odot - 2\,M_\odot$), ambipolar diffusion is the primary factor determining the strength of the MRI-driven accretion.

- To explain the steeper relation seen in the observed accretion rates of very low-mass and less luminous stars [48] in the context of MRI-driven accretion, I find that very low-mass and less luminous stars need to be initially formed with a lower total disk gas mass compared to the high-mass and more luminous counterparts.

In this Chapter, I have showed that the MRI-driven accretion behavior crucially depends on the gas, dust, and the stellar properties. Since they are expected to undergo substantial change throughout the secular evolution of the protoplanetary disk, it is crucial to combine gas, dust, and stellar evolution models with the global MRI-driven disk accretion model of Chapter 3 on million-year timescales. But before doing so, one needs to understand how the dust evolution processes shape the MRI activity. This is addressed in the next Chapter.

4.7   ADDITIONAL CONTENT

4.7.1   *Follow-up on the effect of grain size distribution*

In this section I perform a follow-up on the effect of a fixed power-law dust size distribution on the equilibrium solution. Particularly, I investigate the impact of a variation in the dust distribution minimum grain size as well as its exponent.

4.7.1.1   *Effect of distribution minimum grain size*

I investigate the impact of a variation in a_{min}, while fixing $a_{dist,Max} = 1\,\mu m$ and $p_{dist,Exp} = -3.5$. This set of simulations corresponds to Model XI, and the results are presented in Fig. 38.

A higher a_{min} implies stronger MRI-driven turbulence overall, a higher gas accretion rate, and a more compact dead zone (Figs. 38a, 38e and 38f). Unlike what I showed in Sect. 4.4.8, though, one can notice that a change in a_{min} primarily impacts the dead zone outer edge location, which can be almost twice closer from the

central star for $a_{min} = 0.55\,\mu m$ compared to $a_{min} = 0.1\,\mu m$. The gas accretion rate and the MRI-optimal r.m.s. magnetic field strength appear, indeed, to be weakly dependent on a_{min} (Figs. 38d and 38e).

When a larger grain size is used as the dust distribution minimum size, the gas ionization degree becomes higher closer to the central star (Fig. 38c), since gas-phase recombination can dominate the recombination process from smaller radial distances. For increasing value of a_{min}, the total grain surface area, A_{tot}, decreases and the dust becomes less efficient at sweeping up free electrons and ions from the gas-phase at smaller radial distances, hence the MRI being able to operate more easily.

It is important to note that the distribution minimum grain size, a_{min}, is a free parameter in dust models with a grain size distribution. From Fig. 38, it can be seen that a_{min} is crucial in determining the MRI-driven turbulence.

4.7.1.2   *Effect of distribution exponent*

I investigate the impact of a variation in $p_{dist,Exp}$, while fixing $a_{min} = 0.1\,\mu m$ and $a_{dist,Max} = 1\,\mu m$. This set of simulations corresponds to Model XII, and the results are presented in Fig. 39.

The power-law exponent ($p_{dist,Exp}$) controls the relative proportion of the smaller and larger particles in the grain size distribution: A smaller or more negative value means that the dust distribution is skewed toward the smaller sizes, whereas a larger or more positive value means that it is skewed toward the larger sizes. Looking at Figs. 39a, 39e, 39f, a higher $p_{dist,Exp}$ results in stronger MRI-driven turbulence overall, a higher gas accretion rate, and a more compact dead zone. In the same spirit as the previous section, $p_{dist,Exp}$ mainly changes the dead zone outer edge (although the gas accretion rate and the MRI-optimal r.m.s. magnetic field strength vary more with $p_{dist,Exp}$ than a_{min}). The dead zone outer edge is, indeed, located at ~ 63 au for $p_{dist,Exp} = -4.5$, whereas it is located at ~ 27 au for $p_{dist,Exp} = 0.25$.

The gas ionization degree becomes higher closer to the central star when the dust size distribution is skewed toward the larger sizes (Fig. 39c). For increasing value of $p_{dist,Exp}$, free electrons and ions are less likely to encounter, per unit volume and on average, the smaller particles of the dust size distribution. Instead, they primarily interact with the larger ones. The total grain surface area (A_{tot}) thus decreases, allowing for the gas-phase recombination to dominate closer to the central star, hence the MRI being able to operate more easily.

Since the ionization chemistry is primarily controlled by the smaller sizes of the dust distribution, the MRI activity crucially depends on their relative proportion. Particularly, it suggests that the MRI activity substantially increases in the regions of the disk where the dust size distribution is cut-off at micron-sized particles rather than submicron-sized particles. This can happen when submicron-sized particles get depleted enough due to effective grain coagulation and less frequent fragmentation.

$M_\star = 1\,M_\odot, L_\star = 2\,L_\odot, M_{disk} = 0.05\,M_\star, f_{dg,tot} = 10^{-2}, \alpha_{hydro} = 10^{-4}, a_{dist,Max} = 1\,\mu m, p_{dist,Exp} = -3.5$
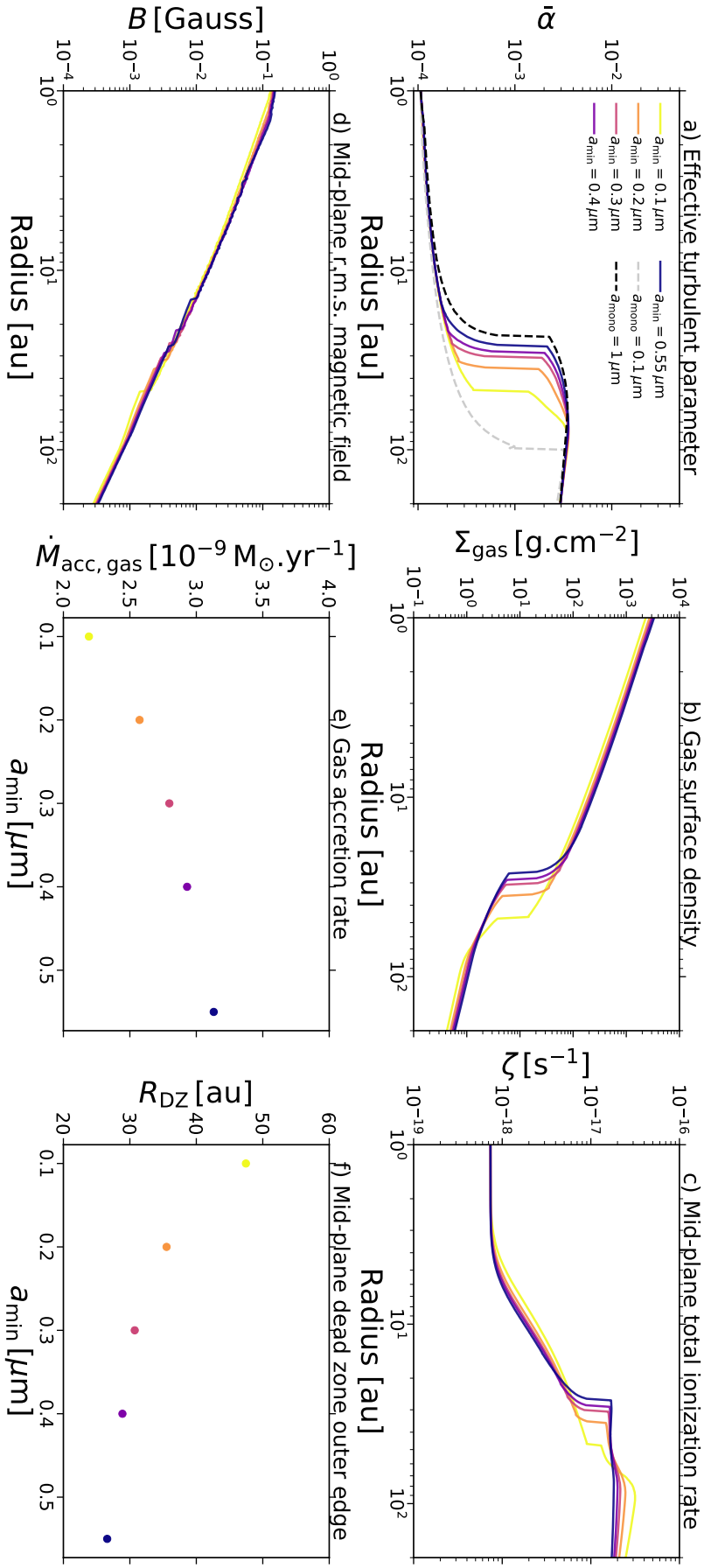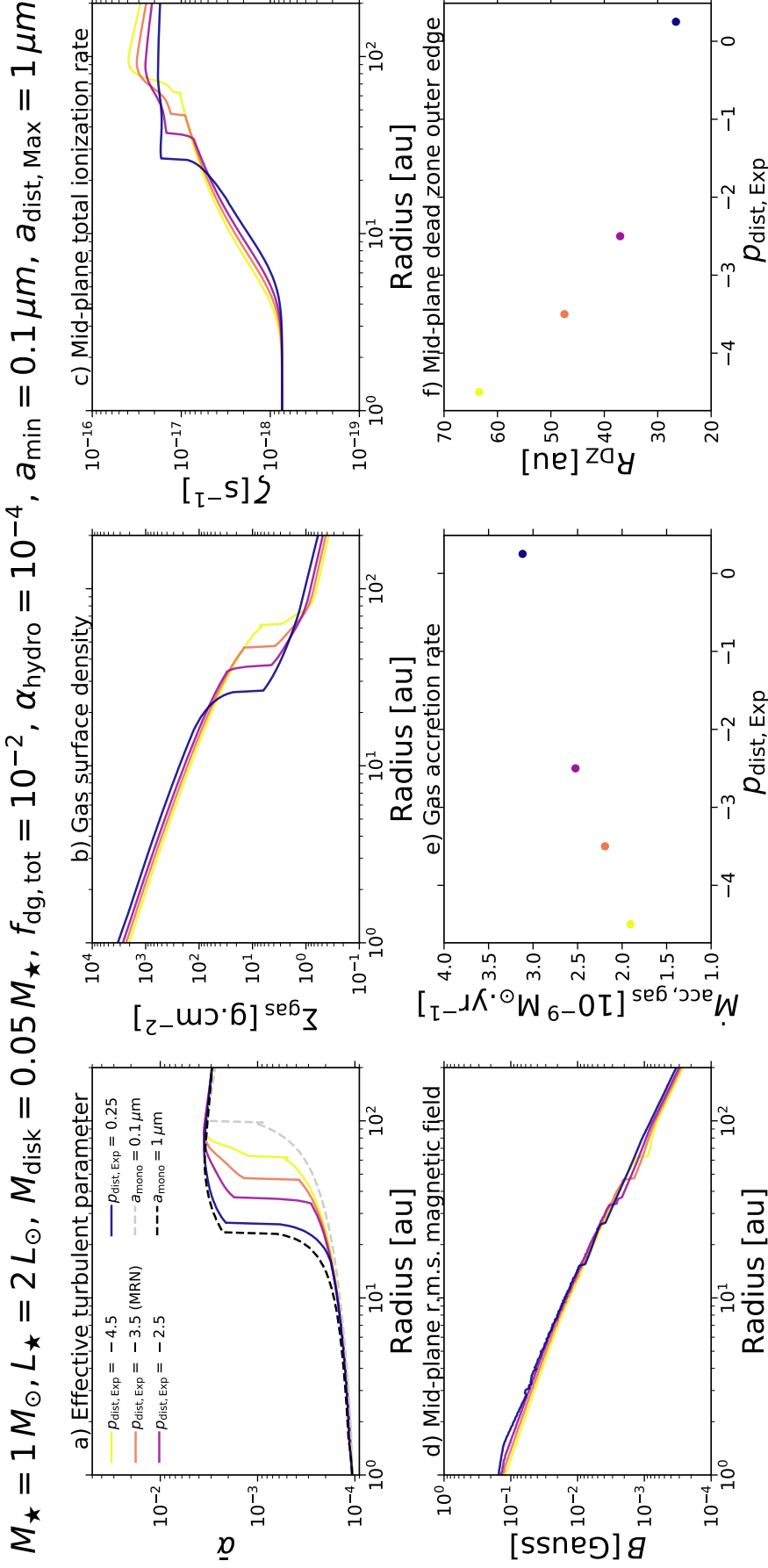

Figure 38: Model XI. Effect of the minimum grain size of a fixed power-law grain size distribution on the equilibrium solution. Going from solid light-colored to dark-colored lines, a_{min} spans the range from 0.1 μm to 0.55 μm. *Panels a–f* show the steady-state radial profiles of the same key quantities as in Fig. 22, but for the model parameters $M_\star = 1\,M_\odot$, $L_\star = 2\,L_\odot$, $M_{disk} = 0.05\,M_\star$, $f_{dg,tot} = 10^{-2}$, $\alpha_{hydro} = 10^{-4}$, $a_{dist,Max} = 1\,\mu m$, and $p_{dist,Exp} = -3.5$. For comparison, the dashed gray and black lines in *Panel a* now display the steady-state quantity $\bar{\alpha}$ obtained assuming the limiting case of a mono-disperse population of dust with size $a_{mono} = 0.1\,\mu m$ and $a_{mono} = 1\,\mu m$, respectively.

Figure 39: Model XII. Effect of the exponent of a fixed power-law grain size distribution on the equilibrium solution. Going from solid light-colored to dark-colored lines, $p_{dist,Exp}$ spans the range from -4.5 to 0.25. Panels a–f show the steady-state radial profiles of the same key quantities as in Fig. 22, but for the model parameters $M_\star = 1\,M_\odot$, $L_\star = 2\,L_\odot$, $M_{disk} = 0.05\,M_\star$, $f_{dg,tot} = 10^{-2}$, $\alpha_{hydro} = 10^{-4}$, $a_{min} = 0.1\,\mu m$, and $a_{dist,Max} = 1\,\mu m$. For comparison, the dashed gray and black lines in Panel a now display the steady-state quantity $\bar{\alpha}$ obtained assuming the limiting case of a mono-disperse population of dust with size $a_{mono} = 0.1\,\mu m$ and $a_{mono} = 1\,\mu m$, respectively.

4.7.2 *Additional plots*

In this section I present additional plots describing the properties of the fiducial model for completeness (see Figs. 40 and 41).
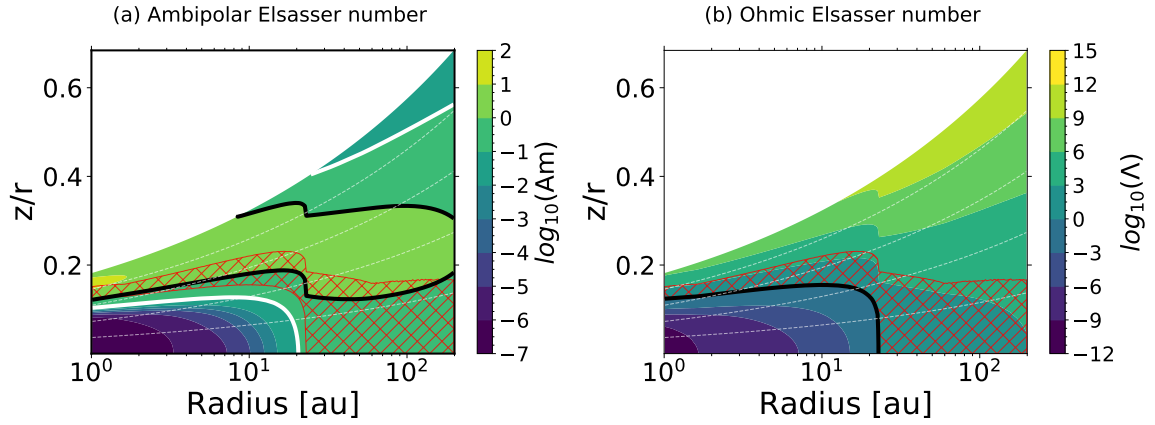
Figure 40: Steady-state ambipolar and Ohmic Elsasser numbers, as a function of location in the disk, for the fiducial model described in Sect. 4.3. In both panels, the red hatched area corresponds to the MRI active layer. Additionally, the dashed white lines correspond to the surfaces $z = 1\,H_{gas}$, $z = 2\,H_{gas}$, $z = 3\,H_{gas}$, and $z = 4\,H_{gas}$, from bottom to top, respectively. *Panel a*: Ambipolar Elsasser number, Am. The region within the solid white lines indicates where Am $\geqslant 0.1$. The region within the solid black contour indicates where Am $\geqslant 1$. *Panel b*: Ohmic Elsasser number, Λ. The solid black line indicates where $\Lambda = 1$.

$$M_\star = 1\,M_\odot,\, L_\star = 2\,L_\odot,\, M_{\mathrm{disk}} = 0.05\,M_\star$$
$$a_{\mathrm{dust}} = 1\,\mu m,\, f_{\mathrm{dg}} = 10^{-2},\, \alpha_{\mathrm{hydro}} = 10^{-4}$$
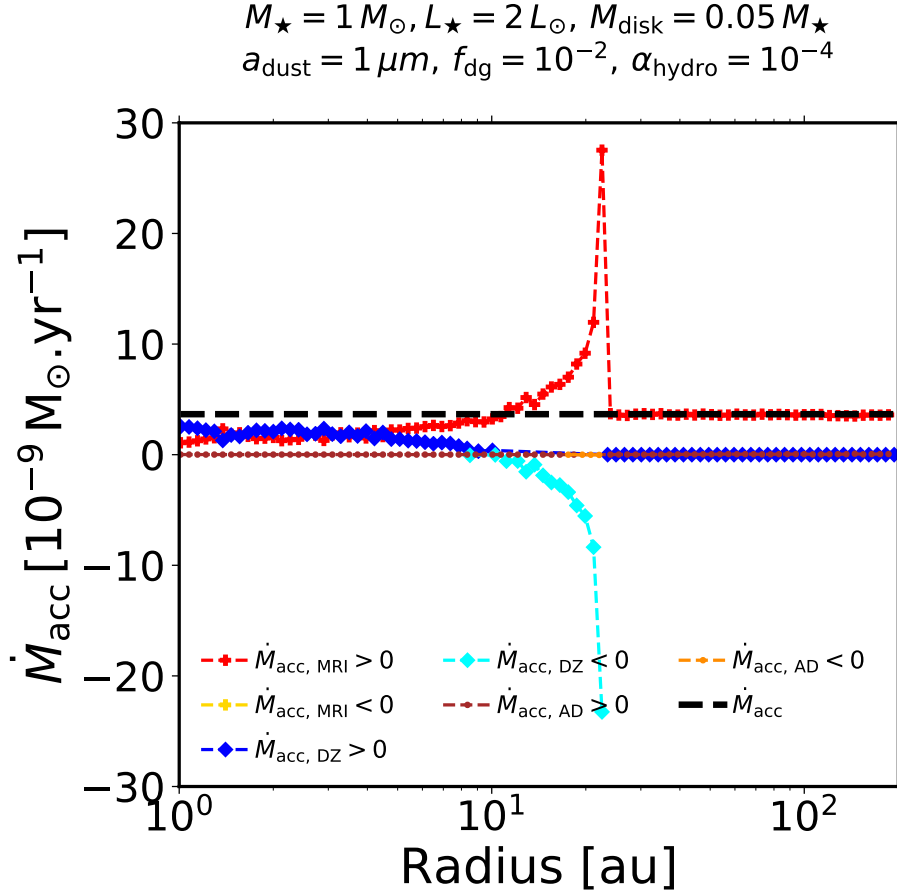
Figure 41: Accretion rates within the individual accretion layers, as a function of radius, for the fiducial model described in Sect. 4.3. The overall steady-state inward accretion rate, $\dot{M}_{\mathrm{acc}}$, is defined as $\dot{M}_{\mathrm{acc}} = \dot{M}_{\mathrm{acc,MRI}} + \dot{M}_{\mathrm{acc,AD}} + \dot{M}_{\mathrm{acc,DZ}}$, where $\dot{M}_{\mathrm{acc,MRI}}$, $\dot{M}_{\mathrm{acc,AD}}$, and $\dot{M}_{\mathrm{acc,DZ}}$ correspond to the radially variable accretion rates within the MRI active layer, zombie zone, and dead zone, respectively. They were computed using the formula provided in Appendix B of [267]. The dashed black line corresponds to $\dot{M}_{\mathrm{acc}} \approx 3.7 \times 10^{-9}\,M_\odot.\mathrm{yr}^{-1}$, obtained for the fiducial protoplanetary disk model.

THE IMPACT OF DUST EVOLUTION ON THE MRI ACTIVITY

*This Chapter is an adapted version of the published research article **Delage T. N.**, Gárate M., Okuzumi S., Yang C.C., Pinilla P., Flock M., Stamler S. M., & Birnstiel T.; "The impact of dust evolution on the dead zone outer edge in magnetized protoplanetary disks"; A&A (2023), vol. 674, A190 [185].*

5.1 MOTIVATION

In the previous Chapter, I have provided some insights regarding the impact of gas, dust and stellar properties on the MRI activity. For example, I showed that the MRI-driven turbulence becomes stronger when the total disk gas mass decreases due to a higher gas ionization degree. Additionally, I showed that the overall MRI activity becomes stronger the bigger dust particles are in the disk and the more depleted they are with respect to the gas. Finally, I indirectly showed that a higher total stellar X-rays luminosity leads to stronger MRI-driven turbulence overall due to a higher stellar X-ray ionization rate.

However, I described the dust component of the protoplanetary disk by assuming either a fixed representative grain size or a fixed power-law grain size distribution. As discussed in Sect. 2.3, the dust can substantially differ from these assumptions because dust particles can constructively/destructively collide with each other leading to coagulation/fragmentation, and they are transported in the disk by various processes such as thermal Brownian motion, vertical stirring/settling, turbulent mixing and azimuthal/radial drift. Okuzumi and Hirose [198] is among the rare studies which investigate the impact of dust evolution on the MRI-driven turbulence by coupling the dust coagulation (Smoluchowski) equation, an analytic model for the disk ionization including charged grains, and an empirical model for the disk viscosity based on nonideal MHD simulations. Nevertheless, their work modeled the dust as a two-population phase instead of considering the full grain size distribution, neglected dust radial drift, and most importantly did not include ambipolar diffusion which is fundamental to accurately describe the MRI activity in disks as I showed in Chapter 4. Consequently, the effect of dust (dynamics and grain growth processes combined) on the MRI activity in protoplanetary disks still remains to be properly looked at on secular evolution timescales.

Armed with the global MRI-driven disk accretion model of Chapter 3 and the knowledge acquired through our first detour (Chapter 4), this Chapter features the second detour of our adventure where I dive in depth into the MRI–dust coevolution on secular timescales. In the same spirit of avoiding the kitchen-sink approach

and gathering as much building blocks of knowledge as possible for the ultimate goal of this thesis, the aim here is to present a pilot study which provides a proof of concept that dust evolution alone has substantial impact on the MRI-driven turbulence. Particularly, I will make some assumptions in order to isolate the first-order effect.

5.2 METHOD

Table 5 summarizes all the models considered in this Chapter. Below I describe them in details, and explain the numerical implementation.

5.2.1 *Approach*

In this Chapter, I study the sole impact of dust evolution on the MRI activity over millions of years. As a result, I make the assumptions that the gas component of the protoplanetary disk as well as the stellar bolometric and total X-rays luminosity –what matters for the MRI activity besides the dust properties as I showed in the previous Chapter– are stationary[1]. Essentially it implies that, $\forall t \; \Sigma_{gas}(t, r) = \Sigma_{gas}(r)$ (i.e., total disk gas mass constant over time), $L_\star(t) = L_\star$ and $L_{XR}(t) = L_{XR}$. Here $\Sigma_{gas}(r)$ is an input radial profile of the model, and $L_\star$ as well as L_{XR} are constant free parameters.

Since the dust now evolves over time in this Chapter, I want to monitor the time evolution of the MRI-induced disk turbulence parameter $\bar{\alpha}$, which is derived for each dust evolution snapshot given the fixed gas and stellar input properties. To do so I couple the global MRI-driven disk accretion model of Chapter 3 (encoded into `mhdpy`) to the dust evolution model of `DustPy` (encoding the dust dynamics and grain growth processes explained in Sect. 2.3). This allows for the first time to have MRI-driven turbulence calculations (leading to $\bar{\alpha}$) and dust evolution (dust dynamics and grain growth processes combined) simultaneously integrated into a single framework. Here I want to emphasize that the coupling between `mhdpy` and `DustPy` is not self-consistent yet, but partial. There are two reasons for this. First, the evolution of the gas in `DustPy` is disabled as discussed above. Second, the evolution of the effective disk turbulence parameter $\bar{\alpha}$ is not treated simultaneously with the evolution of the dust: At each dust evolution snapshot, the new $\bar{\alpha}$ is indeed not reinjected into the dust evolution model for the next steps of dust evolution calculations. This implies that the feedback from a change in the disk turbulence due to dust evolution is not accounted for. I justify this choice by reminding the eager reader that the goal of this Chapter is to isolate the first-order effect of dust evolution on the MRI-driven accretion, and not to study the secular evolution of the disk. In this context, I only want to investigate whether or not dust evolution changes substantially the MRI-induced $\bar{\alpha}$ over time, as well as where in the protoplanetary disk changes would occur if any. I invite the eager reader to check out Chapter 6,

---

1 time-independent

Model	$M_\star$ [$M_\odot$]	$L_\star$ [$L_\odot$]	M_{disk} [$M_\star$]	B & B_z [Gauss]	α_{hydro}	T [K]	$\Sigma_{dust}(t,r,a)$ [g.cm^{-2}]	$\Sigma_{gas}(r)$ [g.cm^{-2}]	a_{min} [μm]	v_{frag} [m.s^{-1}]
I	1	2	0.05	MRI-optimal	10^{-4}	Thin	DustPy	SS	0.55	1
II	1	2	0.05	MRI-optimal	10^{-4}	Thin	DustPy	LBP	0.55	1
III	1	2	0.05	MRI-optimal	10^{-4}	Thin	DustPy	LBP	0.55	10

Table 5: Summary of the parameters used in each model of this Chapter. The grain size distribution, hence the temporal evolution of the dust surface density for each grain species of size a, $\Sigma_{dust}(t,r,a)$, is directly obtained from the dust evolution model encoded into DustPy. It depends on the minimum size of the dust distribution a_{min} and the fragmentation velocity v_{frag}. Initially, at each disk radius, the grain size distribution (hence $\Sigma_{dust}(t=0,r,a)$) is assumed to follow a MRN-like distribution of interstellar grains with a_{min}, $a_{dist,Max} = 1\,\mu$m and $p_{dist,Exp} = -3.5$, as well as a total vertically integrated dust-to-gas mass ratio (accounting for all grain species) $f_{dg,tot} = 10^{-2}$. In order to solely focus on the impact of dust evolution, the gas component of the protoplanetary disk as well as the stellar bolometric and total X-rays luminosity are assumed stationary (i.e., $\forall t\ \Sigma_{gas}(t,r) = \Sigma_{gas}(r)$, $L_\star(t) = L_\star$ and $L_{XR}(t) = L_{XR}$, which are inputs of the model). Here $\Sigma_{gas}(r)$ can follow two profiles given by the conditions referred to as "Steady-State (SS)" or "Lynden-Bell Pringle (LBP)". Also, I assume that $L_{XR} = 10^{-3.5} \times L_\star$. Finally, "Thin" means that the gas temperature model follows Eq. (46), and "MRI-optimal" means that the r.m.s. magnetic field B and the vertical magnetic field B_z are derived following option A of Sect. 3.5.3. For a detailed description of the various models, see Sect. 5.2.

should they wonder how the self-consistent coupling between gas and dust evolution with MRI-driven turbulence calculations shapes the disk secular evolution.

The general methodology adopted in this Chapter is as follows: Initially, at each disk radius, the grain size distribution is assumed to follow a MRN-like distribution of interstellar grains [151] with $a_{min} = 0.55\,\mu m$, $a_{dist,Max} = 1\,\mu m$ and $p_{dist,Exp} = -3.5$, as well as a total vertically integrated dust-to-gas mass ratio (accounting for all grain species) $f_{dg,tot} = 10^{-2}$. I then run the code `DustPy` to let the dust phase evolve until 5 Myrs, hence providing the time evolution of the dust surface density for each grain species of size a, $\Sigma_{dust}(t, r, a)$. For each dust evolution snapshot I can then reconstruct the vertical dust structure of each grain species (Eq. 93). I can then compute the five key dust quantities (Eqs. 94, 96, 114, 117, 145) that enable to capture the feedback of the dust on the gas ionization degree and the MRI activity (see Chapter 3). Assuming some properties for the star (see next section) and given the gas properties described below, the corresponding MRI-induced disk viscosity parameter, $\bar{\alpha}$, can be computed for each dust evolution snapshot, hence providing its time evolution.

Since gas evolution is turned off in this Chapter, I need to provide the radial profile for the fixed gas surface density, $\Sigma_{gas}(r)$, that is used for both the dust evolution model (`DustPy`) and the global MRI-driven disk accretion model (`mhdpy`). It is an input profile of the model that follows what I refer to as either "Steady-State (SS)" condition or "Lynden-Bell Pringle (LBP)" condition in Table 5 (see the profiles in *Panel b* of Figs. 43 and 45, respectively). On the one hand, the SS condition means that $\Sigma_{gas}(r)$ follows the gas surface density profile obtained for the steady-state MRI-driven accretion solution corresponding to Model XI of Chapter 4 (see Fig. 38), with the same initial MRN-like grain size distribution used in the dust evolution model described above ($a_{min} = 0.55\,\mu m$, $a_{dist,Max} = 1\,\mu m$ and $p_{dist,Exp} = -3.5$), and after applying Rayleigh adjustment to it (see Appendix 5.6.1). It means that $\bar{\alpha}$ at $t = 0$ year is such that the gas is in steady-state accretion. On the other hand, the LBP condition means that $\Sigma_{gas}(r)$ follows the classical radial profile of a power-law combined with an exponential cutoff [the self-similar solution, 121] with a total disk gas mass $M_{disk} = 0.05\,M_\star$, and a critical radius $R_c = 80$ au. It means that $\bar{\alpha}$ at $t = 0$ year is such that the gas is *not* in steady-state accretion The idea behind using two different input gas surface density profiles is to make sure that any results drawn in this Chapter are independent of the choice made for this quantity. Here Model I uses the SS condition for the gas surface density profile, while Model II uses the LBP condition.

Finally I need to provide the $\bar{\alpha}$ used to perform the dust evolution calculations, since the coupling between the global disk accretion model (`mhdpy`) and the dust evolution model (`DustPy`) is only partial in this Chapter. Indeed, when solving for the dust evolution, I discussed in Sect. 2.3 that there are δ parameters that control the strength of the turbulent collision velocities (δ_{turb}), the vertical mixing (δ_{vert}), and the radial mixing of dust particles (δ_{rad}). In this thesis these parameters are all taken equal to $\bar{\alpha}$, as I assumed the MRI-driven turbulence to control these processes simultaneously. I set the $\bar{\alpha}$ used by the dust evolution model to the input profile

shown at $t = 0$ year in *Panel a* of Figs. 43, 45 or 47. Such a profile is obtained from the global MRI-driven disk accretion model, with the same MRN-like grain size distribution and gas surface density profile (either following the SS or LBP condition) as described above.

5.2.2   *Numerical implementation*

The parameters used to run the global MRI-driven disk accretion model of Chapter 3 are taken from Table 1. One should note that the electron sticking coefficient, s_e, is now chosen equal to 0.6 (instead of 0.3 as in Chapter 4). This updated value is more compatible with the detailed calculations conducted by Bai [112]. In practice, it does not change the outcome of the semi-analytical chemical model implemented in the global MRI-driven disk accretion model. As a summary, the common parameters across the models of this Chapter have the following definitions:

- STELLAR PROPERTIES. Stellar mass $M_\star = 1\,M_\odot$, stellar bolometric luminosity $L_\star = 2\,L_\odot$, and total stellar X-rays luminosity $L_{XR} = 10^{-3.5} \times L_\star$.

- GAS PROPERTIES. Total disk gas mass $M_{disk} = 0.05\,M_\star$. Furthermore, the gas is assumed vertically isothermal with a radial temperature profile following Eq. (46) (this choice does not have a significant impact on the MRI-driven turbulence as shown in Sect. 4.4.6).

- DUST PROPERTIES. I consider that the dust phase consists of a distribution of dust particles with different sizes. Each grain is assumed to be a perfect compact sphere of intrinsic volume density $\rho_{bulk} = 1.4\,\mathrm{g.cm^{-3}}$. For a grain of size a, the corresponding mass is then $m(a) = \frac{4}{3}\pi\rho_{bulk}a^3$. For the grain size distribution, I always consider a logarithmic grid of grain species whose size range from $a_{min} = 0.55\,\mu m$ to 250 cm. Also, seven mass bins per mass decade are considered (following the work of Ohtsuki, Nakagawa, and Nakazawa [280] and Drążkowska, Windmark, and Dullemond [281]), which leads to a total number of mass bins of $N_m = 141$. In light of the recent laboratory experiments on icy particles [e.g., 168–170] the fragmentation velocity, v_{frag}, is assumed to be radially constant equal to $1\,\mathrm{m.s^{-1}}$ in Models I and II. For completeness, I also adopt the higher value of $10\,\mathrm{m.s^{-1}}$ [e.g, 282–284] in Model III. One should note that Model II and III are identical, except for the value of v_{frag}. The dust inner boundary condition when solving for the dust transport equation in `DustPy` is the default one, while the outer boundary condition is set as follows: In Model I, I impose at each time step a constant power-law on the dust surface density, leading to an inflow of dust particles over time consistent with the input gas surface density profile (initially following steady-state MRI-driven accretion). Indeed, assuming that the gas is initially in steady-state MRI-driven accretion means that there is a gas and dust reservoir outside the simulation domain due to viscous spreading. In Models II and III, I impose a floor value on the dust surface density, which essentially

prevents the inflow of dust particles from the disk outer regions. Finally, I use `DustPy` version 0.5.8.

- IONIZATION CHEMISTRY. Since I consider a grain size distribution for the dust component of the protoplanetary disk, the dust quantities that come into play in the semi-analytical chemical model and nonideal MHD calculations of the global MRI-driven disk accretion model ($a_{dust,rep}$, $\sigma_{dust,rep}$ and $m_{dust,rep}$) are defined by Eqs. (114), (117) and (145). Furthermore, the radionuclide ionization rate $\zeta_{RA}^{(H_2)}$ for H_2 is computed following option A of Sect. 3.3.3.

- MAGNETIC FIELD. The magnetic field strength and topology are set by following option A of Sect. 3.5.3.

By assuming the protoplanetary disk to be geometrically thin, the vertical and radial dimensions can be decoupled into a 1+1D (r, z) problem, where each radial grid-point contains an independent vertical grid. Furthermore, by assuming the disk to be axisymmetric and symmetric about the midplane, it is enough to compute the domain $z \geqslant 0$ to obtain the full solution. The radial grid is computed from r_{min} to r_{max}, with N_r cells logarithmically spaced. For every radial grid-point $r \in [r_{min}, r_{max}]$, the corresponding vertical grid is computed from the disk midplane $(z = 0)$ to z_{max}, with N_z cells linearly spaced. In all the simulations of this Chapter, the radial grid is computed from $r_{min} = 1$ au to $r_{max} = 200$ au, with $N_r = 256$ cells. For every radial grid-point $r \in [r_{min}, r_{max}]$, the corresponding vertical grid is computed from the disk midplane $(z = 0)$ to $z_{max}(r) = 5\,H_{gas}(r)$, with $N_z = 512$. Here H_{gas} corresponds to the vertical gas scale height defined in Eq. (63). One should note that the vertical grid is only used to run the global MRI-driven disk accretion model.

The next sections are organized as follows: In Sect. 5.3 I investigate the impact of dust evolution on the MRI activity. In Sect. 5.4 I discuss the implications of the results. Finally Sect. 5.5 summarizes the findings.

5.3   RESULTS

5.3.1   *The SS condition for the gas surface density profile*

This simulation assumes that the gas surface density profile is stationary, following the steady-state MRI-driven accretion solution corresponding to Model XI of Chapter 4 with a MRN-like grain size distribution $a_{min} = 0.55\,\mu m$, $a_{dist,Max} = 1\,\mu m$ and $p_{dist,Exp} = -3.5$ (see Fig. 38), and after applying Rayleigh adjustment to it (see Appendix 5.6.1). It means that the gas is assumed to be in steady-state at $t = 0$ year. The corresponding $\bar{\alpha}$ computed with the global MRI-driven accretion model of Chapter 3 is used to perform the dust evolution. From the dust phase perspective, therefore, the dead zone is invariant over time, with its outer edge always located at ~ 27 au.

Figure 42 shows that the dust can grow up to sizes larger than millimeters inside the dead zone ($r \lesssim 27$ au), whereas the maximum grain size reaches an upper limit

of $\sim 10\,\mu m$ outside of it, with an abrupt transition at the dead zone outer edge. This is because the maximum grain size can be limited by either drift when the drift timescale exceeds the growth timescale, or fragmentation when the collision velocity between dust particles exceeds the material fragmentation velocity v_{frag} [137, 285]. For each limit, the time-dependent maximum Stokes number reachable by a dust particle is determined by

$$St_{drift} = \left| \frac{d \ln P_{gas,mid}}{d \ln r} \right|^{-1} \left(\frac{v_K}{c_s} \right)^2 f_{dg,tot}, \tag{167}$$

and

$$St_{frag} = \frac{1}{3\bar{\alpha}} \left(\frac{v_{frag}}{c_s} \right)^2. \tag{168}$$

The $\bar{\alpha}$ used to perform the dust evolution is shown at $t = 0\,year$ in Fig. 43a. It has a mean value of $\sim 1.7 \times 10^{-4}$ in the dead zone, and $\sim 3 \times 10^{-3}$ in the MRI active region, with a sharp increase near the dead zone outer edge. Additionally, Fig. 42 indicates that the maximum grain size is set by the fragmentation barrier (dashed cyan line), everywhere in the disk for the entire dust evolution simulation. Since St_{frag} is inversely proportional to $\bar{\alpha}$, and the turbulent collision velocity between grains is proportional to it with $\Delta v_{turb} \approx \sqrt{3\bar{\alpha}/St}c_s$ [for $St \ll 1$, 171], dust particles can grow into larger sizes in the dead zone compared to the MRI active region.

The turbulence level used to perform the dust evolution is so low in the regions within 30 au that grain coagulation is effective during the first stages of dust evolution (from 0 year to 0.1 Myr), even leading to a depletion in the submicron-sized particles in some parts of the dead zone (top row of Fig. 42). One can better appreciate this depletion by looking at Figs. 44a and 44b. These panels show the temporal evolution of the midplane representative grain size (tracing the smallest sizes of the dust distribution), and the midplane equivalent size of the representative grain cross-section (relevant size of the dust distribution involved in the ionization chemistry), respectively. There is a growth wave propagating inside-out from the initial time until 0.01 Myr, which is attributed to the location where the dust size distribution becomes skewed toward larger sizes because submicron-sized particles grow much quicker than fragmentation can replenish them, as shown by Fig. 44c. This panel displays the temporal evolution of the midplane equivalent size of the representative grain mass (tracing the largest sizes of the dust distribution) in the protoplanetary disk. Since this quantity increases quickly in the dead zone within 0.01 Myr, it implies that larger sizes indeed become present in the dust size distribution. The effective growth of submicron-sized particles into larger sizes can also be seen by comparing Figs. 44d and 44e. While the midplane total number dust density ($n_{dust,tot}$) decreases within 0.1 Myr, the midplane total dust density ($\rho_{dust,tot}$) increases. Since the total dust content almost remains constant within this period of time, a decrease in $n_{dust,tot}$ is primarily related to a decrease in the relative proportion of small dust particles in the dust distributions that have grown into larger sizes (hence the increase of $\rho_{dust,tot}$).

The first direct consequence of the initial effective grain growth in the dead zone, within 0.1 Myr of dust evolution, is that more dust particles can settle toward the midplane. Settling causes an increase in the local dust-to-gas mass ratio at the midplane (ρ_{gas} is constant here, while $\rho_{dust,tot}$ increases as shown by Fig. 44d). Consequently, the ionization power of radionuclides increases, leading the midplane total ionization rate to increase for $r \lesssim 30$ au (Fig. 43c). The second direct consequence is that ambipolar diffusion becomes weaker (particularly where grain surface adsorption dominates the recombination process), since the total grain surface area, A_{tot}, decreases when the dust grow (see Sect. 4.4.8) or when the dust distribution is skewed toward larger grain sizes (see Sect. 4.7.1.2). In this regard, Fig. 43d shows that the MRI is allowed by ambipolar diffusion to have stronger magnetic field strengths for $r \lesssim 30$ au, as dust evolves from 0 year to 0.1 Myr, particularly near the dead zone outer edge.

From these two consequences, one can now understand the temporal evolution of $\bar{\alpha}$ for $r \lesssim 30$ au, within the first stages of dust evolution (from 0 year to 0.1 Myr): A higher ionization level combined with a less stringent ambipolar diffusion result in the MRI activity being able to operate closer to the central star (Fig. 43f shows that the dead zone outer edge deceases within 0.1 Myr), with stronger turbulence generated for any regions within 30 au (Fig. 43a). Interestingly, $\bar{\alpha}$ first varies in the very inner regions of the dead zone due to an increase in the radionuclide ionization rate from dust settling, followed by a variation in the outer regions of the dead zone due to a decrease in the total grain surface area, A_{tot}, from dust growth. Looking at Fig. 42, I find that dust particles reach their maximum sizes between 0.01 Myr and 0.1 Myr, which coincides with the timescale over which the MRI activity has substantially changed (see Figs. 43a and 43f). This indicates that the timescale over which dust evolution significantly impacts the MRI-driven turbulence is a timescale of local dust growth [see e.g., Eq. (30) of 135, for the analytic formula].

On another note, $\bar{\alpha}$ continues to increase while R_{DZ} decreases between 0.1 Myr and 1 Myr (Figs. 43a and 43f). Since the maximum grain sizes have already been reached within 0.1 Myr (Fig. 42), the explanation for such behaviors no longer lies in dust growth alone. Figure 44d shows that $\rho_{dust,tot}$ significantly decreases in the regions within ~ 30 au, between 0.1 Myr and 1 Myr. One can infer that the dust content decreases in these regions, due to radial drift which is faster for particles that have grown to larger sizes. When the dust is removed from the disk, the dust-to-gas mass ratio decreases, which allows the MRI to operate closer to the central star with stronger activity [see Sect. 6.3 of 184]. Indeed, although a decrease in the dust-to-gas mass ratio implies a lower midplane total ionization rate for $r \lesssim 30$ au due to less radionuclides (Fig. 43c), the dust is far less efficient at sweeping up free electrons and ions from the gas-phase due to a decrease in the total grain surface area, hence resulting in a net increase in the gas ionization degree.

Despite some dust growth within the first stages of dust evolution for $r \gtrsim 30$ au, one notice that it is not enough to make a real impact on the temporal evolution of the MRI-induced effective turbulent parameter, the midplane total ionization

rate or the MRI-optimal r.m.s. magnetic field strength (Figs. 43a, 43c, and 43d). It is because the dominant recombination process in these regions is gas-phase recombination, which is weakly dependent on the dust properties. Consequently, it is expected not to see much change in terms of MRI activity for $r \gtrsim 30$ au, within 1 Myr.

Finally, let us focus on the late stages of dust evolution ($t > 1$ Myr), where all the five dust quantities used to couple `DustPy` with the global MRI-driven disk accretion model of Chapter 3 reach a quasi-steady-state (Fig. 44). In the present model, I assumed that the gas surface density follows initially steady-state accretion (Fig. 43b). While the steady-state profile describes the inner inward accreting region ($r \lesssim R_t$) of the viscously evolving disk, it cannot capture the outer viscously expanding region ($r \gtrsim R_t$). Here R_t corresponds to the transition radius at which the gas motions changes from inward to outward in a viscously evolving disk [e.g., 268]. The presence of an outer region outside the simulation domain ($r \gtrsim 200$ au) is thus expected, which can feed the disk ($1 \lesssim r \lesssim 200$ au) of submicron- and micron-sized dust particles. Here I aimed to mimic this situation by choosing the dust outer boundary condition such that there is an inflow of (small) dust particles through the outer boundary of the domain. Consequently, the fact that the dust reaches a quasi-steady-state for $t > 1$ Myr appears to be directly linked to such a choice. It leads the MRI-driven turbulence and the dead zone outer edge to be roughly constant from 1 Myr all the way until 5 Myr of dust evolution. Particularly, the apparent temporal dead zone stability whilst the dust evolves is thus a mere artifact of the choice made for the dust boundary condition in this case. It is worth noting that the radioactive decay of ^{26}Al has been ignored in this Chapter (the radionuclide ionization rate is derived following option A of Sect. 3.3.3), which means that the radionuclide ionization rate for $t > 1$ Myr is expected to be smaller than what I assumed. However, it is not too bothersome in the context of this study (investigating the first-order effect of dust evolution on the MRI activity) because [184] (see, e.g., their Fig. C.1) showed that the ionization from radionuclides only dominates the total ionization rate deep within the dead zone (radially and vertically). Consequently, the location of the dead zone outer edge should not significantly vary, in the cases considered, if the decrease over time in the radionuclide ionization rate due to the decay of ^{26}Al is accounted for. This statement also holds for the time evolution for $t > 1$ Myr seen in the next section. I want to emphasize that a better description of the radionuclide ionization rate (following option B of Sect. 3.3.3) is used in Chapter 6, since there the self-consistent feedback of dust evolution on the MRI activity is implemented.

Although the coupling between dust evolution and the global MRI-driven disk accretion model of Chapter 3 is only partial in this Chapter (see Sect. 5.2.1), it is clear that dust evolution has significant impact on the MRI activity: dust settling, grain coagulation, and fragmentation drive the change in the gas ionization degree, hence on $\bar{\alpha}$ at each radius r, on a timescale of local dust growth. In the specific case of Model I, it is thus expected that dust evolution drives the gas away from the assumed initial steady-state MRI-driven accretion (the SS condition for the gas sur-
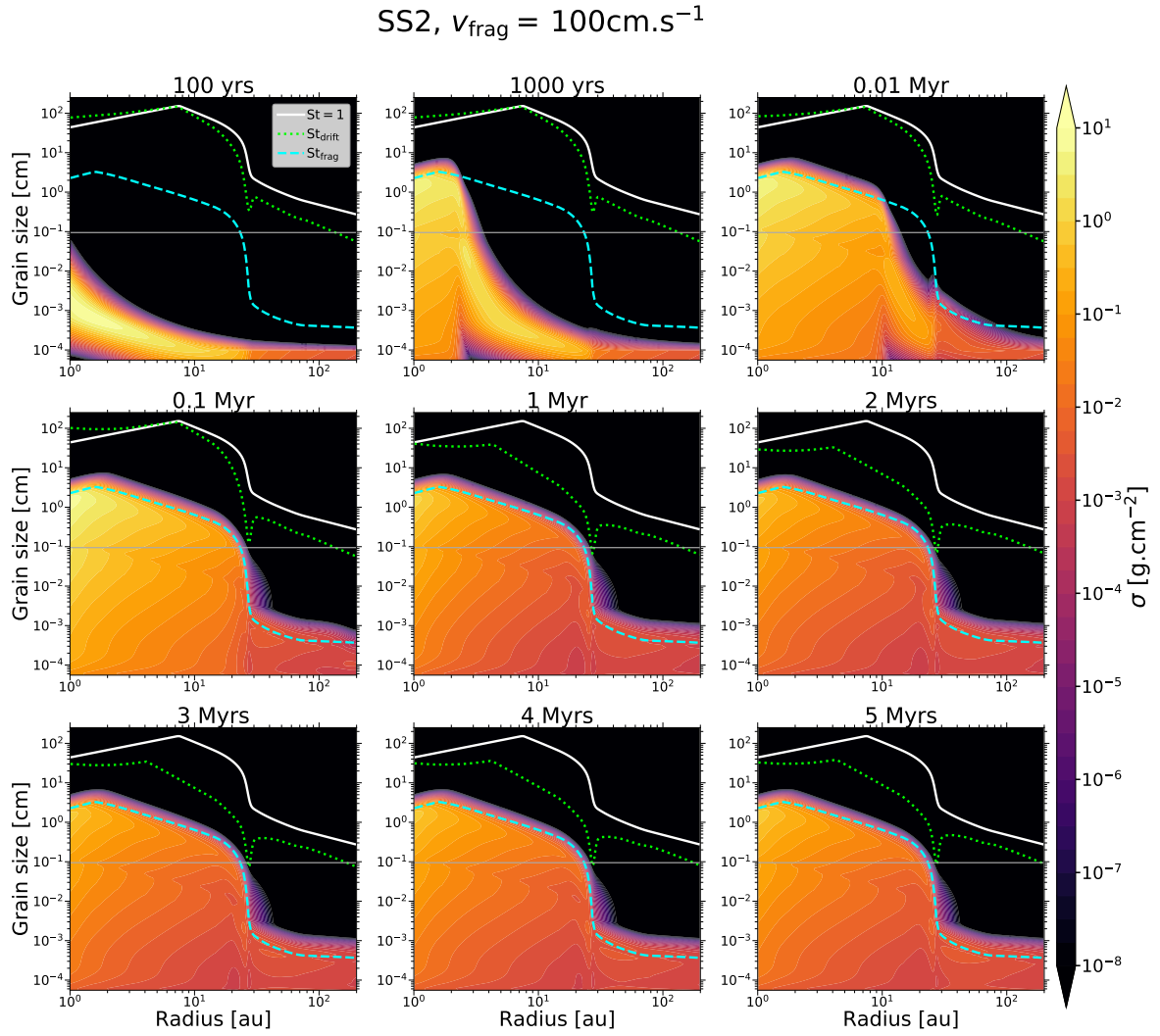
Figure 42: Temporal evolution of the dust surface density distribution per logarithmic bin of grain size $\sigma(t, r, a)$ (see Eq. 186), for Model I. In each panel, the solid white line shows a Stokes number of unity (radial drift reaches its maximal efficiency), the dotted green line shows the drift limit (Eq. 167), and the dashed cyan line shows the fragmentation limit (Eq. 168). The horizontal solid dark gray lines show a grain size of 1 mm.

face density profile), by substantially changing the effective turbulent parameter $\bar{\alpha}$ from early stages. Indeed, any changes in $\bar{\alpha}$ due to dust evolution directly modifies the advection-diffusion equation for the gas. This change is expected to carry on for the next steps of the dust evolution calculations because it depends on $\bar{\alpha}$ and the gas properties. Consequently, I find that the initial steady-state MRI-driven accretion solution imposed on the gas is actually not an equilibrium solution when dust evolution is accounted for. In Chapter 6, I explore the self-consistent interplay of gas, dust and MRI evolution on secular timescales, and confirm that the steady-state accretion for the gas is not reached.
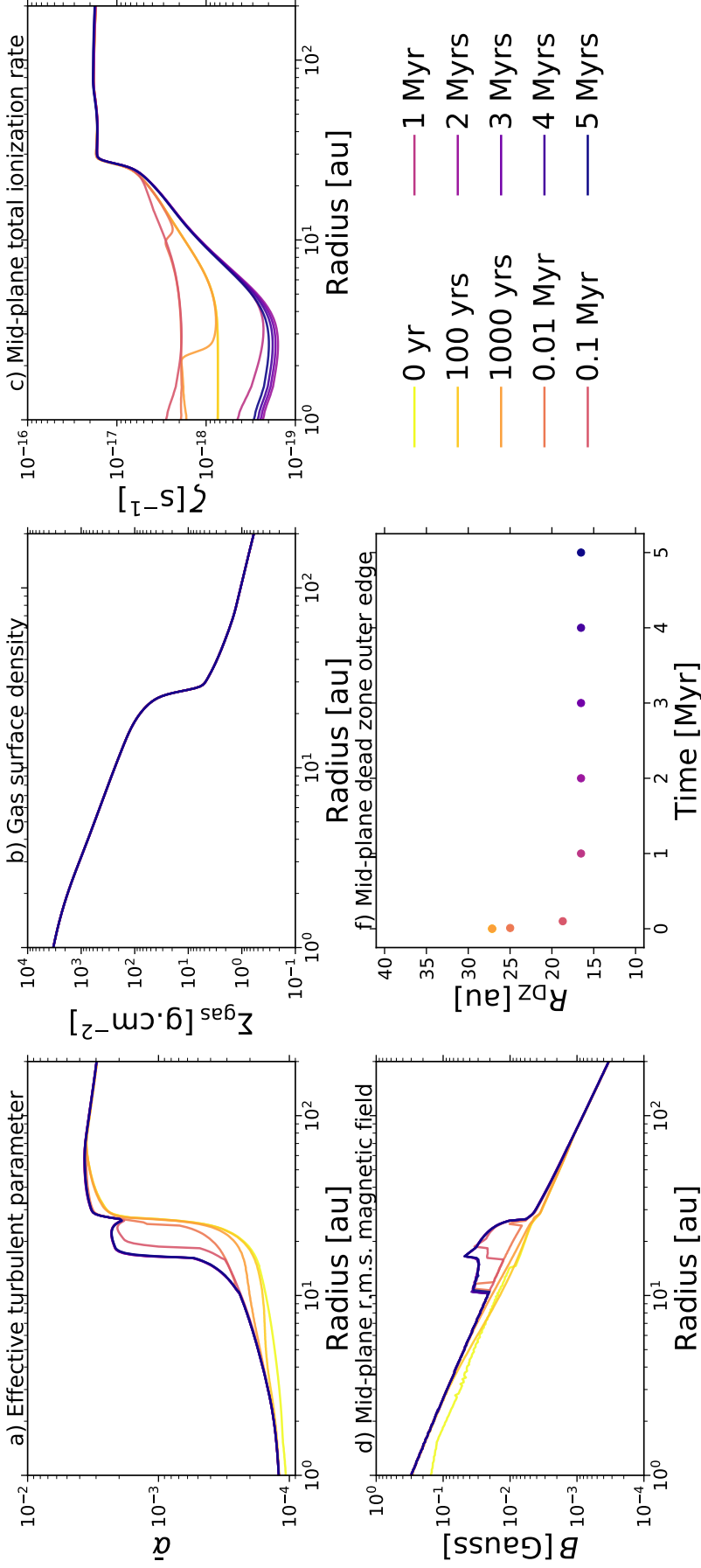
Figure 43: Impact of dust evolution on the MRI-driven turbulence, for Model I. The panels show the temporal evolution of the radial profiles of some key quantities. I want to emphasize that these quantities do not describe steady-state MRI-driven accretion unlike the previous Chapter, since they are recalculated at each dust evolution snapshot, through the partial coupling between the dust evolution model of DustPy and the global MRI-driven disk accretion model of Chapter 3 encoded into mhdpy. On this note, the corresponding temporal evolution of the five dust quantities used to perform such a coupling are shown in Fig. 44. *Panel a*: Pressure-weighted vertically integrated turbulent parameter (Eq. 77). *Panel b*: Gas surface density. One should note that it is stationary to solely focus on the impact of dust evolution on the MRI activity, following the condition referred to as SS. *Panel c*: Midplane total ionization rate (Eq. 102). *Panel d*: Midplane MRI-optimal r.m.s. magnetic field strength, B, that is required for the MRI activity to be at the maximal efficiency as permitted by Ohmic resistivity and ambipolar diffusion (option A of Sect. 3.5.3. *Panel f*: Midplane radial dead zone outer edge location, R_{DZ}, defined as the midplane radial location where both the Ohmic and ambipolar condition are met for the first time (Sect. 3.5.1). One should note that the dead zone outer edge coincides at $t = 0$ year, $t = 100$ years and $t = 1000$ years.
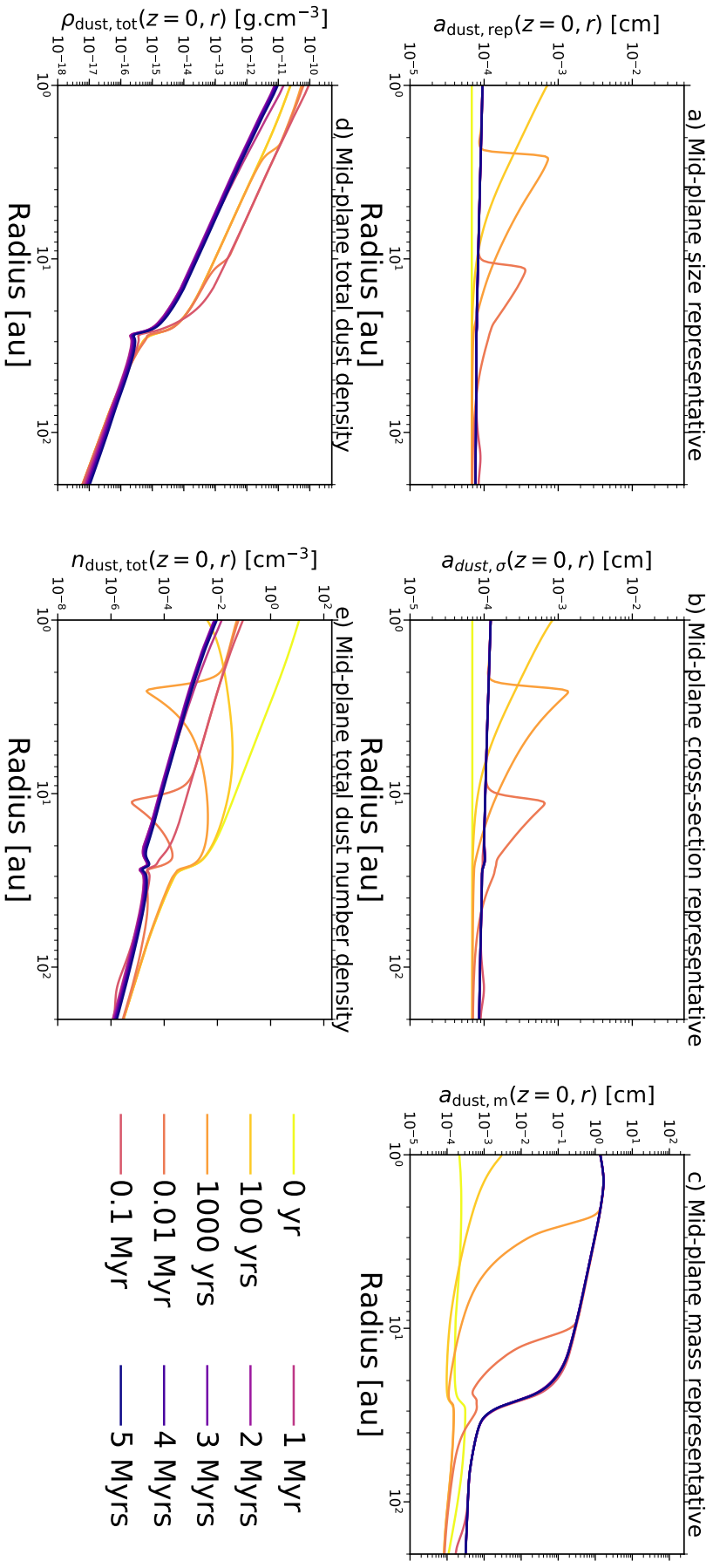
Figure 44: Temporal evolution of the five dust quantities used to couple the dust evolution model of DustPy with the global MRI-driven disk accretion model of Chapter 3, for Model I. These quantities are the representative grain size $a_{dust,rep}$ (Eq. 114) in *Panel a*, the representative grain cross-section $\sigma_{dust,rep}$ (Eq. 117), the representative grain mass $m_{dust,rep}$ (Eq. 145), the total dust density $\rho_{dust,tot}$ (Eq. 94) in *Panel d*, and the total dust number density $n_{dust,tot}$ (Eq. 96) in *Panel e*. Instead of displaying $\sigma_{dust,rep}$ and $m_{dust,rep}$, I show the equivalent grain size $a_{dust,\sigma} = \left(\sigma_{dust,rep}/\pi \right)^{\frac{1}{2}}$ corresponding to $\sigma_{dust,rep}$ (*Panel b*), and the equivalent grain size $a_{dust,m} = \left(3m_{dust,rep}/4\pi\rho_{bulk} \right)^{\frac{1}{3}}$ corresponding to $m_{dust,rep}$ (*Panel c*). These equivalent grain sizes better indicate the dominant size when considering the grain cross-section or the grain mass, each of which is important for the MRI calculations (see Sect. 3.4). The panels particularly show the midplane radial profiles. I want to emphasize that $a_{dust,rep}$ and $a_{dust,m}$ traces the smallest and largest sizes of the dust distribution, respectively, whereas $a_{dust,\sigma}$ is the relevant size of the dust distribution involved in the ionization chemistry.

5.3.2 *The LBP condition for the gas surface density profile*

Here the goal is to see if the results drawn in the previous section still hold with a different set of assumptions for the gas surface density profile and the dust outer boundary condition. In this case, the gas surface density profile follows the classical self-similar solution with a total disk gas mass $M_{disk} = 0.05\,M_\star$, and a critical radius $R_c = 80\,au$ (Fig. 45b). Here I want to emphasize again that the gas surface density profile does not evolve with time, so that the focus is solely about the effect of dust evolution on the MRI-driven turbulence. The dust outer boundary condition is chosen such that there is no inflow of small dust particles in the simulation domain, unlike Model I. Additionally, the $\bar{\alpha}$ used to perform the dust evolution is now derived from the gas surface density profile mentioned above by the global MRI-driven disk accretion model of Chapter 3 (see Fig. 45a at $t = 0$ year). From the dust perspective, it means that the dead zone is still invariant over time, but with its outer edge now always located at $\sim 40\,au$.

Similar to what I find in the previous section, dust growth is fragmentation-limited everywhere in the disk and throughout its whole evolution, with dust particles growing into larger sizes in the dead zone ($r \lesssim 40\,au$) compared to the MRI active region (see Fig. 49). The main difference, though, is that the particles do not reach sizes as large in the dead zone (there are less grains of size $a \geqslant 1\,mm$ than Model I), but do reach larger sizes in the MRI active region (grains can be as large as $\sim 100\,\mu m$), resulting in a much smoother transition in the dust surface density per logarithmic bin of grain size ($\sigma(t, r, a)$) at the dead zone outer edge. This can be explained by the fact that the $\bar{\alpha}$ used to perform the dust evolution in Model II is on average higher in the dead zone and lower in the MRI active region than the one used in Model I, with a much smoother transition at the dead zone outer edge.

Another common feature between the results of this case (Model II) and Model I is the effective grain coagulation in the regions within 40 au, during the first stages of dust evolution (from 0 year to 0.1 Myr). Specifically, it results in a similar growth wave attributed to the depletion of small dust particles that grow into larger sizes (Figs. 46a, 46b and 46c). In the same fashion as in Sect. 5.3.1, effective grain coagulation leads to: (1) more settling of dust particles toward the midplane ($\rho_{dust,tot}$ increases as shown in Fig. 46d), allowing for a higher midplane ionization rate in the regions within 40 au (Fig. 45c); (2) less stringent ambipolar diffusion, implying that the MRI can operate with stronger magnetic field strengths (B increases as shown by Fig. 45d). Consequently, the MRI activity is able to operate closer to the central star as the dust phase evolves (Fig. 45f shows that R_{DZ} decreases over time), with stronger turbulence generated in the regions within 40 au (Fig. 45a). Similar to Model I, $\bar{\alpha}$ (hence the dead zone outer edge) undergoes significant variation within 0.1 Myr, which corresponds to the timescale over which dust particles have reached their maximum size (Fig. 49). This again suggests that the timescale over which dust evolution impacts the MRI-driven turbulence is determined by the timescale of local dust growth.

Comparing Figs. 45a, 45f with Figs. 43a, 43f, respectively, one can notice that the temporal evolution of $\bar{\alpha}$ and R_{DZ} between 0.1 Myr and 1 Myr is less pronounced in Model II compared to Model I. Indeed, the dust particles within 40 au grow into smaller sizes compared to Model I, which makes their radial drift slower. As a result, they can be present in the disk for a longer period of time, meaning that the removal of the dust content is delayed: Fig. 46d shows that $\rho_{dust,tot}$ still increases between 0.1 Myr and 1 Myr and only starts decreasing from 1 Myr, while it decreases from 0.1 Myr in the case of Model I as shown by Fig. 44d.

In regions of the disk beyond $\sim$ 40 au (MRI active region from the dust perspective in Model II), Fig. 45 shows that, within 1 Myr, the effective MRI-induced turbulent parameter, the midplane total ionization rate, and the MRI-optimal r.m.s. magnetic field strength vary a bit more than in Model I. This behavior can be explained by noticing that the dust particles can grow into larger sizes in the MRI active region of Model II, especially near the dead zone outer edge ($r \sim 40$ au). This region marks the transition for the recombination process between grain surface adsorption and gas-phase, and is therefore more sensitive to the dust properties compared to the outer regions. For $r \gtrsim 80$ au, though, the MRI activity is pretty much steady within 1 Myr. This is expected since $R_c = 80$ au corresponds to the critical radius where the gas surface density profile drops exponentially, and therefore where the gas-phase is the main channel for recombination due to a high gas ionization degree.

To complete the comparison between Model I and Model II, I now need to discuss the temporal evolution of the MRI-driven turbulence during the late stages of dust evolution ($t > 1$ Myr). In the previous section, I showed that $\bar{\alpha}$ and R_{DZ} were roughly steady after 1 Myr of dust evolution, since the five dust quantities used to couple `DustPy` with the global MRI-driven disk accretion model reach a quasi-steady-state due to the steady influx of dust from the outer boundary. In Model II, though, $\rho_{dust,tot}$ and $n_{dust,tot}$ keep decreasing from 1 Myr all the way until 5 Myrs (Figs. 46d and 46e), since the dust content is gradually removed by radial drift which is no longer compensated for by an inflow of small particles in the simulation domain as in Model I. This implies that $\bar{\alpha}$ continues to increase while R_{DZ} decreases between 1 Myr and 3 Myr because the MRI can operate closer to the central star with stronger activity for decreasing dust-to-gas mass ratio (as explained in the previous section). Nonetheless, a salient result of Model II is the temporal evolution of the MRI activity between 3 Myrs and 5 Myrs. Although the dust keeps being removed from the disk, $\bar{\alpha}$ and R_{DZ} become stationary (Figs. 45a and 45f). It thus suggests that the MRI activity in the disk becomes weakly dependent on the dust properties when the dust content drops below a certain threshold, which is caused by a lack of dust particles to efficiently sweep up free electrons and ions from the gas-phase. In other words, gas-phase recombination dominates in most of the protoplanetary disk after 3 Myrs, and the dust has no longer a significant impact on the ionization chemistry. The disk dust–gas mixture thus behaves as a grain-free plasma after 3 Myrs, and the dead zone outer edge becomes stationary because the MRI activity evolution becomes primarily controlled by the gas which

is not evolving here. This result suggests that the dead zone may potentially be able to survive the protoplanetary disk evolution over a few million years when the MRI is the main driver for the disk accretion. I further discuss this idea in Sect. 5.4.2.

The results of this section emphasize that dust evolution has significant impact on the MRI activity, regardless of the assumptions made for the gas surface density profile or the dust outer boundary condition. Particularly, the MRI-induced $\bar{\alpha}$ undergoes substantial change within the timescale over which the dust particles grow.

5.4 DISCUSSION

5.4.1 *The effect of the fragmentation velocity*

Laboratory experiments of particle collisions are crucial in understanding the growth of grains from interstellar medium micron-sized dust to millimeter- and centimeter-sized pebbles in protoplanetary disks. First, they demonstrate the potential outcome (sticking, fragmentation, bouncing or mass transfer) after grain collisions with a given initial relative velocity [see e.g., 135, 162]. Second, they help to constrain the velocity threshold (fragmentation velocity v_{frag}) for either effective growth or destructive collisions [e.g., 155, 286–288]. In the classical picture, it has been commonly thought that amorphous water-ice particles are stickier than silicates [282–284]. Theoretical models employing dust evolution thus usually adopt a fragmentation velocity of $10 \, \text{m.s}^{-1}$ for ice particles. However, recent laboratory experiments show that this threshold velocity sensitively depends on the composition and temperature of the colliding particles. They found that water-ice particles may be as fragile as silicates, or even more so, resulting in the fragmentation velocity potentially being as low as $1 \, \text{m.s}^{-1}$ [168–170]. In Models I and II, I have therefore experimented with $v_{frag} = 1 \, \text{m.s}^{-1}$. For completeness, Model III investigates how this parameter impacts the results by taking a value of $10 \, \text{m.s}^{-1}$. One should note that, except for v_{frag}, Model III has the same setup as Model II.

For larger values of the fragmentation velocity (v_{frag}), grain collisions are less destructive which improves the efficiency of coagulation. The fragmentation barrier thus becomes less stringent, allowing grains to grow into larger particles than Model II, everywhere in the disk (Fig. 50). Within $0.1 \, \text{Myr}$ of dust evolution, the grains can grow into such large sizes that their Stokes numbers reach values close to unity. This results in the dust content being quickly removed from the disk between $0.1 \, \text{Myr}$ and $1 \, \text{Myr}$ due to effective radial drift, hence the quick increase in the MRI activity (Fig. 47). Indeed, Fig. 48d shows that $\rho_{dust,tot}$ first increases from $0 \, \text{year}$ to $0.1 \, \text{Myr}$ (caused by dust growth), then plummets by two orders of magnitude between $0.1 \, \text{Myr}$ and $1 \, \text{Myr}$. As a result, the dust-to-gas mass ratio significantly decreases within $1 \, \text{Myr}$ (ρ_{gas} is stationary), implying that the drift barrier gradually becomes more stringent because St_{drift} decreases when $f_{dg,tot}$ decreases (see Eq. 167). The main consequence is that dust growth is no longer solely

LBP, $M_\star = 1\,M_\odot$, $L_\star = 2\,L_\odot$, $M_{disk} = 0.05\,M_\star$, $\alpha_{hydro} = 10^{-4}$, $v_{frag} = 100\,cm.s^{-1}$
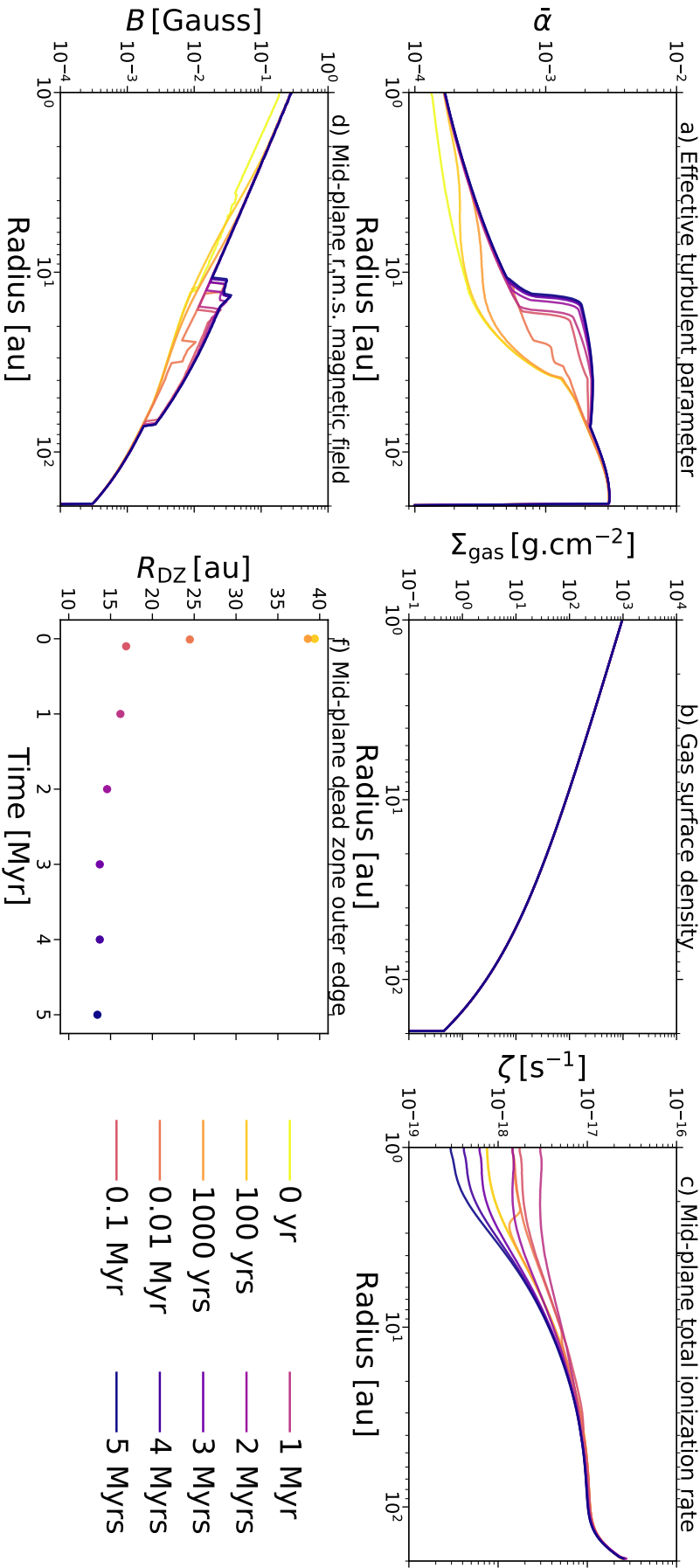
Figure 45: Same as in Fig. 43, except for Model II. The corresponding temporal evolution of the five dust quantities is shown in Fig. 46. The gas surface density (*Panel b*) is still stationary, but follows the LBP condition with a total disk gas mass $M_{disk} = 0.05\,M_\star$, and a critical radius $R_c = 80$ au. As a result, $\bar{\alpha}$ at $t = 0$ year is such that the gas is *not* in steady-accretion, unlike Model I. Here one should note that, in *Panel f*, the dead zone outer edge coincides at $t = 0$ year and $t = 100$ years.
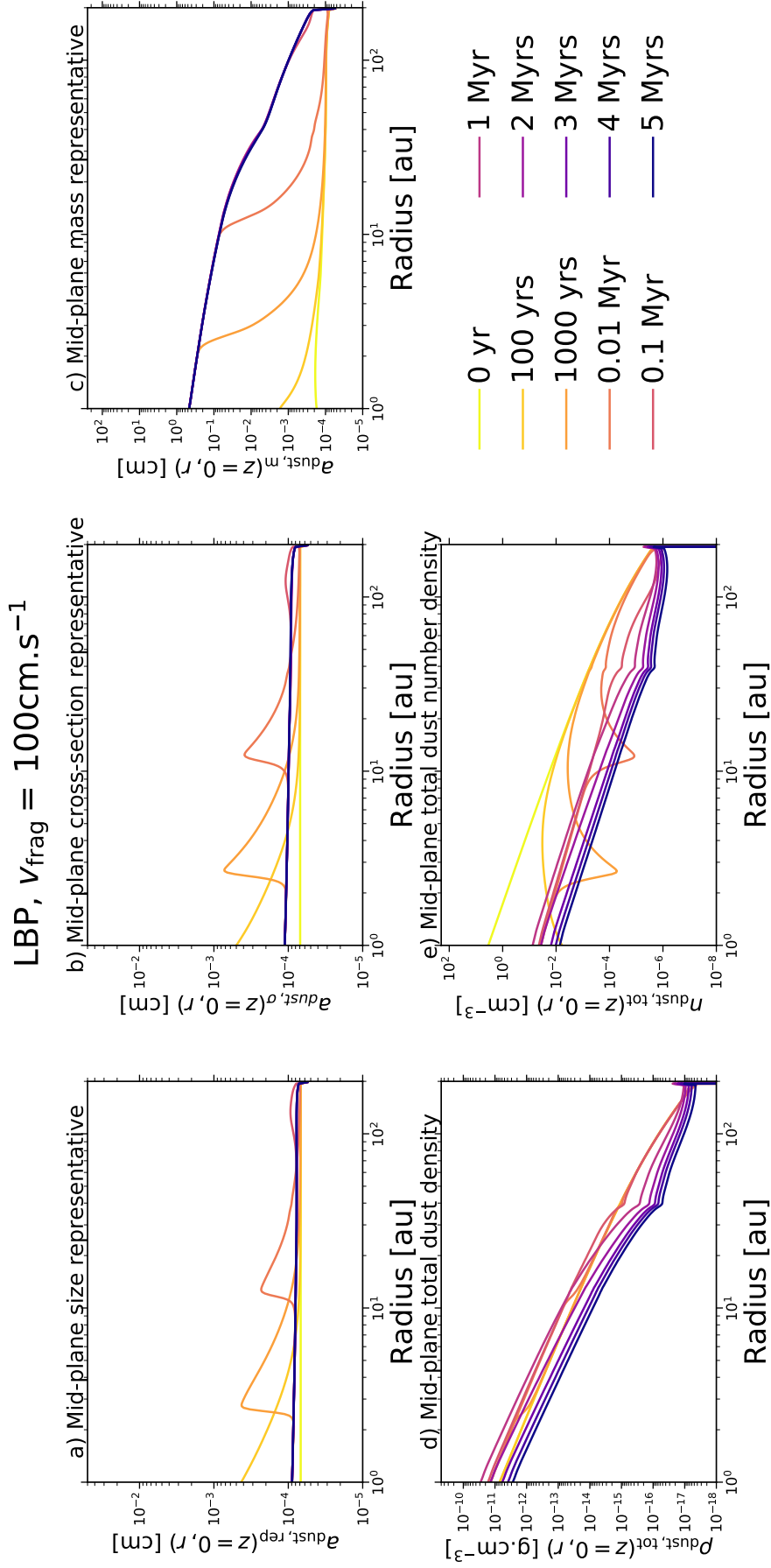
Figure 46: Same as in Fig. 44, except for Model II.

fragmentation-limited, unlike Model II. Instead, the temporal evolution of the dust surface density distribution per logarithmic bin of grain size (Fig. 50) shows that it transitions from being fragmentation-limited to drift-limited in the entire protoplanetary disk, in a million-year timescale. The larger grains thus radially drift inward before they can collide and replenish the smaller ones, resulting in the depletion of the latter at a wide range of radii within the dead zone as seen by the dust particles ($r \lesssim 40\,\mathrm{au}$), from 1 Myr. The lack of small dust particles leads the total dust number density to plummet from 0.1 Myr to $t > 1\,\mathrm{Myr}$ by at least two order of magnitudes (Fig. 48e), and the grain cross-section representative to be skewed toward particles as large as 100 µm in the disk inner regions (Fig. 48b).

Since the rapid drift of the larger particles significantly reduces the dust content in the protoplanetary disk, as well as prevents the smaller ones to be replenished efficiently, the total grain surface area is significantly reduced after 0.1 Myr. Consequently, gas-phase recombination becomes the main channel after 0.1 Myr, which makes the MRI activity weakly dependent on the dust properties. Particularly, it leads the effective MRI-induced turbulent parameter, the dead zone outer edge, and the MRI-optimal r.m.s. magnetic field strength to become stationary (Figs. 47a, 47d, and 47f) because there is no gas evolution accounted for here. This needs to be put in the context of the stationary temporal evolution of the MRI-driven turbulence between 3 Myrs and 5 Myrs seen in Sect. 5.3.2. In the present model, such a stationary behavior occurs much earlier than in Model II because the dust content is removed on a much shorter timescale due to more effective radial drift. In other words, the disk dust–gas mixture behaves as a grain-free plasma much faster for the present model. Once the treatment of dust and MRI calculations is done simultaneously, dust evolution can thus be expected to have a less long-term impact on the MRI activity in the regions of the disk with a higher fragmentation velocity.

5.4.2   *The potential long-lived state of the dead zone in protoplanetary disks*

One of the salient results of this Chapter is that, once the full self-consistent treatment of gas and dust evolution with MRI calculations is done, the temporal evolution of the MRI-driven turbulence is expected to be controlled first by dust evolution, then gas evolution. Indeed, I showed in Sects. 5.3.1 and 5.3.2 that the MRI-induced $\bar{\alpha}$ changes on a timescale of local dust growth, which is significantly shorter than the viscous evolution timescale in general. As long as there are enough dust particles in the disk to dominate the recombination process for the ionization chemistry, the MRI activity evolution is expected to be controlled by dust evolution. Once that is no longer the case, the MRI activity evolution is then expected to be controlled by gas evolution (occurring on viscous evolution timescale) and by the radial transport of net large-scale poloidal field, since the dust would no longer have a significant feedback on the ionization chemistry and the disk dust–gas mixture would behave as a grain-free plasma.

The timescale marking the transition from "dust-dominated" to "gas-dominated" MRI-driven turbulence depends on the physical properties of the protoplanetary

LBP, $M_\star = 1\,M_\odot$, $L_\star = 2\,L_\odot$, $M_{\rm disk} = 0.05\,M_\star$, $\alpha_{\rm hydro} = 10^{-4}$, $v_{\rm frag} = 1000\,{\rm cm.s^{-1}}$

a) Effective turbulent parameter

b) Gas surface density

c) Mid-plane total ionization rate

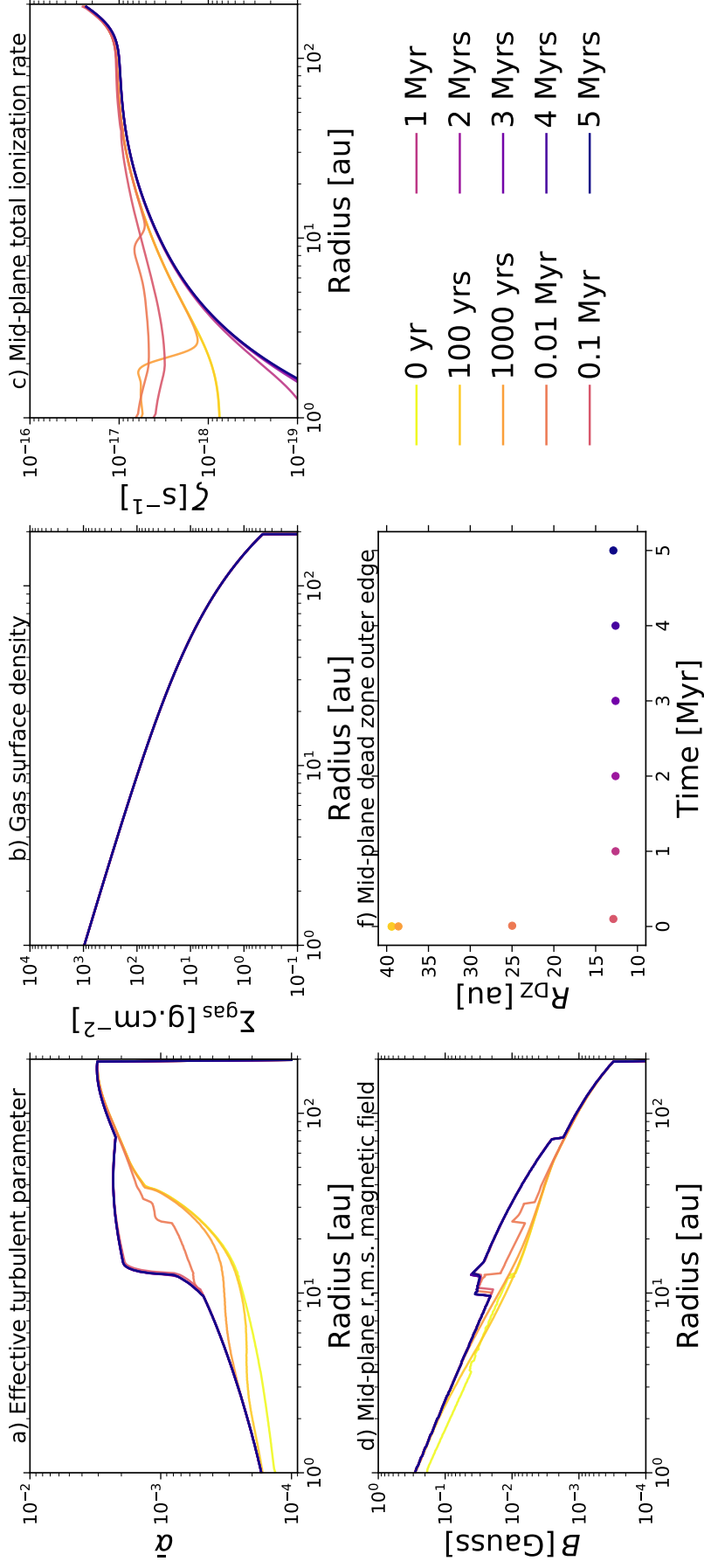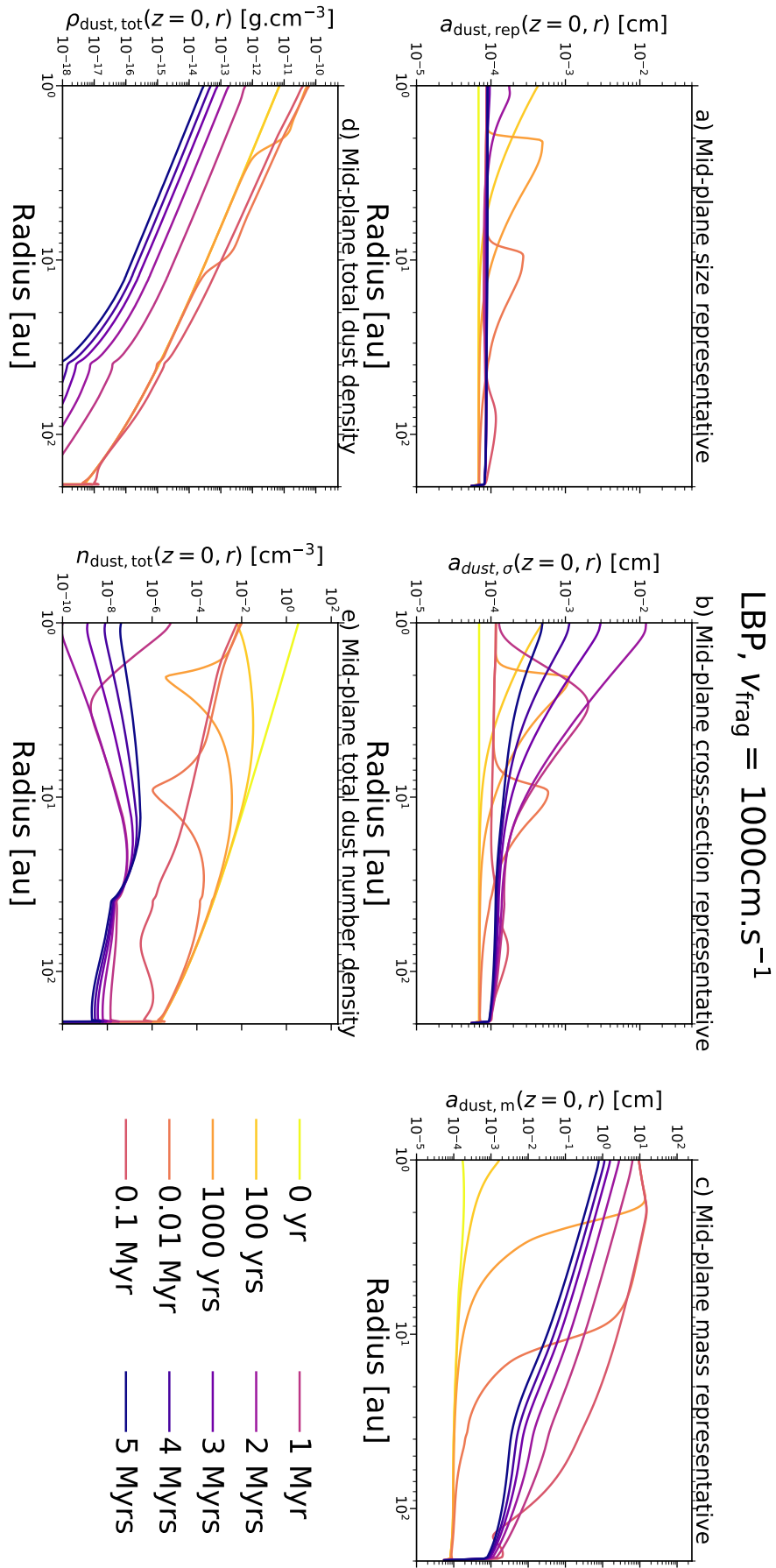d) Mid-plane r.m.s. magnetic field

f) Mid-plane dead zone outer edge

Figure 47: Same as in Fig. 45, except for Model III. The corresponding temporal evolution of the five dust quantities is shown in Fig. 48. Here one should note that, in *Panel f*, the dead zone outer edge coincides at t = 0 year and t = 100 years.

Figure 48: Same as in Fig. 44, except for Model III.

disk. For instance, if the disk initially has a low dust content, the transition is expected to happen earlier in the disk lifetime. Conversely, if the disk initially has a high dust content or if it has pressure bumps (nonsmooth disk), this transition is expected to occur over a longer timescale. Regarding the latter, it is worth remembering that pressure bumps are a possible explanation for the observed disk substructures, and can be created by various mechanisms such as embedded massive planets [see e.g., 96, 97, 100, 102, 103], dust particle growth by condensation near the ice lines [e.g., 289], or MHD disk winds [e.g., 290–293]. If there are pressure bumps in the disk, the main mechanism removing the dust (i.e., radial drift) is not as efficient because a substantial amount of particles can be trapped there. As a result, pressure bumps allow the dust to be in the disk for a longer period of time, hence delaying when the transition from dust-dominated to gas-dominated MRI-driven turbulence occurs.

In Sects. 5.3.2 and 5.4.1, I showed that the dead zone shrinks over time due to dust evolution (R_{DZ} decreases), and eventually becomes stationary after 3 Myrs of disk evolution for Model II, and 0.1 Myr for Model III. Unlike Model I (Sect. 5.3.1), these models have no inflow of small particles feeding the outer boundary of the simulation domain. The stationary nature of the dead zone comes from the fact that the disk dust–gas mixture eventually behaves as a grain-free plasma after some time of evolution, where the MRI activity evolution is primarily controlled by the gas which is not evolving here. Indeed, Figs. 45f and 47f show that the midplane dead zone radial extent is larger than ~ 10 au, at any time and for both Models II and III. Consequently, the present results show that dust evolution alone does not lead to a complete reactivation of the dead zone in protoplanetary disks. As long as there are no mechanisms that can efficiently ionize the gas in the regions of the disk where the dead zone sits at and that the gas dispersal in those regions occurs in timescales of a few million years, the dead zone may potentially be able to survive the protoplanetary disk evolution over a few millions years when the MRI is the main driver for the disk accretion. This supports that a disk evolution model including X-ray photoevaporative dispersal and a dead zone in the inner regions is a feasible idea in order to successfully explain the main observable properties of transitions disks such as extended gaps and high accretion rates [see 52].

5.4.3 *The effect of the dust distribution minimum grain size*

In this Chapter, I used a dust distribution minimum grain size, a_{min}, of $0.55\,\mu m$. This quantity is a free parameter in dust evolution models. From the modeling perspective, the choice of a_{min} should not matter because the dust particles quickly forget their initial grain size due to coagulation and fragmentation. As a result, running a pure dust evolution simulation with $a_{min} = 0.1\,\mu m$ or $a_{min} = 0.55\,\mu m$ should not substantially change the dust density output.

However, this is no longer true if MRI calculations are now combined with the dust evolution model. As I showed in Sect. 4.7.1.1, taking either $a_{min} = 0.1\,\mu m$ or $a_{min} = 0.55\,\mu m$ for the distribution minimum grain size leads to appreciably differ-

ent outcomes in terms of the MRI activity (particularly, the dead zone morphology and the location of its outer edge). Indeed, if a larger grain size is used for the distribution minimum size, the representative grain size involved in the ionization chemistry is skewed toward larger sizes, implying that the total grain surface area, A_{tot}, decreases and the overall MRI activity increases (see Figs. 38a and 38f). In the context of a full coupling between dust evolution and MRI calculations, the MRI-driven turbulence would be sensitive to the dust distribution and its minimum grain size at any point in time (except if it is gas-dominated as discussed in the previous section). The choice for the adopted value of a_{min} is thus crucial.

Tazaki and Dominik [294] recently investigated the effect of monomer size and composition on scattering polarization of dust particles by using an exact light scattering technique. By comparing their simulations to observations, they estimated the monomer radius of dust particles to be no greater than 0.4 µm for several protoplanetary disks. They even found that a minimum grain size of 0.1–0.2 µm appears to explain the recent polarimetric observations of the disk around HD 142527. Nevertheless, they have not excluded the possibility that the monomers could actually be much smaller than 0.1 µm. If that were the case, polycyclic aromatic hydrocarbon (PAH), representing the smallest end of a grain size distribution, would need to be considered in the MRI calculations. Counter-intuitively, though, it has been shown by various works that including PAHs in the dust size distribution reduces ambipolar diffusion, hence enhancing the overall MRI activity [e.g., 295–297]. Consequently, if one wants to accurately describe the MRI-driven turbulence in protoplanetary disks, further studies are required with the aim to provide realistic constraints on the minimum grain size of the dust distribution.

5.5 SUMMARY AND CONCLUSIONS

In this Chapter, I have provided an important step toward a better understanding of the MRI–dust coevolution in protoplanetary disks, with the aim to present a proof of concept that dust evolution ultimately plays a crucial role in the MRI activity on secular timescales. To do so I partially coupled the global MRI-driven disk accretion model of Chapter 3 encoded into mhdpy to the dust evolution model of DustPy, by properly including the feedback of dust evolution on the ionization chemistry. This has unveiled, for the first time, some insights about how the evolution of dust (dynamics and grain growth processes combined) and MRI-driven accretion are intertwined on million-year timescales. I have demonstrated that dust evolution strongly affects the MRI activity, since the MRI-driven turbulence undergoes significant changes as the dust phase evolves. The key findings can be summarized as follows:

- Dust coagulation and settling lead to a higher gas ionization degree (the recombination rate onto grains decreases), resulting in stronger MRI-driven turbulence as well as a more compact dead zone. On the other hand, fragmentation has an opposite effect because it replenishes the disk in small dust particles, which are very efficient at sweeping up free electrons and ions from

the gas-phase (the recombination rate onto grains increases). Since the dust content of the protoplanetary disk decreases over millions of years of evolution due to radial drift, the MRI-driven turbulence overall becomes stronger and the dead zone more compact until the disk dust–gas mixture eventually behaves as a grain-free plasma.

- The MRI activity evolution (hence the temporal evolution of the MRI-induced α parameter) is controlled by dust evolution and occurs on a timescale of local dust growth, as long as there are enough dust particles in the disk to dominate the recombination process for the ionization chemistry. Once that is no longer the case, the MRI activity evolution is expected to be controlled by gas evolution (occurring on viscous evolution timescale) and by the radial transport of net large-scale poloidal field.

- Dust evolution alone does not lead to a complete reactivation of the dead zone since the dust eventually has no significant impact on the ionization chemistry when the disk dust–gas mixture behaves as a grain-free plasma. Such result suggests that the dead zone may potentially be able to survive the protoplanetary disk evolution over a few million years when the MRI is the main driver for the disk accretion, as long as there are no mechanisms that can efficiently ionize the gas in the regions of the disk where the dead zone sits at and that the gas dispersal in those regions occurs in timescales of a few million years.

- For typical T-Tauri stars, the dead zone outer edge is expected to be located roughly between 10 au and 50 au during the protoplanetary disk lifetime for the choice made for the magnetic field strength and configuration.

- The MRI activity evolution in protoplanetary disks is expected to be crucially sensitive to the choice made for the minimum grain size of the dust distribution, especially in the early stages of the disk lifetime when the dust has significant feedback on the ionization chemistry. Further studies focusing on constraining such a minimum grain size are thus fundamental.

In this Chapter, I have showed that dust evolution (dust dynamics and grain growth processes combined) is crucial to describe the MRI activity, due to the feedback of the dust on the gas ionization degree. This thus leads to complex interdependencies between gas, dust and MRI activity in protoplanetary disks. Indeed, gas and dust evolution can change the MRI-driven turbulence which in turns changes the gas dynamics as well as the evolution of dust particles, hence impacting the MRI-driven turbulence. The natural step forward is to explore how disks respond to these interdependencies on secular evolution timescales. This is addressed in the next Chapter.

5.6   ADDITIONAL CONTENT

5.6.1   *Rayleigh adjustment for a nonuniform radial grid*

CONTEXT.   As explained in Chapter 4, a gas surface density profile resulting from steady-state accretion leads to a mathematical discontinuity located at the dead zone outer edge. This discontinuity arises from the on/off criteria for active MRI used, inducing a steep change in the local turbulent parameter α at each transition between the dead zone and the MRI active region. As proposed by [277], though, such a steep gas transition would not happen because the gas would not be stable and would rearrange itself due to turbulent diffusion on a dynamical timescale (Rayleigh adjustment process). In Model I, I chose $\Sigma_{gas}(r)$ to follow the gas surface density profile obtained for the steady-state MRI-driven accretion solution corresponding to Model XI of Chapter 4 with MRN-like grain size distribution $a_{min} = 0.55\,\mu m$, $a_{dist,Max} = 1\,\mu m$, and $p_{dist,Exp} = -3.5$ (see Fig. 38). This means that the gas is assumed to be in steady-state accretion at $t = 0\,year$. Consequently, Rayleigh adjustment needs to be applied in order to smooth the density gradient at the dead zone outer edge, and thus avoid any potential physically inconsistent state while running the dust evolution model employed. After applying Rayleigh adjustment, the new $\Sigma_{gas}(r)$ obtained is the gas surface density profile that I refer to as "Steady-State (SS)" in Table 5.

Below I revisit the simple algorithm put forward by [277] to implement Rayleigh adjustment. Particularly, I describe a new and more robust method that can be applied to any Rayleigh unstable gas surface densities, for a nonuniform radial grid.

ALGORITHM.   A radially one-dimensional diffusion equation in polar coordinates (r, ϕ) reads

$$\frac{\partial \Sigma_{gas}}{\partial t} = \frac{1}{r}\frac{\partial}{\partial r}\left(r\mathcal{D}\frac{\partial \Sigma_{gas}}{\partial r}\right), \tag{169}$$

where Σ_{gas} is the gas surface density and $\mathcal{D}$ is the diffusion coefficient. Eq. (169) represents a conservation law

$$\frac{\partial \Sigma_{gas}}{\partial t} + \frac{1}{r}\frac{\partial}{\partial r}(r\mathcal{F}) = 0, \tag{170}$$

where the flux is defined by $\mathcal{F}(\Sigma_{gas}(r, t); r, t) = -\mathcal{D}\frac{\partial \Sigma_{gas}}{\partial r}$. Integrating Eq. (170) over a concentric ring from $r = r_1$ to $r = r_2$ and dividing the result by the area of the ring gives

$$\frac{\partial}{\partial t}\left(\frac{2}{r_2^2 - r_1^2}\int_{r_1}^{r_2}\Sigma_{gas}\,rdr\right) + \frac{2}{r_2^2 - r_1^2}[r_2\mathcal{F}(r_2, t) - r_1\mathcal{F}(r_1, t)] = 0. \tag{171}$$

Defining the cell average as

$$Q(t) = \frac{2}{r_2^2 - r_1^2}\int_{r_1}^{r_2}\Sigma_{gas}\,rdr \tag{172}$$

and integrating Eq. (171) from $t = t_1$ to $t = t_2$ gives

$$Q(t_2) = Q(t_1) - \frac{2\Delta t}{r_2^2 - r_1^2} \left[r_2 F(r_2) - r_1 F(r_1) \right], \tag{173}$$

where $\Delta t = t_2 - t_1$ and $F(r) = \frac{1}{\Delta t} \int_{t_1}^{t_2} \mathcal{F}(r, t) \, dt$.

Consider a nonuniform grid with a mapping from the index space ρ to the physical space r, that is, $r = r(\rho) = r_\rho$. I adopt the convention that the cell edges are indexed by integers and the cell centers by half-integers. Eq. (173) then gives the Godunov method for the $(n + 1)$-th time step

$$Q_{j+1/2}^{n+1} = Q_{j+1/2}^n - \frac{2\Delta t}{r_{j+1}^2 - r_j^2} \left(r_{j+1} F_{j+1}^n - r_j F_j^n \right), \tag{174}$$

where

$$Q_{j+1/2}^n = \frac{2}{r_{j+1}^2 - r_j^2} \int_{r_j}^{r_{j+1}} \Sigma_{\text{gas}}(r, t_n) \, r \, dr, \tag{175}$$

and

$$F_j^n = \frac{1}{\Delta t} \int_{t_n}^{t_{n+1}} \mathcal{F}(r_j, t) \, dt, \tag{176}$$

with $\Delta t = t_{n+1} - t_n$.

To proceed, one could consider a Riemann problem and use the solution to evaluate Eq. (176). Instead, I approximate it by assuming $\Sigma_{\text{gas}}(t, r)$ is nearly unchanged over $t \in [t_n, t_{n+1}]$ and hence

$$F_j^n \approx \mathcal{F}(r_j, t_n) = -\mathcal{D} \frac{\partial \Sigma_{\text{gas}}}{\partial r} \bigg|_{r=r_j} = -\mathcal{D} \frac{d\rho}{dr} \frac{\partial \Sigma_{\text{gas}}}{\partial \rho} \bigg|_{r=r_j}. \tag{177}$$

It can then be discretized using central differences:

$$F_j^n \approx -\mathcal{D}(r_j) \rho'(r_j) \left(Q_{j+1/2}^n - Q_{j-1/2}^n \right), \tag{178}$$

where $\rho(r)$ is the inverse function of $r(\rho)$. Therefore, Eq. (174) becomes

$$Q_{j+1/2}^{n+1} = Q_{j+1/2}^n + \frac{2\Delta t}{r_{j+1}^2 - r_j^2} \times$$
$$\left[r_{j+1} \rho'(r_{j+1}) \mathcal{D}(r_{j+1}) \left(Q_{j+3/2}^n - Q_{j+1/2}^n \right) - r_j \rho'(r_j) \mathcal{D}(r_j) \left(Q_{j+1/2}^n - Q_{j-1/2}^n \right) \right]. \tag{179}$$

If the diffusion coefficient $\mathcal{D}$ is a constant, it can be simplified as

$$Q_{j+1/2}^{n+1} = Q_{j+1/2}^n + \frac{2\mathcal{D}\Delta t}{r_{j+1}^2 - r_j^2} \times$$
$$\left[r_{j+1} \rho'(r_{j+1}) \left(Q_{j+3/2}^n - Q_{j+1/2}^n \right) - r_j \rho'(r_j) \left(Q_{j+1/2}^n - Q_{j-1/2}^n \right) \right]. \tag{180}$$

Next, I find the stability condition for the time step Δt. Assume that

$$Q_{j+1/2}^n \sim e^{ikj}, \tag{181}$$

where k is any wavenumber in the index space ρ. Substituting this into Eq. (180), a von Neumann stability analysis gives

$$Q_{j+1/2}^{n+1} \sim e^{ikj} \left\{ 1 + \frac{2\mathcal{D}\Delta t}{r_{j+1}^2 - r_j^2} \left[r_{j+1}\rho'(r_{j+1}) \left(e^{+ik} - 1 \right) - r_j\rho'(r_j) \left(1 - e^{-ik} \right) \right] \right\} \quad (182)$$

$$= e^{ikj} \left[1 + (\alpha + \beta) \left(e^{+ik} - 1 \right) - (\alpha - \beta) \left(1 - e^{-ik} \right) \right]$$

$$= e^{ikj} [1 - 2\alpha(1 - \cos k) + 2i\beta \sin k] = Ae^{ikj},$$

where

$$\alpha = \frac{\mathcal{D}\Delta t \left[r_{j+1}\rho'(r_{j+1}) + r_j\rho'(r_j) \right]}{r_{j+1}^2 - r_j^2},$$

$$\beta = \frac{\mathcal{D}\Delta t \left[r_{j+1}\rho'(r_{j+1}) - r_j\rho'(r_j) \right]}{r_{j+1}^2 - r_j^2}, \quad (183)$$

and

$$A = 1 - 2\alpha(1 - \cos k) + 2i\beta \sin k. \quad (184)$$

One should note that $\alpha > 0$ and $\beta < \alpha$ if $r(\rho)$ is a strictly monotonically increasing or decreasing function of ρ, which should be always the case. To be stable, $|A| = (1 - 2\alpha + 2\alpha \cos k)^2 + 4\beta^2 \sin^2 k \leqslant 1$. The extrema of $|A|$ occur at $\sin k = 0$ or $\cos k = \alpha(2\alpha - 1)/2(\alpha^2 - \beta^2)$. The first leads to $(1 - 4\alpha)^2 \leqslant 1$, or $0 \leqslant \alpha \leqslant 1/2$. The second results in $(\alpha - 2\beta^2)^2 \geqslant 0$, which is always true. Therefore, the algorithm of Eq. (180) can be optimized by adopting

$$\mathcal{D}\Delta t = \left\{ 2 \max_j \left[\frac{r_{j+1}\rho'(r_{j+1}) + r_j\rho'(r_j)}{r_{j+1}^2 - r_j^2} \right] \right\}^{-1}. \quad (185)$$

In summary, a general outline of the Rayleigh adjustment procedure would be as follows: Firstly, the stability of the gas surface density profile, Σ_{gas}, should be evaluated using the stability criterion derived in Yang and Menou [277] (either their Eq. (3) for a simple one, or a generalization shown in their Sect. 4). In this Chapter, I chose to follow their Eq. (3). Secondly, if the gas surface density profile is unstable, the unstable profile should be used as the initial condition and Eq. (180) should be iterated with $\mathcal{D}\Delta t$ following Eq. (185) until the profile has relaxed to marginal stability. Lastly, the relaxed gas surface density profile should be used to run the 1D dust evolution model (similar to what is done in this Chapter), or to resume the next time step of the 1D gas and dust evolution model (in this case Rayleigh adjustment needs to be applied at each time step when solving for the gas).

5.6.2 *Temporal evolution of dust surface density distributions*

The vertically integrated dust surface density distribution per logarithmic bin of grain size, σ, is defined as [138]

$$\sigma(t, r, a) = \int_{-\infty}^{+\infty} n'_{dust}(t, r, z, a) \, m(a) \, a \, dz. \quad (186)$$
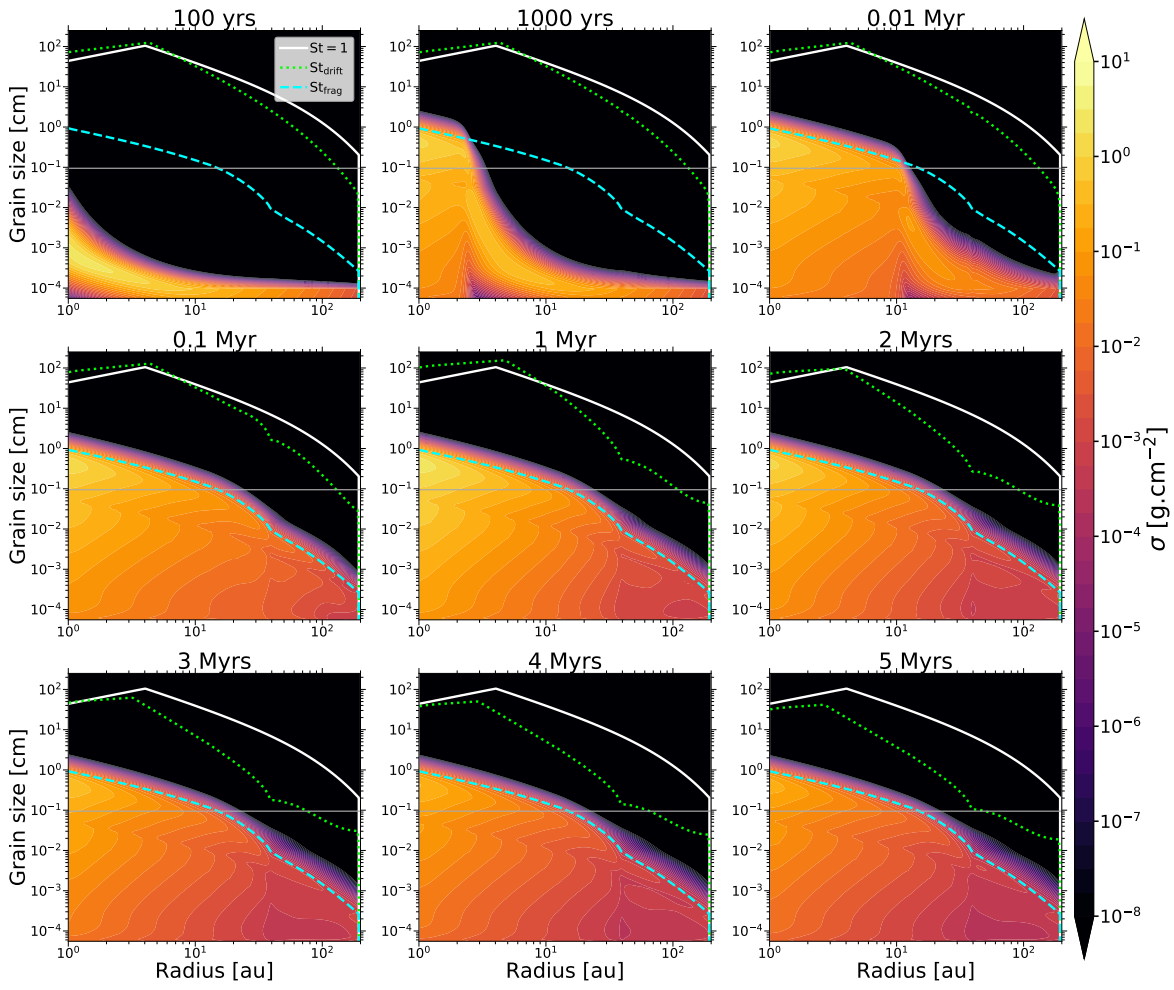
Figure 49: Same as in Fig. 42, except for Model II.

Defining $\sigma(t, r, a)$ as in Eq. (186) makes it a grid-independent dust density unlike the mass integrated over each numerical bin ($\Sigma_{dust}(t, r, a)$). This way, all plots of $\sigma(t, r, a)$ are meaningful without the knowledge of the size grid used. Below I present the temporal evolution of $\sigma(t, r, a)$ for Models II and III. The one for Model I is shown in Fig. 42.

Figure 50: Same as in Fig. 42, except for Model III.
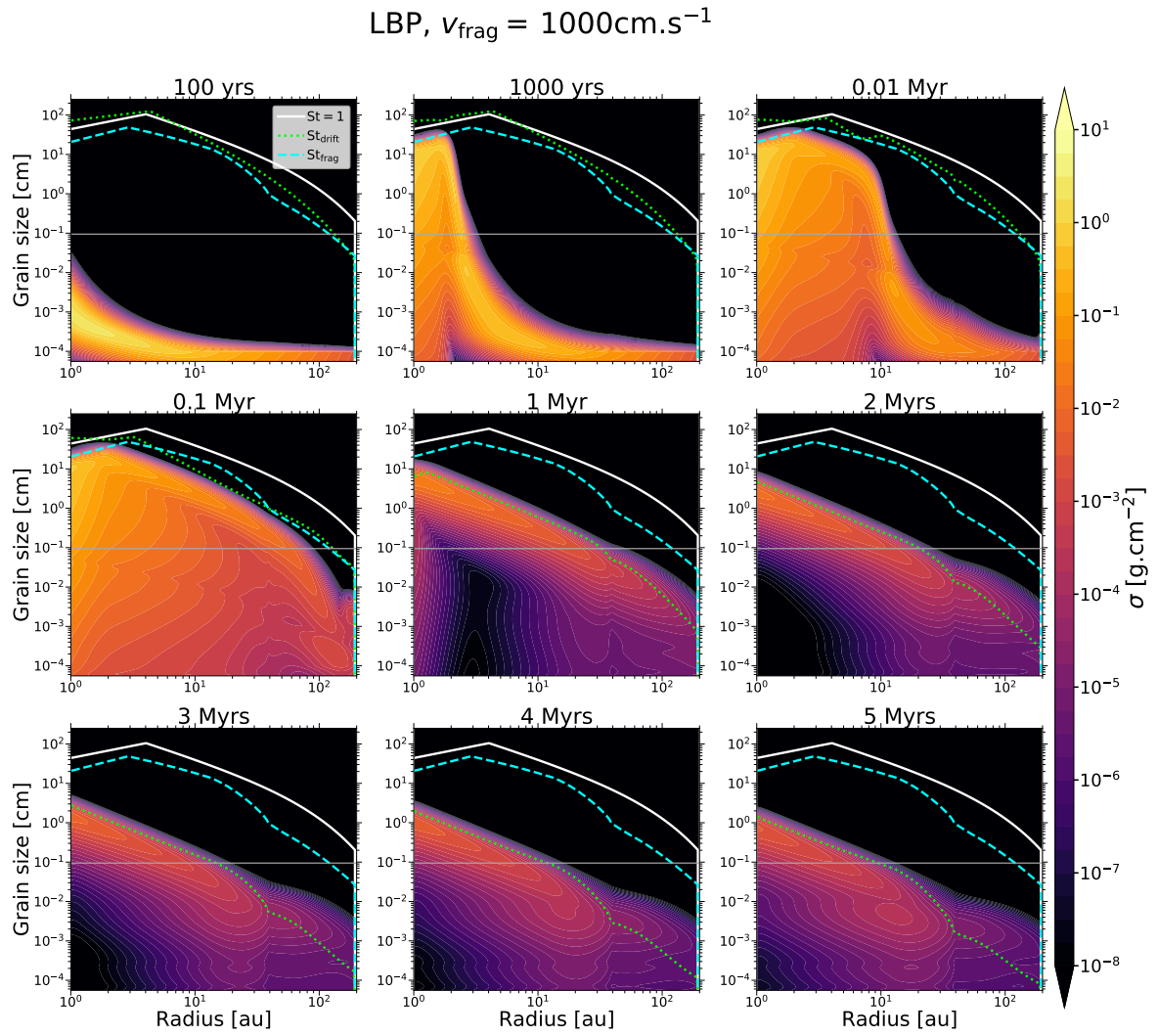
SPONTANEOUS FORMATION OF LONG-LIVED DUST TRAPS IN MRI-DRIVEN ACCRETION

*This Chapter is an adapted version of the soon-to-be submitted research article **Delage T. N. et al.; "Spontaneous formation of long-lived dust traps during the secular evolution of magnetized protoplanetary disks"; to be submitted (2023).** The material presented here might be subject to some change and/or complement until the acceptance of the research article. I refer the eager reader to the published version once it is available.*

6.1 MOTIVATION

One of the most important conclusions reached so far is that the MRI activity is crucially set by the gas, dust and stellar properties of the protoplanetary disk. Since they are expected to undergo substantial change throughout the secular evolution of the disk, it is crucial to simultaneously complement the global MRI-driven disk accretion model with gas, dust, and stellar evolution models. Doing so is fundamental if one wants to capture how gas evolution, dust evolution and MRI-driven turbulence intricate, hence leading to a proper modeling of the non-linear secular evolution of protoplanetary disk powered by the MRI.

Armed with the global MRI-driven disk accretion model of Chapter 3 and the knowledge acquired through our detours (Chapters 4 and 5), this Chapter showcases the pinnacle of our adventure where I finally dive into the complex interdependencies between gas evolution, dust evolution and MRI activity. Here the aim is to investigate how this interplay shapes the secular evolution of the disk, and discuss how it could be of great importance for the *first steps* of planet formation. Particularly, I would like to give closure to this thesis by addressing the questions that motivated it in the first place: *Can the interplay of gas evolution, dust evolution and MRI-driven turbulence explain the dust substructures observed in protoplanetary disks with telescopes such as ALMA or VLT/SPHERE? Can these induced dust substructures host the building blocks of planets and be potential birth-sites for them?*

6.2 METHOD

Table 6 summarizes all the models considered in this Chapter. Below I describe them in details, and explain the numerical implementation.

Model	$M_\star$ [M$_\odot$]	$L_\star(t)$ [L$_\odot$]	$L_{XR}(t)$ [L$_\odot$]	$M_{disk}(t=0)$ [M$_\star$]	B & B$_z$ [Gauss]	α_{hydro}	T [K]	$\Sigma_{dust}(t,r,a)$ [g.cm^{-2}]	$\Sigma_{gas}(t,r)$ [g.cm^{-2}]	a_{min} [μm]	v_{frag} [m.s^{-1}]	δ_{MRI} [years]
Fiducial	1	KT	KT	0.05	Fields constant (B = 5×10^{-3} G, B$_z$ = 10^{-3} G)	10^{-4}	Thick	DustPy	DustPy	0.1	1	200
I	1	KT	KT	0.05	Fields constant (B = 10^{-4} G, B$_z$ = 2×10^{-5} G)	10^{-4}	Thick	DustPy	DustPy	0.1	1	200
II	1	KT	KT	0.05	Fields constant (B = 5×10^{-4} G, B$_z$ = 10^{-4} G)	10^{-4}	Thick	DustPy	DustPy	0.1	1	200
III	1	KT	KT	0.05	Fields constant (B = 10^{-3} G, B$_z$ = 2×10^{-4} G)	10^{-4}	Thick	DustPy	DustPy	0.1	1	200
IV	1	KT	KT	0.05	Fields constant (B = 10^{-2} G, B$_z$ = 2×10^{-3} G)	10^{-4}	Thick	DustPy	DustPy	0.1	1	200
V	1	KT	KT	0.05	Fields constant (B = 5×10^{-2} G, B$_z$ = 10^{-2} G)	10^{-4}	Thick	DustPy	DustPy	0.1	1	200
VI	1	KT	KT	0.05	Plasma-β constant (β$_{mid}$ = 100, β$_{z,mid}$ = 2500)	10^{-4}	Thick	DustPy	DustPy	0.1	1	200
VII	1	KT	KT	0.05	Plasma-β constant (β$_{mid}$ = 200, β$_{z,mid}$ = 5000)	10^{-4}	Thick	DustPy	DustPy	0.1	1	200
VIII	1	KT	KT	0.05	Plasma-β constant (β$_{mid}$ = 400, β$_{z,mid}$ = 10^4)	10^{-4}	Thick	DustPy	DustPy	0.1	1	200

Table 6: Summary of the parameters used in each model of this Chapter. The code mhdpy (computes the disk turbulence parameter $\bar{\alpha}$) is integrated in such a way that it is called by the code DustPy at every fixed timescale δ_{MRI}. The grain size distribution, hence the temporal evolution of the dust surface density for each grain species of size a, $\Sigma_{dust}(t,r,a)$, is directly obtained from the dust evolution model of DustPy. It depends on the minimum size of the dust distribution a_{min} and the fragmentation velocity v_{frag}. Initially, at each disk radius, the grain size distribution (hence $\Sigma_{dust}(t = 0, r, a)$) is assumed to follow a MRN-like distribution of interstellar grains with $a_{min} = 0.1$ μm, $a_{dist,Max} = 1$ μm and $p_{dist,Exp} = -3.5$, as well as a total vertically integrated dust-to-gas mass ratio (accounting for all grain species) $f_{dg,tot} = 10^{-2}$. Similarly the gas surface density, $\Sigma_{gas}(t, r)$, is directly obtained from the viscous gas evolution model of DustPy. The quantity $\Sigma_{gas}(t = 0, r)$ is initially assumed to follow the classical radial profile of a power-law combined with an exponential cutoff, where an initial total disk gas mass $M_{disk}(t = 0) = 0.05\,M_\star$ and a critical radius $R_c = 80$ au have been chosen. Furthermore, the time evolution of the stellar bolometric and total X-rays luminosity ($L_\star(t)$ and $L_{XR}(t)$, respectively) are given by the evolutionary tracks of Kunitomo et al. [133] (see their Fig. 4 (top panel) and Fig. 5, respectively), referred to as "KT". Finally, "Thick" means that the gas temperature model follows Eq. (47). In addition, "Plasma-β constant" means that the r.m.s. magnetic field B and the vertical magnetic field B$_z$ are derived following option B of Sect. 3.5.3, whereas "Fields constant" means that they are derived following option C of this same section. For a detailed description of the various models, see Sect. 6.2.

6.2.1 *Approach*

In this Chapter, I build upon what has been done until now, in order to develop a unique approach that captures self-consistently and into a single framework the evolution of the gas, the dust (dynamics and grain growth process combined), and the MRI-driven turbulence in protoplanetary disks over millions of years. This unified framework allows me to investigate how this interplay shapes the disk secular evolution. Specifically it provides, for the first time, the necessary tools to properly assess whether or not this interplay leads to the generation of dust traps within the disk via the exciting emergent MRI-powered mechanism discussed in Sect. 1.5.

Unlike Chapter 5 where the sole impact of dust evolution on the MRI activity has been studied, gas evolution must now be enabled in the code `DustPy` and the code `mhdpy` must now be integrated into `DustPy` self-consistently. Indeed, as I discussed in Sect. 2.3.4, four key ingredients are required to investigate how the interplay mentioned above shapes the disk secular evolution: (1) the gas transport evolutionary equation (Eq. 79); (2) the dust transport evolutionary equation (Eq. 92); (3) the discretized Smoluchowski coagulation–fragmentation evolutionary equation (Eq. 99); and (4) the parameter $\bar{\alpha}$ (Eq. 77) that determines the strength of the disk turbulence and the radial angular momentum transport as well as the strength of the turbulent collision velocities (δ_{turb}), the radial mixing (δ_{rad}) and the vertical mixing (δ_{vert}) of dust particles. One should indeed remember that $\delta_{\text{turb}} = \delta_{\text{vert}} = \delta_{\text{rad}} = \bar{\alpha}$ in this thesis (Sect. 2.3). The three evolutionary equations are solved by `DustPy`, given the evolution of the quantity $\bar{\alpha}$. The quantity $\bar{\alpha}$ is self-consistently computed by `mhdpy` over time, given the evolution of the stellar, gas and dust properties of the protoplanetary disk. Before passing down the quantity $\bar{\alpha}$ from `mhdpy` to `DustPy` whenever it is needed, the radial profile of $\bar{\alpha}$ needs to be smoothed out so that potential nonphysical steep variations are removed. To do so, at each relevant time `mhdpy` is called by `DustPy`, and at each disk radius, a 1D mean filter with a window of length one local vertical gas scale height is used on $\bar{\alpha}$. In other words, at each relevant time t, and at each disk radius r, the local value $\bar{\alpha}(t, r)$ is replaced by the mean value of $\bar{\alpha}(t, r_1 \leqslant r \leqslant r_2)$, where $[r_1, r_2]$ is a local neighborhood of length $H_{\text{gas}}(t, r)$ around r. This operation is repeated twice to ensure the complete removal of the potential nonphysical features. I choose of window of length at least one local vertical gas scale height because radial features narrower than that would be smeared out very efficiently by the turbulent gas via Rayleigh adjustment [e.g., 277].

The coupling procedure is illustrated by the flowchart in Fig. 51. The code `mhdpy` is integrated in such a way that it is called by `DustPy` at every fixed timescale δ_{MRI} (free parameter) rather than at every time-step. When simulating the whole protoplanetary disk over millions of years, this is indeed necessary in order to obtain reasonable run-times due to the current architecture of `mhdpy` (not optimized yet). When `mhdpy` is called at given time t_k, the relevant stellar, gas and dust quantities of `DustPy` are injected into it. These relevant quantities are the ones above the

arrows in Fig. 12. The code mhdpy can then compute the self-consistent effective disk viscosity parameter $\bar{\alpha}$ at that given time, $\bar{\alpha}(t_k)$, using the global MRI-driven disk accretion model of Chapter 3. The quantity $\bar{\alpha}(t_k)$ is then smoothed out as described above, and used as an input for evolving the gas and dust at time t_{k+1} with DustPy. The time $t_{k+1} = t_k + \Delta t_{k \to k+1}$ is given by computing the right time-step $\Delta t_{k \to k+1}$ as follows: In the default version of DustPy, the time-step between t_k and t_{k+1} is given by the minimum between the gas evolution time-step $\delta_{gas}(t_k)$ and the dust evolution time-step $\delta_{dust}(t_k)$ at time t_k. Since the Courant–Friedrichs–Lewy (CFL) condition must be satisfied, namely the information cannot propagate over more than one grid cell per time-step during the integration scheme, this minimum is further multiplied by a safety parameter called CFL and taken equal to 0.1 by default. The default time-step between t_k and t_{k+1} in DustPy is then defined as $\Delta t_{k \to k+1}^{default} = \text{CFL} \times \min \{\delta_{gas}(t_k), \delta_{dust}(t_k)\}$. To further ensure that mhdpy is called by DustPy every fixed timescale δ_{MRI}, the right time-step between time t_k and t_{k+1} that is needed for the coupling is thus $\Delta t_{k \to k+1} = \min \{\Delta t_{k \to k+1}^{default}, \delta_{MRI}\}$.

In order to properly capture the interplay of gas evolution, dust evolution, and MRI-driven turbulence, mhdpy must be called by DustPy frequently enough. In more quantitative terms, δ_{MRI} must be small compared to the timescales over which the gas and dust components of the protoplanetary disk are expected to significantly evolve. For the gas, the relevant timescale is the viscous evolution timescale $t_{visc} \sim r^2/(3\bar{v})$ (see Sect. 2.2.3), where the typical smallest values are of order of a few 10^5 years. For the dust, the relevant timescale is the minimum between the settling timescale $t_{sett} \sim 2\pi/(\Omega_K St)$, the advection timescale $t_{adv} \sim r/v_{dust,r}$, the diffusion timescale $t_{dust,diff} \sim r^2/D_{dust}$ (see Sect. 2.3), and the growth timescale $t_{growth} \sim (a\rho_{bulk})/(\rho_{dust,mid}\Delta v_{tot})$ [see Eq. (30) of 135]. Here ρ_{bulk} is the dust intrinsic volume density, Δv_{tot} is the total relative velocities (see Sect. 2.3) and $\rho_{dust,mid}$ is the midplane component of Eq. (93). One should note that this definition of t_{growth} is an over simplified estimate that is only used for the sake of the present argument. For the protoplanetary disk regions of interest in this thesis ($r \gtrsim 1\,\text{au}$), the typical smallest values are of order of a few decades, which is much less compared to the gas evolution timescale. Consequently, δ_{MRI} must be chosen of order 10^2 years to ensure that the effective disk viscosity parameter $\bar{\alpha}$ is updated enough.

Finally, mhdpy must be called by DustPy before the simulation starts at $t_0 = 0$ years for the coupling to be successful. Initially, at each disk radius, the grain size distribution is assumed to follow a MRN-like distribution of interstellar grains [151] with $a_{min} = 0.1\,\mu\text{m}$, $a_{dist,Max} = 1\,\mu\text{m}$ and $p_{dist,Exp} = -3.5$, as well as a total vertically integrated dust-to-gas mass ratio (accounting for all grain species) $f_{dg,tot} = 10^{-2}$. The initial gas surface density is assumed to follow the classical radial profile of a power-law combined with an exponential cutoff, where an initial total disk gas mass $M_{disk}(t = 0) = 0.05\,M_\star$ and a critical radius $R_c = 80\,\text{au}$ have been chosen. Furthermore, the time evolution of the stellar bolometric $L_\star$ and total X-rays luminosity L_{XR} are given by the evolutionary tracks of Kunitomo et al. [133] (see their Fig. 4 (top panel) and Fig. 5, respectively). This provides the unified disk evolution framework a very simple model of stellar evolution.
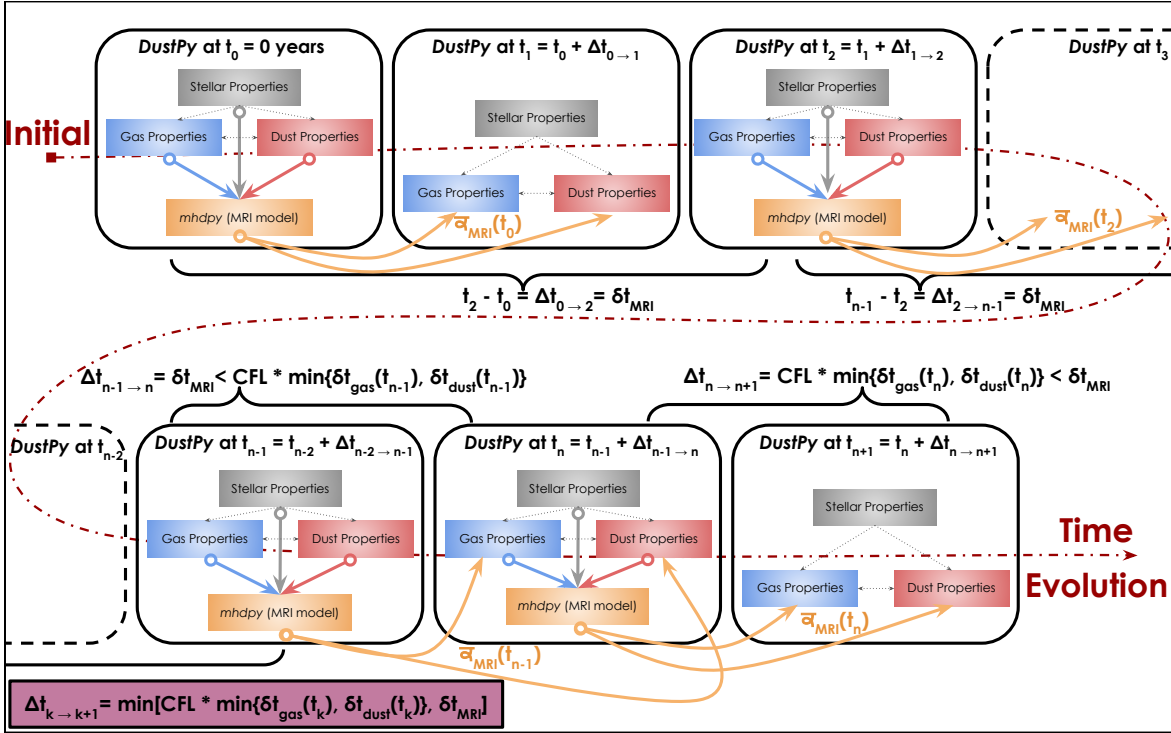
Figure 51: Flowchart explaining the coupling between the codes DustPy and mhdpy. This coupling captures the interplay between the gas evolution, the dust evolution, and the MRI-driven turbulence in protoplanetary disks over millions of years. For further details about the coupling procedure, I invite the eager reader to read the main text in Sect. 6.2.1.

6.2.2 Numerical implementation

The parameters used to run the global MRI-driven disk accretion model of Chapter 3 are taken from Table 1. One should note that the electron sticking coefficient, s_e, is still chosen equal to 0.6 (same as in Chapter 5). As a summary, the common parameters across the models of this Chapter have the following definitions:

- STELLAR PROPERTIES. Stellar mass $M_\star = 1\,M_\odot$. The time evolution of the stellar bolometric luminosity $L_\star$ and total stellar X-rays luminosity L_{XR} are now given by the evolutionary tracks of Kunitomo et al. [133] (see their Fig. 4 (top panel) and Fig. 5, respectively).

- GAS PROPERTIES. Initial total disk gas mass $M_{disk}(t = 0) = 0.05\,M_\star$. Furthermore, the gas is assumed vertically isothermal with a radial temperature profile following Eq. (47) (this choice does not have a significant impact on the MRI-driven turbulence as shown in Sect. 4.4.6). The gas inner and outer boundary conditions when solving for the gas transport equation in DustPy are the default ones.

- DUST PROPERTIES. I consider that the dust phase consists of a distribution of dust particles with different sizes. Each grain is assumed to be a perfect compact sphere of intrinsic volume density $\rho_{bulk} = 1.4\,\text{g.cm}^{-3}$. For a grain of

size a, the corresponding mass is then $m(a) = \frac{4}{3}\pi\rho_{bulk}a^3$. For the grain size distribution, I always consider a logarithmic grid of grain species whose size range from $a_{min} = 0.1\,\mu m$ to $400\,cm$. Also, seven mass bins per mass decade are considered (following the work of Ohtsuki, Nakagawa, and Nakazawa [280] and Drążkowska, Windmark, and Dullemond [281]), which leads to a total number of mass bins of $N_m = 162$. In light of the recent laboratory experiments on icy particles [e.g., 168–170] the fragmentation velocity, v_{frag}, is assumed to be radially constant equal to $1\,m.s^{-1}$ in all the models considered in this Chapter. The dust inner and outer boundary conditions when solving for the dust transport equation in `DustPy` are the default ones. Finally, I use `DustPy` version 0.5.9.

- IONIZATION CHEMISTRY. Since I consider a grain size distribution for the dust component of the protoplanetary disk, the dust quantities that come into play for the semi-analytical chemical model and nonideal MHD calculations of the global MRI-driven disk accretion model ($a_{dust,rep}$, $\sigma_{dust,rep}$ and $m_{dust,rep}$) are defined by Eqs. (114), (117) and (145). Furthermore, the radionuclide ionization rate $\zeta_{RA}^{(H_2)}$ for H_2 is now computed following option B of Sect. 3.3.3 to account for the decay of radionuclides over time.

- MAGNETIC FIELD. The magnetic field strength and topology are now set by following either options B or C of Sect. 3.5.3.

By assuming the protoplanetary disk to be geometrically thin, the vertical and radial dimensions can be decoupled into a 1+1D (r, z) problem, where each radial grid-point contains an independent vertical grid. Furthermore, by assuming the disk to be axisymmetric and symmetric about the midplane, it is enough to compute the domain $z \geqslant 0$ to obtain the full solution. The radial grid is computed from r_{min} to r_{max}, with N_r cells logarithmically spaced. For every radial grid-point $r \in [r_{min}, r_{max}]$, the corresponding vertical grid is computed from the disk midplane ($z = 0$) to z_{max}, with N_z cells linearly spaced. In all the simulations of this Chapter, the radial grid is computed from $r_{min} = 0.8\,au$ to $r_{max} = 500\,au$, with $N_r = 256$ cells. For every radial grid-point $r \in [r_{min}, r_{max}]$, the corresponding vertical grid is computed from the disk midplane ($z = 0$) to $z_{max}(r) = 5\,H_{gas}(t = 0, r)$, with $N_z = 512$ cells. Here H_{gas} corresponds to the vertical gas scale height defined in Eq. (63). One should note that the vertical grid is only used to run the global MRI-driven disk accretion model.

The next sections are organized as follows: In Sect. 6.3 I show how the interplay of gas evolution, dust evolution and MRI-driven turbulence shapes the secular evolution of protoplanetary disks. In Sect. 6.4 I show how the results of a fiducial protoplanetary disk model are crucially set by the magnetic field adopted, and how this interplay could be of great importance for planet formation. Finally Sect. 6.5 summarizes the findings.

Armed with the unified framework discussed above, let us now investigate how the interplay of the gas, the dust and the MRI-driven turbulence shapes the secular evolution of the protoplanetary disk. In the work presented below, I choose the effective disk viscosity parameter $\bar{\alpha}$ in DustPy to be updated every $\delta_{MRI} = 200$ years by mhdpy. Furthermore, in the light of Sect. 1.3.4, the fiducial protoplanetary disk model is assumed to have spatially and temporally constant magnetic fields where $B = 5 \times 10^{-3}$ G and $B_z = 10^{-3}$ G. Lastly, the protoplanetary disk is evolved for 8.5 Myrs for the fiducial model.

6.3.1   *Accretion layers*

Before diving into the time evolution of the gas and dust components of the protoplanetary disk, one needs to understand how the local MRI-driven turbulence evolves on secular evolution timescales. When Ohmic resistivity and ambipolar diffusion are the only nonideal MHD effects considered, the disk can be divided into three distinct accretion layers: the dead zone, the zombie zone and the MRI active layer. In the dead and zombie zones, the MRI is suppressed by Ohmic resistivity and ambipolar diffusion, respectively. The disk turbulence is driven by non-MRI processes there, characterized by the parameter $\alpha_{hydro} = 10^{-4}$ in this work. In the MRI active layer, the MRI operates and generates MHD turbulence that controls the dynamics of the system. Figure 52 shows the time evolution of these three different accretion layers for the fiducial protoplanetary disk model considered. The values taken by the local disk turbulence parameter α are also indicated by the colorbar.

For the magnetic field strength and topology adopted here ($B = 5 \times 10^{-3}$ G, $B_z = 10^{-3}$ G), it is quite striking to see that most of the disk is MRI-dead and that the gas is mostly laminar rather than turbulent, especially at the midplane. Unlike the classical view of the disk midplane being divided into the dead zone and the MRI active layer, one can clearly notice that the zombie zone can also exist at the midplane. This has great implications for the local disk turbulence parameter α. In addition to the expected sharp transition from the midplane dead zone outer edge to the midplane MRI active layer inner boundary, the local disk turbulence can also display a second sharp transition from the midplane MRI active layer outer boundary to the midplane zombie zone inner edge. In the early stages of evolution ($t \lesssim 0.1$ Myr), the dead zone covers the first ~ 25 au of the disk midplane, the MRI active layer covers the next ~ 40 au, and the zombie zone covers the rest of the disk midplane. As time goes and secular evolution timescales are reached ($t \gtrsim 1$ Myr), the midplane dead zone shrinks to reach an extent of ~ 12 au (consistent with the results of Chapter 5), the midplane zombie zone extends from the outside-in, and the midplane MRI active layer almost vanishes entirely. The dead zone shrinks over time (i.e., Ohmic resistivity becomes less stringent) because the average gas and dust densities in the disk decrease on secular evolution timescales due to accretion and expansion for the gas, as well as grain growth and radial drift for the dust.

The temporal behavior of the zombie zone can be understood by noting that lower average gas densities over time imply stronger ambipolar diffusion, since there are less neutrals in the gas-phase and therefore a higher drift speed between ions and neutrals. Lastly, the fact that the midplane MRI active layer almost vanishes entirely over time is because pressure maxima can form there (vertical dashed green lines in Fig. 52). These pressure maxima are characterized by gas and dust accumulation, which causes the local MRI activity to be decreased and even suppressed due to the nonideal MHD effects. This can thus turn a local region within the midplane MRI active layer into a local dead or zombie zone. In addition to the classical dead and zombie zone, it is then worth noting that the protoplanetary disk can also display local dead and zombie zones due to the formation of pressure maxima. I will further discuss this in the next section.

In the vertical direction, one can see that the MRI active layer also shrinks over time. This is the case because of two arguments. First, there is a decrease in the stellar X-rays luminosity when a solar-type star ($M_\star = 1\,M_\odot$) reaches secular evolution timescales [see Fig. 5 of 133]. It leads to less gas ionization, and therefore less MRI activity in the disk over time. Second, the surface $\beta = 1$ (red line in Fig. 52) –above which the MRI cannot operate at all because the gas thermal pressure is dominated by the magnetic pressure– evolves toward the disk midplane over time. This is the case due to the stellar bolometric luminosity that also decreases when a solar-type star reaches secular evolution timescales [see Fig. 4 (top panel) of 133], hence leading to lower gas temperature, and to the evolution of the disk gas that induces lower average gas densities and therefore lower plasma-β parameter values within the disk.

All in all it is clear that the local disk turbulence parameter α overall decreases on secular evolution timescales, especially at the disk midplane. However, one should remember that what matters in the theory of viscously accreting disk is not α that is sensitive to the local gas, but the effective disk turbulence parameter $\bar{\alpha}$ (see Sect. 2.2.3). At a given disk radius, the latter is sensitive to the entire gas column pressing down from above. Although the midplane MRI active layer vanishes over time, there is still a MRI active layer located in the disk atmosphere, especially above the dead zone. As a result, what truly matters for the gas and dust evolution is not what happens to the midplane MRI active layer, but to what I call the effective MRI active layer. This is defined as the regions in the disk where $\bar{\alpha} > \alpha_{\mathrm{hydro}}$, and it is crucially set by the magnetic field strength and topology adopted. It is worth noting that the outer boundary of the effective MRI active layer is always located close to the midplane zombie zone inner edge. This is because a MRI active layer cannot be sustained above the midplane zombie zone. Indeed, the MRI cannot operate at the disk midplane beyond the midplane zombie zone inner edge due to ambipolar diffusion by definition. Therefore it also cannot operate in the regions right above the midplane zombie zone, as ambipolar diffusion becomes even more stringent there due to lower gas densities and stronger magnetization. On the contrary, the inner boundary of the effective MRI active layer is not necessarily located close to the midplane dead zone outer edge. This is because a MRI active layer can

be well sustained right above the dead zone. The effective MRI active layer can thus include a fraction of the dead zone. Consequently, one should still always expect a sharp transition in $\bar{\alpha}$ at the midplane zombie zone inner edge, but not necessarily at the midplane dead zone outer edge. Lastly, it is important to note that the gas is turbulent in the effective MRI active layer, where the MHD turbulence and the angular momentum transport is governed by the MRI by definition. As I will show in the next section, this is the reason why the formation of spontaneous pressure maxima occurs within it.

6.3.2 *Evolution of the gas, the dust and the effective MRI-driven turbulence*

As I discussed above, the fact that the protoplanetary disk has three distinct accretion layers leads to the concept of the effective MRI active layer where $\bar{\alpha} > \alpha_{hydro}$, which is crucially determined by the magnetic field strength and topology adopted. Let us now explore the evolution of the gas, the dust and the effective disk turbulence for the fiducial protoplanetary disk model considered ($B = 5 \times 10^{-3}$ G and $B_z = 10^{-3}$ G). This is shown in Fig. 53. Initially ($t = 0$ year), one should remember that the gas and dust surface densities are assumed to be smooth, following the classical tapered power-law functional form as explained in Sect. 6.2.1. It is thus quite striking to see that, as early as $t \sim 0.01$ Myr, and throughout the disk secular evolution, the gas and dust surface densities are no longer smooth. Instead they display clear perturbations and pressure maxima (vertical dashed green lines) in a specific region of the disk that is none other that the effective MRI active layer.

Gas perturbations are induced by the variations in the effective disk turbulence, $\bar{\alpha}$, at the boundaries (inner and outer) of the effective MRI active layer and within it. The steepest variations cause the gas to become very unsteady, as shown by the gas accretion rates in Fig. 54. In some regions of the effective MRI active layer, the gas is thus accreted (inflow) while in some others it is decreted (outflow), and the accretion (resp. decretion) is strongly differential. Since the gas is accreted (resp. decreted) much faster in some regions than others, it accumulates near the transition between a slowly accreting (resp. decreting) region and a fast accreting (resp. decreting) one. Similarly, it also accumulates at a given disk radius that is sandwiched between an accreting region located beyond that disk radius and a decreting region located anterior to that disk radius. Usually, one would expect these gas surface density inhomogeneities to be quickly and efficiently smeared out by viscous evolution. However, viscous evolution can instead amplify them in some regions of the effective MRI active layer, in the sense that overdense gas regions grow denser while underdense ones become even more rarefied. This viscous instability occurs within the effective MRI active layer because it is where $\bar{\alpha}$ can become a steep non-monotonic function of Σ_{gas}, and more particularly it is where the required condition $\partial \ln \bar{\alpha} / \partial \ln \Sigma_{gas} < -1$ can be satisfied [e.g., 267, 298]. The regions where this condition is satisfied are indicated by the gray shaded boxes in Fig. 54. As expected, one can clearly see that such regions coincide where the gas accretion rate varies steeply, which is exactly where the effective disk turbulence
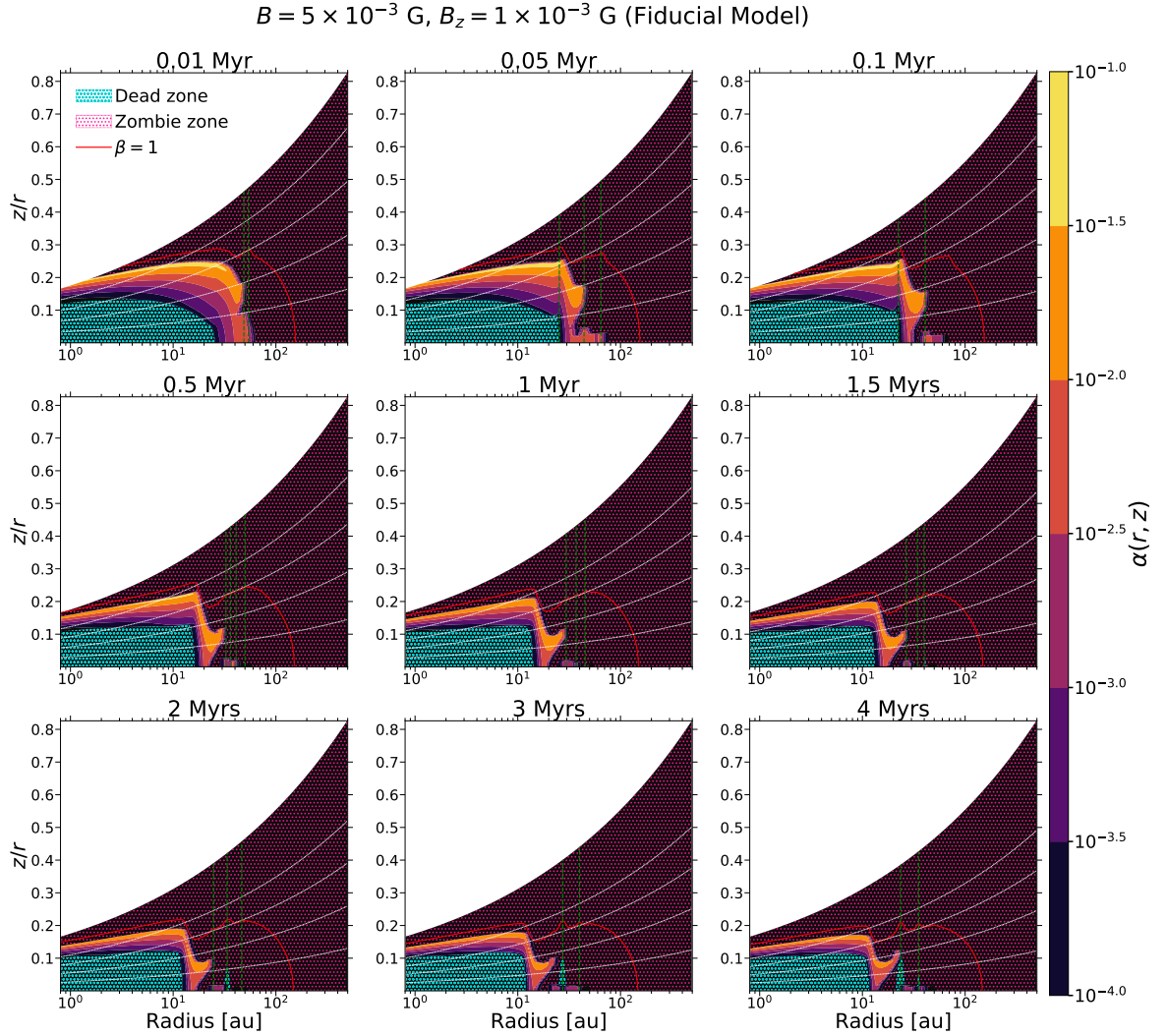
Figure 52: Time evolution of the local disk turbulence parameter, α (Eq. 43), for the fiducial model of this Chapter. In each panel, the MRI active layer (region with the colors of the color bar), the dead zone (blue circled region), and the zombie zone (magenta circled region) are shown. The region above the red line corresponds to where $\beta > 1$, with β the plasma-β parameter. The midplane dead zone outer edge is defined as the first transition from the dead zone to the MRI active layer at the midplane. The midplane zombie zone inner edge is defined as the last transition from the MRI active layer to the zombie zone at the midplane. The dashed white lines represent the surfaces $z = 1\,H_{gas}$, $z = 2\,H_{gas}$, $z = 3\,H_{gas}$, and $z = 4\,H_{gas}$, from bottom to top, respectively. A vertical dashed green line indicates the location of a pressure maximum generated via the MRI-powered mechanism.

varies steeply. When the gas initially accumulates at a given location in the effective MRI active layer, and if the viscous instability described above is at play, the gas accumulation is amplified there and the gas becomes more Keplerian. If this location is where the gas is already not far from being Keplerian (which is the case the closer to the central star), then the gas can actually become super-Keplerian and a pressure maximum is formed near that location. When running a simulation identical to the present fiducial model, but where only the gas component of the protolanetary disk is evolved (not shown here), it is found that the pressure maximum near the midplane dead zone outer edge is formed in such a way. This is consistent with previous studies [e.g., 298]. Nonetheless, it is worth noting that a pressure maximum does not always form near the midplane dead zone outer edge across the various scenarios for the magnetic field strength and topology explored in this work (see Table 6). Interestingly, it is found that a pressure maximum does not form at all near the midplane dead zone outer edge if the magnetic fields are too weak (B $\lesssim 10^{-3}$ G, B$_z \lesssim 2 \times 10^{-4}$ G or $\beta_{\mathrm{mid}} \gtrsim 200$, $\beta_{z,\mathrm{mid}} \gtrsim 5000$). This is the case for two reasons: (1) the condition for viscous instability $\partial \ln \bar{\alpha} / \partial \ln \Sigma_{\mathrm{gas}} < -1$ is not achieved there, as the variations in the effective turbulence are not steep enough; or (2) the condition is achieved there, but the midplane dead zone outer edge is located too far from the central star for the gas to become super-Keplerian.

In the way the aforementioned viscous instability has been explained so far, only the formation of the pressure maximum near the midplane dead zone outer edge (vertical dashed green line located at $\sim$ 23 au for t $= 0.05$ Myr, i.e. within the dead zone) can be explained in the fiducial protoplanetary disk model considered. This is in tension with the clear fact that many more pressure maxima other than this one are found in the simulation (see Fig. 53). This tension is resolved by realizing that the analysis has omitted the crucial role of dust particles until now. When the gas accumulates at a given location within the effective MRI active layer due to the steep variations in $\bar{\alpha}$, the dust particles that are still quite small and well coupled to the gas also tend to accumulate. This local traffic-jam density enhancement effect leads the MRI-driven turbulence to locally decrease (feedback of the dust on the MRI seen in Chapters 4 and 5). This feedback is only possible in the effective MRI active layer because it is where the MRI can operate. When $\bar{\alpha}$ locally decreases, the gas surface density responds by locally increasing, in the theory of viscously accreting disks (see Sect. 4.4.3). The gas thus accumulates even further, which amplifies the local traffic-jam density enhancement effect (local dust-to-gas mass ratio increases), hence leading to an even lower $\bar{\alpha}$ locally. This results in a positive feedback loop where the gas accumulation is amplified by the combined effect of the transport of small dust particles and their effect on the MRI-driven turbulence. Such a scenario is indeed confirmed by looking at the dotted and dashed black lines in the panel t $= 0.01$ Myr of Fig. 53. The dotted black line shows the surface density for the dust particles locally representative of the cross-section, and the dashed one indicates the surface density for the dust particles locally representative of the mass. By definition, the local dust cross-section representative corresponds to the most abundant dust particle bin that is relevant for the ioniza-

tion chemistry at a given disk location (those responsible for changing the local MRI-driven turbulence). Similarly, the local dust mass representative corresponds to the most abundant dust particle bin that accounts for the highest fraction of the total dust mass at a given disk location. One can clearly notice that there is a local traffic-jam density effect for the dust particles relevant for the ionization chemistry near where the two pressure maxima are located (vertical dashed green lines at ~ 49 au and ~ 55 au), while the bigger dust particles do not accumulate there. This local traffic-jam density effect leads to a decrease in the effective disk turbulence $\bar{\alpha}$ (red line). Furthermore, wherever the gas surface density (darkorange line) locally increases, the effective disk turbulence decreases. Consequently, the combined effect of the transport of small dust particles and their effect on the MRI-driven turbulence leads to the viscous instability described above, hence to the formation of pressure maxima within the effective MRI active layer. It is important to note that the feedback of the small dust particles on the MRI is what crucially drive the viscous instability, which can then be triggered even where $\partial \ln \bar{\alpha} / \partial \ln \Sigma_{\mathrm{gas}} \geqslant -1$ initially. This is once again consistent with previous studies [e.g., 299, 300].

6.3.3   *Generation of spontaneous short- and long-lived dust traps*

The complex interdependencies between the gas, the dust and the MRI-driven turbulence distinctively shapes the secular evolution of protoplanetary disks via the dust-driven viscous instability seen in the previous section. This instability is initiated by the transport of small dust particles that can drastically alter the MRI-driven turbulence, and leads to the potential formation of a multitude of pressure maxima within the effective MRI active layer. Since the evolution of small dust particles is a stochastic process by nature, the formation of pressure maxima is spontaneous and can occur anywhere within this specific layer. As Fig. 53 seems to suggest, there exist two classes of pressure maxima: the short- and long-lived ones. To better represent this, Fig. 55 features the time series for the pressure maxima location in the disk throughout its secular evolution, for the fiducial model considered ($B = 5 \times 10^{-3}$ G, $B_z = 10^{-3}$ G).

Some pressure maxima can be formed as early as t ~ 0.01 Myr and live throughout the whole secular evolution of the protoplanetary disk (t ~ 3–10 Myrs), some others can be formed very early on and disappear fast, and some others can be formed quite late. Specifically, a pressure maximum can be very short-lived (dissipation right after their formation), short-lived (dissipation after t $\lesssim 0.1$ Myr) or long-lived (dissipation after t $\gtrsim 1$ Myr). It is quite striking to see that the pressure maximum formed near the midplane dead zone outer edge (shown by the dashed cyan line) is short-lived for the fiducial model adopted here. Let us try to understand why. As already explained, this pressure maximum is formed by the simplest version of the viscous instability, where the gas accumulation and amplification occurs because the condition $\partial \ln \bar{\alpha} / \partial \ln \Sigma_{\mathrm{gas}} < -1$ is satisfied. Once it is formed (t ~ 0.05 Myr), the MRI-driven turbulence slowly adjusts until when $\partial \ln \bar{\alpha} / \partial \ln \Sigma_{\mathrm{gas}} < -1$ is no longer fulfilled. The pressure maximum near the mid-
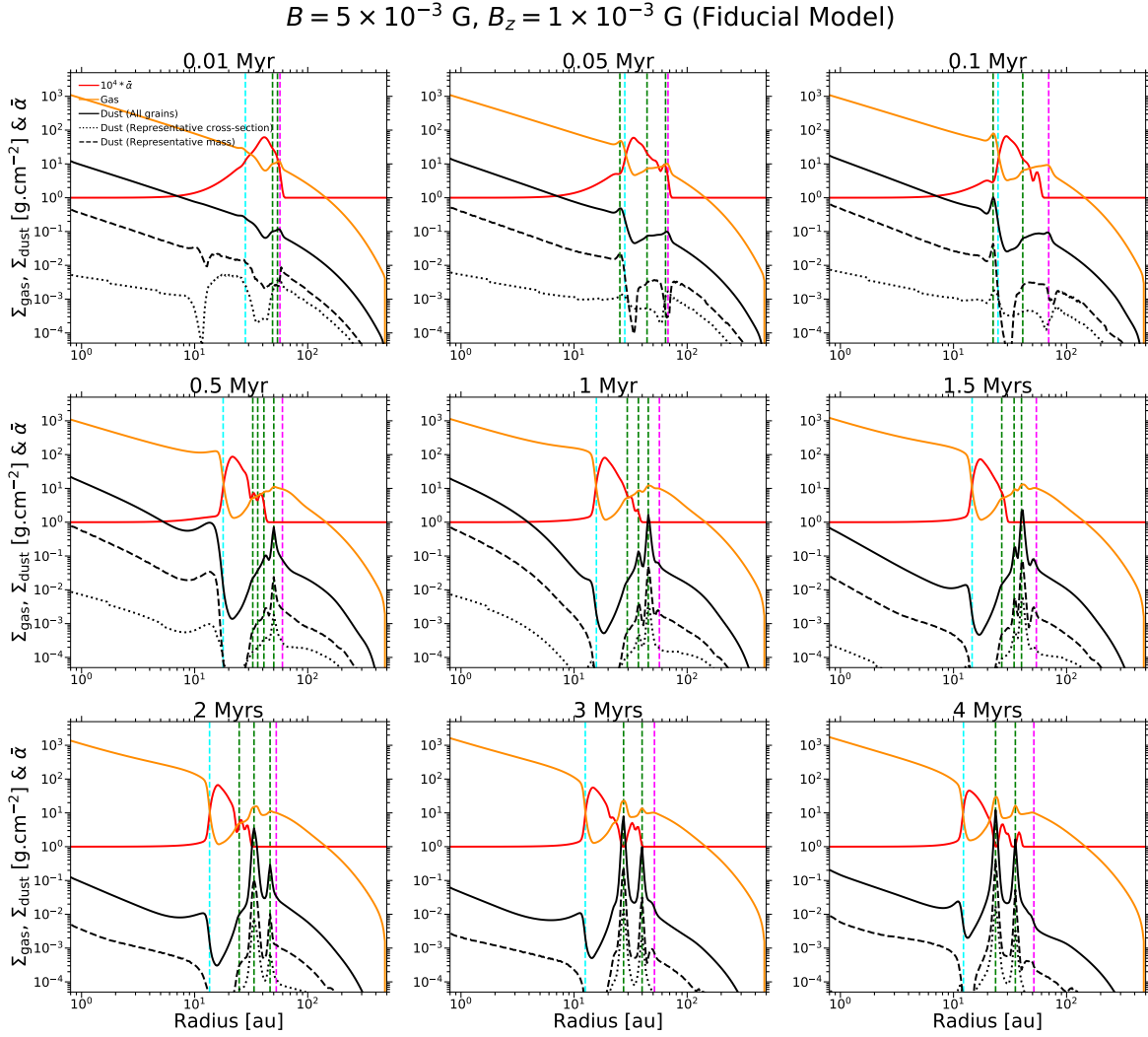
Figure 53: Time evolution of the effective disk turbulence parameter ($\bar{\alpha}$) in red, the gas surface density (Σ_{gas}) in darkorange, and the dust surface densities in black for the fiducial model of this Chapter. About the latter, the solid black line indicates the surface density accounting for all dust particles, the dotted black line shows the surface density for the dust particles locally representative of the cross-section, and the dashed black line shows the surface density for the dust particles locally representative of the mass. By definition, the local dust cross-section representative corresponds to the most abundant dust particle bin that is relevant for the ionization chemistry at a given disk location. Similarly, the local dust mass representative corresponds to the most abundant dust particle bin that accounts for the highest fraction of the total dust mass at a given disk location. In each panel, the vertical dashed cyan line indicates the location of the midplane dead zone outer edge, the vertical dashed magenta line shows the location of the midplane zombie zone inner edge, and a vertical dashed green line represents the location of a pressure maximum generated via the MRI-powered mechanism. Here is only shown the first 4 Myrs of time evolution.

$B = 5 \times 10^{-3}$ G, $B_z = 1 \times 10^{-3}$ G (Fiducial Model)
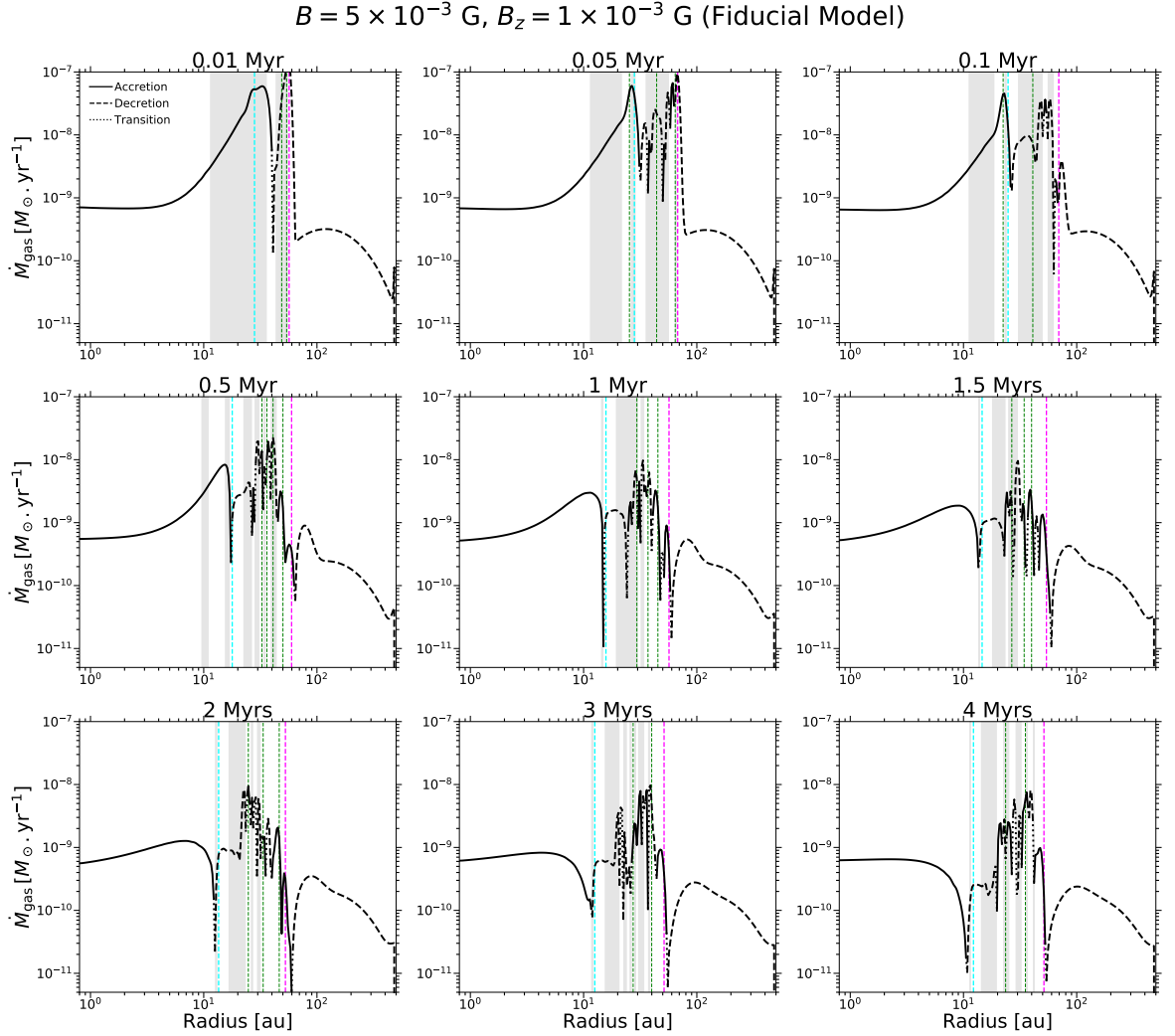
Figure 54: Time evolution of the gas accretion rate for the fiducial model of this Chapter. In each panel, the solid portion of the line means that the gas is transported inward (accretion), the dashed portion of the line means that it is transported outward (decretion), and the dotted portion of the line represents a transition region between gas accretion and decretion. The meaning of the vertical dashed cyan, magenta and green lines are the same as in Fig. 53. Lastly, the gray shaded regions represent where potential gas surface density inhomogeneities are amplified by viscous evolution rather than being smeared out. Here is only shown the first 4 Myrs of time evolution.

plane dead zone outer edge thus starts dissipating on viscous evolution timescales. At this point only the small dust particles can help maintaining this pressure maximum through the dust-driven version of the viscous instability, provided that it can generate a local dust traffic-jam density effect. Figure 56 shows the time evolution of the dust fluxes. Most importantly, it features the flux of the dust particles representative of the mass (blue line) and the flux of the ones representative of the cross-section (black line). As a reminder, the dust particles representative of the cross-section are the ones involved in the ionization chemistry, and therefore in the dust-driven viscous instability. At $t = 0.1\,\mathrm{Myr}$, one can see that the large dust particles (representative of the mass) start being trapped by the pressure maximum near the midplane dead zone outer edge (vertical dashed green line located at $\sim 23\,\mathrm{au}$). Indeed, these dust particles are transported outward anterior to this pressure maximum (dashed blue line) and inward beyond it (solid blue line). However, the small dust particles (relevant for the ionization chemistry) are clearly not. They are transported inward anterior to the pressure maximum near the mdiplane dead zone outer edge, while they are transported outward beyond it. Consequently, there is no local traffic-jam density effect for the small dust particles that can trigger the dust-driven version of the viscous instability, and the pressure maximum near the midplane dead zone outer edge dissipates at $t \sim 0.3\,\mathrm{Myrs}$. It is worth noting that this result holds across the various scenarios for the magnetic field strength and topology explored in this work (see Table 6). Therefore, it seems that the midplane dead zone outer edge is actually not a prime location for efficient dust trapping unlike the popular opinion.

As I touched upon above, sustaining a pressure maximum within the effective MRI active layer requires the dust-driven viscous instability to be triggered through a local traffic-jam density effect for the small dust particles. This corresponds to the linear regime of the dust-driven viscous instability [e.g., 299, 300]. Nonetheless, these dust particles overall follow the gas motion and weakly drift toward the regions of high pressure. It is thus not reasonable to believe that the small dust particles can be efficiently trapped where a pressure maximum is located, implying that one would expect all the pressure maxima to quickly dissipate. This is indeed confirmed by the flux for the dust particles representative of the cross-section in Fig. 56. One can see that the long-lived pressure maxima at $t = 4\,\mathrm{Myrs}$ (vertical dashed green lines at $\sim 23\,\mathrm{au}$ and $35\,\mathrm{au}$) actually do not attract small dust particles. The reason why such long-lived pressure maxima are sustained is because the dust-driven viscous instability can enter a non-linear regime. When a pressure maximum is formed within the effective MRI active layer, the large dust particles (representative of the mass) drift toward it. If pressure gradients are steep near that location, these dust particles can be efficiently trapped. Once it is the case, they can grow until a coagulation–fragmentation equilibrium is reached locally. Small dust particles are thus continuously replenished by the fragmentation of the large ones, and the large ones come from the coagulation of the small ones. Since the continuously replenished small dust particles can impact drastically the local MRI-driven turbulence, the dust-driven viscous instability can be sustained, hence sustaining

the pressure maximum. This two-stage scenario where (1) the small dust particles trigger the formation of the pressure maximum, and (2) the large dust particles are efficiently trapped within it so that the small ones are replenished through coagulation and fragmentation, represents the non-linear regime of the dust-driven viscous instability. This scenario has already been speculated in Dullemond and Penzlin [300], but the unified framework of this Chapter captures it for the first time. Figure 57 shows the time evolution of the dust surface density distribution per logarithmic bin of grain size, $\sigma(t, r, a)$ (see Eq. 186). As the protoplanetary disk evolves, prominent dust traps are formed. These dust traps can harbor dust particles of size larger than 1 mm with typical Stokes numbers in the range 0.005–0.1. A coagulation–fragmentation equilibrium is reached there as the dust size distribution is fragmentation-dominated.

In summary, it is found that the complex interplay between the gas, the dust and the MRI-driven turbulence shapes the secular evolution of protoplanetary disks by generating spontaneous short- and long-lived pressure maxima (dust traps) within the effective MRI active layer. The formation of these pressure maxima is caused by the linear regime of the dust-driven viscous instability. For the pressure maxima around which pressure gradients are steep enough (i.e., strong traps), large dust particles are trapped efficiently and fast. They grow until a coagulation–fragmentation equilibrium is reached locally. Once it is the case, there is a continuous replenishment of small dust particles locally. The dust-driven viscous instability thus enters a non-linear regime where these small dust particles locally present ensure the pressure maximum to be sustained over secular evolution timescales. This non-linear regime is sustained as long as a coagulation–fragmentation equilibrium is locally reached. The pressure maxima that cannot trap efficiently and/or fast enough large dust particles (i.e., weak traps) cannot enter the non-linear regime of the instability. They are thus short-lived and dissipate on viscous evolution timescales, since the linear regime of the instability only lasts until the local traffic-jam density enhancement effect for the small dust particles is smeared out by diffusion.

6.4   DISCUSSION

6.4.1   *Effect of the magnetic field strength and topology*

I have said many times above that the magnetic field strength and topology adopted crucially determine the effective MRI active layer, and therefore where the short- and long-lived dust traps are formed within the protoplanetary disk. Let us quantify this a bit more by exploring various scenarios for the field through a parameter study. Figure 58 shows the time series for the location of the pressure maxima within the disk for nine models including the fiducial one. One should note that some simulations are still running at the time of writing this thesis. For each model, a colored cursor on the vertical axis indicates the current evolution time reached by
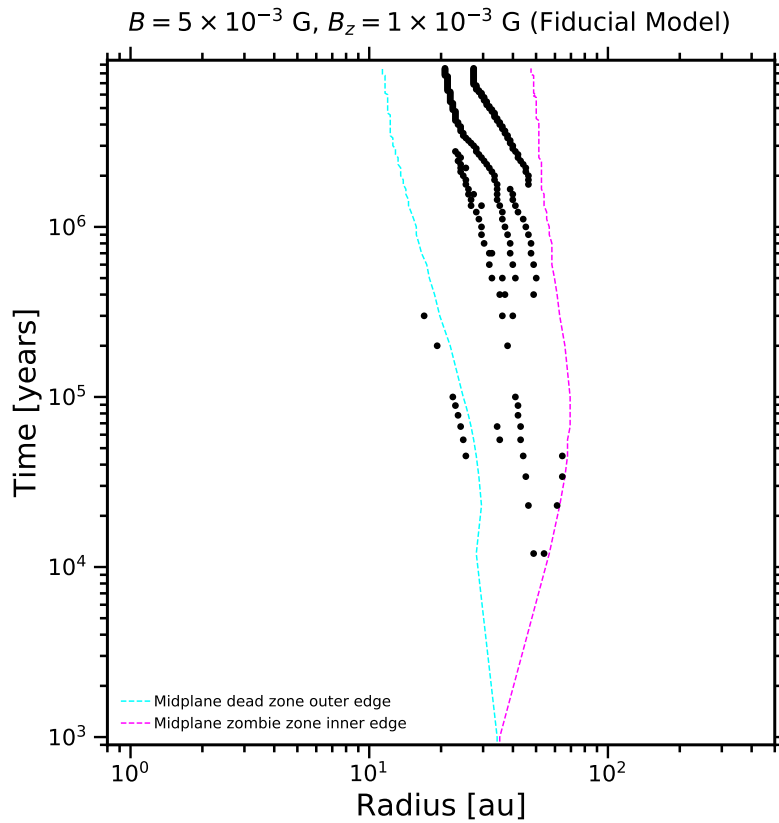
Figure 55: Time series for the pressure maxima location for the fiducial model of this Chapter. Each black dot represents a pressure maximum. The dashed cyan line indicates the time series for the location of the midplane dead zone outer edge, and the dashed magenta line shows the time series for the location of the midplane zombie zone inner edge.
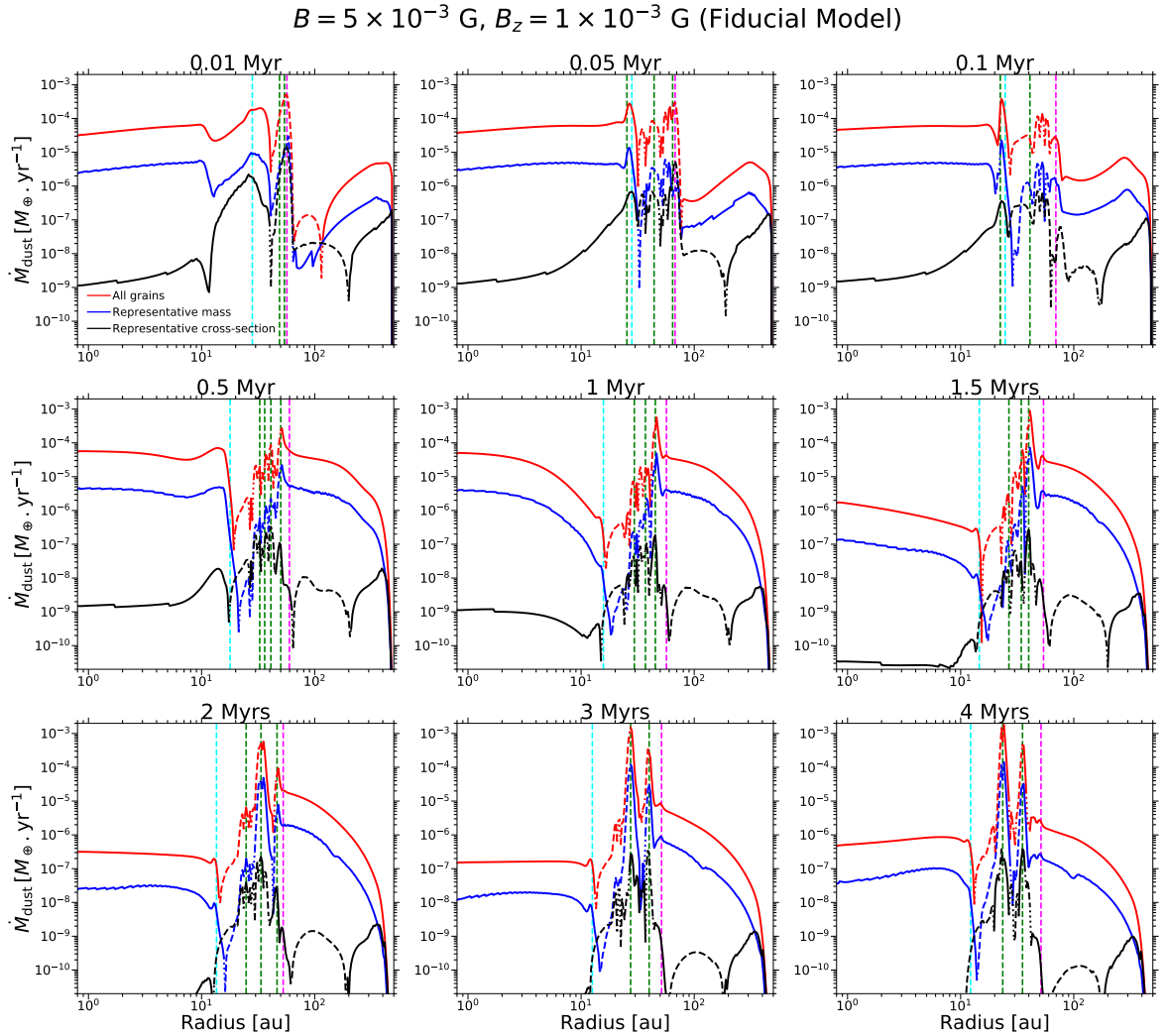
Figure 56: Time evolution of the dust fluxes for the fiducial model of this Chapter. The flux accounting for all dust particles is shown in red, the flux of the dust particles locally representative of the mass is shown in blue, and the flux of the dust particles locally representative of the cross-section is shown in black. The definition of the local dust mass representative and the local dust cross-section representative are the same as in Fig. 53. In each panel, the solid portion of a line means that dust particles are transported inward, the dashed portion of a line means that they are transported outward, and the dotted portion of a line represents a transition region between inward and outward dust transport. The meaning of the vertical dashed cyan, magenta and green lines are the same as in Fig. 53. Here is only shown the first 4 Myrs of time evolution.
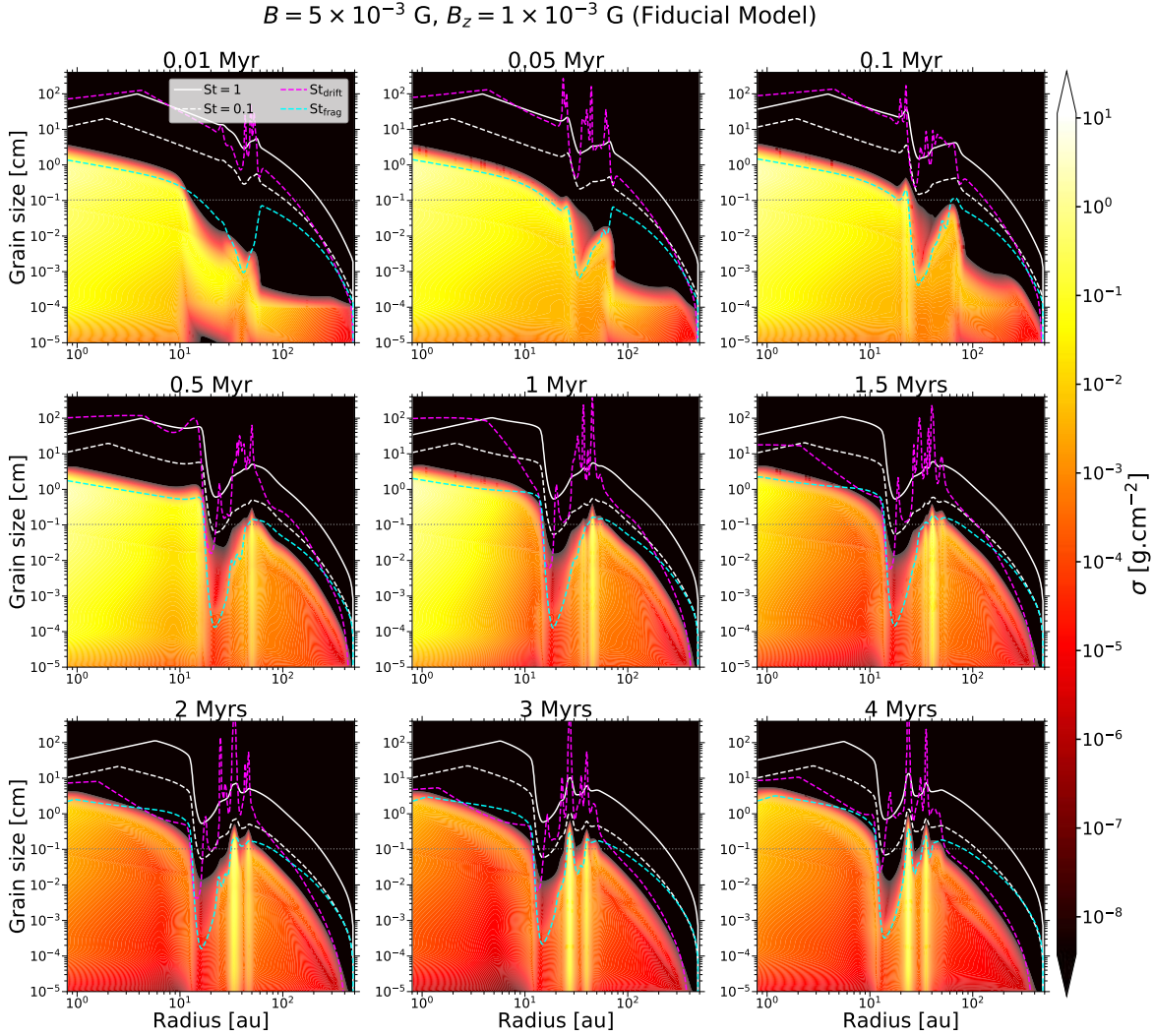
Figure 57: Time evolution of the dust surface density distribution per logarithmic bin of grain size, $\sigma(t, r, a)$ (see Eq. 186), for the fiducial model of this Chapter. In each panel, the solid white line represents Stokes numbers of unity (radial drift reaches its maximal efficiency), the dashed white line is Stokes numbers equal to 0.1, the dashed magenta line shows the drift limit (Eq. 167), and the dashed cyan line indicates the fragmentation limit (Eq. 168). Lastly, the horizontal dotted gray line corresponds to the grain size of 1 mm. Here is only shown the first 4 Myrs of time evolution.

that model so far. Since all the models have reached secular evolution timescales ($t \sim 3–10\,\text{Myrs}$), it is meaningful to compare them to each other.

One of the most salient results is that the effective MRI active layer, and therefore where the short- and long-lived pressure maxima (dust traps) are found in the disk, is bounded to specific regions of the disk for a specific strength of the magnetic field when it is assumed constant (Fig. 58a). Going from weak to strong magnetic field strengths (from Model I to Model V in this order), the effective MRI-active layer is found to probe from disk regions located as far as $\sim 400\,\text{au}$ to regions located as close as $3\,\text{au}$. Here it is thus found that short- and long-lived dust traps can populate the whole radial extent of the protoplanetary disk if the magnetic field strength varies on timescales shorter than secular evolution ones. Interestingly, one can notice that the multiplicity in dust traps increases with increasing magnetic field strength. For $B \lesssim 10^{-3}\,\text{G}$ ($B_z \lesssim 2 \times 10^{-4}\,\text{G}$), only a handful of dust traps are formed, and so exclusively in regions beyond $100\,\text{au}$. Also these dust traps are solely long-lived. For $B \gtrsim 10^{-3}\,\text{G}$ ($B_z \gtrsim 2 \times 10^{-4}\,\text{G}$), the multiplicity in dust traps increases with now a combination of short- and long-lived ones, populating exclusively the disk regions $3\,\text{au} \lesssim r \lesssim 80\,\text{au}$. Lastly, when the magnetic field strength is assumed to be constant, it is found that the first dust traps are always formed within $\sim 0.01\,\text{Myr}$, and so regardless of the exact value adopted for the field strength.

When the midplane plasma-β parameters are assumed to be constant (Fig. 58b), the multiplicity in dust traps still increases with increasing magnetic field strength (i.e., decreasing β going from Model VIII to Model VI in this order). However, it seems that the effective MRI active layer for a specific value of β can overlap the effective MRI active layer for another value. This is because the effective MRI active layer is no longer bounded to specific regions of the disk when the midplane plasma-β parameter is assumed to be constant. Instead, it spans most of the radial extent of the protoplanetary disk, regardless of the specific midplane plasma-β value adopted. Although it is the case, it is quite intriguing to notice that dust traps only populate the disk regions $1\,\text{au} \lesssim r \lesssim 50\,\text{au}$. None are found beyond $50\,\text{au}$ because there are no steep variations in the disk turbulence, and therefore the gas and dust cannot locally accumulate to trigger the linear regime of the dust-driven viscous instability.

Finally, it is worth noting that long-lived dust traps are formed in both the case of constant magnetic fields strength and constant midplane plasma-β parameters. In each panel of Fig. 58, a dot overlaid by a black cross indicates that the corresponding pressure maximum has reached a midplane local dust-to-gas mass ratio $\rho_{\text{dust}}/\rho_{\text{gas}} \gtrsim 0.1$. This shows that regardless of the scenario adopted, some pressure maxima can efficiently trap dust particles so that the non-linear regime of the dust-driven viscous instability is triggered, which then can sustain them over long timescales.
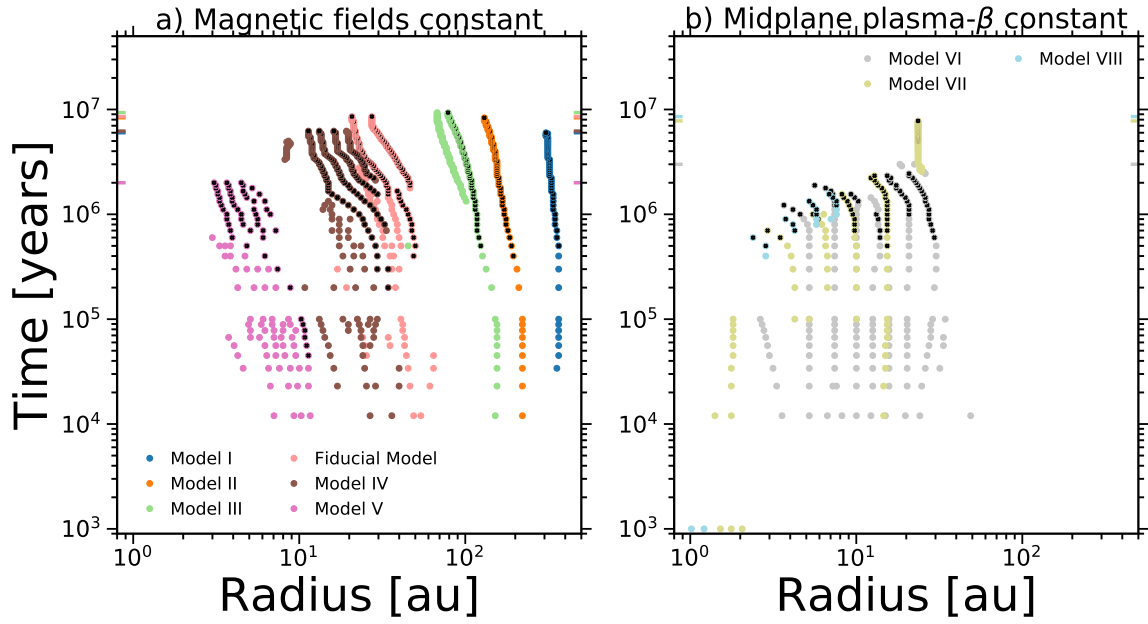
Figure 58: Time series for the location of the pressure maxima within the disk, considering various scenarios for the magnetic field strength and topology. In each panel, each dot represent a pressure maximum. The color of the dot indicates what scenario is adopted for the magnetic field (see Table 6). When a dot is overlaid by a black cross, it means that the corresponding pressure maximum has reached a midplane local dust-to-gas mass ratio $\rho_{dust}/\rho_{gas} \gtrsim 0.1$. Furthermore, a colored cursor on the vertical axis shows what is the current evolution time reached by the simulation corresponding to that color. *Panel a*: The magnetic fields are assumed constant. *Panel b*: The midplane plasma-β parameters are assumed constant.

6.4.2   *Comparison to protoplanetary disk observations*

In light of the parameter study conducted above, many protoplanetary disk observational puzzles can be explained. First, some very old disks (t $\gtrsim$ 3 Myrs) are observed to have a substantial amount of dust (large M_{dust}), while some younger ones (t ~ 1 Myr) appear to be already quite depleted in dust. This is at odds with the fact that the dust is expected to be efficiently removed from the disk on shorter timescales than the secular evolution ones due to radial drift. As a result, the dust mass reservoir is naively expected to be higher in the younger disks than in the older ones. Figure 59 shows the temporal evolution of the total disk dust mass for the various scenarios for the magnetic field strength and topology considered in this work. Clearly, most of the dust mass is kept within the protoplanetary disk on secular evolution timescales for the models where the multiplicity in the dust traps is high. As I discussed in the previous section, the stronger the magnetic field strength is and the higher this multiplicity is. The more there are pressure maxima (dust traps) within the protplanetary disk, the less the dust can efficiently be removed from the disk by radial drift as already found by Pinilla, Benisty, and Birnstiel [97]. It is thus tentatively proposed here that the observed old dust-rich protoplanetary disks have been formed with strong initial magnetic fields, while the young dust-poor ones have been formed with weak initial magnetic fields.

Second, protoplanetary disks display astonishing dust rings (Fig. 8). Disk surveys find that there is no systematic in the location of these dust rings. In other words, when observing many protoplanetary disks that display dust rings, these dust rings are found to be located at any separations from the central star. One of the current puzzle is to understand why this is the case. In this work, it has been found that spontaneous short- and long-lived dust traps are formed by the complex interplay of gas, dust and MRI-driven turbulence evolution via the dust-driven viscous instability. The long-lived ones are strong dust traps where pebbles are formed. Since they emit in the relevant radio wavelengths for ALMA, they can actually be seen by this telescope and appear as dust rings. The first column of Fig. 60 shows the synthetic observations in ALMA Band 6 (λ ~ 1.3 mm) for three models considered that only differ by the magnetic field strengh and topology adopted. Each row of Fig. 60 corresponds to a specific model. The synthetic observation for a specific model is obtained from the dust size distribution taken at t = 1.5 Myrs (second column of Fig. 60), which is the typical age of the average observed protoplanetary disk population. In order to obtain the synthetic observations, these dust size distributions (from the present unified framework) have been post-processed with the radiative transfer code `RADMC-3D` [1] [301]. For the radiative transfer calculations, the dust opacities have been calculated with the code `OpTool` [2] for each grain size. Furthermore, the central star is assumed to be a blackbody point source, and 10^7 photons have been used. Lastly, the resulting .fits file from `RADMC-3D` is further

---

1 https://www.ita.uni-heidelberg.de/ dullemond/software/radmc-3d/
2 https://github.com/cdominik/optool

post-processed with the software SIMIO [3] (Kurtovic submitted). This generates realistic synthetic observations where the disk is assumed to be located at a distance of 140 pc (mean value for the nearest star-forming regions), observed with the highest angular resolution (ellipse shown in the lower left corner of each plot of the first column) and sensitivity currently achieved with ALMA, and where the disk is assumed to have a similar geometry as the well-known disk Elias 24 [302]. Figure 60 clearly shows that the diversity in the magnetic field strength and topology leads the synthetic observed dust rings to easily reproduce the trend that there is no systematic in their location. It is also quite interesting to notice that both the observed compact and extended rings/gaps morphologies can be reproduced in this work. A protoplanetary disk with weak magnetic fields will display extended rings/gaps dust morphologies, while another with strong magnetic fields will feature compact rings/gaps dust morphologies. Consequently, it is tentatively proposed here that the absence of systematic in the dust rings location across the observed protoplanetary disk population can be explained by the simple fact that they have different magnetic field strength (due to their formation or evolution).

Finally, as I mentioned in Chapter 2, dust morphologies such as rings/gaps or ring/cavity can be explained by a plethora of mechanisms. It is then important to understand what distinguish the dust rings formed via the dust-driven viscous instability captured in this work. The first observable is that these dust rings are quite narrow and faint (Fig. 60), where their width is a few local vertical gas scale heights and their flux is of order 1 mJ/beam. The second observable is that the dust rings generated via the dust-driven viscous instability have low $\bar{\alpha}$ values of order $\alpha_{hydro} = 10^{-4}$. Furthermore, typical Stokes numbers there are found in the range 0.005–0.1 (Sect. 6.3.3). It implies that the expected values for $\bar{\alpha}/St$ in the dust rings are in the range 0.001–0.02. The dust particles within the dust rings formed via the dust-driven viscous instability are thus very settled, where H_{dust} only represents a few percent of H_{gas} locally (see Eq. 88). This is actually consistent with edge-on observations of disks. Lastly, the dependence between the normalized width and the normalized depth of the *gas* counterpart of these rings can also be an observable. Using all the models considered in this work, that span various scenarios for the magnetic field strength and topology, it is found that (see Fig. 61)

$$\log_{10}\left(1 + \frac{\Delta r_{bump}}{r_{bump}}\right) = (0.02 \pm 0.03) + (0.5 \pm 0.14) \times \log_{10}\left(1 + \frac{\delta_{bump}}{\Sigma_{gas,bump}}\right), \quad (187)$$

when considering all the dust traps that exist at $t \geqslant 1$ Myr. Future work to investigate how this relation scales for the other mechanisms are needed. If one finds in the simulations that this relation scales very differently for other mechanisms, Eq. (187) could thus be a signature of the dust-driven viscous instability.

---

[3] https://simio-continuum.readthedocs.io/en/main/index.html
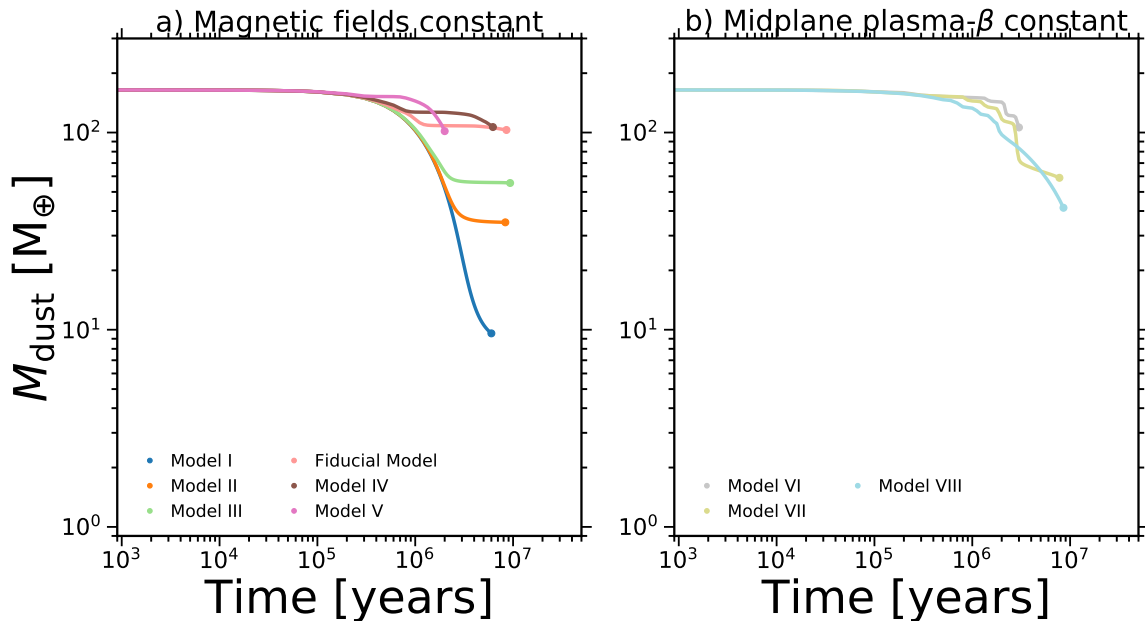
Figure 59: Time evolution of the total disk dust mass for each Model of this Chapter. In each panel, each colored line corresponds to a specific scenario for the magnetic field (see Table 6). The colored dot at the end of each corresponding colored line indicates the current evolution time reached by the simulation corresponding to that color. *Panel a*: The magnetic fields strength are assumed to be constant. *Panel b*: The midplane plasma-β parameters are assumed to be constant.

6.4.3   *Potential formation of planetesimals within the dust traps*

The non-linear regime of the dust-driven viscous instability triggers the formation of spontaneous pressure maxima (dust traps) within the protoplanetary disk. Not only these dust traps can resolve some of the current disk observational puzzles as explained in the previous section, but they could also be key for the *first steps* of planet formation.

The long-lived dust traps identified in this work have been shown to host pebbles. Furthermore, they display midplane local dust-to-gas mass ratios, ρ_{dust}/ρ_{gas}, that can easily exceed 0.1 regardless of the magnetic field strength and topology adopted, as shown by the third column of Fig. 60. Among these long-lived dust traps, the local dust-to-gas mass ratios can even reach and exceed unity over secular evolution timescales. This can be seen in Fig. 62 that shows the time series for the midplane local dust-to-gas mass ratio reached by the various dust traps for the fiducial model considered in this work. For example, one can clearly see that the pressure maximum initially formed at 50 au around 0.4 Myr is sustained throughout the entire disk secular evolution, and it continuously displays $\rho_{dust}/\rho_{gas} \gtrsim 1$ from t ~ 1.5 Myrs. Furthermore, one should remember that the typical Stokes numbers are in the range 0.005–0.1 in these dust traps (see Sect. 6.3.3). The combination of decently high Stokes numbers and midplane local dust-to-gas mass ratios larger than unity represents favorable conditions for the Streaming Instability (SI)
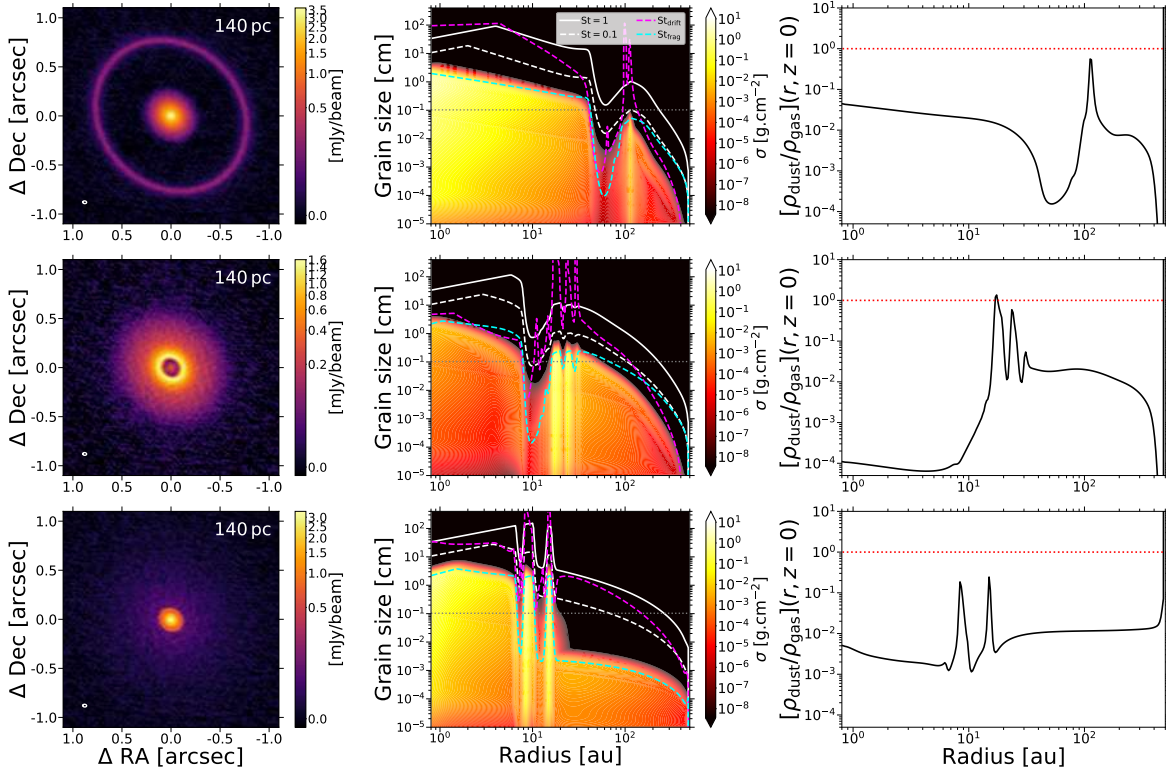
Figure 60: Simulated ALMA continuum emission at $\lambda = 1.3\,\mathrm{mm}$ (first column) that is obtained from the dust size distribution (second column) taken at $t = 1.5\,\mathrm{Myrs}$ of the protolanetary disk evolution. Each row correspond to a specific model (first row: Model III, second row: Model IV, third row: Model VII). The synthetic observed dust rings resembles those commonly observed in disk surveys. They harbor large local dust-to-gas mass ratios that are close to or exceed unity (third column).
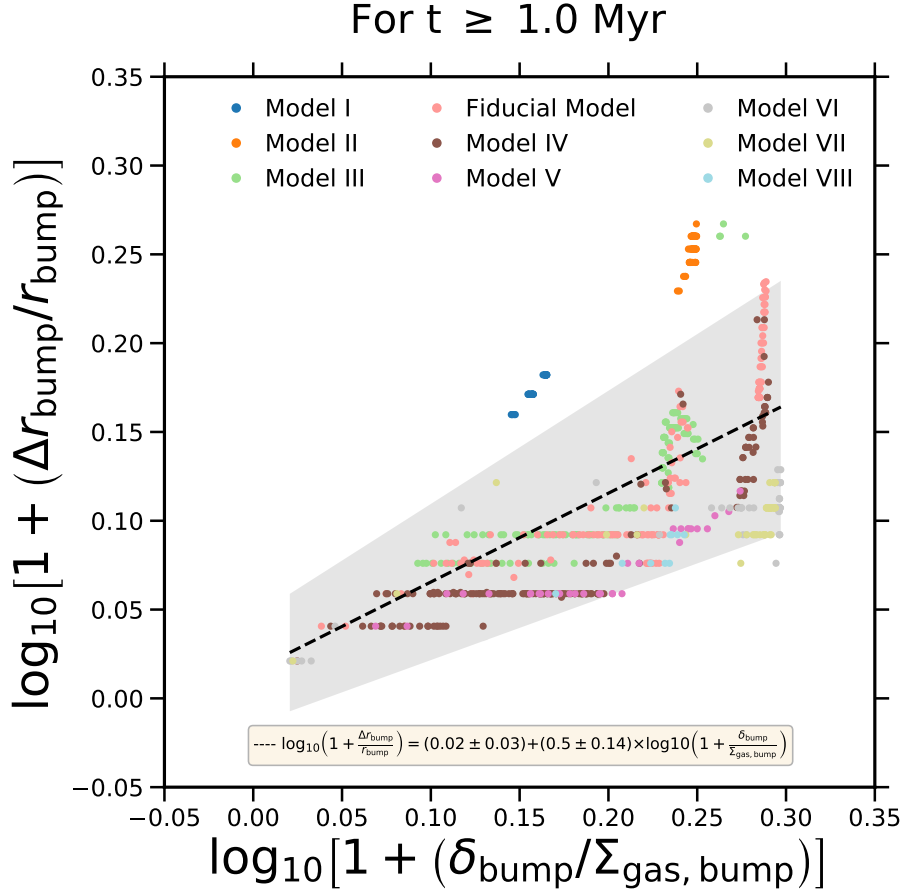
Figure 61: Normalized width–depth relation for the gas component in the disk rings formed via the dust-driven viscous instability, considering various scenarios for the magnetic field strength and topology (see Table 6). Each colored dot represents a pressure maximum for a specific model. Here only the pressure maxima that exist at $t \geqslant 1\,\text{Myr}$ are considered. The normalized width is shown in the vertical axis, and the normalized depth is shown in the horizontal axis. Δr_{bump} is the width of the disk ring in gas, δ_{bump} is the depth of the disk ring in gas, r_{bump} is the location of the disk ring, and $\Sigma_{\text{gas,bump}}$ is the gas surface density at that location. The dashed black line shows the power-law that fits the data best in the least-squares sense. The gray shaded area encloses the 5σ confidence level.

to be triggered there (see Sect. 2.3.3). Consequently, planetesimals could be formed within this long-lived dust trap, implying that it could potentially host the building blocks of planets (pebbles and planetesimals). The dust mass enclosed within this specific long-lived dust trap is in the range 75–80 $M_\oplus$ for t $\gtrsim$ 1.5 Myrs, as shown by Fig. 63. This clearly indicates that there is more than enough dust material to subsequently form planets there. Obviously, the specific long-lived dust trap that is initially formed at 50 au around 0.4 Myr is not the only interesting one found in this work. For example, there is also a long-lived dust trap initially formed at 45 au around 2 Myrs that quickly displays $\rho_{\rm dust}/\rho_{\rm gas} \gtrsim 0.31$ (see Fig. 62), with a dust mass enclosed in the range 20–25 $M_\oplus$ (see Fig. 63). If the SI can also operate in this weaker dust trap, then the fiducial model could potentially have two birth-sites for soon-to-be-planets. Future studies are needed to really understand under which conditions planetesimal formation is efficient via the SI. Then, one could quantity better which ones of the long-lived dust traps formed by the dust-driven viscous instability could potentially trigger planet formation.

In the models considered here, when the midplane local dust-to-gas mass ratio in the long-lived dust traps reaches values close to unity, it happens over a timescale of order 1 Myr. This implies that subsequent planet formation processes can only start after 1 Myr, which leaves a short window of action for planets to be formed within the disk before it is dispersed. Nonetheless, this timing of 1 Myr is quite consistent with the dust mass enclosed in observed dust rings of million-year-old protoplanetary disks. It is indeed found to be larger than 20 $M_\oplus$ in the DSHARP sample [e.g., 303], which can be interpreted as planetesimal formation not having started yet.

6.5   SUMMARY AND CONCLUSIONS

In this Chapter, I have developed the very first unified 1D disk evolution framework that captures self-consistently the evolution of the gas, the dust (dynamics and grain growth process combined), and the MRI-driven turbulence in protoplanetary disks over millions of years. This is achieved by fully integrating the disk accretion model of Chapter 2 implemented in `mhdpy` into the viscous gas evolution model and the dust evolution model implemented in `DustPy`. This framework provides, for the first time, the necessary tools to investigate how this interplay shapes the secular evolution of protoplanetary disks, and how it is related to the *first* steps of planet formation. The key findings can be summarized as follows:

- This interplay triggers the formation of pressure maxima (dust traps) via the linear regime of the dust-driven viscous instability, which is governed by the combined effect of the transport of small dust particles and their effect on the MRI-driven turbulence. The formation of these pressure maxima is spontaneous and can occur anywhere in the so-called effective MRI active layer (regions where $\bar{\alpha} > \alpha_{\rm hydro}$), which is crucially set by the magnetic field strength and topology.
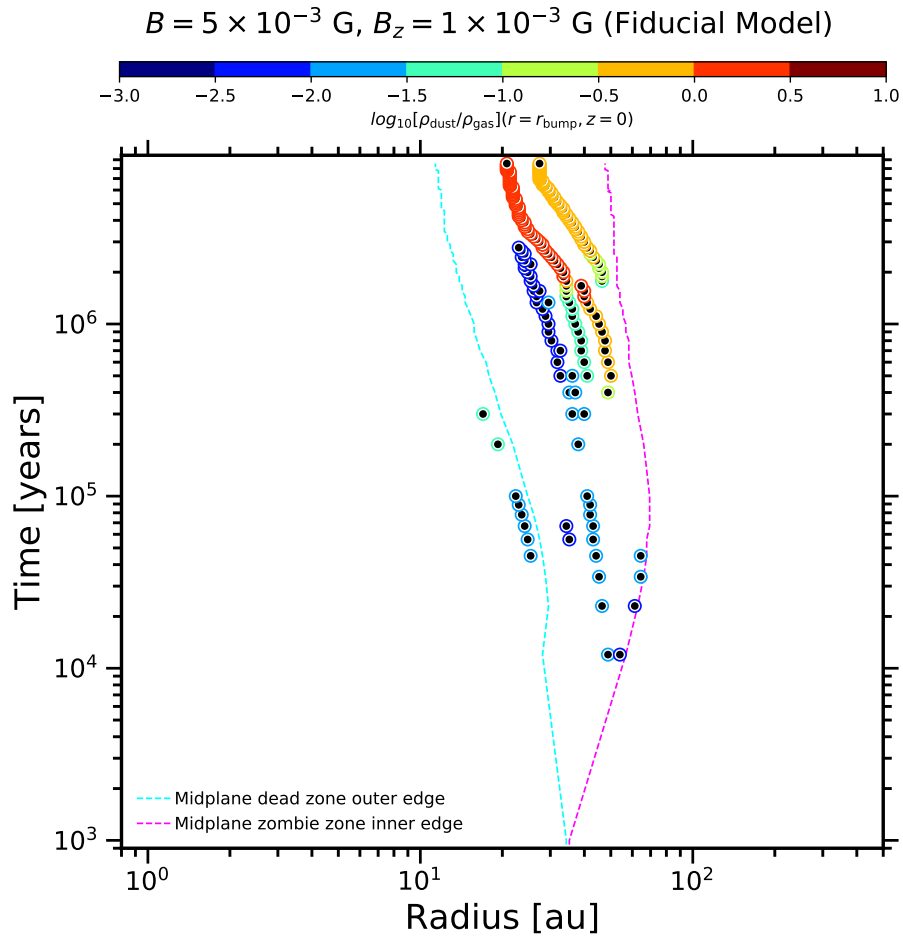
Figure 62: Time series for the midplane local dust-to-gas mass ratio reached by the pressure maxima within the disk for the fiducial model of this Chapter. Each black dot represents a pressure maximum. The color of the circle around a back dot represents the value of the midplane local dust-to-gas mass ratio reached by the corresponding pressure maximum. The dashed cyan line indicates the time series for the location of the midplane dead zone outer edge, and the dashed magenta line shows the time series for the location of the midplane zombie zone inner edge.
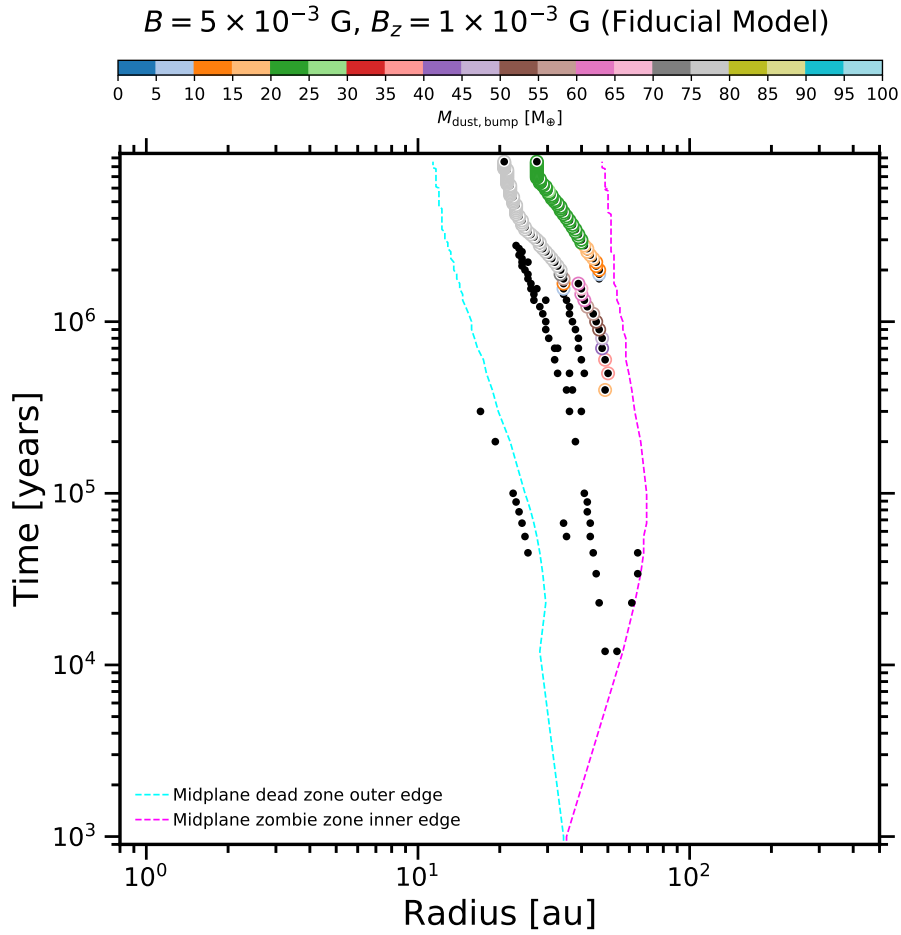
Figure 63: Time series for the dust mass enclosed by some pressure maxima within the disk for the fiducial model of this Chapter. Each black dot represents a pressure maximum. When there is a colored circle around a black dot, it means that the corresponding pressure maximum has reached a midplane local dust-to-gas mass ratio $\rho_{dust}/\rho_{gas} \gtrsim 0.1$. The color of the circle indicates the value of the dust mass enclosed by this pressure maximum. The dashed cyan line indicates the time series for the location of the midplane dead zone outer edge, and the dashed magenta line shows the time series for the location of the midplane zombie zone inner edge.

- There exists two classes of pressure maxima: short-lived and long-lived ones. For the pressure maxima that are strong traps, large dust particles are trapped efficiently and fast. They grow until a coagulation–fragmentation is locally reached. Once it is the case, there is a continuous replenishment of small dust particles locally. The dust-driven viscous instability thus enters a non-linear regime where these small dust particles ensure the pressure maximum to be sustained over secular evolution timescales. The newly identified non-linear regime of this instability is sustained as long as a coagulation–fragmentation equilibrium is locally maintained. For the pressure maxima that cannot trap efficiently and/or fast enough large dust particles, the non-linear regime of the dust-driven viscous instability is not triggered. They are thus short-lived and dissipate on viscous evolution timescales, as the linear regime of the instability that applies there can only last until the local traffic-jam density enhancement of small dust particles is smeared out.

- The long-lived dust traps host pebbles. They are thus observable with ALMA and appear as dust rings. The interplay of the gas, the dust and the MRI-driven turbulence in protoplanetary disks can thus explain some of the observed dust substructures, specifically the rings/gaps and ring/cavity dust morphologies.

- Within some of the long-lived dust traps, favorable conditions for the Streaming Instability can be reached. In addition to pebbles, planetesimals might be forming there. The interplay of the gas, the dust and the MRI-driven turbulence in protoplanetary disks might thus play a key role in the *first steps* of planet formation by creating the birth-sites and initial conditions of soon-to-be planets.

- A pressure maximum near the midplane dead zone outer edge does not form at all if the magnetic fields are too weak ($B \lesssim 10^{-3}$ G, $B_z \lesssim 2 \times 10^{-4}$ G or $\beta_{mid} \gtrsim 200$, $\beta_{z,mid} \gtrsim 5000$). Even when the fields are strong enough, only a short-lived pressure maximum can be formed there. This finding suggests that the midplane dead zone outer edge might not be a relevant location to explain some of the observed dust substructures, unlike what is currently believed.

- By exploring various scenarios for the magnetic field, it is found that the multiplicity and locations of the dust traps are crucially set by the magnetic field strength and topology. When the magnetic fields are assumed to be constant, and for weak fields ($B \lesssim 10^{-3}$ G, $B_z \lesssim 2 \times 10^{-4}$ G), only a handful of dust traps are formed and so exclusively in disk regions beyond 100 au. For strong fields ($B \gtrsim 10^{-3}$ G, $B_z \gtrsim 2 \times 10^{-4}$ G), the multiplicity in dust traps increases with now a combination of short- and long-lived ones populating exclusively the disk regions $3\,\mathrm{au} \lesssim r \lesssim 80\,\mathrm{au}$. When the midplane plasma-β parameters are assumed to be constant, the dust traps only populate the disk

regions $1\,\mathrm{au} \lesssim r \lesssim 50\,\mathrm{au}$, with always a combination of short- and long-lived ones.

- The spontaneous formation of short- and long-lived dust traps might have great implications in the context of protoplanetary disk observations. The puzzle in which some observed old disks display much larger dust mass reservoir than observed younger ones is tentatively explained by saying that these specific old disks are formed with stronger magnetic fields compared to the younger ones. The puzzle in which disk surveys find that there is no systematic in the location of dust rings across the disk population is tentatively explained by saying that this is a natural consequence of the diversity in magnetic fields across disks. The puzzle in which dust rings in million-year-old disks are found to still enclose a large amount of dust mass is tentatively explained by saying that it takes $\sim 1\,\mathrm{Myr}$ for the long-lived dust traps to display favorable conditions for the formation of planetesimals.

- The long-lived dust traps formed via the dust-driven viscous instability have specific characteristics. They are narrow (a few local vertical gas scale height), faint (a few mJ/beam), and settled (the dust scale height represents a few percent of the local vertical gas scale height). Furthermore, the gas component in the rings displays an average scaling relation between the normalized width and the normalized depth given by $\left(1 + \frac{\Delta r_{\mathrm{bump}}}{r_{\mathrm{bump}}}\right) \approx \left(1 + \frac{\delta_{\mathrm{bump}}}{\Sigma_{\mathrm{gas,bump}}}\right)^{(0.5\pm0.14)}$. This might be a signature of the dust-driven viscous instability.

SUMMARY AND OUTLOOK

The rich diversity of exoplanets discovered in various physical environments clearly shows that planet formation is an efficient process with multiple outcomes. To understand the emergence of newborn planets, one can rewind the clock of planetary systems by investigating the formation and evolution of their natal environment, the so-called protoplanetary disks. In the core accretion scenario, rocky planets such as the Earth are thought to be formed from cosmic dust particles that grow into pebbles and planetesimals, the building blocks of planets, later assembling together. An intricate puzzle in this theory is how exactly these building blocks are formed and kept long enough in the natal protoplanetary disk.

Protoplanetary disks are weakly magnetized accretion disks that are subject to the MRI, one of the main candidates for explaining their turbulence and angular momentum transport. The nonideal MHD effects prevent the MRI from operating everywhere in the protoplanetary disk, leading to a complex dichotomy between MRI active regions with high turbulence level and non-MRI regions with low turbulence level. It has been hypothesized that these radial variations in the disk turbulence can lead to pressure maxima where dust particles can be trapped. In these so-called dust traps, dust particles can grow efficiently into pebbles and potentially planetesimals. Yet, it is still an open question how this MRI-powered mechanism shapes the secular evolution of protoplanetary disks, and how it is involved in the *first steps* of planet formation. This is because the interplay of gas evolution, dust evolution (dynamics and grain growth processes combined) and MRI-driven turbulence over millions of years has never been investigated.

In this thesis, which now draws to a close, I have explored a potential way to bridge the gap in the core accretion scenario of planet formation by investigating this interplay. Particularly, this thesis attempts to address two central questions: *Can the interplay of gas evolution, dust evolution and MRI-driven turbulence explain the dust substructures observed in protoplanetary disks with telescopes such as ALMA or VLT/SPHERE? Can these induced dust substructures host the building blocks of planets and be potential birth-sites for them?* To study this interplay in a robust and unique approach, in the context of the *first steps* of planet formation, this thesis features four key milestones. In this Chapter, I provide a brief summary of these milestones, as well as an outlook on the field of planet formation with areas that warrant future thought.

7.1 SUMMARY

- In Chapter 3, I presented a new 1+1D global MRI-driven magnetized disk accretion model implemented in a newly developed code called mhdpy (to be

publicly available soon). This disk accretion model is built to study the outer region of Class II protoplanetary disks ($r \gtrsim 1\,$au, where r is the distance from the central star), which accretes viscously solely due to the MRI and hydro-dynamic instabilities. It has the advantage to capture the essence of the MRI-driven accretion, without resorting to computationally expensive 3D global nonideal MHD simulations. Its main output is an effective radial profile for the MRI-induced disk viscosity parameter (Shakura-Sunyaev α parameter), which is thus derived through detailed but inexpensive MRI calculations. It accounts for both the nonideal MHD effects Ohmic resistivity and ambipolar diffusion, with a sophisticated modeling of the gas ionization degree using a semi-analytical chemical model that captures the feedback of dust particles.

- In Chapter 4, I investigated what stellar and disk parameters the MRI activity crucially depends on as well as the extent to which the MRI-driven accretion is efficient, using the disk accretion model of Chapter 2 implemented in mhdpy, and assuming the specific case of steady-state accretion. I found that the steady-state MRI-driven accretion solution displays no pressure maximum at the dead zone outer edge, except if a sufficient amount of dust particles has accumulated there. Moreover, this solution describes a disk that displays a spatially extended long-lived inner disk gas reservoir (the dead zone) accreting a few times $10^{-9} M_\odot.\mathrm{yr}^{-1}$. Finally, through a comprehensive parameter study, I showed that the MRI activity is primarily set by the local dust and gas properties, the stellar X-rays luminosity, and the magnetic field strength. Since these quantities evolve over time, it strongly suggests that a self-consistent time-dependent coupling between gas, dust, stellar evolution, and MRI-driven accretion on million-year timescales is required to capture the MRI activity evolution in protoplanetary disks.

- In Chapter 5, I provided a crucial step toward a better understanding of the MRI–dust coevolution by investigating the sole effect of dust evolution (dynamics and grain growth processes combined) on the MRI-driven accretion over millions of years. To do so, I partially combined the disk accretion model of Chapter 2 with the dust evolution model (dust advection and diffusion, as well as dust growth by coagulation and fragmentation) employed with the 1D code DustPy. I demonstrated that it is fundamental to account for the feedback of dust coagulation, fragmentation, settling and radial drift onto the gas ionization degree in order to accurately describe the MRI activity evolution. Indeed, I showed that the MRI activity evolution (hence the temporal evolution of the MRI-induced disk viscosity parameter) is controlled by dust evolution and occurs on a timescale of local dust growth, as long as there are enough dust particles in the disk to dominate the recombination process for the ionization chemistry. As a result, one should expect to have complex interdependencies between gas, dust and MRI activity in protoplanetary disks. This is because gas and dust evolution can change the MRI-driven turbulence

which in turn changes the gas dynamics as well as the evolution of dust particles, hence impacting the MRI-driven turbulence.

- In Chapter 6, I presented the very first unified 1D disk evolution framework that captures self-consistently the interplay between gas evolution, dust evolution (dynamics and grain growth process combined) and MRI-driven accretion in protoplanetary disks over millions of years. This is achieved by fully integrating the disk accretion model of Chapter 2 implemented in `mhdpy` into the viscous gas evolution model and the dust evolution model (same as the one mentioned in the previous paragraph) implemented in `DustPy`. Such a framework can simulate the secular evolution of protoplanetary disks (millions of years), which is essential if one wants to further compare its outputs (post-processed with radiative transfer) to current dust continuum observations. I proved that the complex interdependencies between the gas, the dust and the MRI-driven turbulence shapes the secular evolution of the disk by generating the spontaneous formation of both short- and long-lived dust traps within the so-called effective MRI active layer. The underlying mechanism behind the formation of these dust traps is the dust-driven viscous instability. Specifically, the long-lived dust traps are formed because of the non-linear regime of this instability that is captured for the first time in this thesis. The multiplicity and properties of these dust traps (location, lifetime, dust mass enclosed) are found to be crucially determined by the magnetic field strength and topology. By exploring various scenarios for the magnetic field, I demonstrated that short- and long-lived dust traps can be formed at any locations in the disk. This has great implications in the context of protoplanetary disk observations. Finally, among some of the long-lived dust traps, I showed that the local midplane dust-to-gas mass density ratio can reach high enough values for planetesimal formation to be triggered through the Streaming Instability, and that the dust mass enclosed there is much higher than a few Earth masses. These long-lived dust traps could thus be birth-sites of soon-to-be planets, and represent their initial conditions.

7.2 OUTLOOK

In this section, I discuss future avenues of research in light of the findings in this thesis.

7.2.1 *Evolution of the magnetic field in protoplanetary disks*

In this thesis, it has been found that the exact parameterization of the magnetic field strength and topology dictates how the MRI-driven disk turbulence radially varies (Chapter 4). This in turn governs the generation of the spontaneous dust traps in the protoplanetary disk, by directly determining their exact number as well as their properties such as their location, lifetime, or the dust mass they enclose (Chapter 6).

Ultimately the magnetic field strength and topology are what crucially set whether or not these spontaneous dust traps harbor both pebbles and planetesimals, the necessary building blocks of planets.

Although the magnetic field strength and topology are parameterized in various ways in this thesis (Sect. 3.5.3), the eager reader should remember that they are actually *not* free parameters. Instead, the evolution of the magnetic field in the protoplanetary disk is governed by the nonideal induction equation (Eq. 39), which describes the intimate link between magnetic fields, gas neutral particles and charged particles (free electrons, ions and charged grains). This equation has two components: the ideal MHD term that encodes the advection of the field trying to follow the gas motion, and the nonideal MHD term that encodes the diffusion of the field with respect to the gas motion. Since the protoplanetary disk inherits a large-scale poloidal magnetic field (field with only radial and vertical components) from the star-forming molecular cloud during its formation, this poloidal field follows the nonideal induction equation during the secular evolution of the disk.

The radial transport of the large-scale poloidal magnetic field is a long-standing issue in the theory of accretion disks. It has been initially thought that protoplanetary disks can advect it inward to generate strongly magnetized inner regions (low values for the plasma-β parameter) [e.g., 304]. This picture was later confronted by Lubow, Papaloizou, and Pringle [256]. The authors argued that the large-scale poloidal magnetic field would instead diffuse away much faster than it can be dragged inward by the accreted gas, if turbulence is the source of the accretion process as it is the case for the MRI. This argument is based on the comparison between the timescales of the different processes at play: If the advection of the field occurs at the disk midplane, the field advection velocity should be similar to the accretion velocity of the gas. In this case the advection timescale of the large-scale poloidal magnetic field should thus be of order the viscous evolution timescale of the gas. Since the magnetic Prandtl number (classically defined as the ratio between the kinematic disk viscosity and the midplane Pedersen magnetic diffusivity) is much less than unity in typical geometrically thin protoplanetary disks, it can be shown that the diffusion timescale of the magnetic field is much less than the viscous evolution timescale of the gas. This predicts that effective inward transport of the large-scale poloidal magnetic field would not occur. However, there is a main caveat with this simple timescale argument. It is indeed implicitly assumed that the field advection takes place at the disk midplane, and that its advection velocity is similar to the gas advection velocity. Ogilvie and Livio [305] pointed out that the large-scale poloidal magnetic field should instead be dragged by the gas in the disk atmosphere where the electric conductivity is high enough, with a field advection velocity that differs from the gas advection velocity at the disk midplane [e.g., 306]. In the case where the former is much faster than the latter, the large-scale poloidal magnetic field can thus be efficiently transported inward. Such a situation is realized when the gas advection velocity in the disk atmosphere is much larger than the gas advection velocity at the disk midplane [e.g., 257, 307].

Clearly, knowing exactly how the large-scale poloidal magnetic field is radially transported within the protoplanetary disk is fundamental in order to fully grasp how the interplay of gas evolution, dust evolution, and MRI-driven turbulence shapes the disk secular evolution, and how it is involved in the *first steps* of planet formation. An exciting avenue to push forward is thus the implementation of the nonideal induction equation into the current unified disk evolution framework developed in this thesis (Chapter 6). To do so, one could specifically integrate the radial transport model for the large-scale poloidal field developed in Okuzumi, Takeuchi, and Muto [258] and Takeuchi and Okuzumi [259].

7.2.2 *Toward a complete unified model for the secular evolution of protoplanetary disks*

The work conducted in this thesis solely focuses on the MRI as the main driver for the turbulence, the angular momentum transport, and the gas dispersal (due to viscous accretion and expansion) in the protoplanetary disk. This choice to set the MRI as the main protagonist of our quest was justified to address its potential role in bridging the gap in the core accretion scenario of planet formation, namely how the building blocks of planets (pebbles and planetesimals) are formed and kept long enough in their natal environment. The main idea developed here is that a MRI-powered mechanism –that originates from the interplay of gas evolution, dust evolution and MRI-driven turbulence– can potentially shape the disk secular evolution by generating spontaneous dust traps with the right conditions for the emergence of newborn planets.

Other key processes for the turbulence, the angular momentum transport, and the dispersal of the protoplanetary disk have been ignored so far. An exciting avenue to push forward is the inclusion of such processes into the current unified disk evolution framework developed in this thesis (Chapter 6). A complete unified framework for the disk secular evolution will thus obtained, where the interplay of the various key processes in protoplanetary disks can be captured into a single framework. This will be a crucial tool for astronomers, as it will provide a much clearer picture about the origin of the observed dust substructures and their relation to the *first steps* of planet formation. In the following I provide some ideas about how the implementation of these processes could be achieved:

- About disk turbulence. As I discussed in Sect. 1.4, pure hydrodynamic-driven mechanisms can drive disk turbulence, especially in non-MRI regions. In this thesis I assumed the VSI to be the origin of the hydrodynamic-driven turbulence which was encapsulated into the parameter α_{hydro}. This free parameter of the model was assumed to be independent of time and space throughout the disk secular evolution. However, VSI studies clearly show that it is not the case, and α_{hydro} is actually expected to depend on the local disk properties such as the temperature gradient and the cooling timescale [e.g., 308]. A natural improvement for the current unified disk evolution framework of this thesis would thus be to compute locally α_{hydro} at each location and over time. To do so, one could use a parameterized function for α_{hydro} that depends on

the relevant disk properties, such as the one given in Manger, Pfeil, and Klahr [308].

• About angular momentum transport. In Sect. 1.4 I made clear that MHD disk winds are undeniably involved in the accretion process of protoplanetary disks. In order to implement them into the current unified disk evolution framework of this thesis, one first needs to go back to the derivation made of the equation governing the evolution of the gas surface density (Eq. 79). As a reminder for the eager reader, Eq. (79) has been derived by assuming the accretion process to be purely radial and neglecting the component $W_{z\phi}$ of the shear stress tensor. Relaxing this assumption (i.e., the accretion process happens both radially and vertically), one can derive a similar but more complex equation for the evolution of the gas surface density (see Eq. (1) from Lesur et al. [87]). Instead of only depending on $\bar{\alpha}$ as it is the case for Eq. (79), the new equation for the evolution of the gas surface density depends on two additional dimensionless parameters (the ejection efficiency and the magnetic lever arm parameters). Similarly to this thesis where the local disk viscosity α is given as a function of the local plasma-β parameter of the r.m.s. magnetic field (see Sect. 3.5.2), the ejection efficiency and the magnetic lever arm parameters can be related to the midplane plasma-β parameter of the mean vertical magnetic field threading the disk midplane [309]. MHD disk winds can thus be integrated into the current unified framework of this thesis by solving for Eq. (1) of Lesur et al. [87] rather than Eq. (79), complemented with the relevant dependencies of the ejection efficiency and the magnetic lever arm parameters in the midplane plasma-β parameter of the vertical magnetic field (see Lesur [309]).

• About gas dispersal. By implementing MHD disk winds as described above, one will also implement their dispersal effect on the gas component of the protoplanetary disk. Another dispersal mechanism that is believed to play a major role is internal photoevaporation. As there is less and less gas to be accreted onto the central star over time due to the accretion process (see Sect. 1.3.2.2), the accretion rate eventually becomes lower than the mass-loss rate due to internal photoevaporative winds. These winds originate from the X-ray and UV radiation from the central star that tries to gravitationally unbound the gas located in the uppermost layer of the disk [e.g., 310–314]. As a result of internal photoevaporation, the gas component of the disk is dispersed from the inside out. This process can be implemented into the current unified disk evolution framework of this thesis by simply adding a mass-loss term into the equation governing the gas surface density evolution [e.g., 52].

Finally if one wants to truly achieve a complete unified framework for the secular evolution of protoplanetary disks, any processes that can generate dust traps need to be integrated (e.g., icelines [7]). Since the MRI-powered mechanism described in this thesis needs local enhancements of small dust particles to be triggered (see

Chapter 6), it is not inconceivable to believe that other "dust trap-generator" processes could be seed for it. At this stage the eager reader might ask, *If everything is included, then how could theorists understand the outcome of this complete unified disk evolution framework?*. To this legitimate question, a simple answer is: *more disk observations*. The more disk observations (gas and dust) the community has, the better theorists would be able to understand the outcome of such a framework. The kitchen-sink approach can be avoided if the various key processes are implemented one at the time, and if the outcome of the model is compared to disk observations each time a new process is integrated. In the perspective of acquiring more disk observations, new current facilities such as the James Webb Space Telescope (JWST), or future ones such as the Nancy Grace Roman Space Telescope (ROMAN) and perhaps the next-generation Very Large Array (ngVLA) will be game changers. For example, Perotti et al. [315] recently reported water discovery in the inner regions of the protoplanerary disk around PDS 70 with JWST observations. This discovery implies that potential terrestrial planets forming therein would have access to a water reservoir, which is a very important result as water was thought to be more likely delivered from the disk outer regions rather than formed and sustained in the inner regions.

7.2.3 *Connecting the dots between the initial and final stage of planet formation*

Planet formation is a complicated process that can be investigated through two complementary windows: the natal protoplanetary disks (initial stage of planet formation) and exoplanets (final stage of planet formation). Connecting planet formation models to the emerging picture of disks and exoplanet demographics requires one to take a panoptic perspective where all the planet formation mechanisms are considered. In order to gain more insights about how planets form, it is thus crucial to model their birth and life cycle alongside the evolution of their natal environment.

The major inconsistency in the current planet formation models is that they start with various assumptions about the distribution and properties of the planetesimals and planetary embryos within the disk. This assumes implicitly that planet formation would occur as a burst. In light of the observed dust substructures and the theoretical models, though, it seems that it is rather a process that is spatially and temporally fragmented [e.g., 35]. This means that the building blocks of planets are not available at every location in the natal disk, and that planets within one disk do not necessarily form at the same time. That indeed makes more sense as planetesimals and planetary embryos form via the growth of dust particles, which is itself a spatially and temporally fragmented process. Their distribution and properties are thus completely determined by the evolution of their natal protoplanetary disk, hence why work such as this thesis exist in order to connect dust evolution to planetesimal formation.

One of the most important conclusions of this thesis is that spontaneous dust traps are generated by a MRI-powered mechanism, emerging from the interplay

of gas evolution, dust evolution, and MRI-driven turbulence (Chapter 6). Some of these dust traps are found to have the right conditions for the formation of planetesimals within them. However, the current unified disk evolution framework developed in this thesis does not follow the subsequent evolution of planetesimals, and therefore cannot capture the formation of potential planetary embryos. In order to pave the way in connecting the initial and final stage of planet formation, an exciting avenue to push forward is to complement this current unified disk evolution framework with processes related to the formation and evolution of planetesimals and planetary embryos. Such an all-encompassing approach will provide the very first realistic end-to-end simulations of planet formation, from interstellar dust particles to forming planetary systems. This implementation could be achieved by following the work presented in Lau et al. [316]. The authors initially developed a parallelized N-body code SyMBAp that can integrate a large number of gravitationally interacting planetesimals [317]. Then, they coupled the codes DustPy (encodes the evolution of the gas and dust components of the disk) and SyMBAp so that planetesimals can be evolved within their natal protoplanetary disks, accounting for key processes for their subsequent evolution into planetary embryos. In the same fashion, one could thus integrate SyMBAp into the unique framework of Chapter 6, obtained by coupling the codes DustPy and mhdpy (encodes the global MRI-driven disk accretion model of Chapter 3).

[1] A. Wolszczan and D. A. Frail. "A planetary system around the millisecond pulsar PSR1257 + 12." In: *Nature* 355.6356 (Jan. 1992), pp. 145–147. DOI: 10.1038/355145a0.

[2] A. Wolszczan. "Confirmation of Earth-Mass Planets Orbiting the Millisecond Pulsar PSR B1257+12." In: *Science* 264.5158 (Apr. 1994), pp. 538–542. DOI: 10.1126/science.264.5158.538.

[3] M. Mayor and D. Queloz. "A Jupiter-mass companion to a solar-type star." In: *Nature* 378.6555 (Nov. 1995), pp. 355–359. DOI: 10.1038/378355a0.

[4] S. N. Raymond et al. "Migration-driven diversity of super-Earth compositions." In: *MNRAS* 479.1 (Sept. 2018), pp. L81–L85. DOI: 10.1093/mnrasl/sly100.

[5] B. J. Fulton et al. "The California-Kepler Survey. III. A Gap in the Radius Distribution of Small Planets." In: *AJ* 154.3, 109 (Sept. 2017), p. 109. DOI: 10.3847/1538-3881/aa80eb.

[6] S. N. Raymond and A. Morbidelli. "Planet Formation: Key Mechanisms and Global Models." In: *Demographics of Exoplanetary Systems, Lecture Notes of the 3rd Advanced School on Exoplanetary Science*. Ed. by K. Biazzo et al. Vol. 466. Astrophysics and Space Science Library. Jan. 2022, pp. 3–82. DOI: 10.1007/978-3-030-88124-5_1.

[7] J. Bae et al. "Structured Distributions of Gas and Solids in Protoplanetary Disks." In: *arXiv e-prints*, arXiv:2210.13314 (Oct. 2022), arXiv:2210.13314. DOI: 10.48550/arXiv.2210.13314.

[8] N. M. Batalha et al. "Planetary Candidates Observed by Kepler. III. Analysis of the First 16 Months of Data." In: *ApJS* 204.2, 24 (Feb. 2013), p. 24. DOI: 10.1088/0067-0049/204/2/24.

[9] I. P. Williams and A. W. Cremin. "A Survey of Theories Relating to the Origin of the Solar System." In: *QJRAS* 9 (Mar. 1968), p. 40.

[10] V. S. Safronov. *Evolution of the protoplanetary cloud and formation of the earth and planets.* 1972.

[11] S. J. Weidenschilling. "Aerodynamics of solid bodies in the solar nebula." In: *MNRAS* 180 (July 1977), pp. 57–70. DOI: 10.1093/mnras/180.2.57.

[12] C. Hayashi. "Structure of the Solar Nebula, Growth and Decay of Magnetic Fields and Effects of Magnetic and Turbulent Viscosities on the Nebula." In: *Progress of Theoretical Physics Supplement* 70 (Jan. 1981), pp. 35–53. DOI: 10.1143/PTPS.70.35.

[13]   B. A. Smith and R. J. Terrile. "A Circumstellar Disk around β Pictoris." In: *Science* 226.4681 (Dec. 1984), pp. 1421–1424. DOI: 10.1126/science.226.4681.1421.

[14]   C. F. McKee and E. C. Ostriker. "Theory of Star Formation." In: *ARA&A* 45.1 (Sept. 2007), pp. 565–687. DOI: 10.1146/annurev.astro.45.051806.110602.

[15]   M. Heyer and T. M. Dame. "Molecular Clouds in the Milky Way." In: *ARA&A* 53 (Aug. 2015), pp. 583–629. DOI: 10.1146/annurev-astro-082214-122324.

[16]   H. Masunaga, S. M. Miyama, and S.-i. Inutsuka. "A Radiation Hydrodynamic Model for Protostellar Collapse. I. The First Collapse." In: *ApJ* 495.1 (Mar. 1998), pp. 346–369. DOI: 10.1086/305281.

[17]   H. Masunaga and S.-i. Inutsuka. "A Radiation Hydrodynamic Model for Protostellar Collapse. II. The Second Collapse and the Birth of a Protostar." In: *ApJ* 531.1 (Mar. 2000), pp. 350–365. DOI: 10.1086/308439.

[18]   L. Hartmann, G. Herczeg, and N. Calvet. "Accretion onto Pre-Main-Sequence Stars." In: *Annual Review of Astronomy and Astrophysics* 54.1 (2016), pp. 135–180. DOI: 10.1146/annurev-astro-081915-023347.

[19]   M. N. Machida and T. Matsumoto. "The origin and formation of the circumstellar disc." In: *MNRAS* 413.4 (June 2011), pp. 2767–2784. DOI: 10.1111/j.1365-2966.2011.18349.x.

[20]   D. M. Segura-Cox et al. "Four annular structures in a protostellar disk less than 500,000 years old." In: *Nature* 586.7828 (Oct. 2020), pp. 228–231. DOI: 10.1038/s41586-020-2779-6.

[21]   A. J. Cridland et al. "Early planet formation in embedded protostellar disks. Setting the stage for the first generation of planetesimals." In: *A&A* 662, A90 (June 2022), A90. DOI: 10.1051/0004-6361/202142207.

[22]   K. I. Öberg and E. A. Bergin. "Astrochemistry and compositions of planetary systems." In: *Phys. Rep.* 893 (Jan. 2021), pp. 1–48. DOI: 10.1016/j.physrep.2020.09.004.

[23]   G. P. Kuiper. "On the Origin of the Solar System." In: *Proceedings of the National Academy of Science* 37.1 (Jan. 1951), pp. 1–14. DOI: 10.1073/pnas.37.1.1.

[24]   A. G. W. Cameron. "Physics of the Primitive Solar Accretion Disk." In: *Moon and Planets* 18.1 (Feb. 1978), pp. 5–40. DOI: 10.1007/BF00896696.

[25]   A. P. Boss. "Giant planet formation by gravitational instability." In: *Science* 276 (Jan. 1997), pp. 1836–1839. DOI: 10.1126/science.276.5320.1836.

[26]   V. S. Safronov and E. V. Zvjagina. "Relative Sizes of the Largest Bodies during the Accumulation of Planets." In: *Icarus* 10.1 (Jan. 1969), pp. 109–115. DOI: 10.1016/0019-1035(69)90013-X.

[27]   P. Goldreich and W. R. Ward. "The Formation of Planetesimals." In: *ApJ* 183 (Aug. 1973), pp. 1051–1062. DOI: 10.1086/152291.

[28] J. B. Pollack et al. "Formation of the Giant Planets by Concurrent Accretion of Solids and Gas." In: *Icarus* 124.1 (Nov. 1996), pp. 62–85. DOI: 10.1006/icar.1996.0190.

[29] A. Toomre. "On the gravitational stability of a disk of stars." In: *ApJ* 139 (May 1964), pp. 1217–1238. DOI: 10.1086/147861.

[30] T. Matsuo et al. "Planetary Formation Scenarios Revisited: Core-Accretion versus Disk Instability." In: *ApJ* 662.2 (June 2007), pp. 1282–1292. DOI: 10.1086/517964.

[31] S. Nayakshin. "Dawes Review 7: The Tidal Downsizing Hypothesis of Planet Formation." In: *PASA* 34, e002 (Jan. 2017), e002. DOI: 10.1017/pasa.2016.55.

[32] W. Kley and R. P. Nelson. "Planet-Disk Interaction and Orbital Evolution." In: *ARA&A* 50 (Sept. 2012), pp. 211–249. DOI: 10.1146/annurev-astro-081811-125523.

[33] S.-J. Paardekooper et al. "Planet-Disk Interactions." In: *arXiv e-prints*, arXiv:2203.09595 (Mar. 2022), arXiv:2203.09595. DOI: 10.48550/arXiv.2203.09595.

[34] E. J. Lee and E. Chiang. "To Cool is to Accrete: Analytic Scalings for Nebular Accretion of Planetary Atmospheres." In: *ApJ* 811.1, 41 (Sept. 2015), p. 41. DOI: 10.1088/0004-637X/811/1/41.

[35] J. Drążkowska et al. "Planet Formation Theory in the Era of ALMA and Kepler: from Pebbles to Exoplanets." In: *Astronomical Society of the Pacific Conference Series*. Ed. by S. Inutsuka et al. Vol. 534. Astronomical Society of the Pacific Conference Series. July 2023, p. 717. DOI: 10.48550/arXiv.2203.09759.

[36] M. Lambrechts and A. Johansen. "Rapid growth of gas-giant cores by pebble accretion." In: *A&A* 544, A32 (Aug. 2012), A32. DOI: 10.1051/0004-6361/201219127.

[37] S. M. Andrews. "Observations of Protoplanetary Disk Structures." In: *ARA&A* 58 (Aug. 2020), pp. 483–528. DOI: 10.1146/annurev-astro-031220-010302.

[38] E. E. Mendoza V. "Infrared Photometry of T Tauri Stars and Related Objects." In: *ApJ* 143 (Mar. 1966), p. 1010. DOI: 10.1086/148584.

[39] E. E. Mendoza V. "Infrared Excesses in T Tauri Stars and Related Objects." In: *ApJ* 151 (Mar. 1968), p. 977. DOI: 10.1086/149497.

[40] M. Benisty et al. "Optical and Near-infrared View of Planet-forming Disks and Protoplanets." In: *arXiv e-prints*, arXiv:2203.09991 (Mar. 2022), arXiv:2203.09991. DOI: 10.48550/arXiv.2203.09991.

[41] C. R. O'Dell and Z. Wen. "Postrefurbishment Mission Hubble Space Telescope Images of the Core of the Orion Nebula: Proplyds, Herbig-Haro Objects, and Measurements of a Circumstellar Disk." In: *ApJ* 436 (Nov. 1994), p. 194. DOI: 10.1086/174892.

[42] S. V. W. Beckwith et al. "A Survey for Circumstellar Disks around Young Stellar Objects." In: *AJ* 99 (Mar. 1990), p. 924. DOI: 10.1086/115385.

[43] S. V. W. Beckwith and A. I. Sargent. "Particle Emissivity in Circumstellar Disks." In: *ApJ* 381 (Nov. 1991), p. 250. DOI: 10.1086/170646.

[44] A. Miotello et al. "Setting the Stage for Planet Formation: Measurements and Implications of the Fundamental Disk Properties." In: *Astronomical Society of the Pacific Conference Series*. Ed. by S. Inutsuka et al. Vol. 534. Astronomical Society of the Pacific Conference Series. July 2023, p. 501. DOI: 10.48550/arXiv.2203.09818.

[45] I. Kamp et al. "The formation of planetary systems with SPICA." In: *PASA* 38, e055 (Nov. 2021), e055. DOI: 10.1017/pasa.2021.31.

[46] E. A. Bergin and J. P. Williams. "The determination of protoplanetary disk masses." In: *arXiv e-prints*, arXiv:1807.09631 (July 2018), arXiv:1807.09631. DOI: 10.48550/arXiv.1807.09631.

[47] A. Morbidelli and S. N. Raymond. "Challenges in planet formation." In: *Journal of Geophysical Research (Planets)* 121.10 (Oct. 2016), pp. 1962–1980. DOI: 10.1002/2016JE005088.

[48] C. F. Manara et al. "X-shooter study of accretion in Chamaeleon I. II. A steeper increase of accretion with stellar mass for very low-mass stars?" In: *A&A* 604, A127 (Aug. 2017), A127. DOI: 10.1051/0004-6361/201630147.

[49] C. F. Manara et al. "X-shooter survey of disk accretion in Upper Scorpius. I. Very high accretion rates at age > 5 Myr." In: *A&A* 639, A58 (July 2020), A58. DOI: 10.1051/0004-6361/202037949.

[50] E. Gullbring et al. "Disk Accretion Rates for T Tauri Stars." In: *ApJ* 492.1 (Jan. 1998), pp. 323–341. DOI: 10.1086/305032.

[51] C. F. Manara et al. "Demographics of Young Stars and their Protoplanetary Disks: Lessons Learned on Disk Evolution and its Connection to Planet Formation." In: *Astronomical Society of the Pacific Conference Series*. Ed. by S. Inutsuka et al. Vol. 534. Astronomical Society of the Pacific Conference Series. July 2023, p. 539. DOI: 10.48550/arXiv.2203.09930.

[52] M. Gárate et al. "Large gaps and high accretion rates in photoevaporative transition disks with a dead zone." In: *A&A* 655, A18 (Nov. 2021), A18. DOI: 10.1051/0004-6361/202141444.

[53] P. J. Rodenkirch and C. P. Dullemond. "Dust entrainment in magnetically and thermally driven disk winds." In: *A&A* 659, A42 (Mar. 2022), A42. DOI: 10.1051/0004-6361/202142571.

[54] C. F. Manara et al. "Evidence for a correlation between mass accretion rates onto young stars and the mass of their protoplanetary disks." In: *A&A* 591, L3 (June 2016), p. L3. DOI: 10.1051/0004-6361/201628549.

[55] M. Keppler et al. "Discovery of a planetary-mass companion within the gap of the transition disk around PDS 70." In: *Astronomy and Astrophysics* 617 (Sept. 2018), A44. DOI: 10.1051/0004-6361/201832957.

[56] A. Müller et al. "Orbital and atmospheric characterization of the planet within the gap of the PDS 70 transition disk." In: *A&A* 617, L2 (Sept. 2018), p. L2. DOI: 10.1051/0004-6361/201833584.

[57] S. Y. Haffert et al. "Two accreting protoplanets around the young star PDS 70." In: *Nature Astronomy* 3 (June 2019), pp. 749–754. DOI: 10.1038/s41550-019-0780-5.

[58] M. Benisty et al. "A Circumplanetary Disk around PDS70c." In: *ApJ* 916.1, L2 (July 2021), p. L2. DOI: 10.3847/2041-8213/ac0f83.

[59] ALMA Partnership et al. "The 2014 ALMA Long Baseline Campaign: First Results from High Angular Resolution Observations toward the HL Tau Region." In: *ApJ* 808.1, L3 (July 2015), p. L3. DOI: 10.1088/2041-8205/808/1/L3.

[60] H. Nomura et al. "ALMA OBSERVATIONS OF A GAP AND A RING IN THE PROTOPLANETARY DISK AROUND TW HYA." In: *The Astrophysical Journal* 819.1 (Feb. 2016), p. L7. DOI: 10.3847/2041-8205/819/1/l7.

[61] L. M. Pérez et al. "Spiral density waves in a young protoplanetary disk." In: *Science* 353.6307 (Sept. 2016), 1519–1521. DOI: 10.1126/science.aaf8296.

[62] C. Ginski et al. "Direct detection of scattered light gaps in the transitional disk around HD 97048 with VLT/SPHERE." In: *Astronomy and Astrophysics* 595 (Nov. 2016), A112. DOI: 10.1051/0004-6361/201629265.

[63] J. de Boer et al. "Multiple rings in the transition disk and companion candidates around RX J1615.3-3255." In: *Astronomy and Astrophysics* 595 (Nov. 2016), A114. DOI: 10.1051/0004-6361/201629267.

[64] S. M. Andrews et al. "RINGED SUBSTRUCTURE AND A GAP AT 1au IN THE NEAREST PROTOPLANETARY DISK." In: *The Astrophysical Journal* 820.2 (Mar. 2016), p. L40. DOI: 10.3847/2041-8205/820/2/l40.

[65] A. Isella and N. Turner. "Signatures of Young Planets in the Continuum Emission From Protostellar Disks." In: *arXiv e-prints* (Aug. 2016). arXiv: 1608.05123.

[66] N. T. Kurtovic et al. "Size and structures of disks around very low mass stars in the Taurus star-forming region." In: *Astronomy and Astrophysics* 645 (Jan. 2021), A139. DOI: 10.1051/0004-6361/202038983.

[67] K. I. Öberg et al. "Molecules with ALMA at Planet-forming Scales (MAPS). I. Program Overview and Highlights." In: *ApJS* 257.1, 1 (Nov. 2021), p. 1. DOI: 10.3847/1538-4365/ac1432.

[68] S. M. Andrews et al. "The Disk Substructures at High Angular Resolution Project (DSHARP). I. Motivation, Sample, Calibration, and Overview." In: *ApJ* 869.2, L41 (Dec. 2018), p. L41. DOI: 10.3847/2041-8213/aaf741.

[69] L. A. Cieza et al. "The Ophiuchus DIsc Survey Employing ALMA (ODISEA) - I: project description and continuum images at 28 au resolution." In: *MN-RAS* 482.1 (Jan. 2019), pp. 698–714. DOI: 10.1093/mnras/sty2653.

[70] W. H. T. Vlemmings et al. "Stringent limits on the magnetic field strength in the disc of TW Hya. ALMA observations of CN polarisation." In: *A&A* 624, L7 (Apr. 2019), p. L7. DOI: 10.1051/0004-6361/201935459.

[71] R. Fu et al. "Solar nebula magnetic fields recorded in the Semarkona meteorite." In: (2014). DOI: 10.1126/science.1258022.

[72] B. P. Weiss, X.-N. Bai, and R. R. Fu. "History of the solar nebula from meteorite paleomagnetism." In: *Science Advances* 7.1 (Jan. 2021), eaba5967. DOI: 10.1126/sciadv.aba5967.

[73] J. B. Biersteker et al. "Implications of Philae Magnetometry Measurements at Comet 67P/Churyumov-Gerasimenko for the Nebular Field of the Outer Solar System." In: *ApJ* 875.1, 39 (Apr. 2019), p. 39. DOI: 10.3847/1538-4357/ab0f2a.

[74] M. Wardle. "Magnetic fields in protoplanetary disks." In: *Ap&SS* 311.1-3 (Oct. 2007), pp. 35–45. DOI: 10.1007/s10509-007-9575-8.

[75] L. Spitzer. *Physics of Fully Ionized Gases*. 1962.

[76] D. N. C. Lin and J. E. Pringle. "A viscosity prescription for a self-gravitating accretion disc." In: *Monthly Notices of the Royal Astronomical Society* 225.3 (Apr. 1987), pp. 607–613. DOI: 10.1093/mnras/225.3.607.

[77] G. Lodato and W. K. M. Rice. "Testing the locality of transport in self-gravitating accretion discs." In: *Monthly Notices of the Royal Astronomical Society* 351.2 (June 2004), 630–642. DOI: 10.1111/j.1365-2966.2004.07811.x.

[78] E. I. Vorobyov and S. Basu. "Secular evolution of viscous and self-gravitating circumstellar discs." In: *Monthly Notices of the Royal Astronomical Society* 393.3 (Mar. 2009), 822–837. DOI: 10.1111/j.1365-2966.2008.14376.x.

[79] W. Béthune, H. Latter, and W. Kley. "Spiral structures in gravito-turbulent gaseous disks." In: *A&A* 650, A49 (June 2021), A49. DOI: 10.1051/0004-6361/202040094.

[80] V. Urpin and A. Brandenburg. "Magnetic and vertical shear instabilities in accretion discs." In: *Monthly Notices of the Royal Astronomical Society* 294.3 (Mar. 1998), pp. 399–406. DOI: 10.1111/j.1365-8711.1998.01118.x.

[81] R. P. Nelson, O. Gressel, and O. M. Umurhan. "Linear and non-linear evolution of the vertical shear instability in accretion discs." In: *Monthly Notices of the Royal Astronomical Society* 435.3 (Sept. 2013), 2610–2632. DOI: 10.1093/mnras/stt1475.

[82] M.-K. Lin and A. N. Youdin. "COOLING REQUIREMENTS FOR THE VERTICAL SHEAR INSTABILITY IN PROTOPLANETARY DISKS." In: *The Astrophysical Journal* 811.1 (Sept. 2015), p. 17. DOI: 10.1088/0004-637x/811/1/17.

[83]   N. Manger et al. "High resolution parameter study of the vertical shear instability." In: *Monthly Notices of the Royal Astronomical Society* 499.2 (Oct. 2020), 1841–1853. DOI: 10.1093/mnras/staa2943.

[84]   M. Flock et al. "Gas and Dust Dynamics in Starlight-heated Protoplanetary Disks." In: *ApJ* 897.2, 155 (July 2020), p. 155. DOI: 10.3847/1538-4357/ab9641.

[85]   H. H. Klahr and P. Bodenheimer. "Turbulence in Accretion Disks: Vorticity Generation and Angular Momentum Transport via the Global Baroclinic Instability." In: *The Astrophysical Journal* 582.2 (Jan. 2003), 869–892. DOI: 10.1086/344743.

[86]   N. Raettig, W. Lyra, and H. Klahr. "A PARAMETER STUDY FOR BARO-CLINIC VORTEX AMPLIFICATION." In: *The Astrophysical Journal* 765.2 (Feb. 2013), p. 115. DOI: 10.1088/0004-637x/765/2/115.

[87]   G. Lesur et al. "Hydro-, Magnetohydro-, and Dust-Gas Dynamics of Protoplanetary Disks." In: *arXiv e-prints* (Mar. 2022). arXiv: 2203.09821.

[88]   S. A. Balbus and J. F. Hawley. "A Powerful Local Shear Instability in Weakly Magnetized Disks. I. Linear Analysis." In: *ApJ* 376 (July 1991), p. 214. DOI: 10.1086/170270.

[89]   R. D. Blandford and D. G. Payne. "Hydromagnetic flows from accretion disks and the production of radio jets." In: *MNRAS* 199 (June 1982), pp. 883–903. DOI: 10.1093/mnras/199.4.883.

[90]   I. Pascucci et al. "The Role of Disk Winds in the Evolution and Dispersal of Protoplanetary Disks." In: *Astronomical Society of the Pacific Conference Series*. Ed. by S. Inutsuka et al. Vol. 534. Astronomical Society of the Pacific Conference Series. July 2023, p. 567. DOI: 10.48550/arXiv.2203.10068.

[91]   X.-N. Bai and J. M. Stone. "Wind-driven Accretion in Protoplanetary Disks. I. Suppression of the Magnetorotational Instability and Launching of the Magnetocentrifugal Wind." In: *ApJ* 769.1, 76 (May 2013), p. 76. DOI: 10.1088/0004-637X/769/1/76.

[92]   X.-N. Bai et al. "MAGNETO-THERMAL DISK WINDS FROM PROTOPLANETARY DISKS." In: *The Astrophysical Journal* 818.2 (Feb. 2016), p. 152. DOI: 10.3847/0004-637x/818/2/152.

[93]   X.-N. Bai. "TOWARD A GLOBAL EVOLUTIONARY MODEL OF PROTOPLANETARY DISKS." In: *The Astrophysical Journal* 821.2 (Apr. 2016), p. 80. DOI: 10.3847/0004-637x/821/2/80.

[94]   K. Flaherty et al. "Measuring Turbulent Motion in Planet-forming Disks with ALMA: A Detection around DM Tau and Nondetections around MWC 480 and V4046 Sgr." In: *ApJ* 895.2, 109 (June 2020), p. 109. DOI: 10.3847/1538-4357/ab8cc5.

[95] C. Cui and X.-N. Bai. "Global Three-Dimensional Simulations of Outer Protoplanetary Disks with Ambipolar Diffusion." In: *arXiv e-prints* (June 2021). arXiv: 2106.10167.

[96] Z. Zhu et al. "DUST FILTRATION BY PLANET-INDUCED GAP EDGES: IMPLICATIONS FOR TRANSITIONAL DISKS." In: *The Astrophysical Journal* 755.1 (July 2012), p. 6. DOI: 10.1088/0004-637x/755/1/6.

[97] P. Pinilla, M. Benisty, and T. Birnstiel. "Ring shaped dust accumulation in transition disks." In: *Astronomy and Astrophysics* 545 (Sept. 2012), A81. DOI: 10.1051/0004-6361/201219315.

[98] S. Ataiee et al. "Asymmetric transition disks: Vorticity or eccentricity?" In: *Astronomy and Astrophysics* 553 (Apr. 2013), p. L3. DOI: 10.1051/0004-6361/201321125.

[99] M. de Juan Ovelar et al. "Imaging diagnostics for transitional discs." In: *Astronomy and Astrophysics* 560 (Dec. 2013), A111. DOI: 10.1051/0004-6361/201322218.

[100] R. Dong et al. "Observational Signatures of Planets in Protoplanetary Disks: Spiral Arms Observed in Scattered Light Imaging Can be Induced by Planets." In: *ApJ* 809.1, L5 (Aug. 2015), p. L5. DOI: 10.1088/2041-8205/809/1/L5.

[101] A. Pohl et al. "Scattered light images of spiral arms in marginally gravitationally unstable discs with an embedded planet." In: *Monthly Notices of the Royal Astronomical Society* 453.2 (Aug. 2015), 1768–1778. DOI: 10.1093/mnras/stv1746.

[102] P. Pinilla et al. "Gas and dust structures in protoplanetary disks hosting multiple planets." In: *A&A* 573, A9 (Jan. 2015), A9. DOI: 10.1051/0004-6361/201424679.

[103] M. A. Pyerin et al. "Constraining the properties of the potential embedded planets in the disk around HD 100546." In: *A&A* 656, A150 (Dec. 2021), A150. DOI: 10.1051/0004-6361/202141998.

[104] R. Teague et al. "A Kinematical Detection of Two Embedded Jupiter-mass Planets in HD 163296." In: *ApJ* 860.1, L12 (June 2018), p. L12. DOI: 10.3847/2041-8213/aac6d7.

[105] R. Teague, J. Bae, and E. A. Bergin. "Meridional flows in the disk around a young star." In: *Nature* 574.7778 (Oct. 2019), pp. 378–381. DOI: 10.1038/s41586-019-1642-0.

[106] R. Asensio-Torres et al. *Perturbers: SPHERE detection limits to planetary-mass companions in protoplanetary disks.* 2021. arXiv: 2103.05377.

[107] W. Lyra et al. "Planet formation bursts at the borders of the dead zone in 2D numerical simulations of circumstellar disks." In: *A&A* 497.3 (Apr. 2009), pp. 869–888. DOI: 10.1051/0004-6361/200811265.

[108] Z. Regály et al. "Possible planet-forming regions on submillimetre images." In: *MNRAS* 419.2 (Jan. 2012), pp. 1701–1712. DOI: 10.1111/j.1365-2966.2011.19834.x.

[109] M. Flock et al. "Gaps, rings, and non-axisymmetric structures in protoplanetary disks. From simulations to ALMA observations." In: *A&A* 574, A68 (Feb. 2015), A68. DOI: 10.1051/0004-6361/201424693.

[110] P. Pinilla et al. "Can dead zones create structures like a transition disk?" In: *A&A* 596, A81 (Dec. 2016), A81. DOI: 10.1051/0004-6361/201628441.

[111] F. Shu. *Physics of Astrophysics, Vol. II: Gas Dynamics.* 1991.

[112] X.-N. Bai. "Magnetorotational-instability-driven Accretion in Protoplanetary Disks." In: *ApJ* 739.1, 50 (Sept. 2011), p. 50. DOI: 10.1088/0004-637X/739/1/50.

[113] X.-N. Bai and J. M. Stone. "Effect of Ambipolar Diffusion on the Nonlinear Evolution of Magnetorotational Instability in Weakly Ionized Disks." In: *ApJ* 736.2, 144 (Aug. 2011), p. 144. DOI: 10.1088/0004-637X/736/2/144.

[114] S. A. Balbus. "Magnetohydrodynamics of Protostellar Disks." In: *arXiv e-prints*, arXiv:0906.0854 (June 2009), arXiv:0906.0854. DOI: 10.48550/arXiv.0906.0854.

[115] S. Fromang. "MRI-driven angular momentum transport in protoplanetary disks." In: *EAS Publications Series.* Ed. by P. Hennebelle and C. Charbonnel. Vol. 62. EAS Publications Series. Sept. 2013, pp. 95–142. DOI: 10.1051/eas/1362004.

[116] P. J. Armitage. "Physical processes in protoplanetary disks." In: *arXiv e-prints*, arXiv:1509.06382 (Sept. 2015), arXiv:1509.06382. DOI: 10.48550/arXiv.1509.06382.

[117] S. A. Balbus and J. F. Hawley. "Turbulent transport in accretion disks." In: *Accretion processes in Astrophysical Systems: Some like it hot! - eigth AstroPhysics Conference.* Ed. by S. S. Holt and T. R. Kallman. Vol. 431. American Institute of Physics Conference Series. Apr. 1998, pp. 79–88. DOI: 10.1063/1.55947.

[118] C. F. Gammie. "Layered Accretion in T Tauri Disks." In: *ApJ* 457 (Jan. 1996), p. 355. DOI: 10.1086/176735.

[119] J. P. Ruge et al. "Gaps, rings, and non-axisymmetric structures in protoplanetary disks: Emission from large grains." In: *A&A* 590, A17 (May 2016), A17. DOI: 10.1051/0004-6361/201526616.

[120] N. I. Shakura and R. A. Sunyaev. "Reprint of 1973A&A....24..337S. Black holes in binary systems. Observational appearance." In: *A&A* 500 (June 1973), pp. 33–51.

[121] D. Lynden-Bell and J. E. Pringle. "The evolution of viscous discs and the origin of the nebular variables." In: *MNRAS* 168 (Sept. 1974), pp. 603–637. DOI: 10.1093/mnras/168.3.603.

[122] J. F. Hawley, C. F. Gammie, and S. A. Balbus. "Local Three-dimensional Magnetohydrodynamic Simulations of Accretion Disks." In: *ApJ* 440 (Feb. 1995), p. 742. DOI: 10.1086/175311.

[123] J. F. Hawley, C. F. Gammie, and S. A. Balbus. "Local Three-dimensional Simulations of an Accretion Disk Hydromagnetic Dynamo." In: *ApJ* 464 (June 1996), p. 690. DOI: 10.1086/177356.

[124] J. M. Stone et al. "Three-dimensional Magnetohydrodynamical Simulations of Vertically Stratified Accretion Disks." In: *ApJ* 463 (June 1996), p. 656. DOI: 10.1086/177280.

[125] J. B. Simon, J. F. Hawley, and K. Beckwith. "Simulations of Magnetorotational Turbulence with a Higher-Order Godunov Scheme." In: *ApJ* 690.1 (Jan. 2009), pp. 974–997. DOI: 10.1088/0004-637X/690/1/974.

[126] S. W. Davis, J. M. Stone, and M. E. Pessah. "Sustained Magnetorotational Turbulence in Local Simulations of Stratified Disks with Zero Net Magnetic Flux." In: *ApJ* 713.1 (Apr. 2010), pp. 52–65. DOI: 10.1088/0004-637X/713/1/52.

[127] J. Shi, J. H. Krolik, and S. Hirose. "What is the Numerically Converged Amplitude of Magnetohydrodynamics Turbulence in Stratified Shearing Boxes?" In: *ApJ* 708.2 (Jan. 2010), pp. 1716–1727. DOI: 10.1088/0004-637X/708/2/1716.

[128] S. Hirose and N. J. Turner. "Heating and Cooling Protostellar Disks." In: *ApJ* 732.2, L30 (May 2011), p. L30. DOI: 10.1088/2041-8205/732/2/L30.

[129] S. Mori, X.-N. Bai, and S. Okuzumi. "Temperature Structure in the Inner Regions of Protoplanetary Disks: Inefficient Accretion Heating Controlled by Nonideal Magnetohydrodynamics." In: *ApJ* 872.1, 98 (Feb. 2019), p. 98. DOI: 10.3847/1538-4357/ab0022.

[130] S. Mori et al. "Evolution of the Water Snow Line in Magnetically Accreting Protoplanetary Disks." In: *arXiv e-prints* (May 2021). arXiv: 2105.13101.

[131] L. Hartmann. *Accretion Processes in Star Formation: Second Edition*. 2009.

[132] S. Okuzumi and S.-i. Inutsuka. "The Nonlinear Ohm's Law: Plasma Heating by Strong Electric Fields and its Effects on the Ionization Balance in Protoplanetary Disks." In: *ApJ* 800.1, 47 (Feb. 2015), p. 47. DOI: 10.1088/0004-637X/800/1/47.

[133] M. Kunitomo et al. "Photoevaporative Dispersal of Protoplanetary Disks around Evolving Intermediate-mass Stars." In: *ApJ* 909.2, 109 (Mar. 2021), p. 109. DOI: 10.3847/1538-4357/abdb2a.

[134] S. A. Balbus and J. C. B. Papaloizou. "On the Dynamical Foundations of α Disks." In: *ApJ* 521.2 (Aug. 1999), pp. 650–658. DOI: 10.1086/307594.

[135] T. Birnstiel, M. Fang, and A. Johansen. "Dust Evolution and the Formation of Planetesimals." In: *Space Sci. Rev.* 205.1-4 (Dec. 2016), pp. 41–75. DOI: 10.1007/s11214-016-0256-1.

[136] J. B. Pollack et al. "Composition and Radiative Properties of Grains in Molecular Clouds and Accretion Disks." In: *ApJ* 421 (Feb. 1994), p. 615. DOI: 10.1086/173677.

[137] F. Brauer, T. Henning, and C. P. Dullemond. "Planetesimal formation near the snow line in MRI-driven turbulent protoplanetary disks." In: *A&A* 487.1 (Aug. 2008), pp. L1–L4. DOI: 10.1051/0004-6361:200809780.

[138] T. Birnstiel, C. P. Dullemond, and F. Brauer. "Gas- and dust evolution in protoplanetary disks." In: *A&A* 513, A79 (Apr. 2010), A79. DOI: 10.1051/0004-6361/200913731.

[139] F. L. Whipple. "On certain aerodynamic processes for asteroids and comets." In: *From Plasma to Planet*. Ed. by A. Elvius. Jan. 1972, p. 211.

[140] Y. Nakagawa, M. Sekiya, and C. Hayashi. "Settling and growth of dust particles in a laminar phase of a low-mass solar nebula." In: *Icarus* 67 (Sept. 1986), pp. 375–390. DOI: 10.1016/0019-1035(86)90121-1.

[141] T. Takeuchi and D. N. C. Lin. "Radial Flow of Dust Particles in Accretion Disks." In: *ApJ* 581 (Dec. 2002), pp. 1344–1355. DOI: 10.1086/344437. eprint: astro-ph/0208552.

[142] M. Gárate et al. "The Dimming of RW Auriga: Is Dust Accretion Preceding an Outburst?" In: *ApJ* 871.1, 53 (Jan. 2019), p. 53. DOI: 10.3847/1538-4357/aaf4fc.

[143] M. Gárate et al. "Gas accretion damped by dust back-reaction at the snow line." In: *A&A* 635, A149 (Mar. 2020), A149. DOI: 10.1051/0004-6361/201936067.

[144] C. P. Dullemond and C. Dominik. "The effect of dust settling on the appearance of protoplanetary disks." In: *A&A* 421 (July 2004), pp. 1075–1086. DOI: 10.1051/0004-6361:20040284.

[145] A. N. Youdin and Y. Lithwick. "Particle stirring in turbulent gas disks: Including orbital oscillations." In: *Icarus* 192 (Dec. 2007), pp. 588–604. DOI: 10.1016/j.icarus.2007.07.012.

[146] M. Villenave et al. "Spatial segregation of dust grains in transition disks. SPHERE observations of 2MASS J16083070-3828268 and RXJ1852.3-3700." In: *A&A* 624, A7 (Apr. 2019), A7. DOI: 10.1051/0004-6361/201834800.

[147] M. Villenave et al. "Observations of edge-on protoplanetary disks with ALMA. I. Results from continuum data." In: *A&A* 642, A164 (Oct. 2020), A164. DOI: 10.1051/0004-6361/202038087.

[148] B. Dubrulle, G. Morfill, and M. Sterzik. "The dust subdisk in the protoplanetary nebula." In: *Icarus* 114.2 (Apr. 1995), pp. 237–246. DOI: 10.1006/icar.1995.1058.

[149] C. J. Clarke and J. E. Pringle. "The diffusion of contaminant through an accretion disc." In: *Monthly Notices of the Royal Astronomical Society* 235.2 (Nov. 1988), pp. 365–373. ISSN: 0035-8711. DOI: 10.1093/mnras/235.2.365.

[150]   S. Fromang and R. P. Nelson. "Global MHD simulations of stratified and turbulent protoplanetary discs. II. Dust settling." In: *A&A* 496.3 (Mar. 2009), pp. 597–608. DOI: 10.1051/0004-6361/200811220.

[151]   J. S. Mathis, W. Rumpl, and K. H. Nordsieck. "The size distribution of interstellar grains." In: *ApJ* 217 (Oct. 1977), pp. 425–433. DOI: 10.1086/155591.

[152]   A. Zsom and C. P. Dullemond. "A representative particle approach to coagulation and fragmentation of dust aggregates and fluid droplets." In: *A&A* 489.2 (Oct. 2008), pp. 931–941. DOI: 10.1051/0004-6361:200809921.

[153]   J. Drążkowska, F. Windmark, and C. P. Dullemond. "Planetesimal formation via sweep-up growth at the inner edge of dead zones." In: *A&A* 556, A37 (Aug. 2013), A37. DOI: 10.1051/0004-6361/201321566.

[154]   C. P. Dullemond and C. Dominik. "Dust coagulation in protoplanetary disks: A rapid depletion of small grains." In: *A&A* 434.3 (May 2005), pp. 971–986. DOI: 10.1051/0004-6361:20042080.

[155]   J. Blum and G. Wurm. "The growth mechanisms of macroscopic bodies in protoplanetary disks." In: *ARA&A* 46 (Sept. 2008), pp. 21–56. DOI: 10.1146/annurev.astro.46.060407.145152.

[156]   J. S. Dohnanyi. "Collisional Model of Asteroids and Their Debris." In: *J. Geophys. Res.* 74 (May 1969), pp. 2531–2554. DOI: 10.1029/JB074i010p02531.

[157]   R. R. Rafikov, K. Silsbee, and R. A. Booth. "A Fast $O(N^2)$ Fragmentation Algorithm." In: *ApJS* 247.2, 65 (Apr. 2020), p. 65. DOI: 10.3847/1538-4365/ab7b71.

[158]   G. Wurm, G. Paraskov, and O. Krauss. "Growth of planetesimals by impacts at ~25 m/s." In: *Icarus* 178.1 (Nov. 2005), pp. 253–263. DOI: 10.1016/j.icarus.2005.04.002.

[159]   A. Zsom et al. "The outcome of protoplanetary dust growth: pebbles, boulders, or planetesimals? II. Introducing the bouncing barrier." In: *A&A* 513, A57 (Apr. 2010), A57. DOI: 10.1051/0004-6361/200912976.

[160]   K. Wada et al. "Collisional Growth Conditions for Dust Aggregates." In: *ApJ* 702.2 (Sept. 2009), pp. 1490–1501. DOI: 10.1088/0004-637X/702/2/1490.

[161]   S.-i. Sirono. "Conditions for collisional growth of a grain aggregate." In: *Icarus* 167.2 (Feb. 2004), pp. 431–452. DOI: 10.1016/j.icarus.2003.09.018.

[162]   F. Windmark et al. "Planetesimal formation by sweep-up: how the bouncing barrier can be beneficial to growth." In: *A&A* 540, A73 (Apr. 2012), A73. DOI: 10.1051/0004-6361/201118475.

[163]   S. Okuzumi. "Electric Charging of Dust Aggregates and its Effect on Dust Coagulation in Protoplanetary Disks." In: *ApJ* 698.2 (June 2009), pp. 1122–1135. DOI: 10.1088/0004-637X/698/2/1122.

[164]   S. Okuzumi et al. "Electrostatic Barrier Against Dust Growth in Protoplanetary Disks. I. Classifying the Evolution of Size Distribution." In: *ApJ* 731.2, 95 (Apr. 2011), p. 95. DOI: 10.1088/0004-637X/731/2/95.

[165]   S. Okuzumi et al. "Electrostatic Barrier Against Dust Growth in Protoplan-
        etary Disks. II. Measuring the Size of the "Frozen" Zone." In: *ApJ* 731.2, 96
        (Apr. 2011), p. 96. DOI: 10.1088/0004-637X/731/2/96.

[166]   V. Akimkin. "Retention of Small Charged Dust in Planet Forming Disks."
        In: *Origins: From the Protosun to the First Steps of Life*. Ed. by B. G. Elmegreen,
        L. V. Tóth, and M. Güdel. Vol. 345. Jan. 2020, pp. 283–284. DOI: 10.1017/
        S1743921318008608.

[167]   V. Akimkin et al. "Coagulation-Fragmentation Equilibrium for Charged Dust:
        Abundance of Submicron Grains Increases Dramatically in Protoplanetary
        Disks." In: *arXiv e-prints*, arXiv:2306.16408 (June 2023), arXiv:2306.16408.
        DOI: 10.48550/arXiv.2306.16408.

[168]   B. Gundlach et al. "The tensile strength of ice and dust aggregates and its
        dependence on particle properties." In: *MNRAS* 479.1 (Sept. 2018), pp. 1273–
        1277. DOI: 10.1093/mnras/sty1550.

[169]   G. Musiolik and G. Wurm. "Contacts of Water Ice in Protoplanetary Disks—Laboratory
        Experiments." In: *ApJ* 873.1, 58 (Mar. 2019), p. 58. DOI: 10.3847/1538-4357/
        ab0428.

[170]   T. Steinpilz, J. Teiser, and G. Wurm. "Sticking Properties of Silicates in Plan-
        etesimal Formation Revisited." In: *ApJ* 874.1, 60 (Mar. 2019), p. 60. DOI: 10.
        3847/1538-4357/ab07bb.

[171]   C. W. Ormel and J. N. Cuzzi. "Closed-form expressions for particle relative
        velocities induced by turbulence." In: *A&A* 466 (May 2007), pp. 413–420. DOI:
        10.1051/0004-6361:20066899. eprint: astro-ph/0702303.

[172]   T. Birnstiel, C. W. Ormel, and C. P. Dullemond. "Dust size distributions
        in coagulation/fragmentation equilibrium: numerical solutions and analyt-
        ical fits." In: *A&A* 525, A11 (Jan. 2011), A11. DOI: 10.1051/0004-6361/
        201015228.

[173]   A. N. Youdin and J. Goodman. "Streaming Instabilities in Protoplanetary
        Disks." In: *ApJ* 620.1 (Feb. 2005), pp. 459–469. DOI: 10.1086/426895.

[174]   A. Johansen and A. Youdin. "Protoplanetary Disk Turbulence Driven by the
        Streaming Instability: Nonlinear Saturation and Particle Concentration." In:
        ApJ 662.1 (June 2007), pp. 627–641. DOI: 10.1086/516730.

[175]   A. Johansen et al. "Rapid planetesimal formation in turbulent circumstel-
        lar disks." In: *Nature* 448.7157 (Aug. 2007), pp. 1022–1025. DOI: 10.1038/
        nature06086.

[176]   X.-N. Bai and J. M. Stone. "Dynamics of Solids in the Midplane of Pro-
        toplanetary Disks: Implications for Planetesimal Formation." In: *ApJ* 722.2
        (Oct. 2010), pp. 1437–1459. DOI: 10.1088/0004-637X/722/2/1437.

[177]   J. B. Simon et al. "The Mass and Size Distribution of Planetesimals Formed
        by the Streaming Instability. I. The Role of Self-gravity." In: *ApJ* 822.1, 55
        (May 2016), p. 55. DOI: 10.3847/0004-637X/822/1/55.

[178] J. B. Simon et al. "Evidence for Universality in the Initial Planetesimal Mass Function." In: *ApJ* 847.2, L12 (Oct. 2017), p. L12. DOI: 10.3847/2041-8213/aa8c79.

[179] D. Carrera et al. "Protoplanetary Disk Rings as Sites for Planetesimal Formation." In: *AJ* 161.2, 96 (Feb. 2021), p. 96. DOI: 10.3847/1538-3881/abd4d9.

[180] M. Sekiya. "Quasi-Equilibrium Density Distributions of Small Dust Aggregations in the Solar Nebula." In: *Icarus* 133.2 (June 1998), pp. 298–309. DOI: 10.1006/icar.1998.5933.

[181] A. N. Youdin and F. H. Shu. "Planetesimal Formation by Gravitational Instability." In: *ApJ* 580.1 (Nov. 2002), pp. 494–505. DOI: 10.1086/343109.

[182] P. Pinilla and A. Youdin. "Particle Trapping in Protoplanetary Disks: Models vs. Observations." In: *Formation, Evolution, and Dynamics of Young Solar Systems*. Ed. by M. Pessah and O. Gressel. Vol. 445. 2017, p. 91. DOI: 10.1007/978-3-319-60609-5_4.

[183] S. M. Stammler and T. Birnstiel. "DustPy – A Python Package for Dust Evolution in Protoplanetary Disks." In: *arXiv e-prints* (July 2022). arXiv: 2207.00322.

[184] T. N. Delage et al. "Steady-state accretion in magnetized protoplanetary disks." In: *A&A* 658, A97 (Feb. 2022), A97. DOI: 10.1051/0004-6361/202141689.

[185] T. N. Delage et al. "The impact of dust evolution on the dead zone outer edge in magnetized protoplanetary disks." In: *A&A* 674 (2023), A190. DOI: 10.1051/0004-6361/202244731.

[186] M. R. Jankovic et al. "MRI-active inner regions of protoplanetary discs. I. A detailed model of disc structure." In: *MNRAS* 504.1 (June 2021), pp. 280–299. DOI: 10.1093/mnras/stab920.

[187] M. R. Jankovic et al. "MRI-active inner regions of protoplanetary discs - II. Dependence on dust, disc, and stellar parameters." In: *MNRAS* 509.4 (Feb. 2022), pp. 5974–5991. DOI: 10.1093/mnras/stab3370.

[188] O. Gressel et al. "Global Hydromagnetic Simulations of a Planet Embedded in a Dead Zone: Gap Opening, Gas Accretion, and Formation of a Protoplanetary Jet." In: *ApJ* 779.1, 59 (Dec. 2013), p. 59. DOI: 10.1088/0004-637X/779/1/59.

[189] O. Gressel et al. "Global Simulations of Protoplanetary Disks With Ohmic Resistivity and Ambipolar Diffusion." In: *ApJ* 801.2, 84 (Mar. 2015), p. 84. DOI: 10.1088/0004-637X/801/2/84.

[190] O. Gressel et al. "Global Hydromagnetic Simulations of Protoplanetary Disks with Stellar Irradiation and Simplified Thermochemistry." In: *ApJ* 896.2, 126 (June 2020), p. 126. DOI: 10.3847/1538-4357/ab91b7.

[191] S. Fromang and J. Papaloizou. "Dust settling in local simulations of tur-
       bulent protoplanetary disks." In: *A&A* 452.3 (June 2006), pp. 751–762. DOI:
       10.1051/0004-6361:20054612.

[192] Y. Nakagawa, K. Nakazawa, and C. Hayashi. "Growth and sedimentation
       of dust grains in the primordial solar nebula." In: *Icarus* 45.3 (Mar. 1981),
       pp. 517–528. DOI: 10.1016/0019-1035(81)90018-X.

[193] N. Dzyurkevich et al. "Trapping solids at the inner edge of the dead zone:
       3-D global MHD simulations." In: *A&A* 515, A70 (June 2010), A70. DOI: 10.
       1051/0004-6361/200912834.

[194] N. J. Turner, A. Carballido, and T. Sano. "Dust Transport in Protostellar
       Disks Through Turbulence and Settling." In: *ApJ* 708.1 (Jan. 2010), pp. 188–
       201. DOI: 10.1088/0004-637X/708/1/188.

[195] S. Okuzumi and S. Hirose. "Modeling Magnetorotational Turbulence in Pro-
       toplanetary Disks with Dead Zones." In: *ApJ* 742.2, 65 (Dec. 2011), p. 65. DOI:
       10.1088/0004-637X/742/2/65.

[196] M. Flock et al. "Turbulence and Steady Flows in Three-dimensional Global
       Stratified Magnetohydrodynamic Simulations of Accretion Disks." In: *ApJ*
       735.2, 122 (July 2011), p. 122. DOI: 10.1088/0004-637X/735/2/122.

[197] C. E. J. M. L. J. Terquem. "New Composite Models of Partially Ionized Pro-
       toplanetary Disks." In: *ApJ* 689.1 (Dec. 2008), pp. 532–538. DOI: 10.1086/
       592597.

[198] S. Okuzumi and S. Hirose. "Planetesimal Formation in Magnetorotationally
       Dead Zones: Critical Dependence on the Net Vertical Magnetic Flux." In:
       ApJ 753.1, L8 (July 2012), p. L8. DOI: 10.1088/2041-8205/753/1/L8.

[199] C. W. Ormel and S. Okuzumi. "The Fate of Planetesimals in Turbulent Disks
       with Dead Zones. II. Limits on the Viability of Runaway Accretion." In: *ApJ*
       771.1, 44 (July 2013), p. 44. DOI: 10.1088/0004-637X/771/1/44.

[200] N. Dzyurkevich et al. "Magnetized Accretion and Dead Zones in Proto-
       stellar Disks." In: *ApJ* 765.2, 114 (Mar. 2013), p. 114. DOI: 10.1088/0004-
       637X/765/2/114.

[201] T. Umebayashi and T. Nakano. "Fluxes of Energetic Particles and the Ioniza-
       tion Rate in Very Dense Interstellar Clouds." In: *PASJ* 33 (Jan. 1981), p. 617.

[202] S. Matsumura and R. E. Pudritz. "The Origin of Jovian Planets in Protostel-
       lar Disks: The Role of Dead Zones." In: *ApJ* 598.1 (Nov. 2003), pp. 645–656.
       DOI: 10.1086/378846.

[203] E. A. Bergin et al. "The Chemical Evolution of Protoplanetary Disks." In:
       Protostars and Planets V. Ed. by B. Reipurth, D. Jewitt, and K. Keil. Jan. 2007,
       p. 751. DOI: 10.48550/arXiv.astro-ph/0603358.

[204] T. Umebayashi and T. Nakano. "Effects of Radionuclides on the Ionization
       State of Protoplanetary Disks and Dense Cloud Cores." In: *ApJ* 690.1 (Jan.
       2009), pp. 69–81. DOI: 10.1088/0004-637X/690/1/69.

[205] C. Rab et al. "Stellar energetic particle ionization in protoplanetary disks around T Tauri stars." In: *A&A* 603, A96 (July 2017), A96. DOI: 10.1051/0004-6361/201630241.

[206] D. Perez-Becker and E. Chiang. "Surface Layer Accretion in Conventional and Transitional Disks Driven by Far-ultraviolet Ionization." In: *ApJ* 735.1, 8 (July 2011), p. 8. DOI: 10.1088/0004-637X/735/1/8.

[207] J. B. Simon et al. "Turbulence in the Outer Regions of Protoplanetary Disks. II. Strong Accretion Driven by a Vertical Magnetic Field." In: *ApJ* 775.1, 73 (Sept. 2013), p. 73. DOI: 10.1088/0004-637X/775/1/73.

[208] T. Umebayashi and T. Nakano. "Magnetic flux loss from interstellar clouds." In: *MNRAS* 243 (Mar. 1990), pp. 103–113. DOI: 10.1093/mnras/243.1.103.

[209] E. Anders and N. Grevesse. "Abundances of the elements: Meteoritic and solar." In: *Geochim. Cosmochim. Acta* 53.1 (Jan. 1989), pp. 197–214. DOI: 10.1016/0016-7037(89)90286-X.

[210] J. Igea and A. E. Glassgold. "X-Ray Ionization of the Disks of Young Stellar Objects." In: *ApJ* 518.2 (June 1999), pp. 848–858. DOI: 10.1086/307302.

[211] S. Okuzumi, T. Ueda, and N. J. Turner. "A global two-layer radiative transfer model for axisymmetric, shadowed protoplanetary disks." In: *PASJ* 74.4 (Aug. 2022), pp. 828–850. DOI: 10.1093/pasj/psac040.

[212] T. Preibisch et al. "The Origin of T Tauri X-Ray Emission: New Insights from the Chandra Orion Ultradeep Project." In: *ApJS* 160.2 (Oct. 2005), pp. 401–422. DOI: 10.1086/432891.

[213] X.-N. Bai and J. Goodman. "Heat and Dust in Active Layers of Protostellar Disks." In: *ApJ* 701.1 (Aug. 2009), pp. 737–755. DOI: 10.1088/0004-637X/701/1/737.

[214] M. Güdel et al. "The XMM-Newton extended survey of the Taurus molecular cloud (XEST)." In: *A&A* 468.2 (June 2007), pp. 353–377. DOI: 10.1051/0004-6361:20065724.

[215] B. J. McCall et al. "An enhanced cosmic-ray flux towards ζ Persei inferred from a laboratory study of the H_3^+-e^- recombination rate." In: *Nature* 422.6931 (Apr. 2003), pp. 500–502. DOI: 10.1038/nature01498.

[216] L. I. Cleeves, F. C. Adams, and E. A. Bergin. "Exclusion of Cosmic Rays in Protoplanetary Disks: Stellar and Magnetic Effects." In: *ApJ* 772.1, 5 (July 2013), p. 5. DOI: 10.1088/0004-637X/772/1/5.

[217] M. Wadhwa et al. "From Dust to Planetesimals: Implications for the Solar Protoplanetary Disk from Short-lived Radionuclides." In: *Protostars and Planets V*. Ed. by B. Reipurth, D. Jewitt, and K. Keil. Jan. 2007, p. 835.

[218] T. Lee, D. A. Papanastassiou, and G. J. Wasserburg. "Aluminum-26 in the early solar system: fossil or fuel?" In: *ApJ* 211 (Jan. 1977), pp. L107–L110. DOI: 10.1086/182351.

[219] G. J. MacPherson, A. M. Davis, and E. K. Zinner. "The distribution of aluminum-26 in the early Solar System - A reappraisal." In: *Meteoritics* 30 (July 1995), p. 365. DOI: 10.1111/j.1945-5100.1995.tb01141.x.

[220] F. A. Podosek and T. D. Swindle. "Extinct radionuclides." In: *Meteorites and the Early Solar System*. Ed. by J. F. Kerridge and M. S. Matthews. 1988, pp. 1093–1113.

[221] F. H. Shu et al. "X-rays and fluctuating X-winds from protostars." In: *Science* 277 (Jan. 1997), pp. 1475–1479. DOI: 10.1126/science.277.5331.1475.

[222] M. Gounelle et al. "The Irradiation Origin of Beryllium Radioisotopes and Other Short-lived Radionuclides." In: *ApJ* 640.2 (Apr. 2006), pp. 1163–1170. DOI: 10.1086/500309.

[223] A. G. W. Cameron. "The formation of the sun and planets." In: *Icarus* 1.1 (Jan. 1962), pp. 13–69. DOI: 10.1016/0019-1035(62)90005-2.

[224] T. Nakano and E. Tademaru. "Decoupling of Magnetic Fields in Dense Clouds with Angular Momentum." In: *ApJ* 173 (Apr. 1972), p. 87. DOI: 10.1086/151402.

[225] T. Sano et al. "Magnetorotational Instability in Protoplanetary Disks. II. Ionization State and Unstable Regions." In: *ApJ* 543.1 (Nov. 2000), pp. 486–501. DOI: 10.1086/317075.

[226] M. Ilgner and R. P. Nelson. "On the ionisation fraction in protoplanetary disks. II. The effect of turbulent mixing on gas-phase chemistry." In: *A&A* 445.1 (Jan. 2006), pp. 223–232. DOI: 10.1051/0004-6361:20053867.

[227] G. Wurm, F. Jungmann, and J. Teiser. "Ionizing protoplanetary discs in pebble collisions." In: *MNRAS* 517.1 (Nov. 2022), pp. L65–L70. DOI: 10.1093/mnrasl/slac077.

[228] B. T. Draine and B. Sutin. "Collisional Charging of Interstellar Grains." In: *ApJ* 320 (Sept. 1987), p. 803. DOI: 10.1086/165596.

[229] S. Mohanty, B. Ercolano, and N. J. Turner. "Dead, Undead, and Zombie Zones in Protostellar Disks as a Function of Stellar Mass." In: *ApJ* 764.1, 65 (Feb. 2013), p. 65. DOI: 10.1088/0004-637X/764/1/65.

[230] D. Semenov, D. Wiebe, and T. Henning. "Reduction of chemical networks. II. Analysis of the fractional ionisation in protoplanetary discs." In: *A&A* 417 (Apr. 2004), pp. 93–106. DOI: 10.1051/0004-6361:20034128.

[231] D. McElroy et al. "The UMIST database for astrochemistry 2012." In: *A&A* 550, A36 (Feb. 2013), A36. DOI: 10.1051/0004-6361/201220465.

[232] M. Oppenheimer and A. Dalgarno. "The Fractional Ionization in Dense Interstellar Clouds." In: *ApJ* 192 (Aug. 1974), pp. 29–32. DOI: 10.1086/153030.

[233] R. Nishi, T. Nakano, and T. Umebayashi. "Magnetic Flux Loss from Interstellar Clouds with Various Grain-Size Distributions." In: *ApJ* 368 (Feb. 1991), p. 181. DOI: 10.1086/169682.

[234]   R. P. Brent. "Algorithmsfor minimization without derivatives." In: *Prentice-Hall, Englewood Cliffs, NJ* (1973).

[235]   W. H. Press. *Numerical recipes in Fortran 77: the art of scientific computing*. Cambridge university press, 1992.

[236]   T. Umebayashi and T. Nakano. "Recombination of Ions and Electrons on Grains and the Ionization Degree in Dense Interstellar Clouds." In: *PASJ* 32 (Jan. 1980), p. 405.

[237]   B. T. Draine. *Physics of the Interstellar and Intergalactic Medium*. 2011.

[238]   M. Wardle and C. Ng. "The conductivity of dense molecular gas." In: *MN-RAS* 303.2 (Feb. 1999), pp. 239–246. DOI: 10.1046/j.1365-8711.1999.02211.x.

[239]   T. Sano and J. M. Stone. "The Effect of the Hall Term on the Nonlinear Evolution of the Magnetorotational Instability. II. Saturation Level and Critical Magnetic Reynolds Number." In: *ApJ* 577.1 (Sept. 2002), pp. 534–553. DOI: 10.1086/342172.

[240]   N. J. Turner, T. Sano, and N. Dziourkevitch. "Turbulent Mixing and the Dead Zone in Protostellar Disks." In: *ApJ* 659.1 (Apr. 2007), pp. 729–737. DOI: 10.1086/512007.

[241]   T. P. Fleming, J. M. Stone, and J. F. Hawley. "The Effect of Resistivity on the Nonlinear Stage of the Magnetorotational Instability in Accretion Disks." In: *ApJ* 530.1 (Feb. 2000), pp. 464–477. DOI: 10.1086/308338.

[242]   T. Sano and S. M. Miyama. "Magnetorotational Instability in Protoplanetary Disks. I. On the Global Stability of Weakly Ionized Disks with Ohmic Dissipation." In: *ApJ* 515.2 (Apr. 1999), pp. 776–786. DOI: 10.1086/307063.

[243]   M. Wardle. "The Balbus-Hawley instability in weakly ionized discs." In: *MNRAS* 307.4 (Aug. 1999), pp. 849–856. DOI: 10.1046/j.1365-8711.1999.02670.x.

[244]   J. F. Hawley and J. M. Stone. "Nonlinear Evolution of the Magnetorotational Instability in Ion-Neutral Disks." In: *ApJ* 501.2 (July 1998), pp. 758–771. DOI: 10.1086/305849.

[245]   M. W. Kunz and G. Lesur. "Magnetic self-organization in Hall-dominated magnetorotational turbulence." In: *MNRAS* 434.3 (Sept. 2013), pp. 2295–2312. DOI: 10.1093/mnras/stt1171.

[246]   M. W. Kunz. "On the linear stability of weakly ionized, magnetized planar shear flows." In: *MNRAS* 385.3 (Apr. 2008), pp. 1494–1510. DOI: 10.1111/j.1365-2966.2008.12928.x.

[247]   G. Lesur, M. W. Kunz, and S. Fromang. "Thanatology in protoplanetary discs. The combined influence of Ohmic, Hall, and ambipolar diffusion on dead zones." In: *A&A* 566, A56 (June 2014), A56. DOI: 10.1051/0004-6361/201423660.

[248] X.-N. Bai. "Hall Effect Controlled Gas Dynamics in Protoplanetary Disks. II. Full 3D Simulations toward the Outer Disk." In: *ApJ* 798.2, 84 (Jan. 2015), p. 84. DOI: 10.1088/0004-637X/798/2/84.

[249] X.-N. Bai. "Hall-effect-Controlled Gas Dynamics in Protoplanetary Disks. I. Wind Solutions at the Inner Disk." In: *ApJ* 791.2, 137 (Aug. 2014), p. 137. DOI: 10.1088/0004-637X/791/2/137.

[250] J. B. Simon et al. "Magnetically driven accretion in protoplanetary discs." In: *MNRAS* 454.1 (Nov. 2015), pp. 1117–1131. DOI: 10.1093/mnras/stv2070.

[251] M. Barraza-Alfaro et al. "Observability of the Vertical Shear Instability in protoplanetary disk CO kinematics." In: *arXiv e-prints* (June 2021). arXiv: 2106.01159.

[252] T. Sano et al. "Angular Momentum Transport by Magnetohydrodynamic Turbulence in Accretion Disks: Gas Pressure Dependence of the Saturation Level of the Magnetorotational Instability." In: *ApJ* 605.1 (Apr. 2004), pp. 321–339. DOI: 10.1086/382184.

[253] M. E. Pessah. "Angular Momentum Transport in Protoplanetary and Black Hole Accretion Disks: The Role of Parasitic Modes in the Saturation of MHD Turbulence." In: *ApJ* 716.2 (June 2010), pp. 1012–1027. DOI: 10.1088/0004-637X/716/2/1012.

[254] T. K. Suzuki, T. Muto, and S.-i. Inutsuka. "Protoplanetary Disk Winds via Magnetorotational Instability: Formation of an Inner Hole and a Crucial Assist for Planet Formation." In: *ApJ* 718.2 (Aug. 2010), pp. 1289–1304. DOI: 10.1088/0004-637X/718/2/1289.

[255] J. B. Simon et al. "Turbulence in the Outer Regions of Protoplanetary Disks. I. Weak Accretion with No Vertical Magnetic Flux." In: *ApJ* 764.1, 66 (Feb. 2013), p. 66. DOI: 10.1088/0004-637X/764/1/66.

[256] S. H. Lubow, J. C. B. Papaloizou, and J. E. Pringle. "Magnetic field dragging in accretion discs." In: *MNRAS* 267.2 (Mar. 1994), pp. 235–240. DOI: 10.1093/mnras/267.2.235.

[257] J. Guilet and G. I. Ogilvie. "Global evolution of the magnetic field in a thin disc and its consequences for protoplanetary systems." In: *MNRAS* 441.1 (June 2014), pp. 852–868. DOI: 10.1093/mnras/stu532.

[258] S. Okuzumi, T. Takeuchi, and T. Muto. "Radial Transport of Large-scale Magnetic Fields in Accretion Disks. I. Steady Solutions and an Upper Limit on the Vertical Field Strength." In: *ApJ* 785.2, 127 (Apr. 2014), p. 127. DOI: 10.1088/0004-637X/785/2/127.

[259] T. Takeuchi and S. Okuzumi. "Radial Transport of Large-scale Magnetic Fields in Accretion Disks. II. Relaxation to Steady States." In: *ApJ* 797.2, 132 (Dec. 2014), p. 132. DOI: 10.1088/0004-637X/797/2/132.

[260]   X.-N. Bai and J. M. Stone. "Hall Effect-Mediated Magnetic Flux Transport in Protoplanetary Disks." In: *ApJ* 836.1, 46 (Feb. 2017), p. 46. DOI: 10.3847/1538-4357/836/1/46.

[261]   Z. Zhu and J. M. Stone. "Global Evolution of an Accretion Disk with a Net Vertical Field: Coronal Accretion, Flux Transport, and Disk Winds." In: *ApJ* 857.1, 34 (Apr. 2018), p. 34. DOI: 10.3847/1538-4357/aaafc9.

[262]   K. A. Miller and J. M. Stone. "The Formation and Structure of a Strongly Magnetized Corona above a Weakly Magnetized Accretion Disk." In: *ApJ* 534.1 (May 2000), pp. 398–419. DOI: 10.1086/308736.

[263]   J. B. Simon, J. F. Hawley, and K. Beckwith. "Resistivity-driven State Changes in Vertically Stratified Accretion Disks." In: *ApJ* 730.2, 94 (Apr. 2011), p. 94. DOI: 10.1088/0004-637X/730/2/94.

[264]   M. Flock, T. Henning, and H. Klahr. "Turbulence in Weakly Ionized Protoplanetary Disks." In: *ApJ* 761.2, 95 (Dec. 2012), p. 95. DOI: 10.1088/0004-637X/761/2/95.

[265]   E. R. Parkin and G. V. Bicknell. "Equilibrium Disks, Magnetorotational Instability Mode Excitation, and Steady-state Turbulence in Global Accretion Disk Simulations." In: *ApJ* 763.2, 99 (Feb. 2013), p. 99. DOI: 10.1088/0004-637X/763/2/99.

[266]   E. R. Parkin and G. V. Bicknell. "Global simulations of magnetorotational turbulence - I. Convergence and the quasi-steady state." In: *MNRAS* 435.3 (Nov. 2013), pp. 2281–2298. DOI: 10.1093/mnras/stt1450.

[267]   S. Mohanty et al. "Inside-out Planet Formation. V. Structure of the Inner Disk as Implied by the MRI." In: *ApJ* 861.2, 144 (July 2018), p. 144. DOI: 10.3847/1538-4357/aabcd0.

[268]   L. Hartmann et al. "Accretion and the Evolution of T Tauri Disks." In: *ApJ* 495.1 (Mar. 1998), pp. 385–400. DOI: 10.1086/305277.

[269]   P. J. Armitage. "Physical Processes in Protoplanetary Disks." In: *Saas-Fee Advanced Course* 45 (Jan. 2019), p. 1. DOI: 10.1007/978-3-662-58687-7_1.

[270]   A. Scholz, R. Jayawardhana, and K. Wood. "Exploring Brown Dwarf Disks: A 1.3 mm Survey in Taurus." In: *ApJ* 645.2 (July 2006), pp. 1498–1508. DOI: 10.1086/504464.

[271]   S. Mohanty et al. "Protoplanetary Disk Masses from Stars to Brown Dwarfs." In: *ApJ* 773.2, 168 (Aug. 2013), p. 168. DOI: 10.1088/0004-637X/773/2/168.

[272]   R. Beck and P. Hoernes. "Magnetic spiral arms in the galaxy NGC6946." In: *Nature* 379.6560 (Jan. 1996), pp. 47–49. DOI: 10.1038/379047a0.

[273]   T. Fleming and J. M. Stone. "Local Magnetohydrodynamic Models of Layered Accretion Disks." In: *ApJ* 585.2 (Mar. 2003), pp. 908–920. DOI: 10.1086/345848.

[274] J. S. Oishi and M.-M. Mac Low. "On Hydrodynamic Motions in Dead Zones."
In: *ApJ* 704.2 (Oct. 2009), pp. 1239–1250. DOI: 10.1088/0004-637X/704/2/
1239.

[275] I. Pascucci et al. "A Steeper than Linear Disk Mass-Stellar Mass Scaling
Relation." In: *ApJ* 831.2, 125 (Nov. 2016), p. 125. DOI: 10.3847/0004-637X/
831/2/125.

[276] J. Haisch Karl E., E. A. Lada, and C. J. Lada. "Disk Frequencies and Lifetimes
in Young Clusters." In: *ApJ* 553.2 (June 2001), pp. L153–L156. DOI: 10.1086/
320685.

[277] C.-C. Yang and K. Menou. "Rayleigh adjustment of narrow barriers in pro-
toplanetary discs." In: *MNRAS* 402.4 (Mar. 2010), pp. 2436–2440. DOI: 10.
1111/j.1365-2966.2009.16047.x.

[278] J. E. Owen and J. A. Kollmeier. "Radiation pressure clear-out of dusty pho-
toevaporating discs." In: *MNRAS* 487.3 (Aug. 2019), pp. 3702–3714. DOI: 10.
1093/mnras/stz1591.

[279] N. van der Marel and G. Mulders. "A stellar mass dependence of structured
disks: a possible link with exoplanet demographics." In: *arXiv e-prints* (Apr.
2021). arXiv: 2104.06838.

[280] K. Ohtsuki, Y. Nakagawa, and K. Nakazawa. "Artificial acceleration in accu-
mulation due to coarse mass-coordinate divisions in numerical simulation."
In: *Icarus* 83.1 (Jan. 1990), pp. 205–215. DOI: 10.1016/0019-1035(90)90015-2.

[281] J. Drążkowska, F. Windmark, and C. P. Dullemond. "Modeling dust growth
in protoplanetary disks: The breakthrough case." In: *A&A* 567, A38 (July
2014), A38. DOI: 10.1051/0004-6361/201423708.

[282] K. Wada et al. "The Rebound Condition of Dust Aggregates Revealed by
Numerical Simulation of Their Collisions." In: *ApJ* 737, 36 (Aug. 2011), p. 36.
DOI: 10.1088/0004-637X/737/1/36.

[283] B. Gundlach et al. "Micrometer-sized ice particles for planetary-science ex-
periments - I. Preparation, critical rolling friction force, and specific surface
energy." In: *Icarus* 214 (Aug. 2011), pp. 717–723. DOI: 10.1016/j.icarus.
2011.05.005.

[284] B. Gundlach and J. Blum. "The Stickiness of Micrometer-sized Water-ice
Particles." In: *ApJ* 798, 34 (Jan. 2015), p. 34. DOI: 10.1088/0004-637X/798/1/
34.

[285] T. Birnstiel, C. P. Dullemond, and F. Brauer. "Dust retention in protoplane-
tary disks." In: *A&A* 503 (Aug. 2009), pp. L5–L8. DOI: 10.1051/0004-6361/
200912452.

[286] J. Blum and G. Wurm. "Experiments on Sticking, Restructuring, and Frag-
mentation of Preplanetary Dust Aggregates." In: *Icarus* 143.1 (Jan. 2000),
pp. 138–146. DOI: 10.1006/icar.1999.6234.

[287] H. Kimura et al. "Cohesion of Amorphous Silica Spheres: Toward a Better Understanding of The Coagulation Growth of Silicate Dust Aggregates." In: *ApJ* 812.1, 67 (Oct. 2015), p. 67. DOI: 10.1088/0004-637X/812/1/67.

[288] H. Kimura et al. "Is water ice an efficient facilitator for dust coagulation?" In: *MNRAS* 498.2 (Oct. 2020), pp. 1801–1813. DOI: 10.1093/mnras/staa2467.

[289] S. M. Stammler et al. "Redistribution of CO at the location of the CO ice line in evolving gas and dust disks." In: *A&A* 600, A140 (Apr. 2017), A140. DOI: 10.1051/0004-6361/201629041.

[290] S. S. Suriano et al. "Rings and gaps produced by variable magnetic disc winds and avalanche accretion streams - I. Axisymmetric resistive MHD simulations." In: *MNRAS* 468.4 (July 2017), pp. 3850–3868. DOI: 10.1093/mnras/stx735.

[291] S. S. Suriano et al. "The formation of rings and gaps in magnetically coupled disc-wind systems: ambipolar diffusion and reconnection." In: *MNRAS* 477.1 (June 2018), pp. 1239–1257. DOI: 10.1093/mnras/sty717.

[292] S. S. Suriano et al. "The formation of rings and gaps in wind-launching non-ideal MHD discs: three-dimensional simulations." In: *MNRAS* 484.1 (Mar. 2019), pp. 107–124. DOI: 10.1093/mnras/sty3502.

[293] X. Hu et al. "Formation of dust rings and gaps in non-ideal MHD disks through meridional gas flows." In: *MNRAS* (July 2022). DOI: 10.1093/mnras/stac1799.

[294] R. Tazaki and C. Dominik. "How large are the monomers of dust aggregates in planet-forming disks?: Insights from quantitative optical and near-infrared polarimetry." In: *arXiv e-prints* (Apr. 2022). arXiv: 2204.08506.

[295] X.-N. Bai. "The Role of Tiny Grains on the Accretion Process in Protoplanetary Disks." In: *ApJ* 739.1, 51 (Sept. 2011), p. 51. DOI: 10.1088/0004-637X/739/1/51.

[296] B. Zhao et al. "Protostellar disc formation enabled by removal of small dust grains." In: *MNRAS* 460.2 (Aug. 2016), pp. 2050–2076. DOI: 10.1093/mnras/stw1124.

[297] P. Marchand et al. "Protostellar Collapse: Regulation of the Angular Momentum and Onset of an Ionic Precursor." In: *ApJ* 900.2, 180 (Sept. 2020), p. 180. DOI: 10.3847/1538-4357/abad99.

[298] Y. Hasegawa and T. Takeuchi. "Viscous Instability Triggered by Layered Accretion in Protoplanetary Disks." In: *ApJ* 815.2, 99 (Dec. 2015), p. 99. DOI: 10.1088/0004-637X/815/2/99.

[299] A. Johansen, M. Kato, and T. Sano. "A new viscous instability in weakly ionised protoplanetary discs." In: *Advances in Plasma Astrophysics*. Ed. by A. Bonanno, E. de Gouveia Dal Pino, and A. G. Kosovichev. Vol. 274. June 2011, pp. 50–55. DOI: 10.1017/S1743921311006569.

[300] C. P. Dullemond and A. B. T. Penzlin. "Dust-driven viscous ring-instability in protoplanetary disks." In: *A&A* 609, A50 (Jan. 2018), A50. DOI: 10.1051/0004-6361/201731878.

[301] C. P. Dullemond et al. *RADMC-3D: A multi-purpose radiative transfer tool*. Astrophysics Source Code Library, record ascl:1202.015. Feb. 2012. ascl: 1202.015.

[302] J. Huang et al. "CO and Dust Properties in the TW Hya Disk from High-resolution ALMA Observations." In: *ApJ* 852.2, 122 (Jan. 2018), p. 122. DOI: 10.3847/1538-4357/aaa1e7.

[303] C. P. Dullemond et al. "The Disk Substructures at High Angular Resolution Project (DSHARP). VI. Dust Trapping in Thin-ringed Protoplanetary Disks." In: *ApJ* 869.2, L46 (Dec. 2018), p. L46. DOI: 10.3847/2041-8213/aaf742.

[304] R. V. E. Lovelace. "Dynamo model of double radio sources." In: *Nature* 262.5570 (Aug. 1976), pp. 649–652. DOI: 10.1038/262649a0.

[305] G. I. Ogilvie and M. Livio. "Launching of Jets and the Vertical Structure of Accretion Disks." In: *ApJ* 553.1 (May 2001), pp. 158–173. DOI: 10.1086/320637.

[306] D. M. Rothstein and R. V. E. Lovelace. "Advection of Magnetic Fields in Accretion Disks: Not So Difficult After All." In: *ApJ* 677.2 (Apr. 2008), pp. 1221–1232. DOI: 10.1086/529128.

[307] T. K. Suzuki and S.-i. Inutsuka. "Magnetohydrodynamic Simulations of Global Accretion Disks with Vertical Magnetic Fields." In: *ApJ* 784.2, 121 (Apr. 2014), p. 121. DOI: 10.1088/0004-637X/784/2/121.

[308] N. Manger, T. Pfeil, and H. Klahr. "High-resolution parameter study of the vertical shear instability - II: dependence on temperature gradient and cooling time." In: *MNRAS* 508.4 (Dec. 2021), pp. 5402–5409. DOI: 10.1093/mnras/stab2599.

[309] G. R. J. Lesur. "Systematic description of wind-driven protoplanetary discs." In: *A&A* 650, A35 (June 2021), A35. DOI: 10.1051/0004-6361/202040109.

[310] C. J. Clarke, A. Gendrin, and M. Sotomayor. "The dispersal of circumstellar discs: the role of the ultraviolet switch." In: *MNRAS* 328.2 (Dec. 2001), pp. 485–491. DOI: 10.1046/j.1365-8711.2001.04891.x.

[311] C. J. Clarke. "The photoevaporation of discs around young stars in massive clusters." In: *MNRAS* 376.3 (Apr. 2007), pp. 1350–1356. DOI: 10.1111/j.1365-2966.2007.11547.x.

[312] J. E. Owen et al. "Radiation-hydrodynamic models of X-ray and EUV photoevaporating protoplanetary discs." In: *MNRAS* 401.3 (Jan. 2010), pp. 1415–1428. DOI: 10.1111/j.1365-2966.2009.15771.x.

[313] J. E. Owen, B. Ercolano, and C. J. Clarke. "Protoplanetary disc evolution and dispersal: the implications of X-ray photoevaporation." In: *MNRAS* 412.1 (Mar. 2011), pp. 13–25. DOI: 10.1111/j.1365-2966.2010.17818.x.

[314]   J. E. Owen, C. J. Clarke, and B. Ercolano. "On the theory of disc photoevaporation." In: *MNRAS* 422.3 (May 2012), pp. 1880–1901. DOI: 10.1111/j.1365-2966.2011.20337.x.

[315]   G. Perotti et al. "Water in the terrestrial planet-forming zone of the PDS 70 disk." In: *arXiv e-prints*, arXiv:2307.12040 (July 2023), arXiv:2307.12040. DOI: 10.48550/arXiv.2307.12040.

[316]   T. C. H. Lau et al. "Rapid formation of massive planetary cores in a pressure bump." In: *A&A* 668, A170 (Dec. 2022), A170. DOI: 10.1051/0004-6361/202244864.

[317]   T. C. H. Lau and M. H. Lee. "Parallelization of the Symplectic Massive Body Algorithm (SyMBA) N-body Code." In: *Research Notes of the American Astronomical Society* 7.4, 74 (Apr. 2023), p. 74. DOI: 10.3847/2515-5172/accc8a.

DECLARATION

I hereby declare that the material presented in this thesis is a result of my work and that of my acknowledged collaborators, except where otherwise suitably referenced.

Heidelberg, August 2023

Timmy N. Delage